ENGINEERING SKELETAL MUSCLE FOR HISTOLOGICAL AND FUNCTIONAL REGENERATION FOLLOWING VOLUMETRIC MUSCLE LOSS

by

Jordana Gilbert-Honick

A dissertation submitted to Johns Hopkins University in conformity with the requirements for the degree of Doctor of Philosophy

Baltimore, Maryland

March 2020

Abstract

Tissue engineered skeletal muscle has great potential to successfully treat volumetric muscle loss (VML), a condition with no ideal clinical treatment option. A broad range of engineered muscle constructs have been evaluated in preclinical models of VML with a few cases of clinical use as well. Despite improvements to muscle function following treatment, histological regeneration of the muscle tissue has varied broadly with the method of treatment. In addition, few studies have attempted to restore the damaged connection between muscle and nerve and robust neuromuscular regeneration following VML injury has yet to be achieved. To enable functional and histological muscle regeneration post-VML, a broad range of factors must be considered including a biomimetic and biocompatible scaffold design, selection of a translatable cell source, and modification of the regenerating environment to promote neuromuscular regeneration. The **objective** of this thesis was to develop a translatable engineered muscle construct with the ability to promote neuromuscular regeneration of murine VML defects.

This body of work describes a multistep approach towards the fulfillment of the above objective. First, an electrospun fibrin scaffold was developed that mimics the native stiffness and alignment of skeletal muscle and when combined with mouse myoblasts, enables the formation of an implantable skeletal muscle construct and robust muscle regeneration post-VML. The next two chapters describe the myogenic potential of two translatable cell sources on electrospun scaffolds: adipose derived stem cells (ASCs) and human pluripotent stem cells (hPSCs). While ASCs resulted in limited *in vitro* myogenesis on electrospun fibers and provided a minimal regenerative benefit, hPSC-derived myoblasts purified for a Pax7 myogenic subpopulation

demonstrated robust *in vitro* myogenesis in 3D constructs. While the regenerative potential of hPSC-derived myoblast constructs in muscle defects was limited, the results are a promising step towards the use of these cells to treat VML. Lastly, engineered muscle constructs were pre-treated to promote acetylcholine receptor (AChR) clustering and neuromuscular regeneration through the delivery of agrin, a heparan sulfate proteoglycan, by either chemically tethering agrin to the scaffold or providing it in solution. Following implantation in VML defects for four weeks, the agrin pre-treated muscle constructs resulted in increased neuromuscular junctions, regenerating myofibers, vascular infiltration, neural infiltration, and nuclear yes-associated protein within the defect region. In addition, sustained local agrin delivery by the tethered agrin constructs resulted in higher densities of neurofilament and regenerating myofibers than soluble agrin constructs. This investigation revealed the remarkable potential of agrin-modified engineered muscle constructs for neuromuscular regeneration post-VML. Taken together, these findings have significant implications for the development of tissue engineered skeletal muscle and enabling the functional and histological regeneration of skeletal muscle following VML.

Advisor: Warren Grayson, PhD

Thesis Readers: Warren Grayson, PhD and Hai-Quan Mao, PhD

Thesis Committee: Warren Grayson, PhD; Richard Lovering, PhD, PT; Hai-Quan Mao, PhD; Kathryn Wagner, MD, PhD

Acknowledgements

Many people have helped me reach this important milestone in my life. I would like to thank my thesis advisor, Warren Grayson, for offering invaluable support during my time in his lab. He has been a great professional mentor and provided guidance on planning experiments, how to give effective presentations, and helped me develop skills in critical analysis. He has also provided me with the valuable opportunity to lecture several times in his graduate and undergraduate Tissue Engineering course, which was a great experience. Thank you also to the members of my thesis committee, Hai-Quan Mao, Kathryn Wagner, and Rich Lovering, for their helpful suggestions and guidance over the past seven years.

There have been numerous other students who have helped me with my research and I would like to highlight a few who had a major impact. First, thank you to Brian Ginn, Daphne Hutton, Tracy Zhang, and Justin Morrissette-McAlmon for their patience in answering questions and helping to train me in my early years as a Ph.D. student. I would also like to thank the other graduate students who made significant contributions to my research in later years including Sarah Somers, Aaron Black, Lexi Rindone, and Shama Iyer. We collaborated on several parts of this dissertation research and they have always provided helpful feedback on my data. Thank you as well to all other members of the Grayson lab, past and present, for suggestions during lab meeting presentations, help around the lab, and creating a generally collegial environment to work in. I would also like to acknowledge the various other labs that have collaborated with me on this research: the Mao lab, Wagner lab, Lovering lab, and Lee lab. Thank you for all the time and resources that you have invested in this project.

I would not have reached this point without the support of my family. Attempting a Ph.D. in biomedical engineering was not a typical career path within my family or community, and a seed of doubt from someone could have derailed the idea before I began. Thank you to my entire family for their constant support and belief in me, as well as their tolerance of my studying at family functions. I would of course especially like to thank my husband, Moshe, for his unwavering belief in my ability to succeed and constant encouragement. Moshe has done everything from escorting me to lab if I had to feed cells late on a Saturday night to dropping his own experiments so that I could complete mine on days when we needed to unexpectedly pick up our daughter from daycare. I truly could not have done it without him. My parents as well have been instrumental in enabling my education, supporting me every step of the way, and providing valuable guidance. Thank you to them for everything they have done to support me throughout my life and in helping me get to this point. I would also like to thank my mother in-law and father in-law for their invaluable help and support over the years as Moshe and I completed our PhDs and began a family at the same time. Finally, I would like to thank my daughter, Ashira, for enriching my life and truly making me a better researcher. The two years of her life so far have coincided with my most productive and successful years in the lab. She not only inspires me to do my best work, but when I am faced with a research challenge I find myself thinking how I would advise Ashira to approach the problem and a solution immediately presents itself.

I would also like to acknowledge my sources of funding which have been critical to performing this research. The Maryland Stem Cell Research Fund provided financial support for much of the project. I was also fortunate to be awarded a National Research Service Award by the NIH which has supported me over the last two years, and I would like to thank both the

National Institute of Arthritis and Musculoskeletal and Skin Diseases for selecting me for the fellowship as well as the United States taxpayers who have funded the fellowship.

Table of Contents

List of Tables

List of Figures

Chapter 1 Introduction

1.1 Volumetric Muscle Loss

Incidence and Major Causes of Volumetric Muscle Loss

Skeletal muscle comprises around 40% of total human body mass and is the most abundant tissue in the human body[1]. It has a high regenerative capacity following traumatic injury except in cases of volumetric muscle loss. Volumetric muscle loss (VML) is a defect where the muscle's natural repair mechanisms are overwhelmed leading to chronic functional deficits in the affected muscle[2–5]. Causes of VML include combat injury, trauma (e.g. car accidents), tumor ablation, bone fracture fixation, and degenerative disease[3,6]. The incidence of VML in the general US population and the associated economic burden are difficult to estimate since there are no surgical or billing codes specifically dedicated to VML[7]. Estimates obtained from referencing surgical therapies (e.g. free functional muscle transfer), physical and occupational therapies (e.g. gait training and strength exercises), and advanced wound care are little more than educated guesses and may be highly inaccurate. However, some analyses have been performed for military personnel with extremity battlefield wounds. Among medically-retired military service-members, VML is a major cause of service-disqualifying disability, contributing to over 90% of muscle conditions leading to long-term disability and resulting in a projected lifetime disability cost of $341,300 per individual[3]. Of US servicemembers with extremity battlefield wounds from 2001-2005, 53% involved penetrating soft-tissue wounds and 26% were bone fractures, the majority of which (82%) were open fractures with severe soft tissue damage[8]. These results were similar to those of previous wars[8,9]. Among the military patient population, 67% of total cases of VML were

in the lower limb (**Figure 1.1a**) and 58% of patients also had a bone fracture, 14% had a nerve injury, and 5% had a vascular injury in the limb with the VML[3].

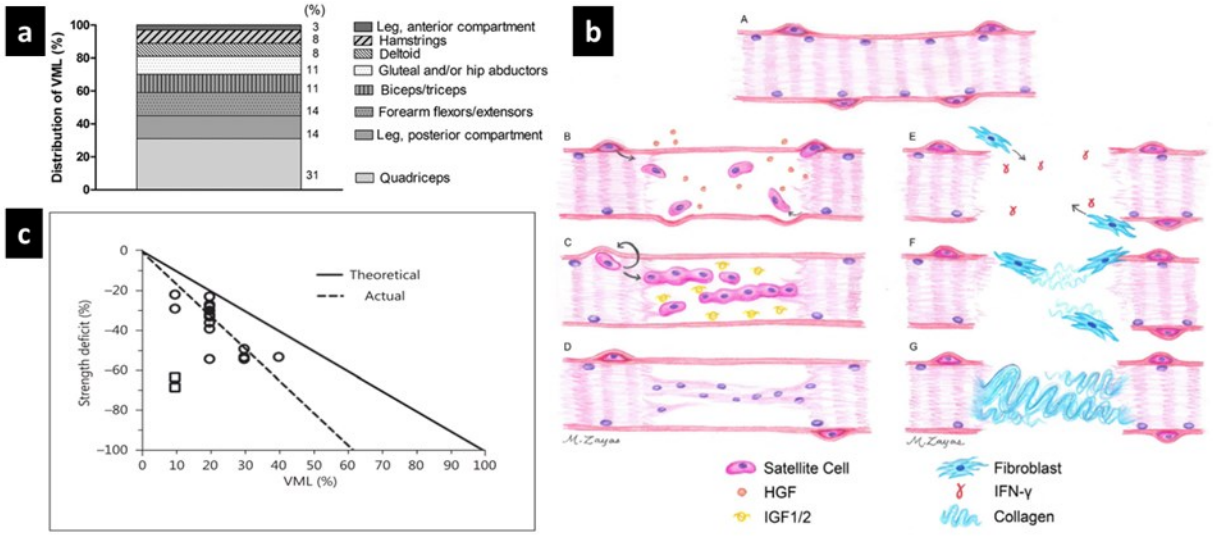

Figure 1.1. Incidence and biology of VML. a) Distribution of VML location in the body among medically retired military servicemembers. **b)** Differences between native skeletal muscle regeneration (left) and deposition of scar tissue following VML (right). **c)** Percent strength deficit post-VML in various pre-clinical models. Models include rat, mouse, and pig defects of the quadricep, TA, LD, EDL, and gastrocnemius muscles. Actual values are significantly higher than theoretical predictions based on mass loss alone.

Biology of VML

VML is characterized by a persistent functional deficit and unlike other causes of muscle injury such as freeze injury, crush, toxin, ischemia reperfusion, and eccentric contractions which fully recover their function after 1-2 months, untreated VML injuries do not regain their full functional capacity[7]. The native regenerative potential of skeletal muscle through its resident satellite stem cell population has been extensively reviewed elsewhere[10,11]. In brief, muscle follows a predictable timeline in its response to injury, progressing through phases of degeneration and inflammation, regeneration, and fibrosis[4,11]. The degeneration and inflammation phase begins within minutes of muscle injury and extends 1-2 weeks post-injury. In this phase, injury-induced

disruption of the sarcolemma and basal lamina allow for the influx of extracellular calcium which causes autodigestion and necrosis of myofibers followed by immune cell invasion. Approximately 1 week post-injury, muscle regeneration begins and peaks at around 2 weeks post-injury. In small injuries like contusions or sprains, the regeneration phase is characterized by satellite cell differentiation to myoblasts and fusion with other myoblasts or the remaining mature myofibers. In tandem, low-level fibrosis deposited by fibroblasts bridges the gap between still-functional myofibers in order to transmit force along the muscle as well as guide the regenerating myoblasts along the injury site. The fibrosis and scarring phase begins around 2 weeks post-injury and increases for up to 4 weeks post-injury and is characterized by increased fibroblast-mediated collagen deposition. There have been numerous prior reviews describing the disruptions to this regenerative pathway caused by VML injuries (**Figure 1.1b**)[4,5,7,12–15]. After the large-scale loss of tissue typified by VML, fibroblasts deposit a large volume of scar tissue faster than the rate of myoblast fusion and regeneration, ultimately preventing muscle regeneration within the defect site[4]. This results in a significant functional deficit to the damaged muscle that persists over time.

Changes to gene expression within a muscle post-VML also have a significant impact on regenerative potential. Aguilar et. al. utilized RNA-sequencing to investigate molecular changes within untreated VML-injured muscle and those treated with a minced muscle graft. In untreated controls they found that inflammation-related genes and genes associated with ECM deposition and fibrotic remodeling remained upregulated up to 28 days post-injury[16]. Interestingly, despite finding significant improvements in both muscle strength and histological regeneration of the defect within the treated muscles, they found no difference in gene expression compared to untreated controls. Persistent upregulation of genes associated with fibrosis (*collagen 3*, *MMP2*, *TGFβ1*, *PDGFRα*, *PDPN*) and negative regulation of myogenesis (*Id2*, MSC, *Snai1*, *MSTN*,

BMP1) was present in both the treated and untreated groups at similar levels. This indicates that histologic and functional regeneration of VML-injured muscle is not sufficient to alter the pro-fibrotic gene expression profile of the muscle at 28 days post-injury. Further research is required on the potential for continued remodeling of the muscle tissue and associated changes in gene expression at later time points.

Understanding Functional Deficits in VML: A Multifaceted Injury

The exact causes of the significant functional deficits observed after VML remain somewhat obscure. Aside from the frank loss of muscle tissue and associated contractile proteins typified by VML, there are a variety of detrimental impacts to the remaining muscle body that lead to sub-optimal strength output by the muscle. In an analysis of 15 preclinical studies, Corona, Wenke, and Ward identified a trend describing the relationship between the strength deficit of VML-injured muscles and the extent of initial injury[7]. Using regression analysis of VML-induced strength deficits compared to initial percent VML, they found that a VML-injured muscle's force output was significantly lower than what would be expected from the loss of muscle mass alone (**Figure 1.1c**). Specifically, the observed strength deficits were 60% higher per percent VML than would be predicted by muscle tissue loss alone. This observation was maintained across various preclinical animal models of VML and at a range of time points up to 4 months post-injury. It was hypothesized that the increased functional deficits were due to persistent detrimental impacts to remaining muscle including denervation, disorganization of myofiber architecture, and impaired force transmission to the tendon.

Further elucidating this trend, Corona et. al. assessed strength deficits and the extent of motoneuron axotomy in a rat tibialis anterior (TA) VML model with an initial 20% TA mass loss[17]. In addition to confirming that the 20% mass loss yielded higher strength deficits ranging

from 45-90%, by labeling motoneurons innervating the entire TA prior to and immediately following the VML injury they found that there was no motoneuron death within the spinal cord due to VML but 57-79% of motoneurons had undergone significant axotomy and lost interaction with the TA muscle. Notably, this loss of motoneuron interaction with the muscle was present as early as 3 days post-injury and remained constant up to 21 days post-injury. Cross-sections of the injured TA revealed an increase in the number of myofibers in the healing muscle over time, which combined with the constant level of motoneuron axotomy suggests the occurrence of motor unit reorganization and expansion with each motoneuron innervating multiple myofibers. Further research is required on the impact of VML-induced motoneuron axotomy and motor unit expansion and the capability to engineer functional muscle-nerve interactions post-VML. Tissue engineered muscle constructs that incorporate methods to encourage neural infiltration and the formation of functional neuromuscular junctions post-VML are a promising avenue to restore interaction between the muscle and nerve post-VML.

Preclinical Models of VML

Tissue engineered muscle grafts have been implanted in a broad range of preclinical models of VML spanning many muscle types within mice, rats, rabbits, dogs, and pigs (**Figure 1.2**)[18]. Variability of preclinical models occurs both within a species, where for example VML defects in mice have been evaluated in at least six different muscles, as well as across species as the defect size scales larger to approach that of VML defects in humans. These VML models have been extremely useful for understanding the biology of injury as well as for testing therapeutic strategies. Experiments in mice and rats provide for the highest throughput and facilitate the study of cell survival, histoarchitecture of the regenerated muscle, vascular and neural ingrowth, and functional regeneration. Scaling-up biomaterial-based interventions from defects where the

average mass of lost tissue is < 20 mg in mice or < 160 mg in rats to clinically relevant scenarios, which may easily be 3 or 4 orders of magnitude larger, is non-trivial. Biomaterial-based treatments of VML in larger preclinical (e.g. dog, pig) and even clinical models have generally resulted in functional improvements although histologic assessments have shown remarkably modest muscle regeneration.

The actual size of the VML defect may not be the only factor driving inconsistencies in reporting therapeutic benefits. The lack of standardization in muscle type and location may also be a factor. For example, biomaterial strategies are agnostic to muscle types, which range from fusiform to bipennate. When comparing studies with differing results it is important to keep in mind the differences in anatomy presented by varying muscles within a single animal as well as anatomical differences between species. Differences between species become particularly relevant when studying regeneration of the neuromuscular junction (NMJ). Striking differences in NMJ morphology and size exist between vertebrate species with an increase in postsynaptic folding and focusing of the NMJ at a single site on the myofiber as one progresses from fish to mammals[19]. Human nerve terminals and NMJs are among the smallest among vertebrates and contain significantly higher levels of postsynaptic membrane folding which in humans increases the synaptic area by 8 times.

Although a broad range of preclinical models of varied VML defect sizes have been investigated along with the associated damage to vasculature and innervation, there is still no universal consensus on the definition of a critical sized defect in skeletal muscle, which might be utilized as a benchmark control and means of standardization in study design. A recent study by Anderson et. al. was the first to define a critical sized skeletal muscle defect within the mouse

quadriceps and characterized changes to fibrosis, macrophage infiltration, myofiber formation, vasculature, and innervation across a range of defect sizes[20].

When muscle is resected longitudinally (as opposed to use of a biopsy punch) or defects are partial-thickness it is difficult to maintain consistency in the defect size. Approaches to maintain reproducibility have included tattooing a region of fixed dimensions prior to removal[21], measuring the weight of muscle removed incrementally during surgery[22,23], measuring the functional deficit as muscle is removed incrementally during surgery[24], and recording the total removed muscle weight per animal[25]. To reproducibly assess differences in muscle damage and regeneration at different VML defect sizes, Anderson et. al. utilized biopsy punches with diameters ranging from 2 to 4 millimeters (corresponding to approximately 4-32% of the quadriceps wet weight) to create full-thickness defects in the mid-belly of the quadriceps with the leg in an extended position. They assessed tissue damage up to 28 days post-injury[20]. Fibrosis, persistence of CD68+ macrophages, and presence of myofibers with relatively small cross-sectional area increased over time with increasing defect size. By 28 days post-injury, the 2 mm size defects exhibited lower amounts of amounts of fibrosis and had similar levels of centrally-nucleated myofibers to uninjured controls demonstrating its status as a sub-critical sized defect with healing potential.

Defects of 3 mm diameters were further investigated for neural and vascular regeneration. Transgenic Thy1-YFP mice, whose motor neurons express yellow fluorescent protein (YFP), were used to visualize innervation within the defect site up to 28 days post-injury. Although motor neurons were visible in uninjured muscle tissue, significant autofluorescence in VML defects prevented visualization of neurons within the injured muscle. Postsynaptic acetylcholine receptor clusters demonstrated marked differences in morphology between control and injured muscle and

were classified into three categories: normal pretzel, abnormal fragmented, and newly-formed. No clusters with a normal pretzel morphology were visible within the defect site at either 14 or 28 days post-injury. Cluster morphology within the defect remodeled over time with significantly more clusters demonstrating a fragmented morphology at 14 days post-injury, decreasing over time to contain more of the newly formed clusters 28 days post-injury. Of the clusters present at 28 days, 44.3% had an abnormal fragmented morphology and 55.7% appeared to be newly formed clusters. Despite remodeling in cluster morphology over time, no clusters were associated with a regenerated motor neuron. Total vascular volume within the defect site was quantified 28 days post-injury using Microfil and micro CT and demonstrated that injured muscle had a larger vascular volume as well as perfused vessels with a larger diameter compared to uninjured controls.

Although significant in its definition and characterization of a skeletal muscle critical sized defect, the previous study did not measure force deficits due to injury, which is a defining feature of VML and standard for the field. They also utilized adult female mice between 3 and 9 months of age and assessed VML injury to the quadriceps muscle alone. When translating the 3 mm critical size defect model to future studies, potential differences in anatomy and regeneration between various different muscle types as well as differences due to species, age, and sex must be considered. Larger animals generally have different muscle fiber type compositions than smaller animals, with a higher prevalence of slow twitch myofibers[26]. Young rodents have a higher density of satellite cells[27] with differences in remodeling post-VML[23] and may therefore require a larger critical sized defect than older animals. Differences in muscle anatomy and regeneration due to sex must also be considered as it has been shown that over 3,000 genes are differentially regulated between male and female muscle[28]. Fiber type composition, myofiber cross-sectional area, fatigue recovery, and endurance testing differ greatly between men and women in various

muscles and sex-based differences in skeletal muscle composition are present across species[26]. Male myofibers generally have a lower type I composition, a larger cross-sectional area, and are more fatigable than those in females, and women typically exhibit longer endurance and faster recovery from muscle exhaustion than men which may have implications for sex-based differences in regeneration following injury. Future studies on the applicability of the 3 mm critical sized defect to alternative preclinical models and potential differences due to muscle type, age, sex, and species would be of great benefit to the field.

Significant advancements have been made in the use of pre-vascularized constructs within VML-injured muscle, including successes in characterization of *in vitro* vascular development, anastomosis with host vasculature post-implantation, and the development of several useful methodologies for *in vivo* vascular quantification. The majority of those studies have utilized a mouse abdominal defect model[29–35], however, and it is unclear if either the constructs implanted or the success of vascular regeneration would translate to muscles with a different anatomy or larger animal models with a higher vascular demand post-injury. As described below, different muscles within the body have varying degrees of heterogeneity in capillary density throughout the tissue and constructs that successfully anastomose with host vasculature within one defect model may not perform as well elsewhere in the body or in the process of scaling up to treat a human VML defect. Further research on the versatility of pre-vascularized constructs under development as well as their feasibility for use in large animal models is required. These differences between species in muscle anatomy, vascularization, and innervation must be considered when comparing

preclinical models to each other and when developing a tissue engineered muscle graft for VML treatment in humans.

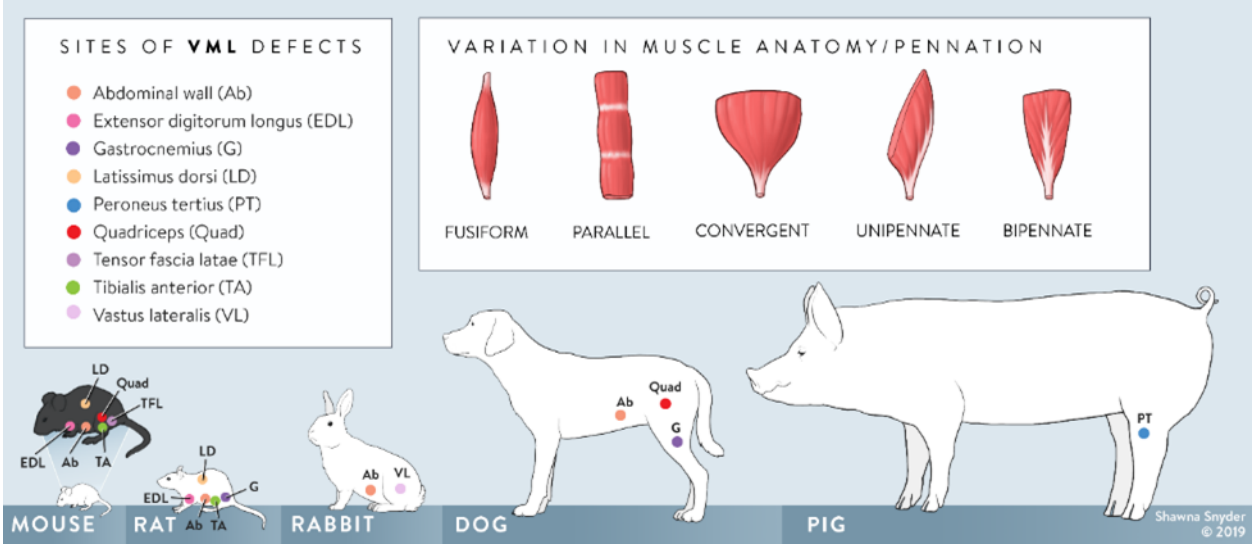

Figure 1.2. Preclinical models of VML. Various models of VML have been developed in mice, rats, rabbits, dogs, and pigs at a range of anatomical locations across species and with differences in muscle anatomy and pennation.

Current Clinical Treatment of VML

Optimal VML treatment depends on the location and size of a specific VML defect. The functional deficits associated with a small VML defect may be ameliorated by hypertrophy of surrounding muscles via physical therapy while muscles with larger VML defects do not respond to physical therapy[16]. Current treatment options for large-scale VML are limited and include transfer of an autologous free muscle flap[2,36], muscle transposition[2,3], or amputation and power bracing[36], all of which have major limitations. Donor site morbidity, lack of donor tissue, and the need for a highly skilled surgical team complicate VML treatment and decrease positive patient outcomes[6,36]. In battlefield injuries, free or rotational muscle flaps are often utilized as soft tissue coverage in the treatment of severe type III open tibia fractures but do not recover the strength deficit of the injured muscle surrounding the fracture[3]. Tissue engineering strategies aim to fill the muscle tissue volume and enable dense regeneration of vascularized and

innervated muscle as well as to recover the full function of VML-injured muscle. An understanding of skeletal muscle vascular biology, neural biology and the impediments to regeneration caused by VML is vital to successful tissue engineered treatments.

1.2 Tissue Engineering Strategies to Regenerate Skeletal Muscle

A range of approaches for the development of tissue engineered skeletal muscle have been reported with previous excellent reviews summarizing the current state of the field[18,37–44]. Tissue engineered skeletal muscle approaches fall into four main categories: acellular scaffolds, cells-only rolled monolayers, minced muscle grafts, and tissue engineered muscle grafts (**Figure 1.3**)[45]. Each of these may be combined with growth factors or other pro-regenerative molecules or peptides to improve the regenerative response. There are benefits and drawbacks to both the acellular or cell-based approaches to skeletal muscle tissue engineering, with acellular scaffolds providing a lower regulatory hurdle and faster translation to the clinic[45] while cell-based approaches often result in significantly more histological muscle regeneration post-VML compared to acellular counterparts[25,46]. Minced muscle grafts have excellent engraftment potential but require *in vitro* expansion or the use of large volumes of host muscle tissue. The following sections will provide a brief overview of each of the four approaches.

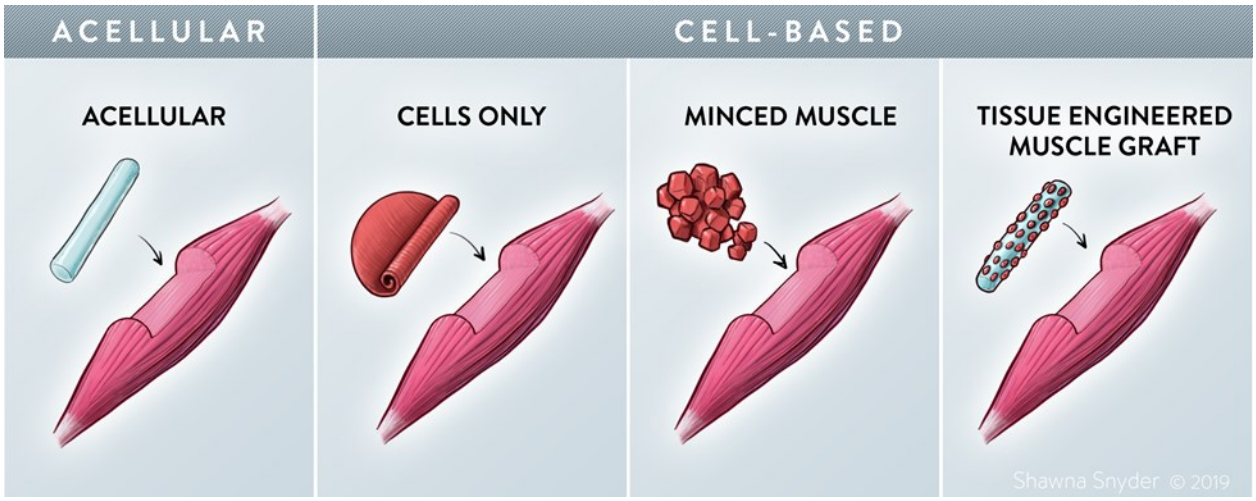

Figure 1.3. Tissue engineered skeletal muscle techniques are either acellular or cell-based.

Four general approaches exist for engineered skeletal muscle: acellular scaffolds, rolled cell monolayers, minced muscle grafts, and cell-seeded scaffolds (here termed Tissue Engineered Muscle Grafts; TEMGs).

Cells-Only Approach

Cell sources for skeletal muscle tissue engineering have been reviewed elsewhere[45,47,48] and include satellite cells or other muscle-derived precursor cells, perivascular stem cells, bone marrow-derived mesenchymal stem cells, umbilical cord mesenchymal stem cells, adipose-derived stem cells, induced pluripotent stem cells, and embryonic stem cells. Major considerations when selecting a myogenic cell source include expansion capacity, immunogenicity, translatability, differentiation potential, and engraftment potential *in vivo.* Muscle precursor cells are frequently combined with a material scaffold to provide mechanical support and assist in cell retention within the defect, or acellular scaffolds are implanted that are designed to promote endogenous muscle repair.

The cells-only approach traditionally involves the injection of a muscle cell suspension with or without a hydrogel carrier[45,49]. However, this strategy, which does not provide significant structural support, is not particularly suitable for the treatment of VML defects. Instead,

implantable cells-only 3D constructs have been developed by culturing muscle-derived cells in monolayer until confluence and subsequent delamination and formation of a cylindrical 3D construct[50,51]. One study cultured primary mouse muscle cells in monolayer for approximately 8 days and implanted the delaminated monolayer as a 3D construct in a mouse VML model of the extensor digitorum longus muscle[51]. Muscle and vasculature were present within the explanted graft after 15 days *in vivo.* In a second study, rat primary muscle precursor cells were cultured as monolayers that were then delaminated and rolled into cylindrical constructs with bone marrow cell-derived bone anchors at each end[50]. The constructs were then implanted in a rat 30% VML model of the tibialis anterior and assessed after 28 days, at which they exhibited the formation of small myofibers and the presence of associated vasculature and nerves. The above cells-only approaches benefit from a high cell density within the constructs and promising results within small VML defects *in vivo*, but may be limited in their ability to scale-up to clinically relevant sizes and can be difficult to surgically manipulate due to the lack of a scaffold.

Acellular Scaffolds

There has been much discussion on the ideal biomaterial for skeletal muscle tissue engineering scaffolds, which has been the focus of several previous reviews[18,39,44,52]. The two main biomaterial categories are natural versus synthetic materials with hybrid materials as a third smaller category. Natural materials used for skeletal muscle tissue engineering include decellularized extracellular matrix (dECM) from various organ and donor sources as well as ECM components and other naturally-derived materials such as fibrin, hyaluronic acid, laminin, collagen, chitosan, silk fibroin, alginate, agarose, keratin, and gelatin. Synthetic materials used for skeletal muscle tissue engineering include polypropylene, poly-(lactic acid), poly-(glycolic acid), poly-lactic-co-glycolic acid, poly(ε-caprolactone), polyurethane, and polyethylene glycol. Natural

materials are bioactive, may contain pro-myogenic growth factors, and are biocompatible but have limitations in batch-to-batch variability, immunogenicity, and a lack of precise design control. Synthetic materials offer improvements in the tunability of mechanical cues and nanoscale topography as well as consistency between batches but may be limited in their biocompatibility, cell adhesion, and need for functionalization due to limited bioactivity. Hybrid materials are combinations of natural and synthetic biomaterials and are promising options for combining the bioactivity of natural materials with the precision of synthetic materials, but they may also retain the limitations of both categories. Biomaterials in all categories can be utilized with a broad range of fabrication methods that each provides different mechanical properties, degradation timeline, topographical cues to cultured cells, and *in vivo* engraftment potential. Generally, naturally derived biomaterials have resulted in improved muscle, vascular, and neural regeneration with significant emphasis placed on the method of fabrication and presence of alignment cues, native growth factors, myogenic stiffness, biocompatibility, and degradation timeline.

There are currently conflicting reports on the ability of acellular scaffolds to consistently promote muscle regeneration and functional recovery post-VML. Acellular scaffolds are more clinically translatable with a lower regulatory burden and acellular decellularized ECM (dECM) scaffolds have the potential to modulate the immune response and macrophage polarization to promote muscle regeneration[53]. Despite these benefits, acellular scaffolds used to treat VML defects often lack histological evidence of muscle regeneration. There has been a broad range of preclinical studies comparing the efficacy of acellular or cell-seeded dECM[21,46,54–59] with mixed results. There have also been two recent clinical trials evaluating the regenerative potential of acellular dECM within human VML defects[58,60–62]. In an effort to address significant variability in reported results, the efficacy of using acellular dECM to treat VML injuries was systematically

evaluated in a large 2015 study with 120 rats (8 rats/group)[46]. Acellular dECM was implanted into two different defect models, a musculotendinous junction (MTJ) model and a VML model, and compared to untreated or autograft-treated controls at a range of time points up to four months post-treatment. In the MTJ model, the implanted ECM scaffold completely resorbed without muscle tissue remodeling. In the VML model, the implanted ECM scaffold improved muscle function by 17% but remodeled into fibrous tissue lacking significant *de novo* myofiber formation and muscle regeneration (**Figure 1.4c**). Physical rehabilitation via voluntary cage wheel running did not improve the regenerative response of the decellularized ECM treatment. The ability of the implanted scaffold to improve contractile properties of the muscle without correlated muscle fiber regeneration within the defect area may be explained by scaffold mediated functional fibrosis and has been demonstrated repeatedly[22,25,46,63–65]. The implanted scaffold likely functions as a mechanical bridge between intact muscle fibers, transmitting the contractile force across the defect and subsequently resulting in a higher measured functional outcome. This is in contrast to force production by regenerating myofibers within the defect, which is the ultimate goal of a tissue engineered treatment for VML.

The first use of a tissue engineered construct for VML treatment in humans was 2010 case report where a single patient with a blast-induced VML injury to the thigh was treated with acellular decellularized porcine ECM. The patient demonstrated improved isokinetic performance four months post-treatment and evidence of muscle formation in CT imaging nine months post-treatment with no histology shown[58]. Following initial testing in mouse quadriceps VML defects with moderate regeneration following 6 months of dECM treatment[54], a recent study assessed 13 human patients with VML injuries at a range of anatomical locations with an average muscle tissue deficit of 66.2% and evaluated the efficacy of an acellular scaffold composed of porcine dECM to

promote muscle regeneration[54,60]. Measurements of force production, improvements in functional task performance, and electromyographical assessments up to six months post-operatively demonstrated that patients showed an average of 37.3% improvement in muscle strength, 27.1% improvement in range of motion, and some electrophysiological improvements compared to pre-operative values[60]. Regeneration and remodeling of the muscle tissue within the defect site was demonstrated through histology of muscle biopsies and CT or MRI imaging (**Figure 1.4a)**. Disconnected islands of muscle tissue were present within the defect site in addition to vasculature, mobilization of perivascular stem cells, and some neurofilament (**Figure 1.4b**). Although the study incorporates robust functional testing and CT data there was limited histological analysis shown. Since muscle tissue engineering data in humans is scarce, the field would benefit from a more detailed quantification of the histological data including muscle, vascular, and nerve density across the biopsy sample as well as a detailed representation of variability among patients.

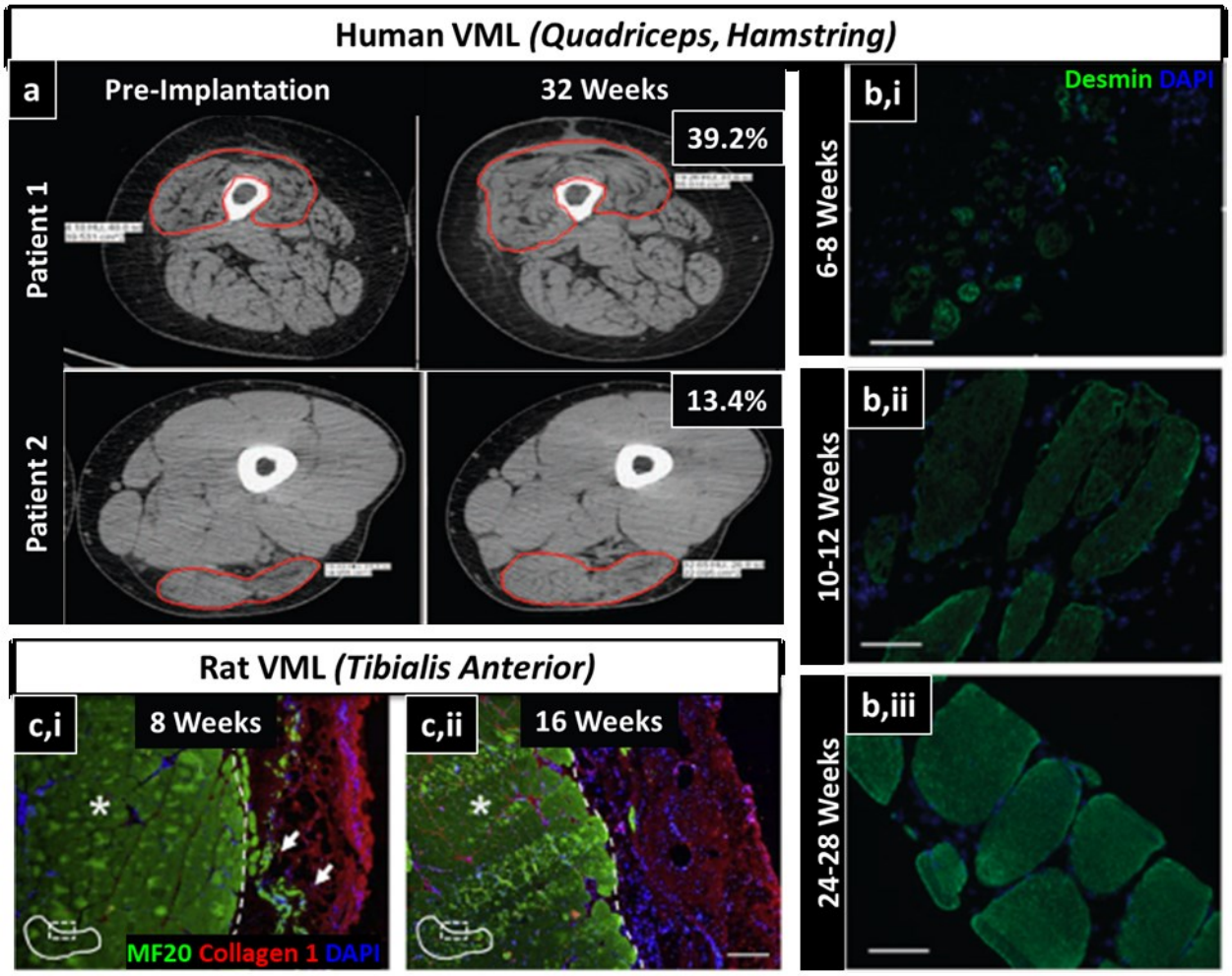

Figure 1.4. Acellular decellularized ECM treatment in VML defects may promote regeneration with some variability. a,b) Minimal regeneration over time in a rat TA VML model following treatment with acellular decellularized ECM (urinary bladder matrix). **c)** Desmin (top) and MHC (bottom) positive muscle cells within mouse quadriceps VML defects following treatment with acellular decellularized ECM (urinary bladder matrix). Inset: center of the ECM implantation site. **d,e)** Computerized axial tomography images of human quadriceps VML defect pre-implantation (top) and 8 months following treatment with acellular decellularized ECM demonstrating the presence of new tissue within the defect region. **f-h)** Histological analysis over time of muscle biopsies from human VML patients treated with acellular decellularized ECM. MF20: pan-isoform myosin; MHC: myosin heavy chain.

Minced Muscle Grafts (MMGs)

A third category investigated pre-clinically for VML treatment is the use of minced muscle grafts. In this approach, autologous or allogeneic muscle is removed via biopsy, minced into small pieces and often expanded *in vitro*, and placed in the VML defect[16,22,66–68]. Minced muscle grafts

can be easily generated from the patient's own muscle and result in excellent muscle regeneration but require *in vitro* expansion or the use of large volumes of host muscle tissue. Due to the need to limit the volume of biopsied muscle removed from the patient, the minced muscle must be expanded for this approach to be feasible for the treatment of large defects. To maximize the regenerative potential of small muscle biopsies, the potential to decrease the percent composition of minced muscle by mixing it with pro-regenerative hydrogels and growth factors is an area of active investigation. Expansion capacity of autologous minced muscle within a collagen hydrogel at a range of muscle compositions was investigated and compared to grafts composed of 100% autologous minced muscle (**Figure 1.5a,b**)[66]. It was found that reducing the percent of muscle by 50% retained its ability to promote functional improvement post-VML but the regenerating defects treated with 50% minced muscle contained less *de novo* myofiber regeneration than the 100% grafts and regenerating myofibers had smaller cross-sectional areas. The potential for improving outcomes of VML treatment with 50% minced muscle grafts via incorporation of laminin-111, a muscle extracellular matrix protein, within a hyaluronic acid hydrogel has also been investigated (**Figure 1.5c**)[67]. The 50% minced graft with laminin-111 and hyaluronic acid resulted in improved function compared to untreated controls but was not significantly different from treatment with 50% minced grafts lacking laminin-111 or lacking hyaluronic acid. *De novo* muscle regeneration remained less than that observed in injuries treated with 100% minced grafts, indicating a need for further research in the expansion and treatment potential of minced muscle grafts composed of less than 100% muscle. In addition, it was recently shown that VML-injured muscles treated with a 100% autologous minced muscle graft have no difference in gene expression compared to untreated controls, with upregulation of pro-fibrotic and inflammation-related genes 28 days post-injury (**Figure 1.5d)**[16]. Although a promising option, more research is

required on efficient *in vitro* expansion methodologies of minced muscle grafts and overall scale-up potential prior to clinical translation.

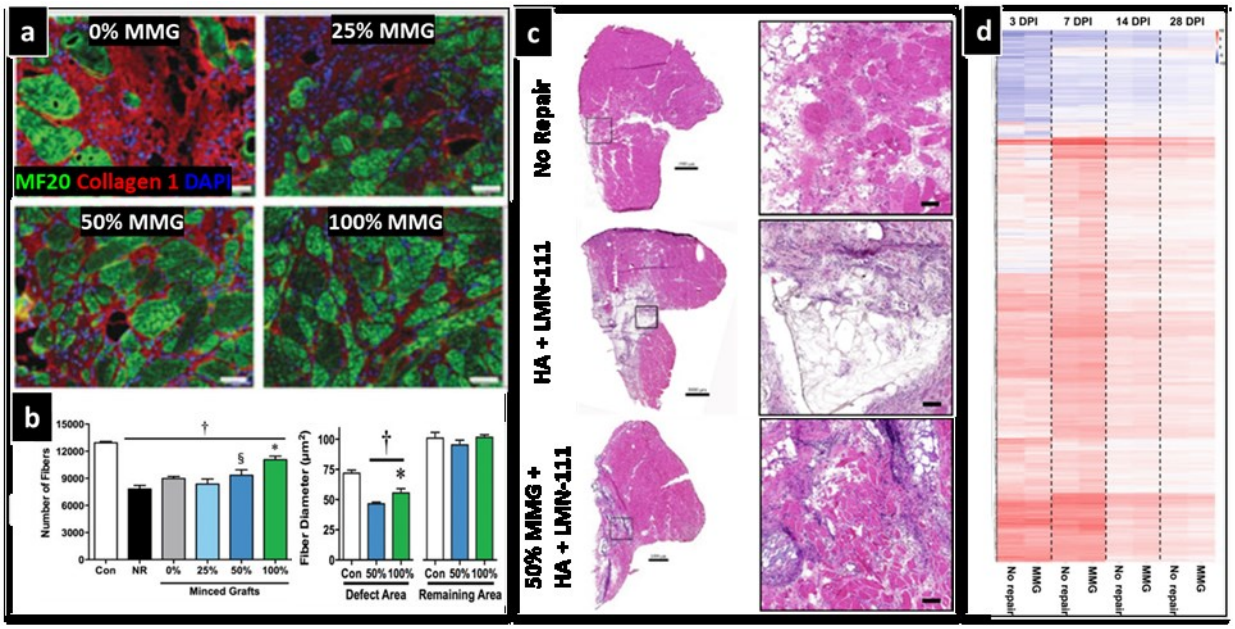

Figure 1.5. Minced muscle grafts of varied composition within VML defects enable histological regeneration but have a persistent pro-inflammatory gene expression profile.

a,b) Collagen hydrogel containing 0-100% MMG within a rat VML defect for 8 weeks and quantification of myofiber number and diameter. (**c)** Histological analysis of a rat VML defect treated with a hyaluronic acid (HA) hydrogel supplemented with laminin-111 (LMN-111) with or without 50% minced muscle graft at 8 weeks post-implantation. **d)** Heatmap of differentially expressed genes comparing rat TA VML defects with no repair to those treated with 100% MMG up to 28 days post-injury demonstrating persistent similarities in transcriptional response regardless of treatment. MF20: pan-isoform myosin; Con: Control; HA: hyaluronic acid; LMN-111: laminin-111.

Tissue Engineered Muscle Grafts (TEMGs)

Tissue engineered muscle grafts (TEMGs) leverage the benefits of acellular and cells-only approaches through the combination of a translatable pro-myogenic cell source with a biomaterial scaffold. Despite their significant regenerative potential, TEMGs may be limited, however, by long *in vitro* pre-culture times, issues with cell distribution within the scaffold, and limited expandable myogenic cell sources. There has been extensive research on the use of various TEMGs to treat

VML defects in a range of preclinical models. Similar to the cells-only approach, there has been a broad range of cell sources incorporated into TEMGs including satellite cells or other muscle-derived precursor cells[21,33,56,69–73], mesenchymal stem cells[74,75], adipose-derived stem cells[76–78], and human pluripotent stem cells[79–81] (**Figure 1.6**). Scaffold materials used in the development of TEMGs include dECM[21,55,56,74,82], collagen[83,84], hyaluronic acid[67,85], fibrin[24,25,49,70,77], poly(lactic acid)/poly(lactic-co-glycolic acid)[32,86], silk fibroin[87], keratin[71,72], gelatin[88,89], and methacrylated gelatin[90]. Regenerative potential of TEMGs following implantation within VML defects has varied widely and comparison between studies is complicated by the broad range of cells and scaffold materials as well as differences in *in vitro* pre-culture time, construct size, and the preclinical VML defect model used. Although TEMGs are limited by the regulatory hurdle and biological variability inherent to cell-based constructs, the combination of pro-myogenic cells with a biomaterial scaffold present has demonstrated increased histological regeneration of VML-damaged muscle compared to acellular constructs in addition to improving muscle contractile function. Additionally, the incorporation of a biomaterial scaffold enhances construct durability and ease of surgical manipulation compared to cells-only constructs. Overall, TEMGs are a promising option for the treatment of VML.

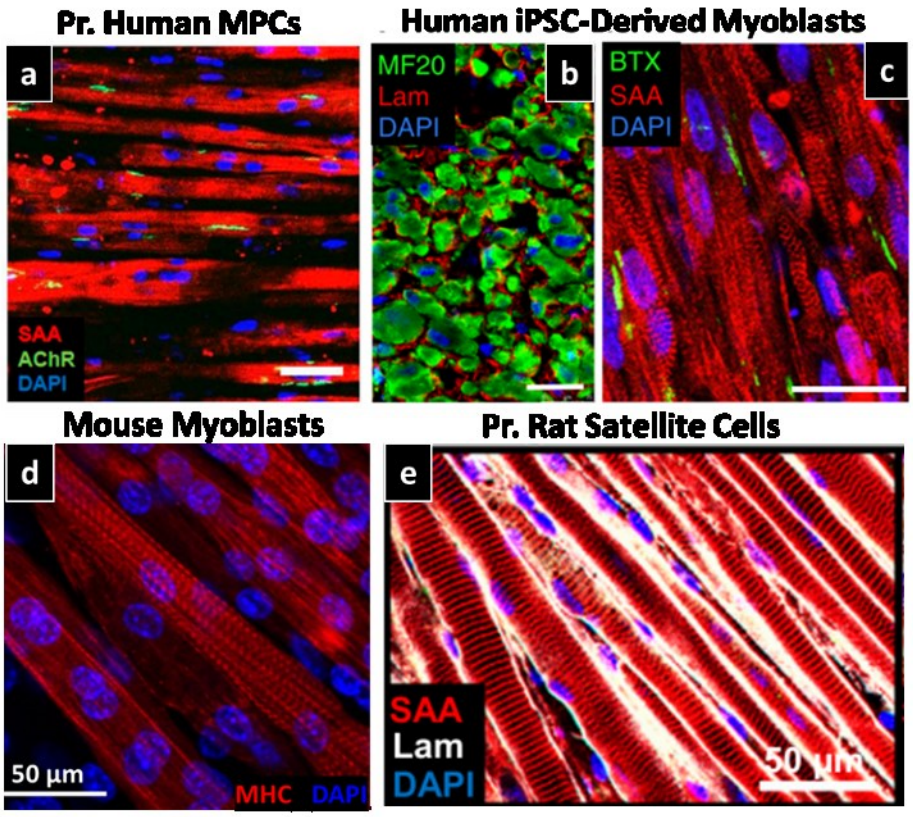

Figure 1.6. Tissue engineered muscle grafts developed for VML treatment have incorporated a broad range of cell sources. a) Primary human muscle progenitor cells within fibrin and Matrigel. **b,c)** Human induced pluripotent stem cell-derived myoblasts within fibrin and Matrigel. **d)** C2C12 mouse myoblasts within electrospun fibrin. **e)** Primary rat satellite cells and muscle progenitors within fibrin and Matrigel. MF20: pan-isoform myosin; Lam: laminin; BTX: α-bungarotoxin; SAA: sarcomeric α-actinin; MHC: myosin heavy chain.

Functional Outcomes

VML is characterized by persistent loss of function over time and functional testing following treatment of VML injuries is a standard assessment. Different studies have tested functional output at a range of time points post-VML from 2 weeks[67] to 6 months post-injury[65]. Functional measurements primarily involve electrical stimulation of a nerve near the graft and subsequent measurement of the muscle's twitch force, maximum isometric force, maximum specific force, and/or the force frequency relationship. Measurement of the force frequency

relationship enables quantification of the muscle's ED_{50}, the frequency of stimulation that elicits its half-maximal contraction amplitude. Often, contralateral uninjured muscles are used as a comparison and forces may be presented as a percent of the contralateral. Ex vivo force measurement is also used to measure muscle contractility independent of innervation, whereby explanted muscle is tethered on both ends and directly stimulated[21,65]. In some cases, there were no differences between treatment groups following neural stimulation but ex vivo force measurement did show differences[21]. An alternative measure of muscle function that is less often utilized in tissue engineering approaches post-VML is the use of electromyography (EMG) and compound motor action potential (CMAP)[59,61,86,91]. In EMG, surface or needle electrodes are placed above or within the muscle and measure motor neuron electrical signals and electrical activity within the muscle in response to nerve activity. Due to the importance of neural regeneration post-VML to ultimate graft integration and function, EMG is a useful tool for muscle tissue engineers and should be more widely utilized to measure functional recovery post-VML.

The vast majority of studies quantifying functional outcomes post-VML in preclinical models have analyzed muscle function at the muscle's optimal length (L_0) and measured standard functional outcomes such as maximum isometric contraction, specific force, twitch force, and force-frequency curves. As mentioned previously, there has been recent discussion on the discrepancy between improved functional outcomes post-implantation despite low and variable *de novo* myofiber regeneration, in particular with respect to implantation of acellular dECM scaffolds[22,25,46,63–65] calling into question the utility of these measurements to determine the extent of regeneration. It has been postulated that functional improvements due to acellular dECM implantation may be due to scaffold mediated functional fibrosis[46,64] . A significant recent study by Passipieri et. al. tested this hypothesis by utilizing a novel computational model to investigate

the biomechanical mechanisms underlying improved functional outcomes despite limited histological regeneration following implantation of acellular and cell-seeded dECM scaffolds in a rat latissimus dorsi (LD) model[65]. They found that increased contractile force measurements of the treated LD (acellular and cell-seeded) compared to non-repaired controls 2 months post-injury were primarily due to increased volume of tissue in the defect region and subsequent improved passive force generating ability. Despite improvements in *de novo* myofiber regeneration near the implant/host interface by cell-seeded grafts and an ~87% recovery of maximum isometric force, 96% of the total measured force recovery was due to passive force generation and differences in measured contractility between acellular and cell-seeded grafts were likely due to graft thickness alone. The model also highlights the contribution of lateral force transmission to contractility of non-repaired VML-injured muscle, which should be a consideration by future studies on VML. In a substantial result, simulated forces predicted by the model demonstrate a significant decrease in the contribution of passive force generation to total measured contractile force when measurements are taken at 80% of the muscle's optimal length. When measured at a suboptimal length, implanted grafts would require active force generation by myofibers within the defect in order to show marked improvements in overall muscle contractility. They also demonstrated decreases in the contribution of passive force generation with increased defect size. The predicted results must be validated experimentally but if true could improve measurement of graft function post-VML through the use of suboptimal muscle length and more accurately reflect histological results.

1.3 Engineering Vascularized Skeletal Muscle

Anatomy of Muscle Vasculature

Due to the high metabolic demands of skeletal muscle, tissue engineering techniques for skeletal muscle regeneration must consider the design constraints imposed by the limits of oxygen diffusion. Previous studies with pancreatic islet cells and lung-derived fibroblasts have shown that the limiting oxygen diffusion distance in order to prevent necrotic cores in cultured tissues is 150-200 μm[92–94]. Native muscle myofibers have diameters ranging from approximately 30-100 μm[5,95], which, when combined with the diffusion distance of oxygen, demonstrate the need for perfusable vasculature within the large-scale regenerating muscle environment post-VML. The dense and organized structure of vasculature within native skeletal muscle is optimized for efficient nutrient transfer throughout the entire tissue and must be considered in tissue engineered constructs. Blood vessels within skeletal muscle are highly organized to provide optimal nutrient and gas diffusion to myofibers with arterioles and venules branching into terminal arterioles and terminal venules that are perpendicular to the skeletal muscle myofibers (**Figure 1.7a**)[96]. These terminal arterioles and venules are interspersed and alternate with one terminal venule present between two terminal arterioles, and a terminal arteriole is present approximately every 1 millimeter down the length of each myofiber. The terminal arterioles and venules then branch into tortuous capillaries that run parallel to the myofibers and form organized networks called microvascular units[97]. To further the efficiency of gas transfer from blood vessels to muscle cells, capillaries are embedded within grooves in the myofiber sarcolemma and mitochondria within the myofiber interior congregate around these grooves, minimizing the required distance of gas and fatty acid diffusion[96].

Microvascular units (MVUs) are the smallest unit of control for vascular perfusion in skeletal muscle tissue and consist of a terminal arteriole and the group of 20-30 capillaries that it supplies[98] (**Figure 1.7b**). Each MVU covers approximately 1 millimeter of the myofiber length

after which a new MVU supplied by a different terminal arteriole begins. The width of a MVU is approximately 500 μm and it extends around 100 μm deep into the muscle, and there are approximately 20 MVUs per milligram of skeletal muscle tissue[98]. Capillaries within an MVU are 4-10 μm in diameter and have a tortuous architecture along the myofibers which functions to increase the capillary to myofiber surface area and maximize oxygen diffusion to the muscle[97,99]. Skeletal muscle is a highly plastic tissue with the capacity to adapt to increased oxygen and nutrient demands[99]. In resting muscle, the skeletal muscle microvasculature and MVUs are intermittently and unequally perfused. The skeletal muscle vasculature dilates in response to exercise with changes in oxygen demand sensed by muscle microcirculation and transmitted upstream to larger vessels inducing vasodilation and vasomotion, rhythmic oscillations in blood vessel diameter that impact blood flow. In addition, muscle vasculature and blood flow is modified in response to exercise by local factors released by the muscle as well as neurovascular changes to increase vessel perfusion[96,100]. When regenerating a large volume of skeletal muscle tissue after injuries such as VML, the microvascular architecture and capacity of the muscle vasculature to adapt to changing environmental and exercise demands should be considered.

A variety of mechanisms to quantify the extent of vascularization are utilized in the analysis of skeletal muscle biology. These may also be applied to the quantification of vasculature in engineered muscle constructs and regenerated muscle post-VML. For an excellent review of quantification methods of skeletal muscle vascularity see Olfert and Baum et al[100]. Capillary density (CD) is perhaps most frequently used and is defined as the number of capillaries per millimeter squared when counted in cross-section. Increases in skeletal muscle CD have been linked to increased muscle functional performance, mitochondrial volume density, and maximal aerobic capacity and decreased skeletal muscle CD is associated with poor prognoses for a variety

of diseases including peripheral arterial disease, diabetes, cachexia, and chronic obstructive pulmonary disease[100]. Despite the utility of CD to measure muscle vascularity, it does not account for changes in the capillary to myofiber surface area caused by differences in capillary vessel tortuosity or myofiber diameter. Capillary length density, the length of capillaries per unit volume of muscle fibers, incorporates vessel tortuosity but requires more technically challenging longitudinal sectioning and quantification methods. The capillary to fiber ratio (C/F ratio) is counted in cross section similar to CD but more accurately represents differences in capillary surface area and overall vascular density due to changes in myofiber area. Use of CD alone does not capture the impact of changes to myofiber cross-sectional area which can adapt in response to exercise and tissue remodeling after injury[100]. A final consideration when assessing muscle vascularity is the heterogeneity of vascular density throughout the depth of the native muscle tissue. Different muscles within the body have varying degrees of heterogeneity in both the muscle fiber type as well as capillary density throughout the tissue (**Figure 1.7c**)[100]. Tissue engineered constructs for skeletal muscle regeneration post-VML should consider the native capillary density and C/F ratio pattern for the specific muscle being treated, and analysis of regenerating muscle should consider differences in capillary density across a section of the native tissue. Engineered constructs with tunable vascular density or incorporation of a vascular density gradient depending on the intended site of implantation would be a potentially beneficial addition to the field.

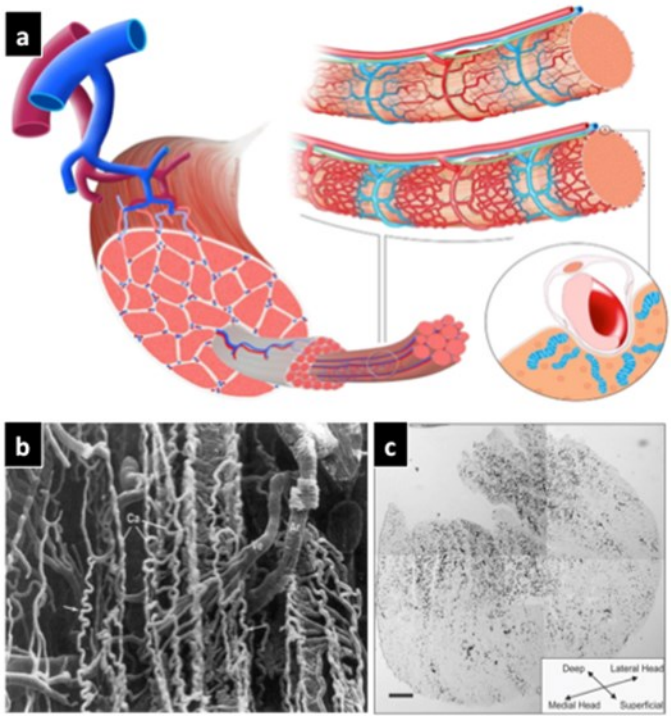

Figure 1.7. Tissue engineered muscle grafts developed for VML treatment have incorporated a broad range of cell sources. a) Primary human muscle progenitor cells within fibrin and Matrigel. **b,c)** Human induced pluripotent stem cell-derived myoblasts within fibrin and Matrigel. **d)** C2C12 mouse myoblasts within electrospun fibrin. **e)** Primary rat satellite cells and muscle progenitors within fibrin and Matrigel. MF20: pan-isoform myosin; Lam: laminin; BTX: α-bungarotoxin; SAA: sarcomeric α-actinin; MHC: myosin heavy chain.

Strategies to Enhance Vascularization of TEMGs

Approaches to engineer vascularized skeletal muscle with the use of implantable 3D constructs fall into two main categories: muscle constructs relying on host vessel infiltration and constructs that are pre-vascularized *in vitro* prior to implantation with or without an incorporated myoblast cell source (**Figure 1.8**). Scaffold material may encourage host vascular infiltration, and constructs designed to promote vascularization post-VML have included fibrin, decellularized ECM, collagen, and combinations of poly-(lactic acid) and poly-lactic-co-glycolic acid. Fibrin in

particular has a demonstrated pro-angiogenic potential[101] and has been utilized in combination with other biomaterials to promote vascularization *in vivo.* Defect size is also a critical determining factor in the feasibility and practicality of host vessel infiltration. While host vessel infiltration may be sufficient for the survival of implanted grafts within smaller defects in mice and rats, larger animal models of VML and human patients would likely require an implanted vascular source for graft survival over time[102]. Significant work has been done with both approaches to engineer vascularized muscle yielding promising results with the potential for clinical translation.

Host Vessel Infiltration

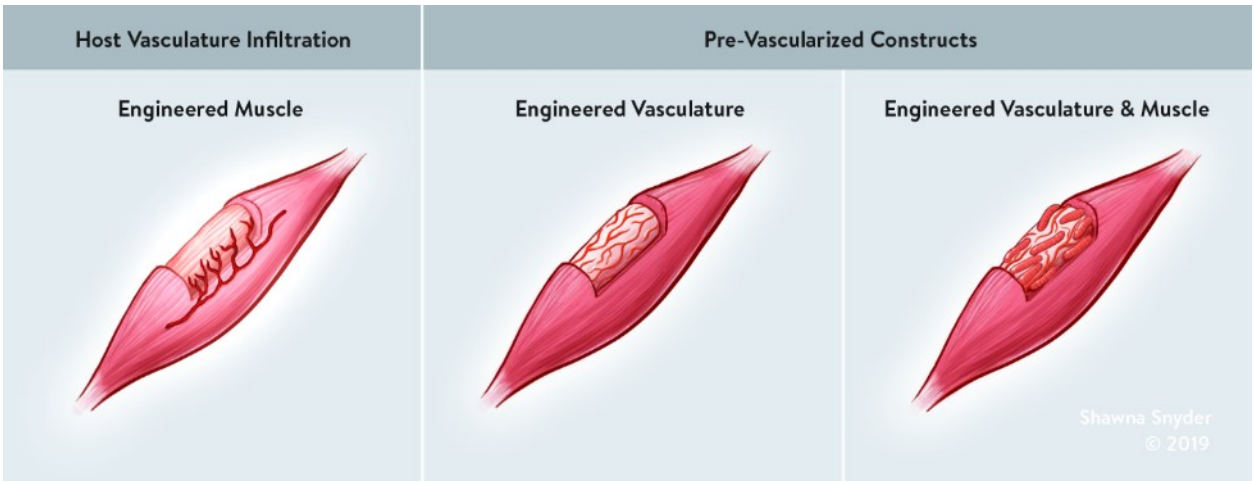

Figure 1.8. Engineering Vascularized Skeletal Muscle. Strategies to vascularize tissue engineered constructs include host vessel infiltration (left) and implantation of pre-vascularized constructs (middle and right).

Infiltration of the host blood vessels into an implanted construct is impacted by a variety of factors including ischemia within the defect site, paracrine signaling by regenerating muscle cells, pro-angiogenic biomaterial scaffolds, and mobilization of immune cells. Approaches to encourage host vessel infiltration often utilize microsurgical techniques to graft portions of major host vessels onto implanted muscle constructs or the implantation of muscle constructs adjacent to a major vessel. Early studies utilizing host vessel infiltration were mainly concerned with

supporting the survival of implanted muscle tissue and focused on graft survival over time while later studies prioritized analysis of the infiltrating vasculature itself and developed advanced quantitative techniques to do so. A variety of skeletal muscle tissue engineering studies that rely on host vessel infiltration post-VML have been summarized in **Table 1.1**. There are also numerous studies investigating host vessel infiltration following muscle injuries other than VML (ischemia, myotoxin, etc) that are outside the scope of this review.

Table 1.1. Tissue engineering studies utilizing host vessel infiltration to vascularize implanted muscle constructs post-VML.

Cells	Scaffold	Animal Model	Vascular Analysis	Major Results	Ref
Primary rat myoblasts	Fibrin	Construct implanted around rat femoral vessels	Gross examination of blood flow, histology	Vascular infiltration and muscle survival 3 weeks post-implant, construct contractile	[102]
Rat or hu muscle tissue	----	Muscle in semi-sealed chamber connected to host AV loop (rat)	Gross examination	Tissue survived 6 weeks post-implant and appeared vascularized	[103]
Primary rat myoblasts	Fibrin	Myoblasts injected into scaffold site pre-vascularized *in vivo* by host AV loop for 2 wks	India Ink injection, histology	Host vessel infiltration enabled myoblast survival for 8 wks	[104]
Primary rat myoblasts	----	Construct sutured to tendons of biceps femoris with transected sural nerve and blood vessel attached	Histology	Host vessels within graft after 1 wk	[105]
Primary rat satellite cells	Fibrin	Construct implanted in dorsal skinfold window (mouse)	Intravital imaging, CD, cross-sectional lumen density, immunostaining	Infiltrating blood vessels were perfused by RBCs after 1 wk; pre-differentiated muscle induced higher blood vessel density & cross-sectional lumen density	[73]
Primary rat myoblasts (transfected to express VEGF/SDF)	Collagen sponge	Construct implanted in back muscle defect (rat)	Gross examination, histology, CD	Co-culture of VEGF and SDF transfected myoblasts induced higher capillary density and larger lumens than each growth factor alone	[106]
C2C12s	Fibrin +/- tethered HGF	VML defect in TA muscle (mouse)	Gross examination, histology, immunostaining, CD	Higher CD in treatment groups over time compared to controls	[24]

----	Porcine decellularized ECM	Abdominal wall defect (rat)	Histology, vessel number	Vessels containing RBCs present in implanted graft at 8 weeks	[107]
----	Collagen (aligned or randomly-oriented)	VML defect in TA muscle (mouse)	Histology, immunostaining, isolectin perfusion, perfused vascular density, CD	Scaffold implantation + exercise significantly increased revascularization	[84]

The feasibility of encouraging host vasculature to infiltrate an implanted muscle construct was initially assessed with a microsurgical arteriovenous (AV) loop implantation model. In one study, rat or human muscle was implanted within the groin in a semi-sealed chamber connected to host AV vessels. Gross examination of the tissue demonstrated survival of vascularized muscle tissue 6 weeks post-implantation[103]. A second study further elucidated the potential of the AV loop and examined the potential of host vessels to vascularize an implanted acellular fibrin scaffold. After vascularizing the scaffold *in vivo* for 2 weeks, they then injected fluorescent primary rat myoblasts into the scaffold site to test its ability to support muscle growth *in vivo* over time[104]. Myoblasts implanted into vascularized scaffolds were visible up to 8 weeks post-implantation while control myoblasts implanted into the contralateral groin lacking an AV loop were not detectable. Yet another study utilized a different technique to promote vascularization of an implanted muscle construct by creating a fibrin scaffold seeded with primary rat myoblasts and implanting it within a cylindrical silicone chamber surrounding the host femoral artery and vein[102]. Three weeks post-implantation, host vessels had infiltrated the muscle construct and the explanted construct contained desmin positive muscle cells and was contractile when electrically stimulated.

Other studies have attempted to encourage host vessel infiltration by transecting a major blood vessel and attaching the transected end to the implanted construct. To vascularize and innervate a construct composed of primary rat myoblasts, Williams et. al. implanted the construct

along the biceps femoris muscle of rats and attached transected ends of the sural nerve and blood vessel to the implant[105]. After just one week post-implantation they saw host vessels within the graft. In a unique animal model enabling intravital imaging of blood vessel infiltration, Juhas et. al. implanted engineered muscle bundles composed of primary rat satellite cells in fibrin into a mouse dorsal skinfold window model after two weeks of *in vitro* pre-cultivation (**Figure 1.9a,b**)[73]. The dorsal skinfold model enabled direct visualization of constructs and blood vessels through a glass coverslip in the live animal and a broad range of quantification techniques. Host blood vessels rapidly infiltrated the implanted constructs with pre-differentiated constructs that contained more mature muscle cells inducing a higher blood vessel density over time than undifferentiated constructs that contained an immature satellite cell-like phenotype. Additionally, the infiltrating blood vessels were perfused by host blood flow after just one week *in vivo, which* is visible via video. To further quantify the blood vessel maturity, they also quantified the cross-sectional lumen density of the blood vessels and found that constructs containing more mature muscle cells had an overall higher lumen density. The average lumen diameter increased over time to reach 7 μm, similar to native hindlimb muscle, and the average rate of vessel ingrowth in pre-differentiated constructs was 18.9 ± 2.1 vessels$\cdot$mm$^{-2}\cdot$day^{-1}. Although their muscle constructs were not implanted in a VML model, the dorsal skinfold window model is an important advancement for the field due to its ability to enable live intravital imaging and detailed analysis of host vessel infiltration into implanted muscle constructs.

Another interesting approach to encourage host vessel infiltration is the use of gene therapy to encourage vessel growth. Zhou et. al. utilized primary rat myoblasts transfected to overexpress human vascular endothelial growth factor 165 (VEGF-165) or human stromal cell-derived factor 1 (SDF-1) on a calf skin-derived collagen sponge to encourage vessel growth after implantation in

a back muscle defect[106] (**Figure 1.9c**). They implanted four groups of cells pre-cultured on the collagen sponge: non-transfected myoblasts, VEGF-165 transfected myoblasts, SDF-1 transfected myoblasts, and a 1:1 ratio of VEGF-165 and SDF-1 transfected myoblasts. After up to 8 weeks post-implantation they found that the while the VEGF-165 and SDF-1 transfection groups had more vessels than non-transfected controls they contained varied degrees of vascular infiltration to the graft. The combined co-culture of VEGF-165 and SDF-1 myoblasts, however, had enhanced vascular infiltration than either growth factor group alone as well as larger vascular lumens. Upon analysis of microvascular density they found that capillary density in all three transfection groups decreased slightly over time as the tissue remodeled, with each group displaying different temporal changes in capillary density over the eight week regenerative period.

Host vessel infiltration serves as a useful tool to demonstrate viability and regenerative potential of tissue engineered muscle constructs during initial testing within small VML defects. Reliance on host vasculature for graft survival when scaling to large, clinically-relevant defect sizes is not feasible and alternative methods of promoting construct vascularization are vital to clinical translation. Despite this eventual need, studies that utilize host vessel infiltration in small defect sizes are relatively high throughput and provide useful and important information on early-stage muscle regenerative potential of an engineered construct. Additionally, critical vascular quantification metrics have been developed through the use of host vessel infiltration that can inform future studies within larger defects that contain an implanted vascular source.

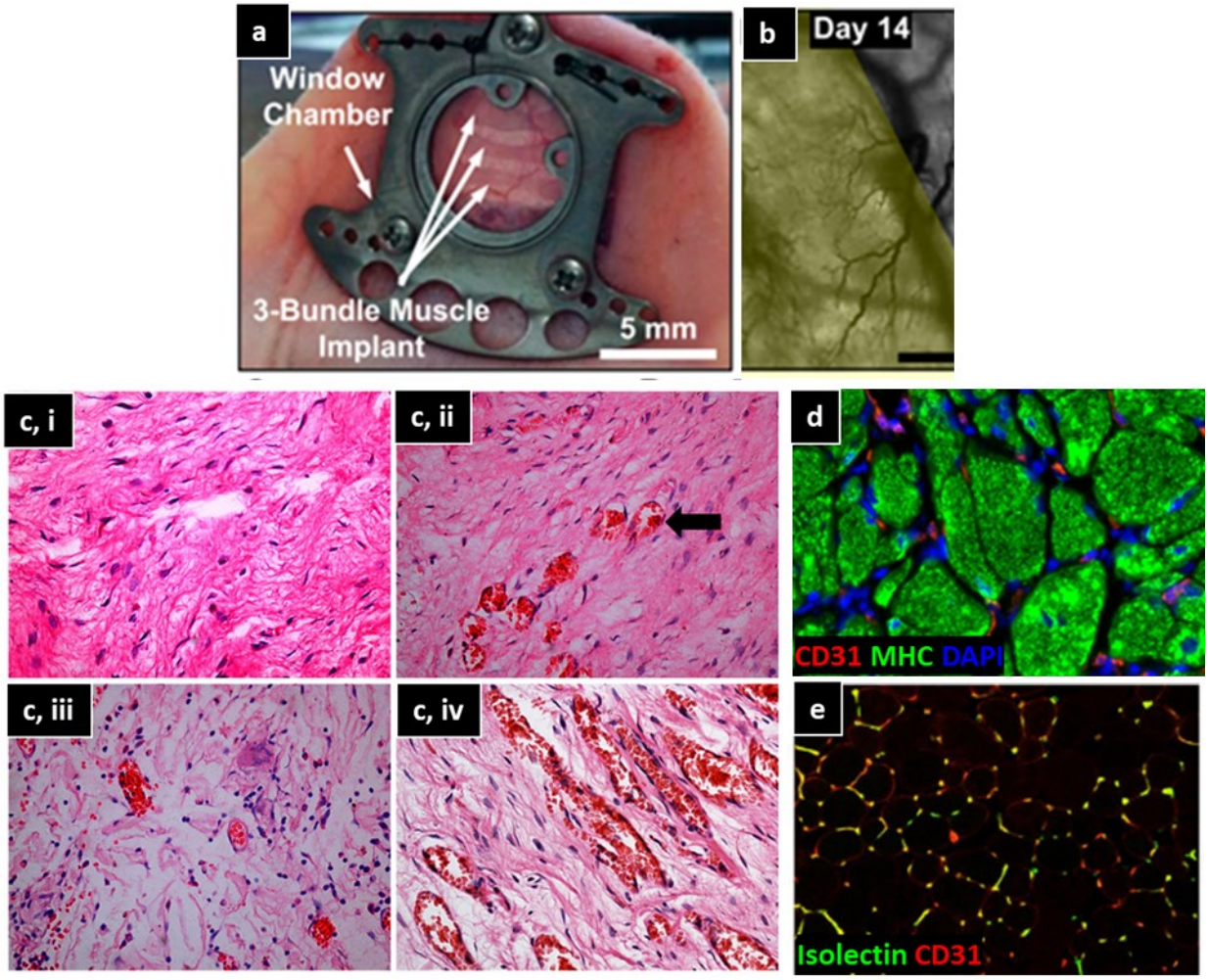

Figure 1.9. Host vessel infiltration to various implanted engineered muscle constructs. a,b) Dorsal skinfold window containing constructs composed of primary rat satellite cells in fibrin. Vessels are visible in real time infiltrating constructs. **c)** Angiogenic gene-modified primary rat myoblasts in collagen implanted within VML defect. i) control; ii) VEGF+ myoblasts; iii) SDF+ myoblasts; iv) VEGF+SDF+ myoblasts. **d)** Mouse myoblasts on electrospun fibrin scaffold implanted in VML defect**e)** Acellular aligned collagen scaffolds implanted in VML defect followed by exercise. MHC: myosin heavy chain.

Pre-Vascularized Constructs

Pre-vascularized constructs for skeletal muscle tissue engineering include both constructs containing vessels alone and co-cultures of vessels and muscle cells. Major skeletal muscle tissue engineering studies that rely on pre-vascularized scaffolds for VML treatment have been summarized in **Table 1.2**. Early successes in vascularized skeletal muscle tissue engineering

included the development of a 3D tri-culture system containing cell sources for the three major components of vascularized muscle: skeletal muscle cells, human endothelial cells, and pericytes to support the developing vascular network[29]. Mouse embryonic fibroblasts were used as a pericyte cell source and it was found that inclusion of fibroblasts in the 3D construct significantly improved vascular maturity over time and that fibroblasts differentiated to express smooth muscle actin and were located around endothelial cells as a support for vessels. Constructs implanted in a mouse abdominal wall VML defect model contained perfusable human vessels after 2 weeks as well as desmin and myogenin positive muscle, with tri-culture constructs resulting in greater vascular perfusion in both lectin perfusion and luciferase injection assays **(Figure 1.10d)**.

Table 1.2. Tissue engineering studies that utilize pre-vascularized constructs to vascularize implanted muscle constructs post-VML.

Cells	Scaffold	Animal Model	*In Vivo* Vascular Analysis	Major Results	Ref
C2C12s, HUVECs, embryonic fibroblasts	1:1 PLLA:PLGA sponge	Ab. wall defect (mouse)	Histology, lectin perfusion, luciferase injection, CD	Fibroblasts stabilize vessels; pre-vascularization improves survival *in vivo*	[29]
C2C12s, GFP-HUVECs, HFFs	Porcine dECM	Ab. wall defect (mouse)	Mean vessel diameter, intravital imaging, dextran perfusion, CD, C/F ratio, smooth muscle actin	Constructs pre-cultured for 3 weeks had faster anastomosis and maturation upon implantation, followed by replacement by host vessels	[31]
C2C12s, GFP/RFP-HUVECs, HFFs (co-culture vs. tri-culture)	1:1 PLLA:PLGA +/- fibrin	Ab. wall defect (mouse)	Vessel length, vessel diameter, % area CD31, immunostaining, dextran perfusion, vascular network length/area, histology	*In vitro* vessel maturity higher with co-culture compared to tri-culture; composite PLLA:PLGA + fibrin with or without cells resulted in most perfused host vessels within graft *in vivo*	[30]
Primary ms muscle progenitors, endothelial cells, + fibroblasts	----	TA and EDL muscle defects (mouse)	Histology	Muscle cells and vasculature present within defect after 2 wks	[51]

Primary rat GFP+ MVFs or primary rat ASCs	Collagen	TA muscle defect (rat)	Histology, CD, DiI perfusion	MVF treatment groups had faster vascular growth and higher vessel density; Vessels within defect were perfusable but overall perfusion level was low	[78]
C2C12s, HUVECs, human dermal fibroblasts	1:1 PLLA:PLGA sponge	Initial implantation around femoral vessels then transfer to abdominal wall defect (mouse)	Gross examination, histology, CD, dextran perfusion, immunostaining functional vessel density, ultrasound following contrast agent injection, vessel circumference	Tri-culture constructs have more rapid and complete integration with host vessels	[32]
C2C12s, HUVECs, mouse embryonic fibroblasts	Rat dECM	Rat forearm transplant	Gross examination, histology, immunostaining, intraoperative blood pressure (radial artery)	Perfusable vessels formed *in vitro* within graft were perfused by host blood upon implantation; measurable blood pressure; red blood cells present in graft vessels	[108]
GFP+ HUVECs, neonatal human dermal fibroblasts	Gelatin-based sponge or fibrin	Ab wall defect (mouse)	Histology, immunostaining, pro-angiogenic factor secretion, CD, dextran perfusion, vessel length	Static stretch induced aligned, vertical vessels *in vitro*; Static constructs maintained vessel alignment post-implantation, were perfusable, had inc. vessel length; Vessel alignment with host muscles improved mechanical outcomes	[34]
Primary rat myoblasts (GFP+) +/- Primary rat MVFs	Collagen	VML in biceps femoris (rat)	Histology, micro-CT angiography, vascular volume, vessel diameter, Microfil perfusion	MVFs + myoblasts had better vessel network *in vitro* than MVF alone; No difference in vascular volume between groups *in vivo;* Significant collagen within MVF treated defects	[109]
Primary mouse satellite cells and muscle resident cells	Mouse dECM	VML defect in TA muscle (mouse)	Histology, immunostaining, # blood vessels/field	Constructs containing muscle resident cells (including ECs) resulted in significantly more blood vessels in the defect	[21]
HUVECs, ASCs	Fibrin	VML in TA muscle (mouse)	Histology, immunostaining, % area CD31	Anastomosis and perfusion of implanted human vessels with host vessels; ASCs on pre-vascularized scaffold are source of significant collagen in defect	[25]
Primary hu. venous endothelial cells, hu. dermal	1:1 PLLA:PLGA + fibrin	Ab wall defect (mouse)	Histology, dextran perfusion, systemic ms-CD31 stain, fluorescent hu. ECs, total vessel length, vascularized area, host vessel	Adult primary ECs form more mature vascular network than HUVECs; 3D tri-culture with adult hu. ECs successfully anastomosed with host vessels post-VML	[35]

fibroblasts, hu. myoblasts			invasion radius, laser speckle blood flow imaging		
Primary hu. venous endothelial cells$^{ANGPT1+}$ and smooth muscle cells^{VEGF+}, Primary hu. myoblasts	1:1 PLLA:PLGA + fibrin	Ab wall defect (mouse)	Gross examination, histology, Intravital imaging, total vessel length, dextran perfusion, systemic ms-CD31 stain, fluorescent hu. ECs	Constructs with transduced ECs and SMCs resulted in faster host vessel infiltration, increased total vessel length, and faster loss of implanted human ECs	[33]
Hu. myoblasts, HUVECs	Porcine dECM	TA muscle defect (rat)	Gross examination, histology, Immunostaining, vessel number, hu. CD31+ cells	Pre-vascularized constructs fabricated via coaxial 3D printing significantly increased vessel number and CD31+ cells post-VML compared to mixed printing	[110]
Primary hu. ASCs	PEGylated platelet free plasma hydrogel & porcine dECM	TA muscle defect (rat)	Histology, immunostaining, # blood vessels, # pericytes	Implanted constructs with ASCs had higher CD31+ cells; ASCs from implanted constructs homed to perivascular space within defect	[111]

Further work on the tri-culture system utilizing C2C12 myoblasts, GFP-positive human umbilical vein endothelial cells (HUVECs), and human foreskin fibroblasts (HFFs) investigated the impact of *in vitro* culture time on vascular maturity and integration following implantation in an abdominal wall defect model[31]. Tri-culture scaffolds were compared to empty scaffolds or those containing just C2C12s and all implanted constructs were evaluated after 2 weeks *in vivo.* Grafts implanted after different pre-culture times displayed differences in vessel alignment and maturity 2 weeks post-implantation with increased incubation time *in vitro* causing more mature morphology post-implantation. The three-week pre-culture group exhibited the most mature morphology with parallel, aligned myofibers and vessels, similar in morphology to native abdominal muscle. Functionality of the implanted vessels was assessed through tail-vein injection of fluorescent dextran and tri-culture constructs resulted in improved blood flow through implanted grafts compared to acellular or myoblast-only constructs. Blood flow, blood vessel

density, C/F ratio, and smooth muscle actin density increased with *in vitro* pre-culture time among the tri-culture groups. Interestingly, the signal of implanted GFP-HUVECs decreased in the three-week pre-culture group despite the increase in overall blood flow, indicating remodeling of the more mature implanted vasculature and replacement by the host.

To further investigate vascular network formation within 3D constructs, Lesman et. al. directly compared vascular morphogenesis of HUVEC:HFF co-cultures versus HUVEC:HFF:C2C12 tri-cultures in 3D constructs of varied scaffold composition (50% PLLA:PLGA, fibrin and thrombin at different concentrations, composite of PLLA:PLGA + fibrin)[30]. Quantification of vascular network maturity via live cell imaging of fluorescent vessels over 7 days of *in vitro* culture was performed through a maturity scoring system that classified the extent of network connectivity into four categories **(Figure 1.10a,b)**. In an interesting result, they found that the incorporation of myoblasts slightly impeded *in vitro* vascular network maturity over time compared to the co-culture lacking myoblasts. They evaluated integration of the co-culture constructs with host vasculature *in vivo* by implanting co-cultures on a range of scaffold compositions in an abdominal wall defect for 10 days and determined that while both fibrin and composite scaffolds with cells resulted in some anastomosis with host vessels, the composite scaffolds containing both PLLA:PLGA and fibrin resulted in the highest amount of perfused host vessels within the graft regardless of whether or not cells were included. Although significant perfusion of infiltrating host vessels was visible along with some mosaic vessels composed of mouse and human cells, few of the implanted RFP+ human vessels were perfused with dextran at 10 days (**Figure 1.10e**).

To avoid the lengthy *in vitro* cultivation times of pre-vascularized constructs and develop a more clinically translatable VML treatment, Pilia et. al. assessed the vascular regenerative

potential of freshly isolated microvascular fragments (MVFs) versus adipose derived stem cells (ASCs) in a collagen scaffold implanted in a rat VML model of the TA muscle for 1 or 2 weeks[78]. MVFs and ASCs were isolated from rat epididymal fat pads and while MVFs were freshly isolated prior to implantation, ASCs were cultured and utilized at passage 2. VML defects treated with MVFs contained vessels earlier with a higher vessel density than those treated with ASCs or acellular controls but all treatment groups had a vessel density that remained lower than control native skeletal muscle. Vascular perfusion measured via DiI systemic injection was present as early as 7 days in the MVF group and after 14 days in the ASC group, although total vascular perfusion was low and unevenly distributed throughout the defect. MVFs isolated from GFP+ rats were then used to determine whether perfusable vessels within the defect were derived from implanted MVFs or host vessel ingrowth and the majority of vessels within the defect area were GFP-positive. Although overall vascular perfusion was low in this study, it is noteworthy that MVFs freshly isolated on the day of surgery enabled significant vascularization of implanted constructs and is a step toward a more clinically translatable treatment.

The vascular potential of MVFs in 3D muscle constructs was further investigated by a recent study that utilized co-culture of freshly isolated primary rat MVFs and *in vitro* expanded primary rat myoblasts in a collagen gel for regeneration of a large VML defect to the rat biceps femoris muscle[109]. Constructs containing MVFs with or without myoblasts were pre-cultured for 4 days *in vitro* before implantation and compared to muscle autografts or the empty defect. Interestingly, the *in vitro* constructs containing both MVFs and myoblasts had increased vascular network formation with a higher number of branches and total vessel length compared to MVF-only constructs (**Figure 1.10c**). This is in contrast to previous research comparing 3D tri-culture to co-culture systems where the inclusion of myoblasts slightly impeded vascular network

formation[30]. After 2 weeks post-implantation, micro-CT angiography demonstrated that all treatment groups had equal vascular volumes, primarily composed of small vessels. Defects treated with constructs containing MVFs had a higher proportion of small vessels compared to empty or autograft groups. Both MVF treatment groups contained high levels of fibrosis, adipose infiltration, low levels of muscle regeneration, and poor maintenance of tissue volume within the defects demonstrating a need for further research on the capability of muscle constructs pre-vascularized with MVFs to improve regeneration post-VML.

Utilizing a unique host vessel infiltration technique, Shandalov et. al. investigated the potential to promote increased perfusion and anastomosis of their pre-vascularized constructs by following a two step implantation protocol[32]. The construct was cultured *in vitro* for 10 days then first implanted around the mouse femoral artery and vein for 1-2 weeks, after which it was transferred as a vascularized axial flap to an abdominal wall VML defect site. The study used a 50% PLLA:PLGA scaffold and tested differences between acellular constructs and those containing C2C12s alone, co-culture of HUVECs and human dermal fibroblasts, or a tri-culture of C2C12s, HUVECs, and fibroblasts. In the cohort of constructs that had been implanted around femoral vessels for 1 week, tri-culture constructs had the highest capillary density and functional vessel density (FVD) while among those that had been implanted for 2 weeks, both tri-culture and C2C12 monoculture constructs had high CDs and FVDs. Interestingly, for both implantation timelines the HUVEC-fibroblast co-culture and acellular constructs resulted in comparatively low CD and FVD. The perfusion rate and perfused vascular volume in implanted grafts were quantified through the use of ultrasound imaging following injection of a microbubble contrast agent. One week of implantation increased both the perfusion rate and perfused vascular volume of tri-culture constructs compared to other groups while 2 weeks of implantation caused both tri-culture and

C2C12 monoculture constructs to have highly perfused vascular volumes with no difference in perfusion rate among all three groups. Overall, earlier vascular network maturity was seen in implanted tri-culture constructs with monoculture muscle constructs following close behind given an extra week of implantation around femoral vessels. This indicates that implanted myoblasts promote vasculogenesis by femoral vessels compared to co-culture constructs containing vessels alone. Despite differences between groups after incubation around femoral vessels, fewer differences were seen following transfer to an abdominal wall VML defect. Tri-culture constructs that had incubated around femoral vessels for 1 week had the highest CD and vessel size but no difference was seen between groups for constructs that had incubated around femoral vessels for 2 weeks. Overall, these results indicate that tri-culture constructs have more rapid integration with host vessels when transplanted as a vascularized flap pre-incubated *in vivo.* Constructs containing myoblasts or pre-cultured vessels alone have the potential for equal vascular integration post VML when the initial incubation time around host femoral vessels is increased.

The impact of vessel alignment on engraftment within VML-injured muscle as well as methods to tune that alignment were investigated by Rosenfeld et. al[34]. 3D co-cultures of HUVECs and neonatal human dermal fibroblasts on gelatin-based scaffolds were cultured for 4 days then subjected to cyclic strain (10% strain, 1 Hz) for an additional 4 days of culture, resulting in vessels aligned diagonal to the direction of strain. Static strain was applied to other constructs prior to cell seeding and maintained for the entire 8-day culture period, resulting in vessels aligned parallel to the direction of strain. After implantation for 2 weeks in an abdominal wall VML defect model, statically-strained constructs preserved their pre-implantation vessel alignment and vessels were on average 2.5 times longer than vessels in implanted unstrained control constructs. Furthermore, by comparing statically-strained constructs implanted with vessels either aligned

with or perpendicular to host musculature, they demonstrated that vessel alignment with host muscle cells provides improvements in integration and mechanical durability upon implantation. Native skeletal muscle is a highly organized tissue with myofiber and vascular alignment and this study provides strong evidence for the importance of promoting blood vessel alignment in engineered muscle constructs implanted in VML defects.

Our group recently demonstrated that electrospun fibrin hydrogel scaffolds induce alignment of a vascular network formed by 1:1 HUVEC:ASC co-culture after 11 days *in vitro*[112]. When cultured with C2C12 myoblasts, the electrospun scaffolds promoted dense muscle and vascular regeneration in a mouse VML defect of the TA muscle. To enable scale-up to larger defect sizes, we tested the ability of pre-vascularized scaffolds lacking myoblasts to anastomose with host vessels after a 10-day implantation within the mouse TA VML defect. Implanted human vessels anastomosed with host vessels and mosaic vessels were visible that were partially of human and partially of mouse origin (**Figure 1.10f**). In addition, implanted human vessels that were perfused with mouse red blood cells were visible within the defect. Despite integration with host vasculature, the implanted pre-vascularized scaffolds were ringed with a collagen boundary that prevented full integration with the host musculature. Upon further investigation we determined that significant collagen was deposited by the ASCs during *in vitro* culture prior to implantation. Previous work utilizing adipose-derived MVFs in a large VML defect reported similar high levels of collagen in MVF treatment groups[109], indicating a need for further research into the regenerative potential of adipose-derived MVFs and ASCs within the highly fibrotic VML environment.

In a step forward for clinical translation of pre-vascularized constructs, tri-culture constructs containing primary human adult venous endothelial cells (ECs), smooth muscle cells,

and myoblasts have been developed and tested in an abdominal wall VML defect model[33,35]. In a direct comparison to HUVECs as an endothelial cell source, it was found that the constructs containing adult human ECs with adult supporting cells had a higher vessel network complexity in both co-culture and tri-culture than those with HUVECs[35]. Upon implantation in an abdominal wall defect for 9 days, human vessels at the implanted graft perimeter were mainly replaced by host vessels that had vascularized more than 80% of the implants. The host vessels had infiltrated an average of 2 mm into the grafts with no difference based on EC source. Genetic modification of primary human adult venous endothelial cells and primary human adult venous smooth muscle cells transduced to express angiopoietin 1 (ANGPT1) and vascular endothelial growth factor (VEGF), respectively, resulted in increased vessel elongation and maturation in 3D constructs *in vitro* compared to constructs containing non-transduced cells[33] **(Figure 1.10g-j)**. An abdominal imaging window was developed to facilitate intravital imaging of vessel growth within the defect over time and is a beneficial tool for further research in the vascularization of implanted constructs post-VML. Constructs with genetically modified cells also resulted in faster host vessel infiltration and increased total vessel length within the defect up to 7 days post-implantation. Interestingly, the implanted endothelial cells decreased within the graft area over time and this occurred more rapidly with genetically modified cells than controls.

There has been significant recent success in the development and characterization of pre-vascularized muscle constructs both *in vitro* and *in vivo.* As stated above, due to the high metabolic demands of skeletal muscle tissue, any large-scale VML defect will likely need an implanted vascular source to sustain the regenerating muscle tissue. Previous work described above has characterized differences in vascularization and muscle regenerative potential related to cell sources, *in vitro* pre-cultivation time, scaffold composition, the application of mechanical strain,

and pre-incubation around major host vessels *in vivo*. A broad range of quantification metrics have been developed including the use of trackable fluorescent endothelial cells, vascular perfusion, intravital imaging techniques, analysis of blood flow rate, and micro-CT angiography, among others. Despite the broad successes in the field thus far, the majority of studies evaluating pre-vascularized constructs *in vivo* post-VML have been limited to a rodent abdominal wall defect model and it is as yet unclear if similar results would be generated in other muscle types that may have significant variations in anatomy. In addition, there is a strong need to evaluate the above pre-vascularization technologies in larger animal models of VML that have an increased vascular demand.

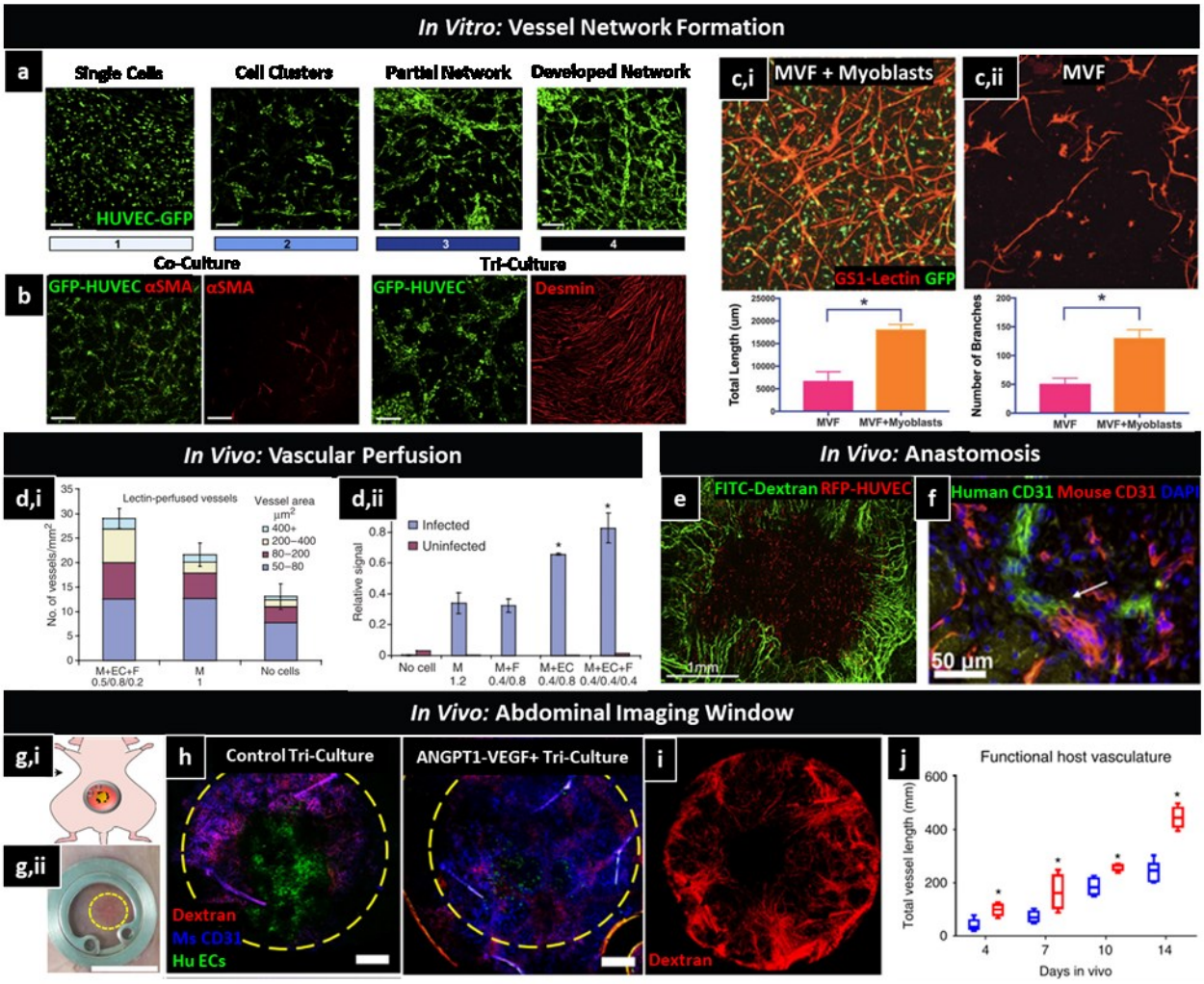

Figure 1.10. Pre-vascularized constructs for VML treatment composed of varying cell populations and demonstrating a variety of *in vitro* and *in vivo* quantification methods. a) Classification of *in vitro* network maturity from single endothelial cells to a fully-developed vascular network. **b)** Differences in *in vitro* vascular morphology between endothelial cell + fibroblast co-culture compared to myoblast+ endothelial cell + fibroblast tri-culture. Dense desmin+ myotubes are visible in tri-culture. **c)** Comparison of vascular network morphology in *in vitro* constructs containing GS1-Lectin + freshly-isolated MVFs (i) in combination with GFP+ primary rat myoblasts or (ii) MVFs alone. **d)** Comparison of perfusable vessels within abdominal wall VML defects via lectin (i) and luciferin (ii) perfusion. VML treatments contained either myoblast monoculture, myoblast + endothelial cell co-culture, or myoblast + endothelial cell + fibroblast tri-culture. **e)** Co-culture of RFP+ HUVECs and HFFs implanted in abdominal wall VML defect. Perfusion with FITC-dextran demonstrates anastomosis of host and implanted vessels. **f)** Immunohistochemistry demonstrating anastomosis of a human vessel (Hu-CD31) from pre-vascularized electrospun scaffolds (ASCs + HUVECs) with a host vessel (Ms-CD31) within a TA VML defect. **g)** Abdominal imaging window (AIW) provides novel method for intravital confocal imaging of vascular infiltration into an abdominal wall VML defect. **h)** Visualization of host vessels (blue; Ms CD31), perfused vessels (red; dextran), and implanted human endothelial cells (green; Hu ECs) below the abdominal imaging window. Implanted tri-culture constructs contained human endothelial cells, smooth muscle cells, and myoblasts and were compared to those angiopoietin 1- and VEGF-expressing tri-cultures. Host vessel perfusion with TRITC-dextran (i) enables quantification of functional host vasculature (j) when compared to total Ms CD31+ host vessels. HUVEC: human umbilical vein endothelial cell; GFP: green fluorescent protein; αSMA: α-smooth muscle actin; RFP: red fluorescent protein; ANGPT1: angiopoietin 1; VEGF: vascular endothelial growth factor.

1.4 Engineering Innervated Skeletal Muscle

Biology of the Neuromuscular Junction

The neuromuscular junction (NMJ) is the site of contact between motor neurons and the myofibers within skeletal muscle that they innervate. Motor neuron axons travel from the central nervous system to skeletal muscles primarily unbranched and upon reaching the target muscle they branch extensively to contact individual myofibers at the NMJ[19]. The primary purpose of the NMJ is to convert motor neuron action potentials into muscle contraction. In response to motor neuron action potentials and subsequent release of acetylcholine, myofibers undergo membrane depolarization, the opening of voltage-gated calcium channels, and an increase in intracellular calcium concentration to trigger activation of the contractile apparatus[113]. Postsynaptic

acetylcholine receptors (AChR) are organized into dense clusters optimized to intercept the acetylcholine signal from the nerve terminal. The highly specialized NMJ structure ensures the efficiency of signal transfer across the synapse between a motor neuron and skeletal myofiber and effective muscle contraction.

Pre- and Postnatal Development of the Neuromuscular Junction

During prenatal development of skeletal muscle tissue, primitive clusters of acetylcholine receptors form in the center regions of developing myofibers prior to innervation and independent of neuronal signals in a process termed pre-patterning[114,115]. The density of acetylcholine receptors within pre-patterned myofibers during embryonic development is approximately 1000 receptors/μm^2. Pre-patterned cluster formation and stabilization is partially induced by the myofiber membrane-associated cytoplasmic protein rapsyn[114]. Rapsyn forms aggregates with acetylcholine receptors in the developing myofiber membrane, facilitating cluster formation, and mice lacking rapsyn do not form AChR clusters within their muscles. The muscle specific receptor tyrosine kinase, MuSK, is also vital to proper AChR clustering and NMJ formation and mice lacking MuSK also have no clusters of AChR. As motor neuron axons grow into the developing muscle, AChR clusters at synaptic sites contacted by a nerve are stabilized and enlarged while AChR clusters not contacted by the infiltrating nerve axons disperse over time (**Figure 1.11**). At this stage in development the AChR clusters are each poly-innervated by two or more axons. Agrin, a large heparan sulfate proteoglycan, is secreted by the nerve terminal and is vital for AChR cluster stabilization and prevention of AChR dispersal[114]. In fact, mice lacking agrin die in utero or at birth due to NMJ dysfunction[116]. The AChR density at synaptic sites increases dramatically as the muscle develops to approximately 10,000 receptors/μm^2 and in adult muscle can reach

20,000 receptors/μm^2 at the NMJ[117]. Non-synaptic AChR, by contrast, are present at a low density of <10 receptors/μm^2.

During postnatal development, neurons are pruned to single contact at each synaptic site and as the muscle matures, around half of the motor neurons innervating the developing muscle degenerate[114]. The AChR clusters mature and undergo a morphological change from an immature oval-shaped plaque morphology to a more mature pretzel shape[117]. This transition is caused by folding of the postsynaptic membrane and localization of dense AChR clusters at the fold crests[114]. Additionally, as the muscle matures, locations along the nerve terminal outside of the synaptic cleft are covered by a synaptic non-myelinating Schwann cell. Interestingly, ECM proteins within the neuromuscular synapse differ from the general basal lamina surrounding myofibers outside of the synapse. The two major basal lamina proteins, collagen IV and laminin, have different isoforms within the synaptic region. Differences between synaptic and extrasynaptic

ECM proteins has been reviewed elsewhere[117] and synaptic ECM proteins have been shown to play a vital role in NMJ development.

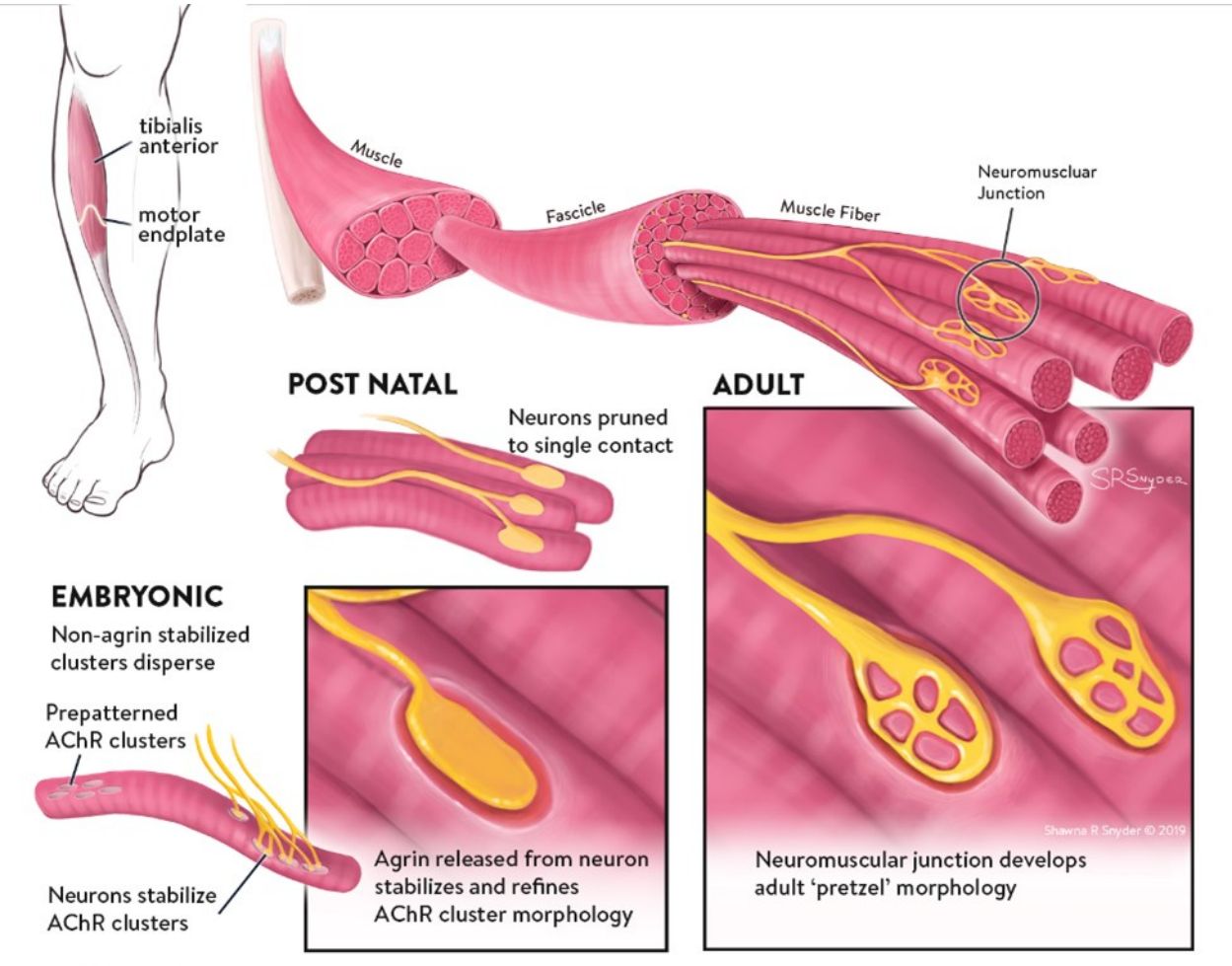

Figure 1.11. Pre- and Post-Natal Development of the Neuromuscular Junction. During embryonic development the immature muscle is pre-patterned with immature plaque-shaped AChR clusters prior to nerve contact. Following polyinnervation, nerve-secreted agrin stabilizes contacted AChR clusters while extrasynaptic clusters disperse. During postnatal development, neurons are pruned to single contact with myofibers and agrin helps to refine AChR clusters morphology. Adult skeletal muscle is highly organized with one neuron innervating each myofiber at the NMJ, which exhibits a mature, pretzel morphology with direct overlap between the presynaptic nerve terminal bouton and the postsynaptic AChR clusters.

Mature Neuromuscular Junctions in Adult Muscle

The adult vertebrate NMJ exhibits a complex pretzel morphology due to folds within the postsynaptic membrane that correlate with the spatial location of nerve terminal boutons to enable a high efficiency of signal propagation[19]. The folds penetrate approximately 1 μm into the

cytoplasm of the muscle cell and significantly increase the area of the postsynaptic membrane. Each terminal bouton is 1-5 μm wide and upon activation releases numerous 50 nm diameter membrane-bound synaptic vesicles containing acetylcholine to be received by the highly dense postsynaptic AChR clusters. The synaptic cleft, the space between the presynaptic nerve terminal and postsynaptic myofiber membrane, is approximately 50 nm wide and filled with large molecules that ensure NMJ ultrastructural organization and efficient signal propagation from nerve to muscle[115]. In adults, each myofiber is innervated at its NMJ by a single axon from a motor neuron[115]. Motor neurons branch within the muscle tissue to innervate multiple myofibers, termed its motor unit, and myofibers within a motor unit are generally distributed throughout the muscle to ensure uniform contraction.

Native neuromuscular regeneration and repair of NMJs can occur following peripheral nerve lesions depending on the severity of injury[115]. Nerve axons undergo Wallerian degeneration whereby the axon cell membrane degrades, axon cytoskeleton and organelles disintegrate, and terminal Schwann cells invade the NMJ synaptic cleft with the debris cleared by recruited and resident macrophages. Interestingly, it has been shown that despite severe disruptions to pre-synaptic nerve axons following denervation, the number of acetylcholine receptors remains unchanged up to 20 days post-injury then drops by 50 and 70% at 30 and 60 days post-injury[118]. Despite this, after denervation the AChR become dispersed from their synaptic clusters and are present throughout the myofiber surface[119]. Regeneration begins at the axon proximal end and in small injuries, the regenerating axon grows following its previously occupied location to preferentially re-innervate original synaptic locations or axons may sprout from neighboring NMJs[120]. Following severe injury where the basal lamina is disrupted, regenerating nerves may innervate new locations along the myofiber with the potential for poly-innervation. As the

regenerated NMJ matures, reorganization occurs to ensure mono-innervation and AChR cluster arrangement. Concurrent muscle regeneration is vital for proper maintenance of regenerated NMJs and re-innervated NMJs on basal lamina ghosts lacking myofibers decline over time. In addition, satellite cell function has been connected to NMJ regeneration post-injury with reductions in postsynaptic morphology, loss of postsynaptic myonuclei, and deficits in NMJ reinnervation linked to satellite cell depletion[115].

Strategies to Enhance Neural Ingrowth and Formation of NMJs in TEMGs

The formation of neuromuscular junctions in tissue engineered muscle constructs both *in vitro* and post-implantation is important for ultimate function of the engineered muscle. Significant research has been performed on NMJ biology, development, and regeneration using *in vitro* NMJ models and is described briefly below. *In vivo* formation of NMJs has included the incubation of 3D skeletal muscle constructs along major nerves, neurotization, and the use of rehabilitative exercise. The following sections will provide an overview of *in vitro* engineered NMJs and focus on studies promoting NMJ formation *in vivo* within VML-injured muscles. Methods and biomaterials utilized to encourage neuromuscular regeneration post-VML are summarized in **Table 1.3**.

Table 1.3. Studies that assess neurotization or rehabilitative exercise and subsequent neural regeneration post-VML.

Cells; Scaffold	Animal Model	Innervation Stimulus	*In Vivo* Innervation Analysis	Major Results	Ref
Primary rat muscle progenitors and bMSCs	VML defect in TA muscle (rat)	Neurotization (peroneal nerve)	Immunostaining, neural electrical stimulation	Treated group had increased contractile force; nerve branching from host to graft visible with NMJs	[50]
C2C12s, HUVECs, human dermal fibroblasts; 1:1	Ab wall defect (mouse)	Neurotization (femoral nerve)	EMG, CMAP, immunostaining, β3-tubulin+ area	Neurotized grafts lacked spontaneous EMG activity, had measurable CMAP, and higher β3-tubulin+ area; NMJs present in both groups	[86]

PLLA:PLGA + fibrin					
Acellular porcine decellularized ECM	VML defect in TA muscle (rat)	Voluntary caged wheel exercise	Neural electrical stimulation, histology	No improvement in histology or function due to exercise	[46]
Minced muscle graft	VML defect in TA muscle (rat)	Voluntary caged wheel exercise	Neural electrical stimulation, myofiber glycogen depletion post-neural stim., histology	Exercise resulted in lower fibrosis within defect, increased torque output, and increased macrophage presence	[121]
Primary ms. satellite cells and muscle resident cells; Murine decellularized ECM	VML defect in TA muscle (mouse)	Voluntary caged wheel exercise or treadmill exercise	Gait analysis, neural electrical stimulation, histology (cross-section), AChR clusters/myofibers, % NMJs	Exercise improved force output and NMJ formation within defect compared to sedentary	[21]
Acellular aligned collagen	VML defect in TA muscle (mouse)	Voluntary caged wheel exercise	Histology (cross-section), # of AChR clusters, # of NMJs	Exercise increased # of AChR clusters and NMJs near the defect region	[84]

Engineered NMJs In Vitro

The development of *in vitro* NMJs has been the focus of previous reviews and has provided a vital tool for the analysis of NMJ development and function[122]. Co-culture of neurons and myoblasts both in monolayer or 3D constructs has enabled *in vitro* NMJ formation where electrically induced nerve stimuli result in measurable post-synaptic potentials and contractile activity in myofibers[123–125]. To demonstrate that this interaction functions via conventional NMJ interactions, nerve-induced myofiber activity can be prevented by application of the AChR blocker D-tubocurarine[126]. Dixon et. al. recently described the development of the first fully human 3D nerve and muscle co-culture system using human primary skeletal myoblasts and human induced neural stem cells within a collagen/Matrigel scaffold[127]. In a recent study by Vila et. al., the first human patient-specific tissue engineered *in vitro* NMJ system was developed using primary human skeletal muscle cells and muscle-derived hiPSCs differentiated into motoneurons within a collagen/Matrigel scaffold[128]. To monitor NMJ function, they utilized photosensitive

motoneurons to form light-sensitive NMJs and developed an optical stimulation platform to quantify NMJ activity and muscle contraction. The significant advancements in the development of human NMJs within 3D *in vitro* constructs in recent years have provided useful tools for patient disease monitoring and drug screening and could provide significant benefit to studies assessing neuromuscular regeneration following VML.

In vitro AChR clusters are a vital postsynaptic component of the NMJ and have been induced in both monolayer and 3D culture of myoblasts through the use of various pharmacologic agents (including agrin and laminin) as well as via electrical stimulation[129]. Agrin is present in the developing and adult NMJ responsible for stabilizing AChR clusters and has been extensively researched for its ability to induce AChR clustering and promote NMJ formation in cultured myotubes[130–138]. Laminin is an extracellular matrix protein present in skeletal muscle with various isoforms present at different stages of development as well as within the neuromuscular synapse versus extrasynaptically[117]. Significant variability exists in protocols of agrin application with concentrations ranging from 10 ng/ml to 10 μg/ml and inconsistencies in time point and duration of application. Despite variability in application, it remains clear that agrin application provides a significant stimulus to cultured myotubes to cause clustering of AChRs. Interestingly, this differs from the native biological function of agrin during embryonic development, which as described above does not induce AChR clustering itself but rather stabilizes the pre-formed clusters in the developing muscle. Additionally, the morphology of agrin-induced clusters appears limited to an immature plaque shape as opposed to developing into a mature cluster pretzel morphology as demonstrated by an interesting study by Bruneau et. al[137]. In that study, cluster formation induced by both agrin and laminin was evaluated with AChR fluorescence tracked over time. Significant differences in cluster morphology were present when induced with the two agents and it was

demonstrated that agrin application following an initial laminin application stimulated acetylcholine receptors to transfer from a pretzel-shaped laminin-induced cluster to the more immature agrin-induced cluster. This effect was seen after just one hour of agrin application and resulted in the complete disappearance of the larger laminin-induced clusters after just 24 hours. Other studies have found that the combined application of agrin and laminin induced significantly more AChR clustering than agrin or laminin alone[131,138]. The potential of agrin pre-treated constructs to promote innervation post-implantation was assessed using a fibrin gel containing C2C12 myoblasts and 1 μg/ml agrin[130]. Following subcutaneous implantation near the peroneal nerve for up to 8 weeks, implanted constructs that had been pre-treated with agrin exhibited significantly more nerve infiltration *in vivo.* While this study is a promising first step, further investigation is required on the potential for agrin or other pharmacologic agents to encourage neuromuscular regeneration within the severely damaged VML environment.

Neurotization Post-VML

Neurotization is the process of surgically re-innervating muscle fibers by insertion of a donor nerve within the muscle tissue[119]. Clinical use of neurotization to repair peripheral nerve injuries is limited as it is considered an inefficient method to repair innervation at the motor endplate[119]. Despite this, neurotization continues to be a useful experimental tool to study innervation of implanted engineered tissues including skeletal muscle. Few studies have directly investigated neurotization as a method to innervate an implanted 3D construct in VML-injured muscle. Most studies assessing the benefits of neurotization for muscle tissue engineering have utilized non-VML models such as denervation of host muscle via nerve transection[139], subcutaneous implantation[140], and other non-muscle defect models[141]. Due to differences in neural infiltration and NMJ recovery between small muscle injuries versus after VML with its

associated gross loss of the basal lamina, further investigation is necessary on the innervation potential of neurotization within the extensively damaged VML environment.

The potential regenerative benefits of neurotization were characterized post-VML and compared to non-neurotized controls in a notable recent study. Kaufman et. al[86] implanted a pre-vascularized 3D muscle construct within a mouse abdominal wall VML defect model and nerve infiltration was encouraged via neurotization of the femoral nerve within the femoral bundle, which was transferred to the implanted construct. In control constructs, the femoral vessels were transferred to the implant without the femoral nerve. After 6 weeks spontaneous electrical activity, a marker of poor muscle innervation, was measured via EMG within the implant region. Neurotized grafts had no spontaneous activity while 5 out of 7 control non-neurotized grafts presented with spontaneous activity. Compound motor action potential (CMAP) was measured following stimulation of the transferred portion of the femoral nerve and compared to uninjured muscle as well as non-neurotized controls. CMAP amplitude for neurotized samples reached 0.6 mV whereas control samples had no measurable CMAP. Both neurotized grafts and controls contained β3-tubulin-positive neurofilament with significantly more area coverage in neurotized grafts. Longitudinal sections enabled visualization of NMJ size and morphology and although smaller than within uninjured muscle, NMJs with overlapping neurofilament or synaptophysin and acetylcholine receptor clusters were visible within the implanted constructs in both groups (**Figure 1.12**). The promotion of increased innervation within implanted 3D muscle constructs post-VML is significant and NMJs were visualized longitudinally, allowing for proper assessment of NMJ

size and morphology. Despite this, no quantification of NMJ size, morphology, or extent of neural and acetylcholine receptor cluster overlap was reported and would be of benefit to the field.

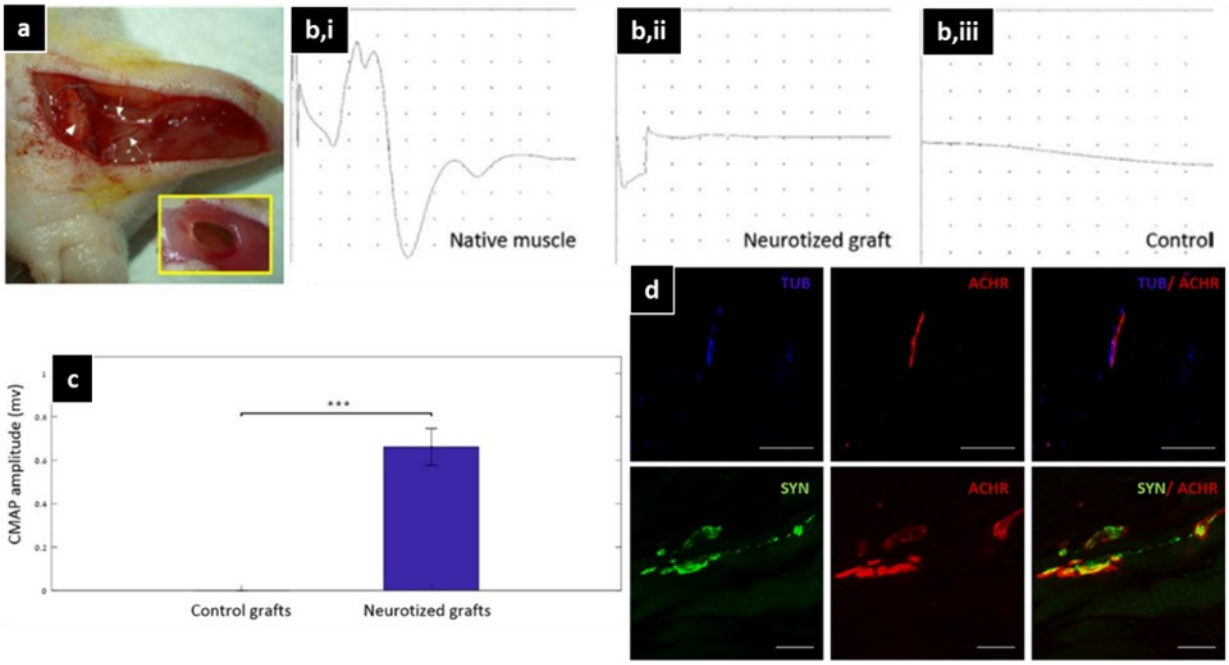

Figure 1.12. Improved functional outcomes and NMJs within VML-injured muscle following neurotization. a) Abdominal wall defects treated with a neurotized pre-vascularized construct. **b,c)** Compound muscle action potential (CMAP) of native muscle, neurotized graft, and non-neurotized control. CMAP amplitude of neurotized grafts was significantly higher than non-neurotized control. **d)** Longitudinal view of NMJ morphology present within the defect site. TUB: tubulin; ACHR: acetylcholine receptors; SYN: synaptophysin.

Rehabilitative Exercise Post-VML

Physical rehabilitation is often considered to be beneficial for muscle healing and accelerates the repair of small, acute muscle injuries via immune modulation, promotion of vascularization, release of pro-myogenic growth factors, and reduction of fibrosis[142–144]. Following VML, physical rehabilitation has been used clinically in an attempt to promote increased muscle strength in the remaining muscle and synergist muscles in order to offset the funtional deficit cause by the injury but results have been limited and physical therapy has not resulted in clinically meaninful improvements in range of motion, limb function, or muscle strength post-VML[15,16]. The emerging field of regenerative and rehabilitative medicine aims to

combine the rehabilitative effects of physical exercise with regenerative outcomes and *de novo* tissue formation. Application of this aproach to VML injured muscle has been recently reviewed[15,145].

To investigate the potential of physical rehabilitation to enhance regeneration of the lost muscle tissue, Aurora et. al. utilized a rat VML defect of the TA muscle and assessed the regenerative impact of 1 or 7 weeks of voluntary caged wheel exercise on the injured muscle beginning 1 week post-injury[142]. After 7 weeks of exercise, maximal torque output of TA muscles in exercised rats was 17% higher than in sedentary rats. Despite improved function, muscles in exercised rats contained signficantly more fibrosis within the defect region compared to those of sedentary rats and had upregulated pro-fibrotic genes. Exercise also resulted in double the amount of centrally-nucleated myofibers within the remaining muscle compared to sedentary controls, an indication of chronic injury and remodeling. Clinical use of physical rehabilitation following ECM treatment of VML-injured muscle has also resulted in improved functional outcomes[60,62] and may be a useful tool for encouraging neural infiltration post-VML.

Quarta et. al. recently directly assessed the impact of exercise on neural regeneration following a VML defect in mice of the TA muscle through the use of either voluntary caged wheel running or higher intensity treadmill running[21]. Using caged wheel exercise, it was determined that mice regained their pre-injury daily running habits 1 week post-injury. To further validate this, forced treadmill exercise within the first week post-injury resulted in delayed muscle regeneration and increased fibrosis while exercise delayed by one week post-injury resulted in accelerated myogenesis and decreased fibrosis. Following treatment with 3D constructs composed of primary mouse satellite cells and muscle resident cells on a decellularized ECM scaffold and one week of recovery post-injury, mice were exercised on treadmills for one hour per day over a period of 3

weeks. Exercised mice demonstrated a 20% improvement in gait analysis and significant improvements in neural-stimulated and *ex vivo* force output compared to sedentary controls. In addition, exercised mice had increased levels of AChR clusters and NMJs within the defect compared to muscles in sedentary mice (**Figure 1.13a-c**). Interestingly, differences between groups was more pronounced in the distal portion of the muscle, perhaps due to variability in NMJ location and motor endplate patterning of the native muscle tissue. While significant in its detailed analysis of functional output and NMJ formation following exercise, this study would benefit from further analysis of the morphology and maturity of regenerating NMJs through the use of longitudinal sectioning and image analysis of the entire NMJ structure.

The impact of voluntary caged wheel exercise on muscle regeneration post-VML was further investigated by Nakayama et. al., who implanted either topographically aligned or randomly-oriented collagen scaffolds within a mouse VML defect of the TA muscle and began voluntary exercise 1 week post-injury for a period of 2 weeks[84]. The presence of AChR clusters and NMJs was quantified in muscle within 500 μm or 1000 μm of the implanted scaffold (**Figure 1.13d,e**). Aligned scaffolds with exercise resulted in increased levels of AChR clusters and NMJs in muscle within a 500 μm distance from the scaffold. Randomly-oriented scaffolds with exercise demonstrated increases in AChR clusters and NMJ formation when the analysis was expanded to include muscle within a 1000 μm distance from the scaffold. Although it is signficant that exercise increased neural regeneration within muscle at varying distances surrounding the defect, it would be more informative to quantify neural regeneration within the defect and the implanted scaffold itself. In addition, analysis of nerve-evoked muscle function would further demonstrate any improvements to neural regeneration and muscle function due to exercise. Future studies on the regenerative potential of rehabilitative exercise should include a broad array of quantitive

measures including both muscle function and histological regeneration as well as neurally-stimulated force output and/or EMG with CMAP. To robustly assess neural regeneration post-VML and provide further understanding of this complex injury environment, studies should also quantify nerve infiltration to the defect site, the presence of NMJs (with overlapping AChR cluster and nerve stains), and 3D NMJ morphology and size.

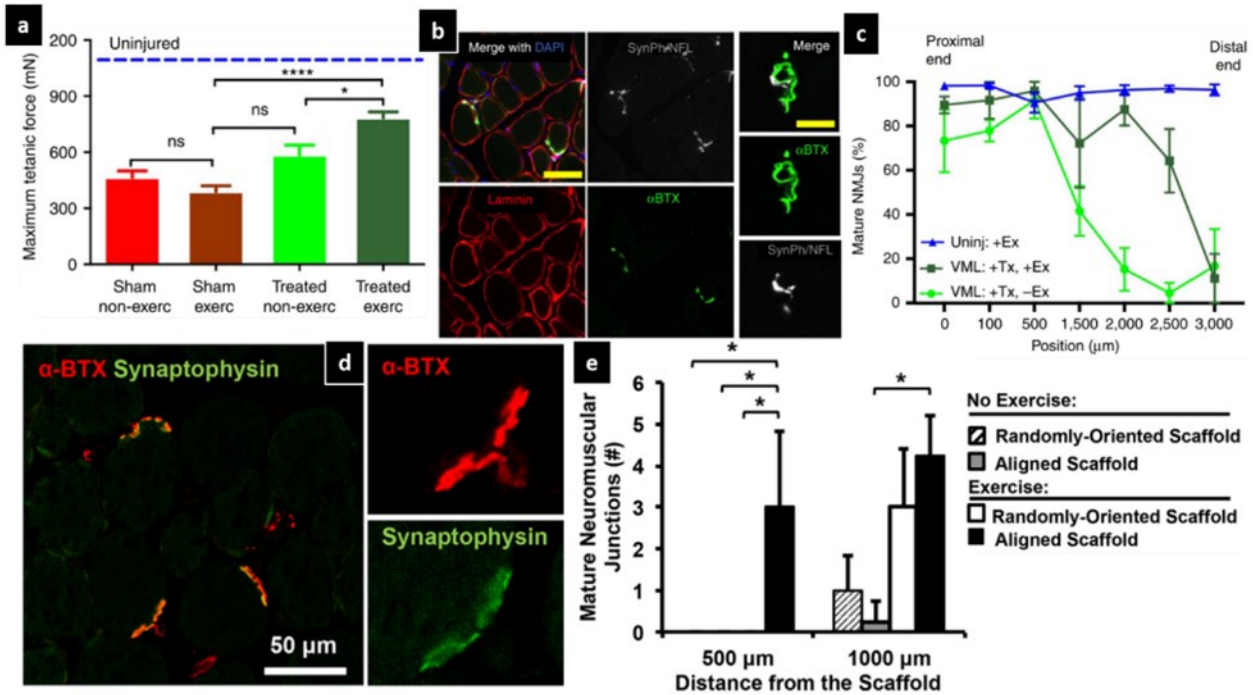

Figure 1.13. Improved functional outcomes and NMJs within VML-injured muscle following rehabilitative exercise. a-c) Primary mouse satellite cells and muscle resident cells in TA VML defects had improved force output and NMJ formation following treadmill exercise. **d,e)** Acellular aligned collagen scaffolds implanted in TA VML defects had increased NMJ formation in muscle surrounding the defect area following voluntary caged wheel exercise. SynPh: synaptophysin; NFL: neurofilament; αBTX: α-bungarotoxin.

1.5 Conclusion and Future Directions

In this review we have summarized the current state of the field of skeletal muscle tissue engineering for VML treatment with a focus on engineering vascularized and innervated muscle. Significant variability exists in the composition of engineered muscle constructs, preclinical VML

defect models, and measured outcomes following implantation. In order to effectively compare results between studies, the field would benefit from increased standardization of defect models and outcome measures. Native skeletal muscle has highly organized vascular and neural networks which must be considered when engineering skeletal muscle constructs and analyzing *in vivo* data.

Host vessel infiltration or pre-vascularization of constructs prior to implantation are reliable methods to promote vascularization of implanted constructs. Significant progress has been made in the field of vascularized skeletal muscle tissue engineering but continued research on pre-vascularized construct translatability to varied muscle types and within large animal VML defect models is required. Promoting neural regeneration post-VML is a relatively early area of research and primary methods to encourage innervation of regenerating muscle post-VML are neurotization and rehabilitative exercise. Although both methods have resulted in moderate successes, there is a need for further research on innervation post-VML and for the incorporation of improved quantification techniques to measure nerve ingrowth and NMJ morphology and maturity within the defect site. Intravital imaging has recently enabled real-time monitoring of vascular infiltration post-VML and would be an exciting and beneficial method for assessing nerve ingrowth as well. Additionally, growth factor release from implanted constructs within VML defects has been investigated for its pro-angiogenic potential. Growth factor release is an obvious choice to promote neural regeneration as well. Based on current publications, there is no evidence that it has been investigated in the VML environment to date. Future studies should focus on the development of novel technologies to encourage robust vascular and neural regeneration following VML as well as useful quantification metrics. Future studies should also incorporate robust quantification of immature, developing vasculature and nerves and enable a correlation between the regeneration state of the tissue and any improvements in functional outcome in order to delineate minimum

requirements for functional regeneration post-VML **(Figure 1.14)**. Further investigation into the presence of potential synergistic effects of regenerating vasculature and nerves in the post-VML environment may also improve the design of engineered treatments.

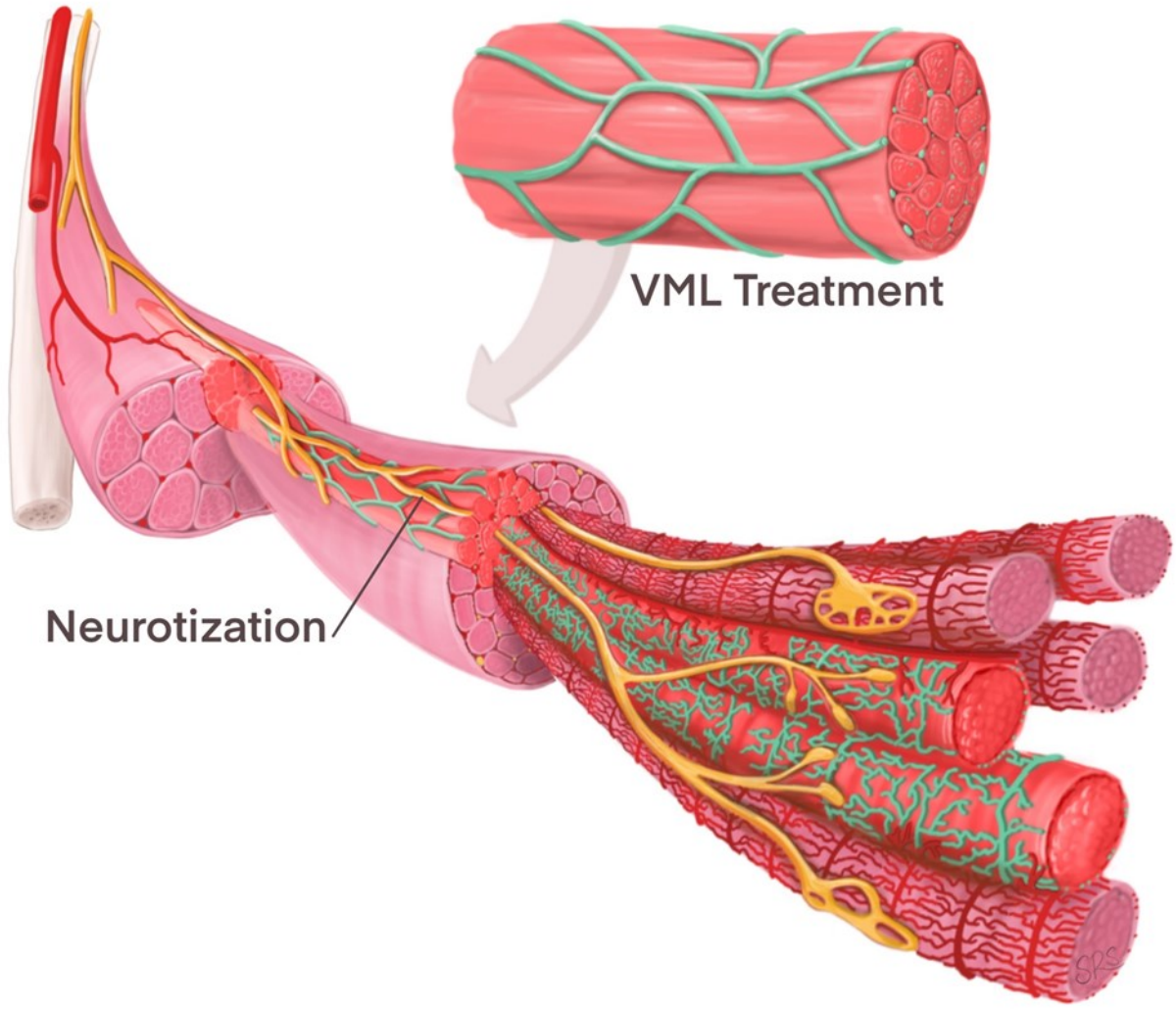

Figure 1.14. Integration of implanted pre-vascularized and neurotized engineered skeletal muscle construct into host musculature. VML treatment with an in vitro pre-vascularized muscle construct results in anastomosis with host vasculature and dense perfusable vessels. Neurotization enables host neural infiltration to the implanted construct with regenerating neuromuscular junctions. Vasculature and nerves within the construct region show a mid-stage regenerating phenotype post-VML, with lower vascular density and organization, poly-innervation, and immature plaque-shaped neuromuscular junctions.

Future studies developing treatments for VML should also consider differences in regenerative potential between acute and chronic VML defects. Most prior studies have evaluated engineered skeletal muscle constructs within acute VML defects, where the VML injury was created immediately before construct implantation. In the clinical reality, however, chronic VML is much more common whereby a VML injury is sustained and treatment is only available months or even years later. Few studies have directly compared the regenerative potential of an engineered muscle construct in acute versus chronic VML[21] and significant differences in regeneration are likely due to variation in the muscle regeneration timeline. In addition to incorporating consideration of variability due to the age, sex, and anatomical location of preclinical models, future studies should also consider treatments that would translate well to a chronic VML environment.

1.6 Specific Aims

The overall goal of this thesis was to develop an implantable 3D muscle construct to regenerate volumetric muscle loss defects. To accomplish this goal, initial studies focused on scaffold design and regenerative capabilities when cultured with C2C12 myoblasts. Next, the myogenic potential of two translatable human cell sources was evaluated *in vitro* on electrospun scaffolds and *in vivo* in a range of critical and sub-critical muscle defects. Lastly, scaffolds were chemically modified to promote neuromuscular regeneration through the delivery of a proteoglycan to cultured myoblasts *in vitro* and within the regenerating VML environment following implantation. These studies are summarized by three Specific Aims:

Aim 1: Develop a 3D engineered muscle construct with C2C12s on electrospun fibrin and successfully treat a murine VML defect (**Chapter 2**)

Aim 2: Investigate the myogenic potential of translatable cell sources on electrospun scaffold in vitro and in vivo (**Chapters 3-4**)

Aim 3: Enhance neuromuscular regeneration in VML defect via in vitro pre-treatment of muscle constructs (**Chapter 5**)

Chapter 2 Development of a 3D Engineered Muscle Construct for the Treatment of Murine Volumetric Muscle Loss

2.1 Introduction

Volumetric muscle loss (VML) is a defect impacting greater than 20% of an individual muscle volume overwhelming muscle's natural repair mechanisms and leading to chronic functional deficits [146]. Current treatments are limited and include transfer of an autologous free muscle flap [36], muscle transposition [146], or amputation and power bracing [36], all of which have major limitations. Donor site morbidity, lack of donor tissue, and the need for a highly skilled surgical team complicate VML treatment and decrease positive patient outcomes [36]. Tissue engineered grafts have great potential to create clinical treatment options for regeneration of VML. Decellularized extracellular matrix (dECM), both acellular and cell-seeded, has been extensively investigated as a scaffold to treat VML and evaluated in preclinical [6,21,46,55–57] and clinical [58,60,61] models with varied results. Despite some improvements to muscle function, results with acellular dECM lack significant myofiber formation, while cell-seeded dECM is limited by batch-to-batch variability, poor mechanical durability, and potential immunogenicity. Other scaffold materials used in preclinical models to treat VML include collagen [83], hyaluronic acid [85], fibrin [24,49,70], poly(lactic acid)/poly(lactic-co-glycolic acid) [32], keratin [71,72], gelatin [88,89], and methacrylated gelatin [90]. Despite improvements to muscle function, formation of regenerating myofibers, and vascular infiltration, there has yet to be a scaffold system that enables the formation and long-term survival of dense myofibers and vasculature to mimic that of native skeletal muscle.

Our group has recently demonstrated the capacity to enhance the bioactivity and biocompatibility of naturally occurring fibrin by electrospinning it into microfiber bundles with alignment topography, tunable substrate stiffness, and controllable porous architecture [147]. Fibrin is an ideal scaffold material because it is FDA-approved, biodegradable, has tunable chemical and mechanical properties, and has been used previously for tissue engineered skeletal muscle with promising results [24,49,70]. Alignment cues enhance stem cell myogenic differentiation as well as myocyte fusion [148,149] and substrate stiffness impacts stem cell differentiation and myogenesis [150,151]. The electrospun hydrogels are also suturable and can be bundled to offer scale-up capabilities. Here we developed axially aligned fibrin hydrogel microfiber bundles with an elastic modulus similar to native muscle and evaluated their ability to support the development of mature, contractile skeletal muscle constructs using C2C12 myoblasts. Moreover, we assessed the ability of the electrospun hydrogels with and without C2C12s to treat VML in a murine model in which 30-50% of the tibialis anterior (TA) muscle was removed. We tested the hypothesis that the combination of C2C12s on electrospun hydrogels promotes muscle regeneration and functional recovery compared to scaffold alone or no repair. In addition, we tested the ability of pre-vascularized electrospun hydrogels to provide an implanted vascular source and enable eventual scale-up to larger injury models.

2.2 Materials and Methods

Electrospinning Fibrin Scaffolds

Scaffolds were fabricated as described previously [147]. Briefly, 1% fibrinogen (Sigma) or sodium alginate (Sigma) were extruded in parallel with 3-5 kV applied to form hydrogel microfiber bundles. Fibrinogen remained constant at 4 ml/hr while alginate concentrations and extrusion rates

were varied to alter scaffold properties (**Fig. 3.2E)**. Scaffolds with 15% alginate were utilized for experiments. Additional details are described in **3.5 Supplemental Methods.**

Characterization of Scaffold Pore Size, Porosity, and Stiffness

Scaffolds frozen in OCT (Tissue Tek) were sectioned with a cryostat (10 μm; Leica). Porosity was quantified using Hematoxylin & Eosin (H&E, Sigma) stained sections with ImageJ (NIH) and defined as the pore areas divided by total scaffold area (n=2–6). Scaffolds were also loaded into a custom bioreactor and stiffness analyzed as described previously [152]. Briefly, scaffolds were adjusted to zero strain then stretched to 10% strain at 1% strain/s as force sensors generated a stress-strain curve. Stress data was filtered using the Savitzky-Golay filter to remove cyclic noise from the motor.

Cell Culture and Seeding on Scaffolds

C2C12s (ATCC) were used at passage 8. A seeding volume of 40 μl at 7,500 cells/μl was pipetted onto scaffolds in 5 μl droplets and incubated for 1 hour at 37°C, after which C2C12 Growth Medium with 30 μg/ml aprotinin (Affymetrix) was added. Samples were differentiated on day 3 of culture. Pre-vascularized scaffolds were seeded with a 1:1 ratio of human umbilical vein endothelial cells (HUVECs; Lonza) and passage 3 primary human adipose-derived stem cells (ASCs) isolated as previously described [153] for a total seeding density of 300,000 cells/scaffold.

Whole Mount Immunostaining

Samples fixed in methanol at -20°C overnight were washed with PBS then blocked and permeabilized for 3 hours at 4°C. Scaffolds were incubated with primary antibodies overnight at 4°C (135 rpm) followed by three 1-hour washes. Scaffolds were then incubated with DyLight 488-conjugated goat anti-mouse or DyLight 649-conjugated goat anti-rabbit (1:400; Jackson

ImmunoResearch) overnight at 4°C (135 rpm) followed by three 1 hour washes with DAPI in the second wash (1:2000; Sigma). Samples were imaged with a confocal microscope (Zeiss).

In Vitro Force Measurement

Day 7 C2C12-seeded scaffolds were loaded into a custom bioreactor described previously [152] with one end clamped to a force sensor. Field stimulation was applied with platinum electrodes every 5 seconds at 5-7 V and 50-100 Hz and the resulting force of contraction was measured with the force sensor.

VML Defect Model

Animal and surgical procedures were approved by the Institutional Animal Care and Use Committee at Johns Hopkins University School of Medicine. Bilateral VML defects in female NOD-scid IL2Rg^{null} (NSG) immunodeficient mice (Jackson Lab) were used for all experiments. Treatment groups per experiment are detailed in **SI.** Mice were anesthetized with isofluorane, the TA muscle was exposed, and approximately 30-50% of the muscle removed. After bleeding ceased, scaffolds were placed in the defect site and ligated on both ends to the remaining TA muscle with non-absorbable sutures (6-0 Nylon, Express Medical Supplies) (**Fig. 2**). Surgical glue (Histoacryl, B. Braun) and Reflex wound clips (CellPoint Scientific) were used to close the skin. Rimadyl was injected subcutaneously post-surgery for pain management (5 mg/kg). Mice were sacrificed by isoflurane overdose and cervical dislocation. Upon harvest, implanted scaffolds and surrounding TA muscle tissue were removed and cryopreserved.

Histology

Harvested TA muscles were weighed and flash-frozen in OCT with 2-methylbutane (Sigma). Samples were sectioned with a cryostat (10 μm) and rehydrated in DI water before staining with H&E or Masson's Trichrome (MT; Sigma). For immunohistochemistry, slides were

fixed in methanol or acetone at -20°C for 10 min, rinsed with PBS three times, then blocked for 1 hour at RT. Slides were incubated with antigen-specific primary antibodies overnight at 4°C. After three 15 min washes with PBS, slides were incubated with secondary antibody for 1 hour at RT. Slides were washed then mounted with 50% glycerol and imaged on a fluorescence microscope (Zeiss).

In Vivo Functional Testing

In vivo assessment of mouse TA muscle contractility was performed at 2 and 4 weeks as previously described [154]. Briefly, mice were anesthetized with isoflurane and the leg was stabilized in a custom-made apparatus. The foot was taped to a foot plate connected to a torque sensor and stepper motor and the ankle was positioned at 20° of plantarflexion, which has been shown to be the optimum length to achieve maximum ankle dorsiflexor torque (in which the TA muscle accounts for the majority of ankle dorsiflexion). Electrodes were placed subcutaneously at the fibular head to stimulate the fibular nerve and induce dorsiflexion. Voltage and frequency were optimized for each leg during tetanic contractions (300 ms duration) and the maximal isometric torque was quantified per leg at each time point (n=7). To also assess resistance to fatigue, each TA was subjected to a series of 50 isometric tetanic contractions (one contraction every 2 seconds) and the resulting drop in maximal isometric torque and recovery after 2 and 5 minutes were quantified (n=7).

Statistics

Statistical analysis was performed using GraphPad Prism 5 software. Statistical significance for most experiments was determined by one-way ANOVA with Dunnet post-test utilizing the uninjured values as control. Statistical significance for myofiber and vascular densities

was determined by one-way ANOVA with Tukey's post-test. Error bars represent standard error of the mean (SE). *: $p < 0.05$; **: $p < 0.01$; ***: $p < 0.001$; ǂ: not significant.

2.3 Results

Electrospun Scaffold Properties Tailored for Tissue Engineered Skeletal Muscle

Electrospun fibrin scaffolds were designed to mimic the hierarchical structure and native characteristics of skeletal muscle (**Fig. 3.1A**). The optimized fibrin scaffolds contain intrinsic alignment on the micro-scale, have a porous interior, and are suturable (**Fig. 3.1B-D**). To control porosity and stiffness, fibrin scaffolds were electrospun containing various amounts of alginate, which served as a sacrificial polymer to induce porosity (**Fig. 3.2**). A 15% alginate composition was selected for subsequent studies due to its myomimetic stiffness similar to the 12 kPa stiffness of native skeletal muscle [151] (**Fig. 3.1E**) and high internal porosity. Topographical alignment cues enable alignment of a range of cell types (**Fig. 3.3**), a vital component of functional skeletal muscle

constructs that enables uniaxial contraction and has been shown to contribute to myogenesis [148,149].

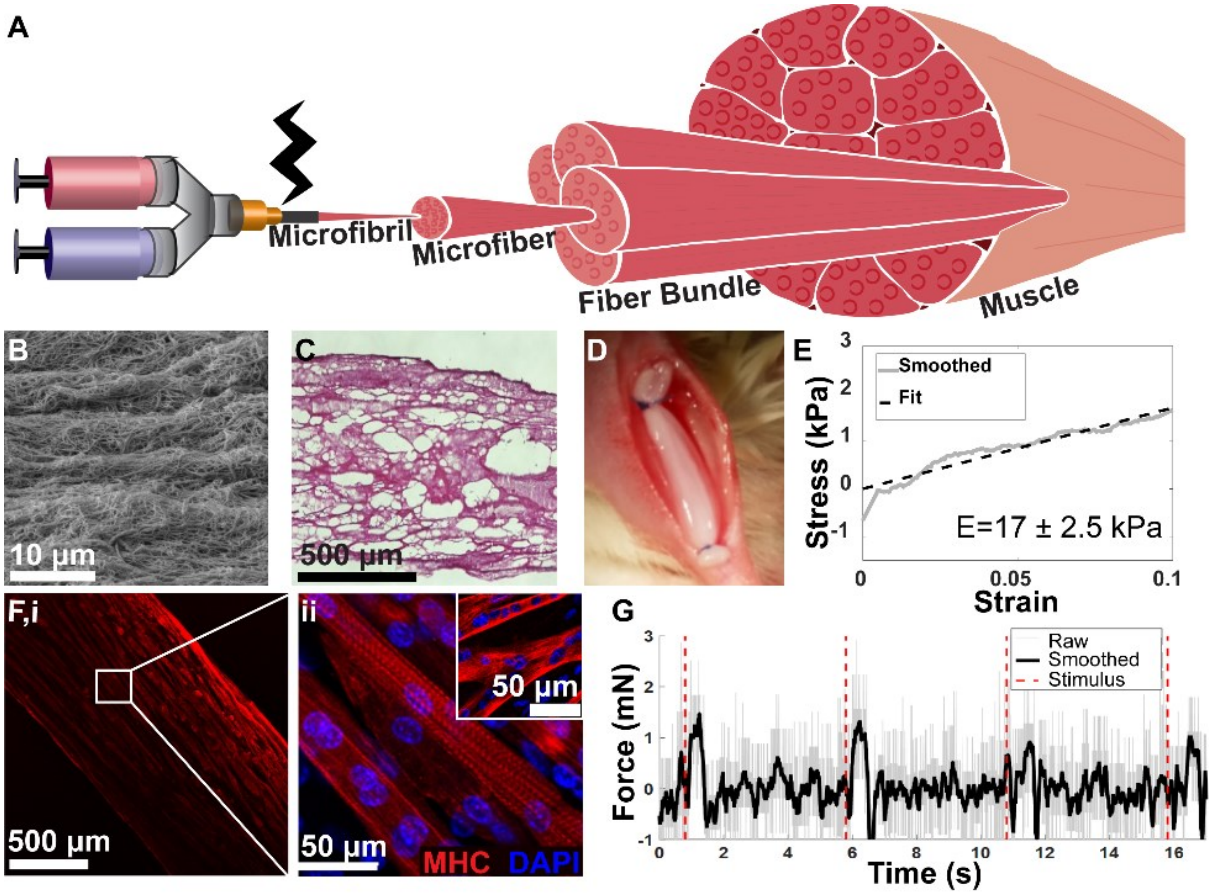

Figure 2.1. Fabrication of electrospun fibrin scaffolds. A) Schematic of hierarchical structure of electrospun scaffolds. **B)** Scanning EM of microscopic scaffold structure and alignment. **C)** Longitudinal section of 15% alginate scaffolds stained with H&E demonstrating internal porosity. **D)** Scaffolds bundled and sutured into muscle defects. **E)** Representative stress-strain curve. **F)** (i) MHC (red) and DAPI (blue) staining of aligned, multinucleated myotubes on scaffolds at day 7 with (ii) sarcomeric striations. Inset: C2C12s on glass substrate. **G)** Representative contractile force generation in response to electrical stimulation.

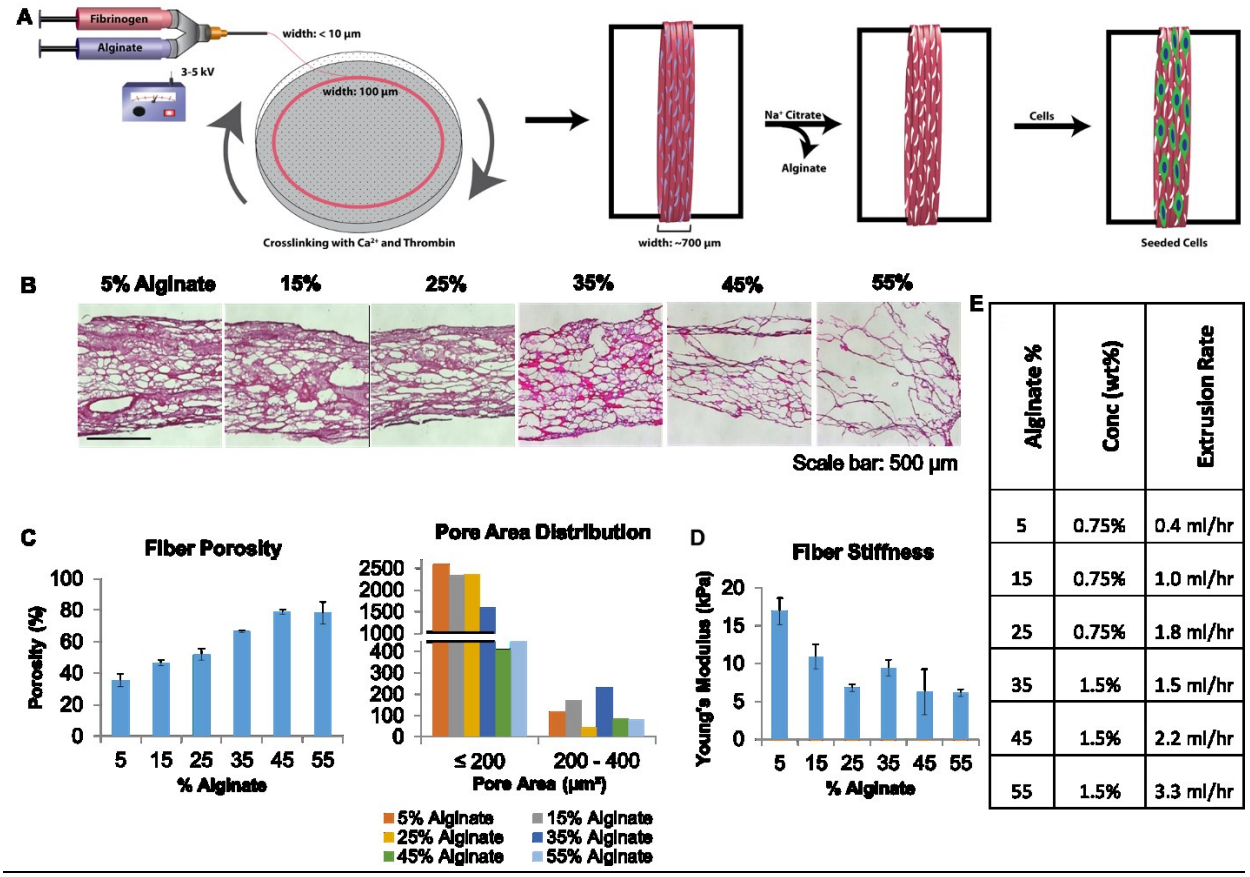

Figure 2.2. Electrospinning fibrin scaffolds and cell seeding. A) Schematic of scaffold fabrication via electrospinning, alginate removal, and subsequent cell seedin. **B)** Longitudinal sections of scaffolds stained with H&E at increasing alginate percentages to assess changes in porosity. **C)** Scaffold porosity and pore area distribution at a range of alginate percentages. **D)** Scaffold stiffness at a range of alginate percentages. **E)** Concentrations and flow rates of alginate during electrospinning. The fibrinogen solution had a constant 1% concentration and 4 ml/hr flow rate.

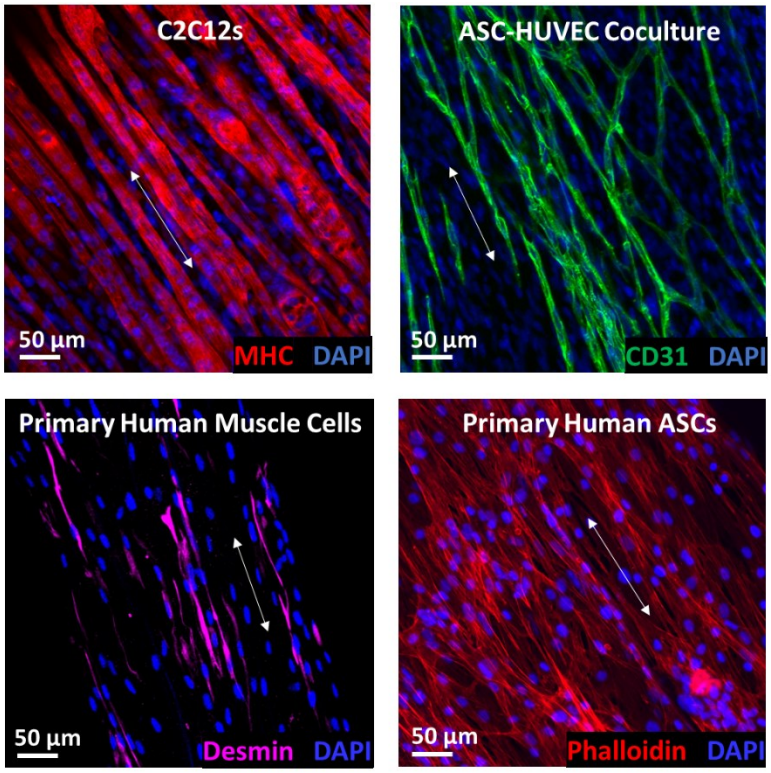

Figure 2.3. Electrospun scaffolds induce alignment of various cell types. Scaffold alignment cues induce cellular alignment of C2C12 myoblasts, vasculature formed by human umbilical vein endothelial cells (HUVECs) and adipose-derived stem cells (ASCs), primary human myoblasts, and primary human ASCs. Arrows: direction of scaffold alignment.

Myoblast-Seeded Scaffolds Form Mature Contractile Muscle Constructs *In Vitro*

To test the suitability of electrospun fibrin scaffolds as a substrate for mature muscle constructs, C2C12 myoblasts were seeded and cultured for 7 days. C2C12s formed densely aligned myosin heavy chain positive (MHC+) myotubes along the scaffolds and exhibited multinucleation and sarcomeric striations, hallmarks of mature muscle (**Fig. 2.1F**). In comparison, C2C12s cultured on glass coverslips for 7 days formed disorganized myotubes lacking similar alignment

and features. C2C12-seeded scaffolds also exhibited spontaneous contractions and contracted in response to electrical stimulation generating approximately 1 mN of force (**Fig. 2.1G**). To potentially increase cell uniformity, an alternate 'spread' scaffold structure was fabricated (**Fig. 2.4A,B**) and its myogenic potential assessed. C2C12-seeded spread scaffolds exhibited a similar density of aligned, multinucleated myotubes compared to 'bulk' scaffolds (**Fig. 2.4C-E**) and spontaneous contractions.

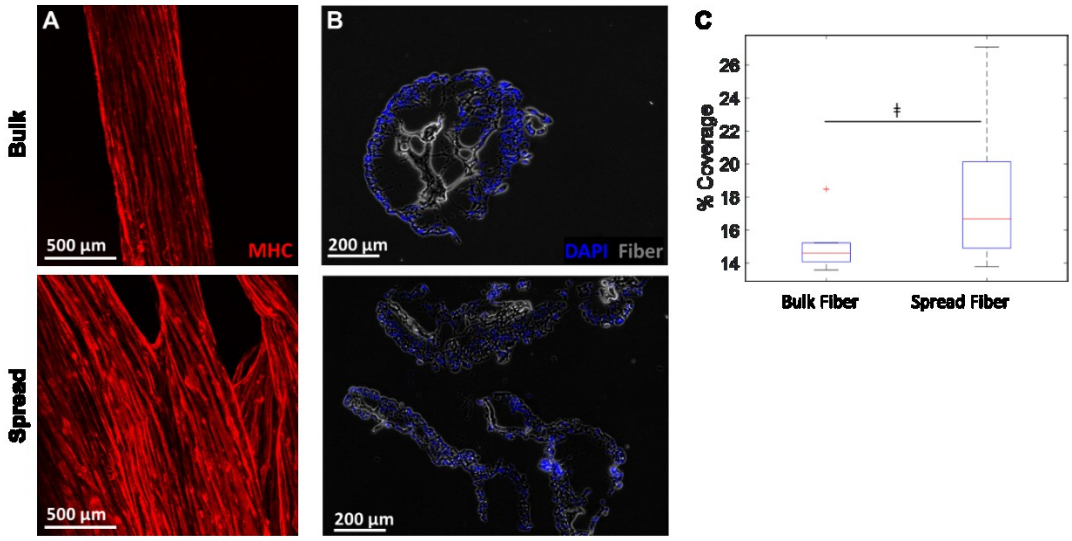

Figure 2.4. Altering electrospun scaffold morphology maintains alignment cues with C2C12 cell density. (A) Dense alignment of MHC-positive C2C12 myotubes are present on both bulk and spread scaffolds at day 7. **(B)** DAPI (blue) and brightfield (gray) images of scaffold cross-sections demonstrating no significant difference in cell density between bulk and spread scaffolds at 7 days. **(C)** Quantification of C2C12 percent coverage between bulk and spread scaffolds demonstrated no significant difference in C2C12 density. ǂ: not significant

Regeneration of Murine VML Defects with Myoblast-Seeded Electrospun Scaffolds

An established murine VML defect model [21,46,50] was used to test the regenerative potential of C2C12-seeded electrospun scaffolds. Scaffolds were bundled and sutured into the defect (**Fig. 2.5**) for 2 or 4 weeks. Each mouse was treated with bulk scaffolds in the right leg and

spread scaffolds in the left leg (n=3). Both bulk and spread C2C12-seeded scaffolds resulted in significant levels of muscle regeneration at 2 weeks (**Fig. 2.6C**) with graft areas densely populated with centrally-nucleated MHC+ myofibers and a robust, dense capillary network. Myofiber density increased from 2 to 4 weeks for both groups, approaching that of native skeletal muscle, whereas vascular density remained high at both time points (**Fig. 2.6D**). Individual myofiber diameters in all groups averaged ~23 μm, which is roughly half the diameter of myofibers in native TA muscle (**Fig. 2.6E**). Treatment groups also exhibited significant volume recovery of the graft areas, with total TA cross-sectional areas in treatment groups mimicking that of native TA muscle (**Fig 2.6F**). As spread scaffolds did not confer any advantage in regenerative outcomes, bulk scaffolds were utilized for future experiments.

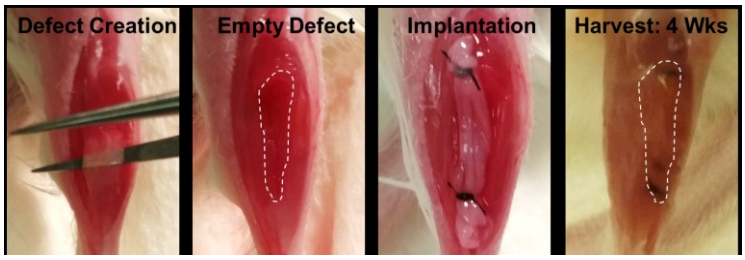

Figure 2.5. Murine VML defect and scaffold implantation model. Macroscopic depiction of VML defect creation via partial TA resection, an empty VML defect, scaffold implantation, and morphology of the scaffolds within the defect at 4 weeks post-implantation.

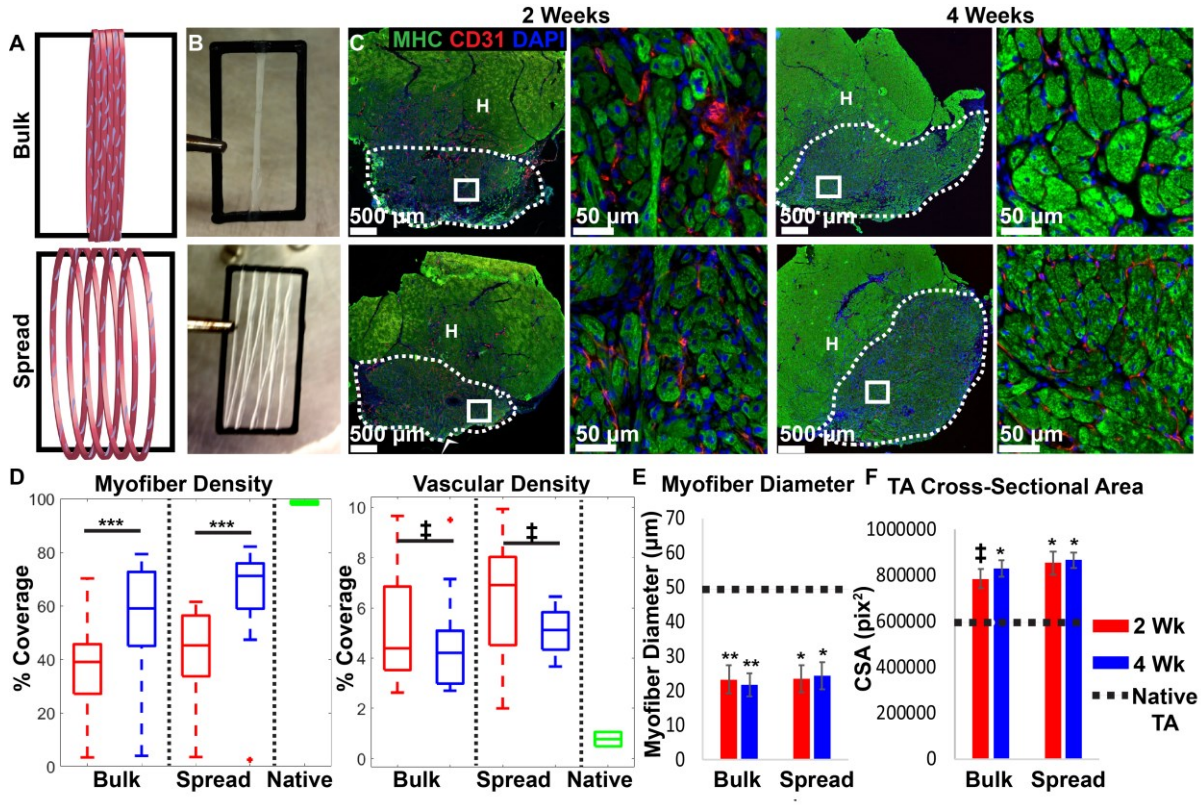

Figure 2.6. In vivo regeneration of VML defects. A, B) Bulk and spread scaffolds. **C)** MHC (green), CD31 (red), and DAPI (blue) staining of VML defects treated with C2C12-seeded scaffolds at 2 and 4 weeks. High densities of centrally-nucleated myofibers (arrows) and vasculature are present. Dotted line denotes approximate graft region. H: host muscle tissue. **D)** Myofiber and vascular densities at 2 and 4 weeks (n=18). Red: 2 weeks; Blue: 4 weeks; Green: native muscle. **E)** Myofiber diameters (n=24) and **F)** cross-sectional areas (n=11) following treatment. *: $p < 0.05$; **: $p < 0.01$; ***: $p < 0.001$; ǂ: not significant. Error bars are SE.

Myoblast-Seeded Scaffolds Enable Muscle Regeneration but Acellular Scaffolds Do Not

We directly compared three experimental groups (n=7): (i) untreated defects; (ii) acellular scaffolds; or (iii) C2C12-seeded scaffolds in the VML model to assess the role of cells and scaffolds in regeneration. Approximately 11 ± 3 mg of muscle tissue was resected per defect and the contralateral leg remained as an uninjured control. Bundles of 4 acellular or C2C12-seeded scaffolds were sutured into the defect site in treatment groups and the defect remained empty for the untreated group. Constructs remained *in vivo* for 4 weeks.

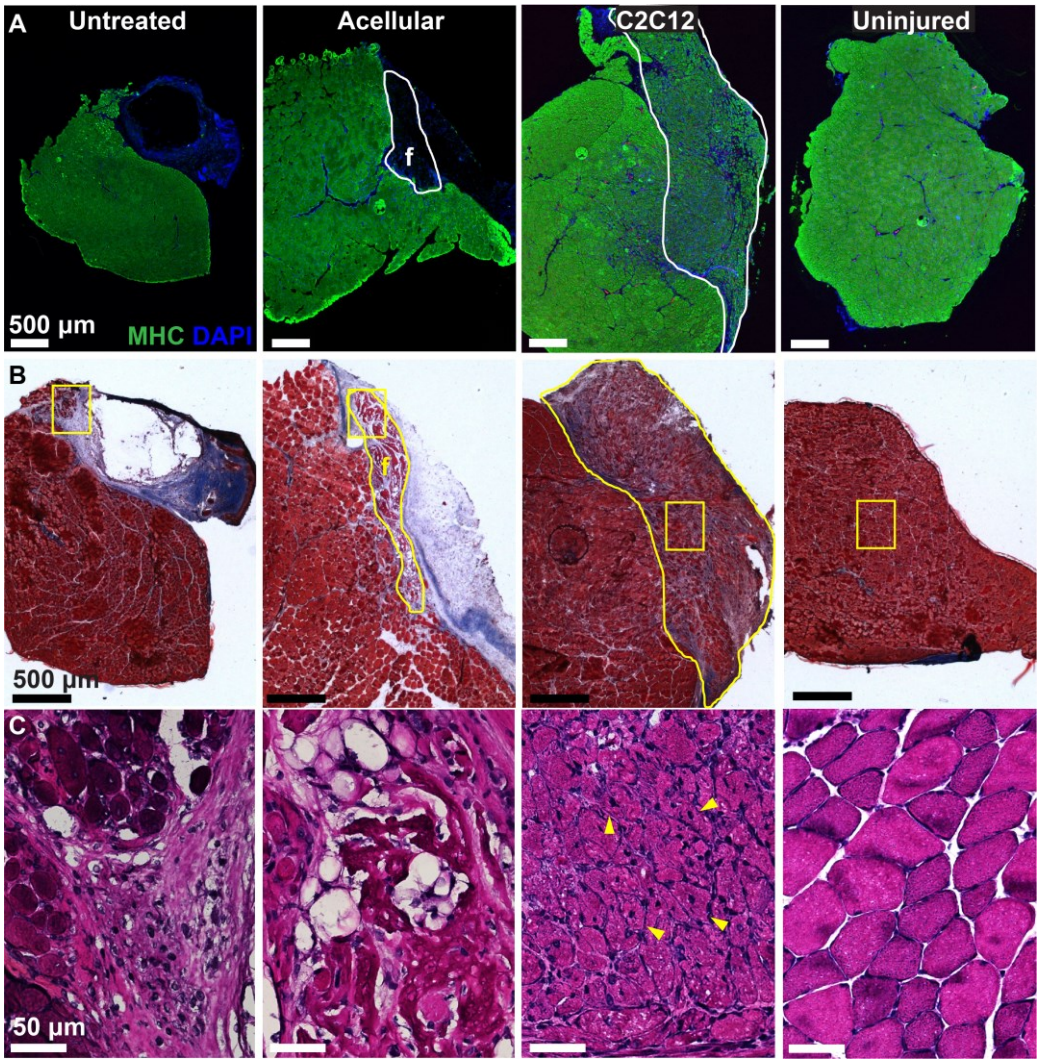

Figure 3.7. Evaluation of muscle morphology. **A)** MHC (green) and DAPI (blue) staining at 4 weeks post-injury compared to uninjured muscle (f: acellular fibrin scaffold). Outlines denote approximate graft region. **B)** Masson's Trichrome staining demonstrating low fibrosis and integration of C2C12 samples. **C)** H&E staining of cell morphology within the defects. Arrowheads denote centrally-nucleated myofibers.

Untreated defects exhibited loss of muscle tissue at the defect site, lacked myofibers, and contained significant fibrotic tissue (**Fig. 2.7A-C**). Remnants of acellular scaffolds could be observed at 4 weeks, but exhibited varying levels of fibrosis and lacked the presence of any MHC. In stark contrast, defects treated with C2C12-seeded scaffolds exhibited significant volume recovery, muscle mass increase, lack of fibrosis, and high myofiber density (**Fig. 2.8**). In the

C2C12 treatment group, myofibers were primarily centrally-nucleated and began to approximate the structure of native uninjured TA muscle.

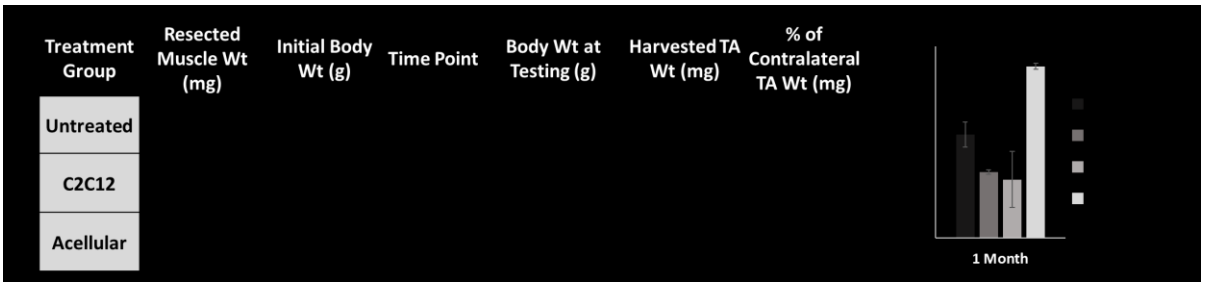

Figure 3.8. Morphological Characteristics. A) Mouse body and TA weights at various time points. **B)** TAs containing C2C12 constructs weighed significantly more than other groups. Values are means ± SE (n=4-5). * $p < 0.05$.

Defects treated with acellular scaffolds exhibited disorganized laminin deposition within the scaffold interior, but had no myofibers present at 2 weeks. In contrast, defects treated with C2C12s had organized circular myofibers with a laminin structure similar to uninjured muscle (**Fig. 2.9A**). Embryonic myosin, a transient marker of regenerating skeletal muscle, was evident in C2C12-treated defects at 2 weeks with expression decreasing by 4 weeks. Defects treated with acellular scaffolds did not express embryonic myosin at 2 weeks, suggesting that the regeneration seen in C2C12-treated groups was due to the implanted cells (**Fig. 2.9B**). Myofibers in C2C12 treatment groups stained positively for the slow-twitch myofiber marker BA-D5 at 4 weeks (**Fig. 2.9C**). Significantly, C2C12 treatment groups also exhibited host neurofilament within the graft area, suggesting the possibility of functional connectivity between the host nerve and implanted muscle constructs (**Fig. 2.9D**).

To track implanted cells in C2C12-seeded scaffolds, a subset of C2C12s was transduced to express mCherry and luciferase and seeded onto scaffolds. Transduced C2C12s formed aligned MHC+ myotubes on the scaffold surface that had similar morphology to non-transduced samples and expressed mCherry and luciferase (**Fig. 2.10B-E**). Bundles of 4 scaffolds containing

transduced C2C12s were implanted into bilateral VML defects and luciferase expression was quantified. Implanted C2C12s were retained within the defect areas, remained viable, and proliferated *in vivo* up to 28 days (**Fig. 2.10A**). Vascular perfusion was observed in uninjured muscles (**Fig. 2.10F**) and C2C12-seeded scaffolds (**Fig. 2.10G**) via tail vein injection of FITC dextran and confocal imaging.

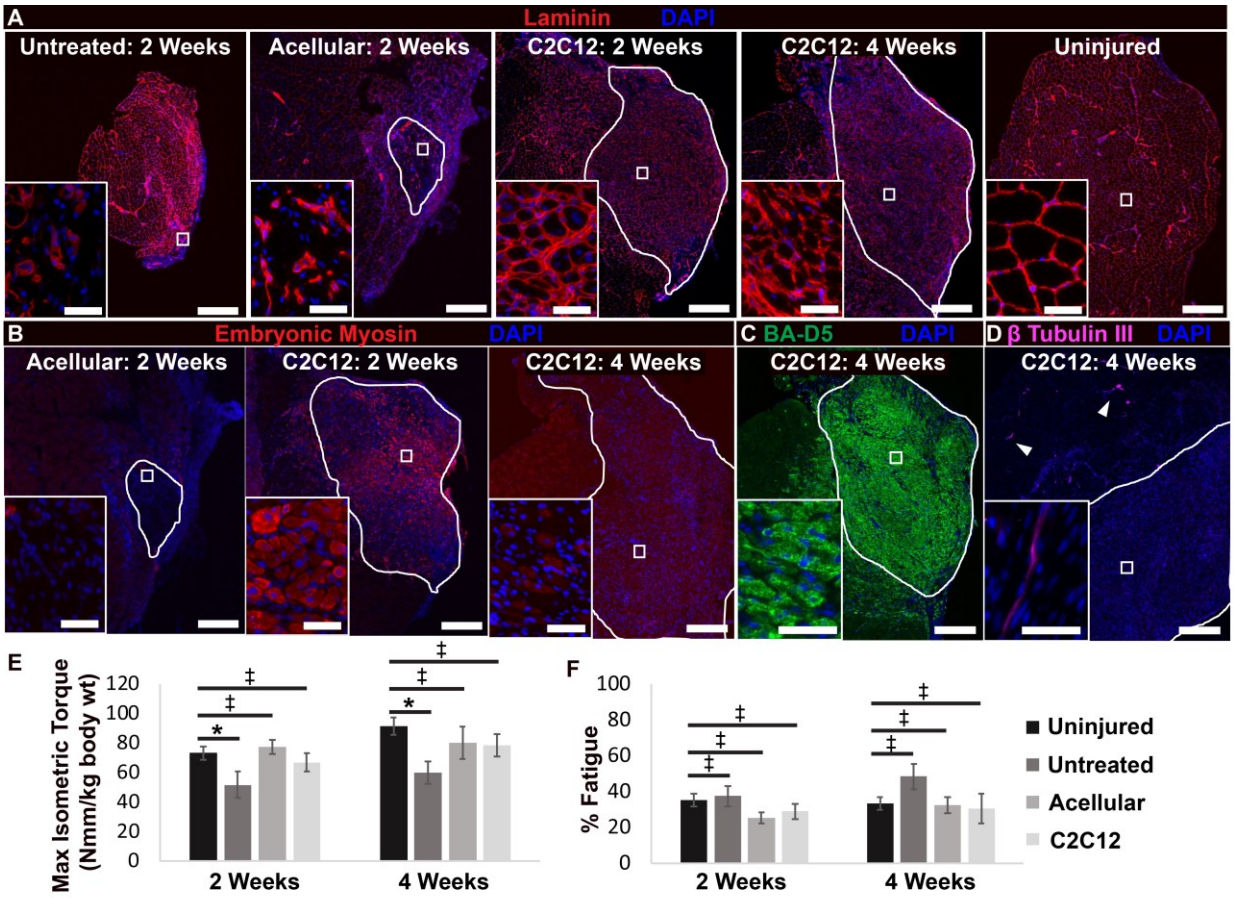

Figure 3.9. Morphologic and functional characterization of regenerating muscle. A) Laminin (red) and DAPI (blue) staining demonstrates differences in myofiber size and morphology between groups. **B)** Embryonic myosin (red) and DAPI (blue) staining. **C)** Slow-twitch myosin (green; BA-D5) and DAPI (blue) staining. **D)** Neurofilament ingrowth into the graft region of C2C12 samples at 4 weeks is visible with β-tubulin III (pink) and DAPI (blue) staining. Arrowheads show neurofilament within host muscle. Scale bars: 500 μm, inset- 50 μm. Outlines denote approximate graft region. **E)** Maximal isometric torque (n=7). (F) Percent fatigue (n=7). * $p < 0.05$; ǂ: not significant. Error bars are SE.

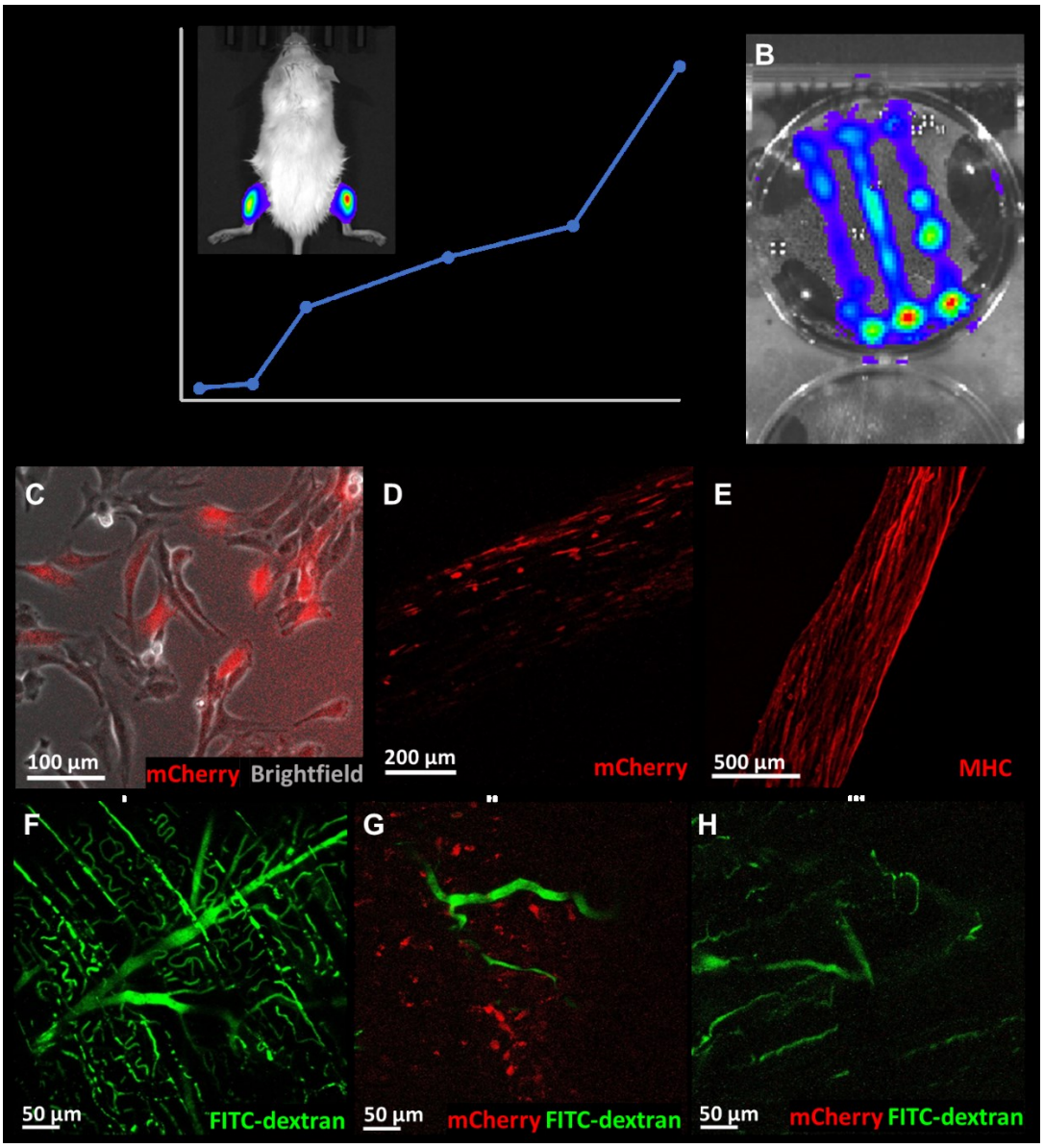

Figure 3.10. Luciferase-expressing C2C12s proliferate within VML defects and contain perfusable vasculature. A) Average total flux at each time point demonstrating that C2C12s proliferate up to 4 weeks post-transplantation (n=2). Inset: BLI of bilateral VML defects treated with scaffolds seeded with luciferase-expressing C2C12s. Signal was localized to the defect region indicating a lack of cell migration away from the defects. **B)** Bioluminescence imaging (BLI) of a scaffold seeded with C2C12s transduced to express luciferase (day 8). **C)** C2C12s expressing mCherry (red) in monolayer and **D)** seeded onto fibrin scaffolds at day 6. **E)** MHC (red) staining of transduced C2C12s at day 7 demonstrates that transduced C2C12s continue to form aligned myotubes on scaffolds. **F)** FITC-dextran (green) injection enables visualization of vascular perfusion within native TA muscle and **G)** defects treated with mCherry+ C2C12-seeded scaffolds (red). **H)** A control region outside the scaffold area was used as a mCherry negative control.

Myoblast-Seeded and Acellular Scaffolds Both Enable Functional Recovery

The effects of acellular and C2C12-seeded scaffolds on muscle contractile function were evaluated by measurement of maximal isometric torque of the ankle dorsiflexor muscles (**Fig. 3.11A**). Muscles containing untreated defects demonstrated ~30% torque deficit compared to uninjured controls at 2 and 4 weeks post-injury (**Fig. 3.9E**). Interestingly, defects treated with both acellular and C2C12-seeded scaffolds demonstrated complete functional recovery at both 2 and 4 weeks post-injury, with maximum isometric torque levels equal to uninjured controls (**Fig. 3.9E**). Muscle resistance to fatigue was also tested via the loss in maximal torque after 50 isometric contractions. No significant differences in percent fatigue were present between groups at both time points (**Fig. 3.9F**) although untreated muscles were slower to recover (**3.11C**).

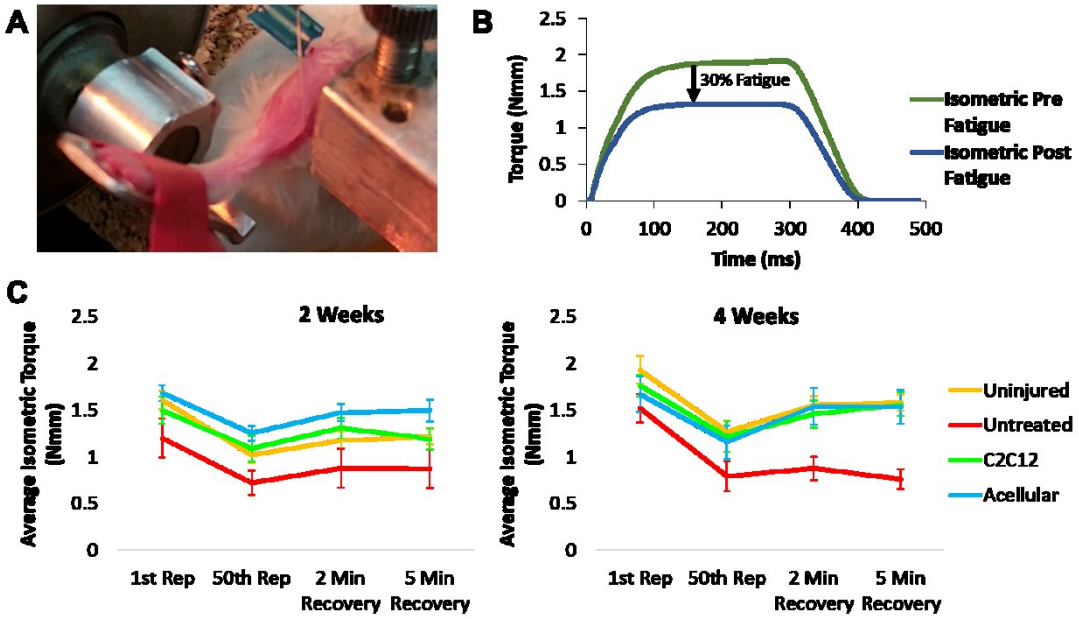

Figure 3.11. Fatigue testing between groups. A) Macroscopic depiction of setup for measurement of in vivo torque within mouse dorsiflexor muscles. The tibia is stabilized and the foot secured against a motor-driven plate, enabling stimulation of the ankle dorsiflexor muscles via the fibular nerve and force measurement. **B)** Representative graph from uninjured TA muscle depicting the drop in maximal isometric torque of the dorsiflexor muscles between the first and final repetitions of fatiguing isometric contractions enabling the calculation of percent fatigue. **C)** Average isometric torque for all groups was measured over time to quantify resistance to fatigue of TA muscles at 2 and 4 weeks post-implant.

Pre-Vascularized Scaffolds Anastomose to Host Vessels

Although C2C12-seeded scaffolds implanted in VML defects exhibited a high density of vascular infiltration and myoblast survival up to 4 weeks, scale-up to large animal models would likely require an implanted vessel source to meet the increased nutrient and oxygen demands of larger tissues. Therefore, we tested whether engineering scaffolds with pre-formed vascular networks would expedite blood flow throughout the grafts. Electrospun scaffolds were seeded with human umbilical vein endothelial cells (HUVECs) and human adipose-derived stem cells (ASCs) in a 1:1 ratio and cultured for 11 days to form aligned vessels along the scaffold length (**Fig. 3.12A**). Bundles of 4 pre-vascularized scaffolds were implanted into VML defects and harvested after 10 days. Implanted human vessels successfully anastomosed with host vessels and exhibited perfusion by host red blood cells (**Fig. 3.12B-C**).

Interestingly, the implanted pre-vascularized scaffolds exhibited low levels of degradation and were each surrounded by a thick collagen boundary (**Fig. 3.12D**). This is in contrast to C2C12-seeded scaffolds implanted for a similar amount of time where scaffolds were completely replaced by dense myofibers and host vessels, lacking significant collagen deposition. In addition, although pre-vascularized scaffolds retained the implanted human vessels, there was little host vessel infiltration to the scaffold interior as well as a complete lack of myofibers within the scaffolds (**Fig. 3.12E-F**). Cross-sections of *in vitro* pre-vascularized and C2C12-seeded scaffolds stained with Masson's Trichrome demonstrated a similar difference in collagen deposition on the scaffold surface by ASC:HUVEC co-cultures compared to C2C12s (**Fig. 3.12G**). To test our hypothesis that the collagen on the scaffold surface was deposited by ASCs and prevents integration with surrounding host tissue, scaffolds seeded with ASCs were implanted into VML defects for 2 weeks. ASC-seeded scaffolds had dense collagen boundaries preventing scaffold degradation and

integration with host tissue (**Fig. 3.13**), similar to those seen in implanted pre-vascularized scaffolds.

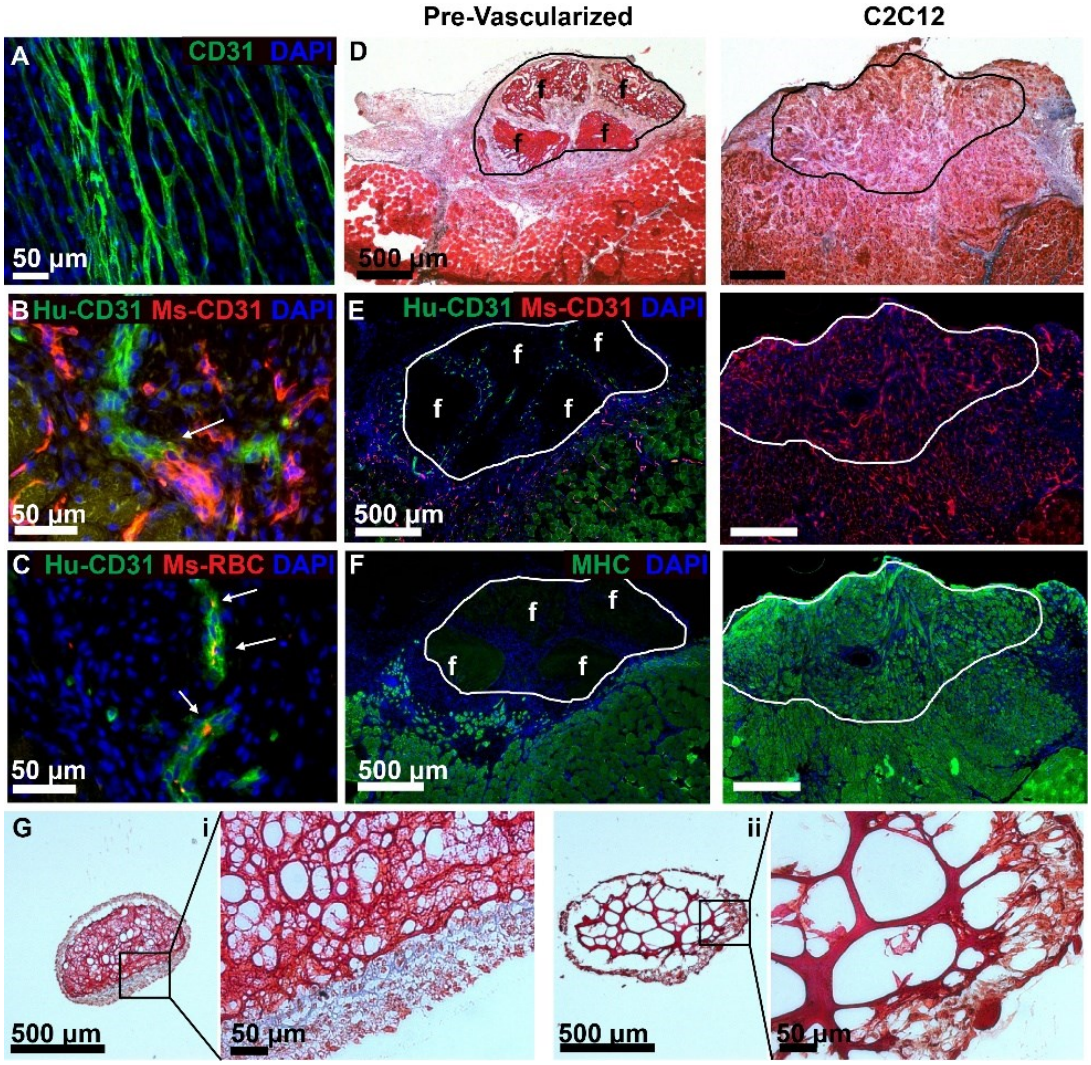

Figure 3.12. Pre-vascularized scaffolds in VML defect. A) CD31 (green) and DAPI (blue) staining of vasculature on scaffolds. **B)** Pre-vascularized scaffolds implanted in VML defects for 10 days contained human vessels (green) that anastomosed with host mouse vessels (red; arrow). **C)** Implanted human vessels (green) were perfused with mouse red blood cells (red; arrows). **D)** Masson's Trichrome staining demonstrating differences in muscle regeneration, collagen deposition, and scaffold degradation. **E)** Mouse (red) and human (green) CD31 staining. **F)** MHC (green) staining. **G)** Masson's Trichrome staining of cross-sections from in vitro pre-vascularized scaffolds and C2C12-seeded scaffolds demonstrating differences in collagen deposition, scaffold porosity, and swelling. f: fibrin scaffold.

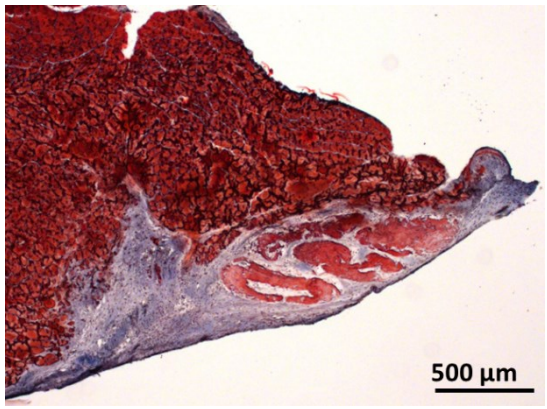

Figure 3.13. ASC-seeded scaffolds implanted in VML defects form collagen boundaries. Scaffolds seeded with ASCs and implanted in murine VML defects for 2 weeks exhibit significant collagen deposition that prevents scaffold degradation and integration with the host.

2.4 Discussion

Electrospun fibrin scaffolds mimic the hierarchical structure and mechanical properties of muscle and provide a pro-regenerative environment for cells. The scaffolds also have the potential to be used off-the-shelf and can be stored long-term and rehydrated prior to cell seeding and implantation [147]. Prior reports indicate that treatment with acellular scaffolds relies on muscle stem/progenitor cell and vascular ingrowth from the remaining muscle tissue and provides demonstrable improvements to muscle contractile function, but muscle regeneration has been limited [46,54,60] and the need for inclusion of a myogenic cell source to regenerate muscle tissue following VML has been demonstrated [46,56,57,72]. Yet cell-seeded scaffolds have been typically impaired by fibrosis, an inability to fully recapitulate the myofiber and vascular density present in native skeletal muscle, and poor cell viability. This study demonstrates that the pro-regenerative environment created by electrospun scaffolds stimulates remarkable vascular and myogenic regeneration with little to no fibrosis at the graft-host interface.

Fibrin has been used previously in skeletal muscle constructs to treat VML with mixed results. Murine TA VML defects treated with fibrin microthreads seeded with C2C12s enabled

some muscle regeneration, vascular infiltration, and functional recovery 60 days post-implantation, but regenerated myofibers were bounded by significant collagen deposition and were disorganized despite microthread alignment cues [24]. Fibrin microthreads seeded with human muscle cells and used to treat murine TA VML defects resulted in high levels muscle regeneration and some collagen deposition within the defect at 10 weeks post-implantation, but no vascular regeneration was shown [70]. Another study assessed the efficacy of progressive injections of C2C12s or human muscle progenitor cells in fibrin to treat murine TA VML defects, which resulted in a variable density of vascularized myofiber formation at 4 weeks post-implantation with high interior myofiber density but a low density at the graft outskirts [49]. A recent study where dECM seeded with primary muscle cells was used to treat a murine TA VML defect resulted in high levels of vascularized muscle regeneration 30 days post-implantation where the number of total blood vessels per field mimicked native muscle. However, the number of vessels per myofiber was around 0.2 and was not compared with native skeletal muscle [21]. In addition, although myofiber density within the defect appeared to be high in histological images, the value was not compared to native skeletal muscle. In the current study, the electrospun fibrin scaffolds provided alignment cues and unique mechanical properties that overcame these limitations.

The extent of muscle and vascular regeneration following VML injury when treated with C2C12-seeded electrospun scaffolds seen here is a significant improvement over previous treatment modalities. Although regenerating myofibers had roughly half the diameter of native TA myofibers, the density of myofibers seen as well as the high prevalence of perfusable vasculature within the defect was substantial. Myofiber density within the grafts reached 68% coverage of the field of view with remaining areas composed of blood vessels and connective tissue, as demonstrated by CD31 and laminin staining. Myofibers within the defect contained thicker

laminin boundaries and smaller myofiber diameters than native skeletal muscle, which may explain the overall difference in myofiber densities. Vascular density in the grafts was higher than in native skeletal muscle with an average coverage of 5.3% of the field of view. The blood vessels in C2C12-treated defects were significantly larger in cross-sectional area than those seen in native muscle, increasing the total area of vessel coverage per field of view compared to native muscle. *In vivo* degradation of electrospun fibrin scaffolds varies depending on the cell type with which it is seeded. We have found that C2C12-seeded scaffolds completely degrade 2 weeks post-implantation and are replaced with dense regenerating muscle and vasculature, while ASC-seeded and pre-vascularized scaffolds maintain much of their structure after 2 weeks *in vivo* and lack corresponding regeneration. Interestingly, cross-sections of *in vitro* C2C12-seeded scaffolds exhibit increased porosity and swelling compared to cross-sections of pre-vascularized scaffolds, which also contain a dense collagen boundary. It is thus likely that differences in cell-biomaterial interactions and subsequent scaffold swelling and degradation contribute to variations in regeneration, and that rapid scaffold degradation in response to C2C12s enables the robust muscle and vascular regeneration seen here.

The recovery of volume in C2C12-treated versus acellular or untreated defects is likely due to beneficial cell-matrix interactions coupled with survival and growth of implanted cells. It is unlikely to be due to hypertrophy of the remaining host muscle in response to injury as this would have been present in defects that were untreated or treated with acellular scaffolds as well. ASC-seeded scaffolds also demonstrate good volume recovery, but cell-scaffold interactions differed between ASCs and C2C12 myoblasts. C2C12-seeded scaffolds were completely degraded by 2 weeks post-implantation, while pre-vascularized and ASC-seeded scaffolds were still present after 2 weeks and acellular scaffolds were still present after 4 weeks *in vivo*. Cross-sections of *in vitro*

C2C12-seeded scaffolds exhibited large internal pores and increased swelling compared to cross-sections of pre-vascularized scaffolds, demonstrating that scaffold remodeling exhibits marked differences depending on cell type. In fact, an interesting result of the study was the apparent "insulation" of scaffolds seeded with ASCs. The increased collagen deposition surrounding pre-vascularized scaffolds is unlikely due to an immune response by the host, since immunodeficient animals were used and a similar response was not present when C2C12-seeded scaffolds were implanted. Our hypothesis that ASCs were the collagen source was supported by experiments with ASC-seeded scaffolds without HUVECs, which resulted in distinct collagen boundaries surrounding the scaffold as well as a complete lack of scaffold degradation or integration with the host. This result was unexpected, as ASCs have been utilized for their pro-regenerative paracrine signaling [155–157] and as a myogenic cell source both *in vitro* [158–161] and *in vivo* [162–164]. Nevertheless, in a study where pre-vascularized collagen scaffolds containing adipose-derived microvascular fragments and primary myoblasts were implanted in a full-thickness VML defect in the biceps femoris, there was no muscle regeneration and instead significant collagen deposition within the defect, supporting our results [109]. The integrative capacity of scaffolds with cultured ASCs and the contribution of ASCs to collagen deposition within muscle defects requires further investigation.

Interestingly, both C2C12-seeded and acellular scaffolds recovered the contractile function of injured muscle at both 2 and 4 weeks despite the inability of acellular scaffolds to support muscle regeneration and the vast difference in myofiber formation between C2C12-seeded and acellular treatment groups. A possible explanation for this discrepancy could be the presence of scaffold mediated functional fibrosis that has been recently described [46], where the implanted scaffold provides a mechanical bridge to prevent prolonged overload injury to the remaining

muscle after injury. Implanted acellular scaffolds are thus able to transiently augment or repair contractile function without a corresponding presence of regenerating myofibers in the defect area [57].

In conclusion, the current study provides a novel construct system containing electrospun fibrin scaffolds that, when combined with a myoblast cell source, enable unprecedented levels of functional muscle and vascular regeneration. The electrospun scaffolds mimic the stiffness of native muscle, contain intrinsic alignment cues, are suturable, biodegradable, mechanically robust, and are made from an FDA-approved biomaterial. Interestingly, VML defects treated with acellular electrospun scaffolds recovered the muscle's contractile function similar to C2C12-seeded scaffolds, despite their lack of corresponding regenerating myofibers. The electrospun scaffolds have scale-up potential to larger animal models and support the formation of implantable vasculature.

2.5 Supplemental Methods

Electrospinning Fibrin Scaffolds

Fibrin scaffolds were electrospun in a sterile environment with sterile solutions. Parallel syringes containing solutions of fibrinogen (Sigma) or sodium alginate (Sigma) were connected via a y-syringe and extruded by syringe pumps with an applied voltage of 3-5 kV applied to a 27G needle tip to form hydrogel microfiber bundles with a range of alginate percentages. The fibrinogen solution remained constant at 1% fibrinogen with an extrusion rate of 4 ml/hr. Porosity and stiffness was varied by altering alginate solution concentrations and extrusion rates as listed in Fig. S1E. Polyethylene oxide (average MZ ~ 4 000 kDa, Sigma) was added to each solution at 0.2 wt% to increase viscosity during electrospinning. The electrospun hydrogel solutions were

collected for 5.75 minutes on a rotating dish (~35rpm) containing 50 mM CaCl2 and 20 U/ml thrombin (Sigma) as crosslinking agents. Samples were allowed to crosslink and additional 3-5 min after electrospinning and were then wrapped around a 1.5 × 3.0 cm acrylonitrile-butadiene-styrene frame 4 times to yield a hydrogel microfiber bundle ~700 μm in diameter termed "bulk scaffolds". To fabricate "spread scaffolds" the hydrogel was wrapped 8 times along the frame. Scaffolds were incubated overnight in 250 mM sodium citrate (Sigma) to dissolve the alginate and then transferred to DI water until cell seeding or implantation

Cell Culture and Seeding on Scaffolds

C2C12 myoblasts were expanded in C2C12 Growth Medium: high-glucose DMEM (Invitrogen), 10% fetal bovine serum (FBS; Atlanta Biologicals), and 1% penicillin/streptomycin (P/S; Invitrogen) and used for experiments at passage 8. In preparation for cell seeding, scaffolds were incubated in high glucose DMEM for 20 min at 37 °C. The scaffolds were then transferred to 6-well cell culture plates coated with 2% agarose type VII (Sigma) to minimize cell adhesion to the plate surface, which increases the seeding efficiency. For all experiments, a total seeding volume of 40 μl at 7,500 cells/μl was pipetted onto the scaffold surface in a series of 5 μl droplets (for a total seeding density of 300,000 cells/scaffold). Scaffolds with cells were incubated for 1 hour at 37°C with hydration levels maintained by addition of 15 μl of C2C12 Growth Medium halfway through. After the 1 hour incubation, 3 ml of C2C12 Growth Medium containing 30 μg/ml aprotinin (Affymetrix) was added to each well and care was taken to ensure the scaffolds had been submerged in the media. On day 3 of culture myoblasts were transferred to C2C12 Induction Medium: high-glucose DMEM, 2% horse serum (ThermoFisher Scientific), 1% P/S, 1% insulin-tranferrin-selenium (ITS; Corning Cellgro), and 30 μg/ml aprotinin and remained in C2C12

Induction Medium for the extent of in vitro culture. Media was changed every other day and C2C12-seeded scaffolds were used for experiments on day 7 of culture.

Scaffolds seeded with other cell types were seeded following the same protocol and seeding density. Pre-vascularized scaffolds were seeded with a 1:1 ratio of human umbilical vein endothelial cells (HUVECs; Lonza) to primary human adipose-derived stem cells (ASCs) isolated as previously described (41) and cultured in HUVEC Medium: 2% FBS (Lonza), 1% P/S, EGM2-BulletKit (Lonza), and 30 μg/ml aprotinin. For in vivo experiments pre-vascularized scaffolds were implanted on day 11 of culture. Primary human ASCs were expanded in ASC Growth Medium: high-glucose DMEM, 10% FBS, 1% P/S, and 1 ng/ml FGF-2 (PeproTech) and seeded on scaffolds at passage 3.

Whole Mount Immunostaining

Methanol-fixed scaffolds were blocked and permeabilized (Block/Perm) for 3 hours with 0.2% Triton X-100 and 5% normal goat serum (Sigma) in PBS with 0.1% Tween (PTw). Scaffolds were then incubated with primary antibodies diluted in blocking solution overnight at 4°C on a rocker at 135 rpm, followed by three 1-hour washes. Primary antibodies included mouse anti-myosin heavy chain, fast (1:400; Sigma), mouse anti-CD31 (1:500; Sigma), and rabbit anti-desmin (1:50; Santa Cruz Biotechnology). Scaffolds were then incubated with DyLight 488-conjugated goat anti-mouse or DyLight 649-conjugated goat anti-rabbit (both 1:400; Jackson ImmunoResearch) diluted in blocking solution overnight at 4 °C on a rocker at 135 rpm, followed by three 1 hour washes. DAPI was incorporated in the second wash at a dilution of 1:2000. Samples were then imaged with a Zeiss LSM 510 confocal microscope. To visualize cell morphology of ASC constructs scaffolds were fixed with 3.7% formaldehyde at 4°C for 3 hours and then washed with PBS three times for 20 min each. Scaffolds were then incubated in Block/Perm for 3 hours at

4 °C. A staining solution containing Phalloidin-TRITC (12.5 µg/ml; Sigma Aldrich) and DAPI (1:2000) was diluted in 0.1% PTw and incubated with scaffolds for 1 hour at RT on a slow rocker. Scaffolds were washed three times for 20 min each in 0.1% PTw then imaged with a confocal microscope.

VML Defect Model

For initial in vivo testing of C2C12-seeded scaffolds and comparison of bulk versus spread scaffold structures, bilateral VML defects in 6 five-month-old female NOD-scid IL2Rgnull (NSG) immunodeficient mice (Jackson Lab) were treated with C2C12-seeded bulk or spread scaffolds. Each mouse received 4 bulk scaffolds in the right leg and 2 spread scaffolds in the left leg (n=3) to maintain equal total amounts of fibrin implanted per leg, as each bulk scaffold is half the volume of a spread scaffold. Mice were sacrificed at 2 and 4 weeks post-implantation and samples were cryopreserved by flash-freezing in 2-methylbutane (Sigma-Aldrich). For the subsequent C2C12 in vivo study 21 two-month-old female NSG mice (Jackson Lab) were used with the right leg receiving the VML defect and the left contralateral leg remaining as uninjured control. We compared three experimental groups (n=7): (i) untreated defects; (ii) acellular scaffolds; or (iii) C2C12-seeded scaffolds. In scaffold-treated groups, 4 scaffolds were bundled and placed in the defect site. Acellular scaffolds were incubated for 24 hours in C2C12 Induction Medium with aprotinin before implantation. For untreated defects, after muscle removal and cessation of bleeding the skin was closed over the empty defect. One mouse from the untreated group was euthanized 2 days post-surgery due to complications from the procedure and was excluded from analysis. Mice underwent in vivo functional testing at 2 and 4 weeks post-implantation and were sacrificed at 4 weeks as described above. The implanted scaffolds were removed along with surrounding native TA muscle, weighed, and cryopreserved for histology. For the analysis of

scaffolds seeded with mCherry+Luciferase+ C2C12s in vivo, 5 three-month-old female NSG mice (Jackson Lab) received bilateral VML defects following the same surgical protocol that were treated with bundles of 4 mCherry+Luciferase+ C2C12-seeded scaffolds (n=2), regular C2C12-seeded scaffolds (n=4), or acellular scaffolds (n=2). Mice were sacrificed at 4 weeks post-implantation as described above and their TA muscles harvested and cryopreserved. For the pre-vascularized scaffold in vivo study 4 four-month-old female NSG mice (Jackson Lab) received bilateral VML defects following the same surgical protocol as above. Defects were treated with bundles of 4 pre-vascularized scaffolds or acellular scaffolds (n=3) or compared to uninjured controls. Acellular scaffolds were incubated for 24 hours in HUVEC Medium with aprotinin before implantation. Mice were sacrificed at 10 days post-implantation as described above and their TA muscles harvested and cryopreserved. For the comparison of ASC-seeded scaffolds in vivo, 5 two-month-old female NSG mice (Jackson Lab) received bilateral VML defects treated with ASC-seeded or acellular scaffolds (n=3) compared to untreated controls. Mice were sacrificed at 2 weeks post-implantation and their TA muscles harvested and cryopreserved.

Histology

H&E and Masson's Trichrome stains were imaged on a Zeiss Axio Imager upright microscope. For immunohistochemistry, slides were fixed in ice-cold methanol for 10 min and rinsed with PBS three times for 15 min each, then blocked in 10% normal donkey or goat serum (Sigma) in PBS for 1 hour at RT. For CD31 staining, slides were fixed in ice-cold acetone for 10 min instead of methanol, rinsed with PBS, then blocked in 10% normal goat serum (Sigma). Slides were incubated with antigen-specific primary antibodies in blocking solution overnight at 4°C. Primary antibodies included rabbit anti-laminin (1:100; Sigma Aldrich), mouse anti-embryonic myosin (4 μg/ml; DSHB), mouse anti-myosin heavy chain (fast-twitch) (1:400; Sigma Aldrich),

mouse anti-myosin (slow-twitch) (5 μg/ml; DSHB), rat anti-mouse CD31 (1:50; BD Biosciences), mouse anti-human CD31 (1:500; Sigma Aldrich), mouse anti-mouse TER-119 (1:50; BD Biosciences), and rabbit anti-β tubulin III (1:200; Sigma). After three 15 min washes with PBS, slides were incubated with Cy3-conjugated donkey anti-mouse, DyLight 488-conjugated goat anti-mouse, Alexa Fluor 647-conjugated donkey anti-rabbit (all 1:400; Jackson ImmunoResearch), or Alexa Fluor 594-conjugated goat anti-rat (1:500; Invitrogen) and DAPI (1:2000) diluted in blocking solution for 1 hour at RT. Slides were washed three times for 15 min then mounted with 50% glycerol and imaged on a Zeiss Axio Observer inverted fluorescence microscope.

C2C12 Transduction and BLI Imaging

Serial dilution of lentivirus was performed to determine the optimal multiplicity of infection (MOI) for transduction. C2C12s at passage 5 were seeded in a well plate in C2C12 Growth Medium at a density of 4000 cell/cm2 and allowed to adhere for approximately 5 hours. Cells were then transduced with a CMV-mCherry-Luciferase lentivirus (MOI 25) in C2C12 Growth Medium with 5 μg/ml polybrene. Cells were incubated with lentivirus for 48 hours, washed with PBS, and fed with C2C12 Growth Medium. After approximately 8 hours the transduced cells were passaged and expanded for further use. Transduced C2C12s were used at passage 8 for all experiments and seeded on scaffolds following the above standard protocol. Bioluminescence imaging (BLI) was performed on mice implanted with transduced C2C12s to assess cell retention. Mice were anesthetized using isoflurane and injected with 150 mg/kg of D-Luciferin Potassium Salt (Gold Biotechnology, Inc.) 5 min prior to imaging. Images were acquired every 2-3 min using an IVIS Spectrum (PerkinElmer Inc.) with medium binning until peak luminescence signal was observed. Total proton flux of the region with the implanted scaffold was quantified using Living Image Software (Perkin Elmer Inc.). To image in vitro scaffolds seeded

with transduced C2C12s, D-Luciferin Potassium Salt was added to culture medium at 150 ug/mL 30 minutes prior to imaging. Scaffolds were imaged and analyzed using an IVIS Spectrum and Living Image Software.

Vascular Perfusion

After anesthetizing mice with isoflurane, 100 µl of 10 mg/ml FITC-Dextran (Sigma Aldrich) was injected into the tail vein to enable systemic perfusion. Mice were immediately sacrificed via isoflurane overdose and cervical dislocation and the TA muscles were harvested and stored on ice. Samples suspended in cell culture medium in chamber slides were immediately imaged with a Zeiss LSM 510 confocal microscope.

Quantification of Muscle Morphology

In the bulk versus spread scaffold study, myofiber and vascular densities at 2 and 4 weeks were quantified via ImageJ analysis of areas staining positive for MHC or CD31 in 3 thresholded high magnification images within the graft region at 2 different locations per leg. Myofiber diameters were quantified using SMASH Matlab analysis (43) of laminin staining in 4 high magnification images within the graft region at 2 different locations per leg. TA cross-sectional areas were quantified using ImageJ software and manual outlining of whole-muscle section cross-sectional areas in low magnification images at 4 locations per leg.

Chapter 3 Human Adipose-Derived Stem Cells: Assessment of Myogenic Potential *In Vitro* and *In Vivo*

3.1 Introduction

Volumetric muscle loss (VML) occurs when a tissue defect exceeds 20% of an individual muscle volume, which overwhelms the natural repair mechanism and leads to chronic functional deficits in the affected muscle[146]. Limited treatment options for VML include transfer of an autologous free muscle flap[36], muscle transposition[146], amputation, and power bracing[36]. These treatments have low success rates in restoring muscle function and at best provide aesthetic benefits and prevent further necrosis[36,146]. They are also limited by donor site morbidity, lack of donor tissue, and the need for a highly skilled surgical team, which complicate VML treatment and lead to unsatisfactory patient outcomes[36]. Tissue engineered (TE) grafts offer a potentially more effective regenerative medicine treatment option for VML that may alleviate the varied limitations of current treatments and lead to improved functional outcomes.

A range of materials have been utilized as scaffolds to treat VML with varied results, including decellularized extracellular matrix (ECM)[21,46,54–58,60], collagen[83], hyaluronic acid[85], fibrin[24,49,165], keratin[71,72], gelatin[88,89], and poly(lactic acid)/poly(lactic-co-glycolic acid) (PLA/PLGA)[32]. Our group has demonstrated the capacity to enhance the bioactivity and biocompatibility of fibrin by electrospinning it into microfiber bundles with alignment topography, tunable substrate stiffness, and controllable porous architecture[147]. Alignment cues have been shown to strongly enhance stem cell myogenic differentiation as well as myocyte fusion[148,149]. Electrospun hydrogels can be tuned to physiological stiffness to enhance myogenesis, as substrate stiffness has been reported to strongly affect stem cell differentiation and myogenesis[150,151]. We

have recently successfully treated a murine VML defect consisting of partial resection of the tibialis anterior muscle by combining the electrospun fibrin microfiber bundles and C2C12 myoblasts[25].

Adipose-derived stem/stromal cells (ASCs) are clinically translatable and previous studies have shown them to be a promising cell source for applications in skeletal muscle regeneration[158,162,166–168]. While a number of groups have researched myoblasts[50], satellite cells[85], or mesangioblasts[169] for skeletal muscle tissue engineering, the practicality of using these cell types for clinical treatments is limited by their low accessibility, low yield, and difficulty in long-term culture and expansion[85]. In contrast, ASCs are isolated from lipoaspirate involving a more mild procedure and lipoaspirate has 100 times higher stem cell yields than bone marrow, another mesenchymal stem cell source with myogenic potential[170]. ASCs also have high stem cell proliferation rates[166], can differentiate down the myogenic pathway[158,162,166], provide a pro-regenerative environment[171], and evade the host immune system[172]. Although many studies have assessed *in vitro* ASC myogenic potential[158,159,173,174,160–164,166,168,170], there have been few studies assessing *in vivo* muscle regeneration using ASCs. It has been shown that ASCs injected into the muscles of dystrophic mice could differentiate into dystrophin+ mature muscle cells[162] with a pool of replenished Pax7+ satellite cells[168], ASCs seeded onto PLGA microsphere carriers transplanted subcutaneously in nude mice formed new muscle tissue after 60 days[164], and NG2+ ASCs seeded onto hyaluronic acid scaffolds transplanted subcutaneously in nude mice expressed muscle markers after 30 days[175]. Another study assessed the regenerative potential of rat ASCs in collagen within a murine VML defect and did not see muscle regeneration, although implanting adipose-derived microvascular fragments did result in low levels of muscle regeneration[78]. The

ability of rat ASCs in a decellularized ECM matrix to regenerate a murine VML defect was also assessed and resulted in low levels of ASC contribution to regenerating myofibers[76].

Here, we utilized axially aligned fibrin hydrogel microfiber bundles with an elastic modulus similar to that of native muscle tissues to evaluate the growth and myogenic differentiation of human ASCs seeded on electrospun fibrin microfiber bundles *in vitro* in the absence or presence of biochemical induction cues. Moreover, we assessed the ability of the microfiber bundles with and without ASCs to treat a robust murine VML model, in which the entire tibialis anterior (TA) and extensor digitorum longus (EDL) muscles were both removed. We tested the hypothesis that the combination of human ASCs on electrospun fibrin fibers promotes muscle regeneration and that *ex vivo* differentiation of ASCs down a myogenic lineage prior to transplantation would significantly enhance this response.

3.2 Materials and Methods

Electrospinning Fibrin Fiber Bundles

Fibrin fibers were electrospun in a sterile environment with sterile solutions using a protocol that has been described previously[25,147]. Briefly, parallel syringes containing sterile solutions of fibrinogen (Sigma-Aldrich, St. Louis, MO, USA) or sodium alginate (Sigma-Aldrich, St. Louis, MO, USA) were connected via a y-syringe and extruded by syringe pumps with an applied voltage of 3-5 kV applied to a blunted 27G needle tip to form hydrogel microfiber bundles. Polyethylene oxide (average MZ ~ 4,000 kDa, Sigma-Aldrich, St. Louis, MO, USA) was added to each solution at 0.2 wt% to increase viscosity during electrospinning. The electrospun hydrogel solutions were collected for 5.75 minutes on a rotating dish (~35rpm) containing 50 mM $CaCl_2$ and 20 U/ml thrombin (Sigma-Aldrich, St. Louis, MO, USA) as crosslinking agents. Samples were

crosslinked an additional 3-5 min after electrospinning and were then wrapped around a 1.5 × 3.0 cm mylar frame 3-4 times to yield a hydrogel fiber bundle ~1 mm in diameter. Fibers were incubated overnight in 250 mM sodium citrate (Sigma-Aldrich, St. Louis, MO, USA) to dissolve the alginate and then transferred to DI water until cell seeding or implantation. The resulting fibers have a tensile modulus of 11 kPa and are suturable and remain elastic when strained up to 50% of their length.

Cell Culture

ASCs were isolated from lipoaspirate tissue under an IRB approved protocol as previously described[153]. Two female donor sources were used: a 39-year old Caucasian and a 63-year old African American. *In vitro* studies utilized ASCs from both donors while *in vivo* studies utilized ASCs from the first donor. Briefly, tissue was digested with collagenase (1 mg/mL; Worthington Biochemical Corp., Lakewood, NJ, USA) to isolate the stromal vascular fraction of cells. These cells were plated onto tissue culture plastic and were termed "passage 0 ASC" when they reached 80–90% confluence. ASCs were thawed and expanded for two passages in Growth Medium: high-glucose DMEM (ThermoFisher Scientific, Waltham, MA, USA) with 10% fetal bovine serum (FBS; Atlanta Biologicals, Flowery Branch, GA, USA), 1% penicillin/streptomycin (P/S; ThermoFisher Scientific, Waltham, MA, USA), and 1ng/mL FGF-2 (PeproTech, Rocky Hill, NJ, USA). The ASCs were then trypsinized and used at passage 3 for all experiments. The phenotypic profile of the cells at this passage from both donors was examined via flow cytometry for mesenchymal (CD73, CD90, CD105) and vascular markers (CD31, CD34). Briefly, ASCs at passage 1 were thawed and expanded as described above. Passage 3 ASCs were then suspended in phosphate-buffered saline (PBS) containing 2% FBS and incubated with monoclonal antibodies conjugated to fluorescein isothiocyanate or phycoerythrin for 30 min at 4°C. Cells were then

analyzed with a flow cytometer (BD Accuri C6, BD Biosciences, San Jose, CA, USA). All antibodies were purchased from BD Biosciences.

Cell Seeding and Growth on Fibers

Fibers with 15% removed alginate were utilized for all experiments. In preparation for cell seeding, fibers were incubated in high glucose DMEM for 20 min at 37°C. The fibers were then transferred to cell culture plates coated with 2% agarose type VII (Sigma-Aldrich, St. Louis, MO, USA) to minimize cell adhesion to the plate surface and increase seeding efficiency onto the fibers. For the seeding density study a seeding volume of 15 µl at either 10,000, 20,000, or 40,000 cells/µl was pipetted onto the fiber surface. All subsequent *in vitro* and *in vivo* studies used 15 µl at 40,000 cell/µl (for a total seeding density of 600 000 cells/fiber bundle). Fibers with cells were incubated for 1 hour at 37°C with hydration levels maintained by addition of 15 µl of Growth Medium halfway through. After the 1-hour incubation, Control Medium (high-glucose DMEM, 10% FBS, 1% P/S, 30 µg/ml aprotinin (ThermoFisher Scientific, Waltham, MA, USA), and 1 ng/mL FGF-2) was added to fully submerge the fibers. Media was changed 24 hours post-seeding and then every other day until harvest.

Myogenic Induction

Induction of ASCs toward myogenesis was performed with an adapted protocol previously described[176]. After 7 days of growth in Control Medium fibers were transferred to Induction Medium: low glucose DMEM (ThermoFisher Scientific, Waltham, MA, USA) with 1% FBS, 5% horse serum (HS; ThermoFisher Scientific, Waltham, MA, USA), 1% P/S, 30 µg/ml aprotinin, and 10 µM 5-Azacytidine (Aza; Sigma-Aldrich, St. Louis, MO, USA). After 24 hours the fibers were rinsed with PBS and returned to Control Medium for the duration of the experiment.

Cell Viability

To compare cell viability and morphology a Live/Dead Viability/Cytotoxicity Kit (ThermoFisher Scientific, Waltham, MA, USA) was used at a range of seeding densities. Samples were incubated with calcein AM and ethidium homodimer-1 for 20 min then imaged with a confocal microscope (Zeiss LSM 510, Oberkochen, Germany).

PicoGreen Assays

DNA content of seeded cells on the fibers at various densities was quantified using a PicoGreen dsDNA quantitation kit (ThermoFisher Scientific, Waltham, MA, USA). Cells were lysed by placing whole fibers in 500 µl of digestion buffer (10mM Tris, 1mM EDTA, 0.1% Triton X-100, and 0.1 mg/mL proteinase K) before incubation with PicoGreen and reading with a fluorescent plate reader (BioTek, Winooski, VT, USA) at excitation 485 nm and emission 530 nm. Cellular infiltration into the fiber interior was assessed using 10 µm-thick cryosections and staining for 30 min with DAPI (Sigma-Aldrich, St. Louis, MO, USA).

Whole Mount Immunostaining

Samples were fixed in ice-cold methanol at -20°C overnight then rinsed three times for 20 min each. Fibers were then cut from their frames and placed in 0.5 ml tubes for subsequent staining steps. Fibers were blocked and permeabilized (Block/Perm) for 3 hours with 0.2% Triton X-100 and 5% normal goat serum (Sigma-Aldrich, St. Louis, MO, USA) in PBS with 0.1% Tween (PTw). Fibers were then incubated with primary antibodies diluted in blocking solution overnight at 4°C on a rocker at 135 rpm, followed by three 1-hour washes with PTw. Primary antibodies included mouse anti-myogenin (5 µg/ml; DSHB, Iowa City, IA, USA) and rabbit anti-desmin (2.7 µg/ml; Santa Cruz Biotechnology, Dallas, TX, USA). Fibers were then incubated with DyLight 488-conjugated goat anti-mouse and DyLight 649-conjugated goat anti-rabbit (both 1:400; Jackson ImmunoResearch, West Grove, PA, USA) diluted in blocking solution overnight at 4°C on a rocker

at 135 rpm, followed by three 1 hour washes with PTw. DAPI was incorporated in the second wash at a dilution of 1:2,000. Samples were then imaged with a confocal microscope.

To visualize cell morphology and multinucleation, fibers were fixed with 3.7% formaldehyde at 4°C for 3 hours and then washed with PBS three times for 20 min each. Fibers were then cut from their frames and incubated in Block/Perm for 3 hours at 4°C. A staining solution containing Phalloidin-TRITC (12.5 μg/ml; Sigma-Aldrich, St. Louis, MO, USA) and DAPI (1:2,000) was diluted in 0.1% PTw and incubated with fibers for 1 hour at RT on a slow rocker. Fibers were washed three times for 20 min each in 0.1% PTw then imaged with a confocal microscope.

VML Defect Model

Animal and surgical procedures were approved by the Institutional Animal Care and Use Committee at Johns Hopkins University School of Medicine. For the acellular scaffold study 10 two-month old male NOD-Rag1^{null} IL2rg^{null} (NRG) immunodeficient mice (Jackson Lab, Bar Harbor, ME, USA) were used and for the cell-seeded scaffold study 14 two-month old female NOD-scid IL2Rg^{null} (NSG) immunodeficient mice (Jackson Lab, Bar Harbor, ME, USA) were used. Two strains of immunodeficient mice were utilized due to mice availability at the time of the study. NRG and NSG mice are phenotypically very similar and both are highly immunodeficient with the only known phenotypic difference related to radiation/chemotherapy sensitivity which was not relevant to this study. Mice were anesthetized with isofluorane and the TA and EDL muscles were removed from the anterior tibial compartment in a bilateral defect on all mice, as described previously[177]. Care was taken to ensure bleeding had ceased before 1 or 3 fiber bundles were placed in the empty defect site and ligated on both ends to the tendons of the peroneus longus muscle with non-absorbable sutures (6/0 POLYPRO, CP Medical, Norcross, GA,

USA). Surgical glue (Histoacryl, B. Braun Medical, Bethlehem, PA, USA) and stainless steel wound clips (Reflex Wound Clips, CellPoint Scientific, Gaithersburg, MD, USA) were used to close the skin. Rimadyl (Patterson Veterinary, Greeley, CO, USA) was given at 5 mg/kg subcutaneously post-surgery for pain management. For the cell-seeded study, acellular fibers were incubated for 24 hours in Control Medium before implantation. Upon harvest, fibers were removed along with the surrounding native muscle tissue. One mouse containing acellular and uninduced fibers died before the 3-month study ended and was excluded from data analysis.

Histology

Mice were sacrificed at 2 (male NRG, n=,) , 4, and 12 weeks; and the portion of their hind-limb containing the scaffold and surrounding muscle tissue was harvested and frozen in OCT. Samples were cut into 10 μm sections on a cryostat, dried on Superfrost Plus slides, and rehydrated in DI water before staining with Masson's Trichrome (Sigma-Aldrich, St. Louis, MO, USA) stain. Slides were imaged on an Axio Imager upright microscope (Zeiss, Oberkochen, Germany). Fibrosis was quantified with Image J software (NIH, Rockville, MD, USA) by measuring the collagen area and fiber cross-sectional area (n=15: 5 samples with 3 cryosections per sample). In both the acellular and cell-seeded *in vivo* studies, fibrosis was normalized to the cross-sectional area of the implanted fibrin fiber for each sample. In the cell-seeded *in vivo* experiment, relative cross-sectional area was determined by comparing the cross-sectional areas of cell-seeded samples to the average cross-sectional area of 2 week acellular controls (containing 3 fibers/defect).

Immunohistochemistry

Samples were cryosectioned as described above. Slides were fixed in ice-cold methanol for 10 min and rinsed with PBS three times for 15 min each, then blocked in 10% normal donkey serum (Sigma-Aldrich, St. Louis, MO, USA) in PBS for 1 hour at RT. For CD31 staining, slides

were fixed in ice-cold acetone for 10 min, rinsed with PBS, then blocked in 10% normal goat serum (Sigma-Aldrich, St. Louis, MO, USA). Slides were incubated with antigen-specific primary antibodies in blocking solution overnight at 4°C. Primary antibodies included rabbit anti-mouse CCR7 (2.6 μg/ml; Abcam, Cambridge, UK), rabbit anti-human LaminAC (1.1 μg/ml; Abcam, Cambridge, UK), mouse anti-human LaminAC (1:20; Abcam, Cambridge, UK), mouse anti-embryonic myosin (4 μg/ml; DSHB, Iowa City, IA, USA), mouse anti-myosin heavy chain (24.3 μg/ml; Sigma-Aldrich, St. Louis, MO, USA), rabbit anti-laminin (4.5 μg/ml; Sigma-Aldrich, St. Louis, MO, USA), and rat anti-mouse CD31 (0.3 μg/ml; BD Biosciences, San Jose, CA, USA). The embryonic myosin, myosin heavy chain, and laminin antibodies have reactivity for both mouse and human proteins. After three 15 min washes with PBS, slides were incubated with Cy3-conjugated donkey anti-mouse, Alexa Fluor 647-conjugated donkey anti-rabbit (both 1:400; Jackson ImmunoResearch, West Grove, PA, USA), or Alexa Fluor 594-conjugated goat anti-rat (1:500; ThermoFisher Scientific, Waltham, MA, USA) and DAPI (1:1,000) diluted in blocking solution for 1 hour at RT. Slides were washed three times for 15 min then mounted with 50% glycerol and imaged on an Axio Observer inverted fluorescence microscope (Zeiss, Oberkochen, Germany). To quantify immunostaining, CCR7 area was measured with ImageJ and cells staining positive for eMHC and MHC were counted manually.

Statistics

Statistical analysis was performed using GraphPad Prism 5 software (GraphPad Software, La Jolla, CA, USA). Statistical significance for the DNA assay was determined by one-way ANOVA with Tukey's post-test (n=3). In the first *in vivo* study assessing acellular scaffolds, statistical significance for fibrosis and CCR7 areas (n=14-16) was determined by unpaired two-tailed t-test. For the second *in vivo* study assessing cell-seeded scaffolds, statistical significance

for fibrosis areas and immunostained samples (n=9-15) was determined with one-way ANOVA with Dunnet post-test. Statistical significance when assessing percent of ASCs in the defect (n=12-15) was assessed with an unpaired two-tailed t-test.

3.3 Results

ASCs Align on Fiber Surface and Infiltrate into the Interior of Fiber Bundle

ASCs at passage 3 from both donors highly expressed the mesenchymal markers CD73, CD90, and CD105 and had negligible to very low expression of the vascular markers CD31, CD34. ASCs were seeded onto the fibers and proliferated to cover the fiber surfaces, aligning with the major axis of the fibers with good cell viability at a range of seeding densities and time points (**Fig. 3.1A**). There were no visible differences in cell morphology at the three seeding densities from days 7-21. ASCs became confluent on the fiber surface by day 7 and maintained their confluency through day 21. In addition to covering the fiber surface, ASCs also migrated into the porous fiber interior (**Fig. 3.1B**). DNA quantification was used to assess cell numbers at different times in culture. Differences in DNA content were statistically significant among the three seeding densities at day 0 and day 7 but not later time points (**Fig. 3.1C**). The maximum total DNA content was statistically similar among all groups on days 14 and 21. A seeding density of 40,000 cell/μl was selected for subsequent studies because of its higher DNA content at earlier time points.

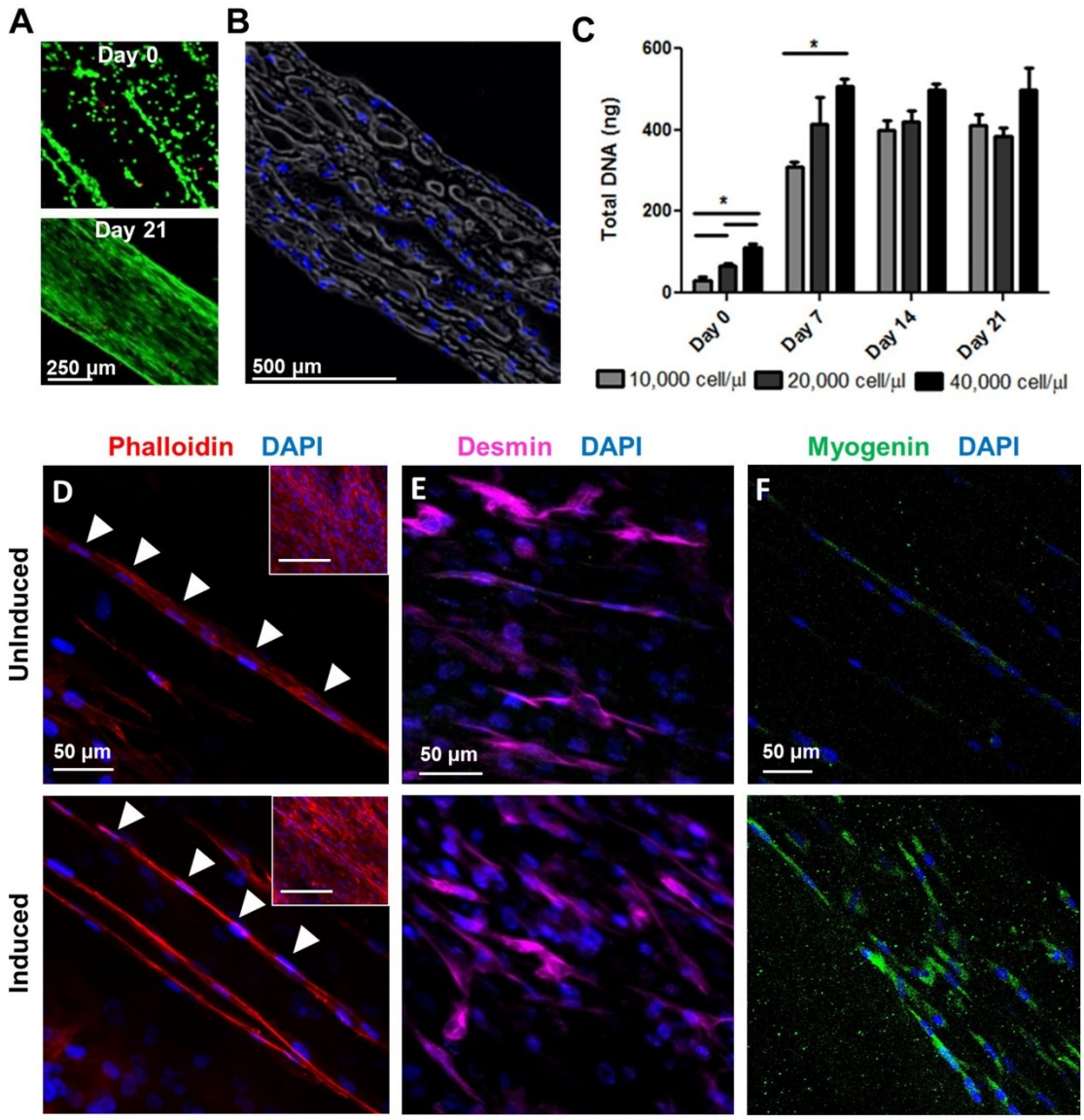

Figure 3.1. ASC growth and myogenesis on electrospun fibrin fibers. A) Live (green)/Dead (red) staining of cells seeded at 40 000 cells/µl at days 0 and 21. **B)** Histological cross-section stained with DAPI (blue) showing ASC infiltration to the fiber interior at day 21. **C)** Quantification of total DNA content of fibers seeded with ASCs at the three seeding densities at days 0, 7, 14, and 21. *$p<0.05$ **D)** Phalloidin (red) and DAPI (blue) staining illustrating some multinucleation of ASCs on fibers at 2 months in both uninduced and induced groups. Arrows demonstrate aligned and elongated nuclei within potential myotubes. Inset: lower magnification image of phalloidin staining. Scale bar: 200 µm. **E)** Desmin (purple) and **F)** myogenin (green) staining ASCs grown on fibers in both uninduced and induced groups at 2 months.

ASCs Do Not Fully Replicate Myotube Characteristics at Two Months In Vitro

After 2 months of *in vitro* culture, phalloidin staining of both uninduced and induced ASCs on the fibers revealed the presence of long tubes of cells in the fiber interior with elongated and aligned nuclei that paralleled the fiber's major axis and mimicked the appearance of multinucleated myotubes (**Fig. 3.1D**). Although both uninduced and induced groups expressed high levels of desmin, a muscle structural protein (**Fig. 3.1E**), expression of the muscle transcription factor myogenin was low and non-nuclear (**Fig. 3.1F**). Interestingly, although ASCs cultured for 2 months did not replicate myotube multinucleation and protein expression completely, there were no significant differences between uninduced and induced samples. This indicates that 5-azacytidine did not provoke a significant pro-myogenic benefit and suggests that the fiber alignment and stiffness alone may encourage ASCs to begin mimicking myotube characteristics.

Fiber Number Determines Fibrotic Response In Vivo

When acellular fibers were implanted, native tissue surrounding the defect sites had a healthy appearance upon removal at 2 and 4 weeks with no visible scarring for both 1 and 3 fibers/defect (**Fig. 3.2B**). There was less fibrosis at both time points when 3 fibers/defect were implanted than there was for 1 fiber/defect, as evident by collagen staining with Masson's Trichrome stain (**Fig. 3.2C**). When quantifying total collagen area per sample, the mean values at 2 weeks were 1.36 mm^2 for 1 fiber/defect and 1.05 mm^2 for 3 fibers/defect, and at 4 weeks were 0.72 mm^2 for 1 fiber/defect and 0.73 mm^2 for 3 fibers/defect. Only the two 4-week groups had a significant difference with 1 fiber yielding significantly more collagen than 3 fibers although fibrosis in both groups did decrease over time (**Fig. 3.2D**). There were significant differences in normalized fibrosis (fibrotic area (mm^2) /scaffold cross-sectional area (mm^2)) between 1 fiber and 3 fibers at both time points. When quantifying normalized fibrosis, the mean values at 2 weeks

were 5.28 (mm^2/mm^2) for 1 fiber/defect and 0.99 mm^2/mm^2 for 3 fibers/defect, and at 4 weeks were 5.43 mm^2/mm^2 for 1 fiber/defect and 1.19 mm^2/mm^2 for 3 fibers/defect. Differences between normalized fibrosis levels for 1 fiber/defect and 3 fibers/defect were statistically significant at both 2 and 4 weeks. Samples were stained with the M1 macrophage marker CCR7 and areas stained within the fibers were quantified. There were no statistically significant differences in macrophage content between groups at both time points (**Fig. 3.2E**).

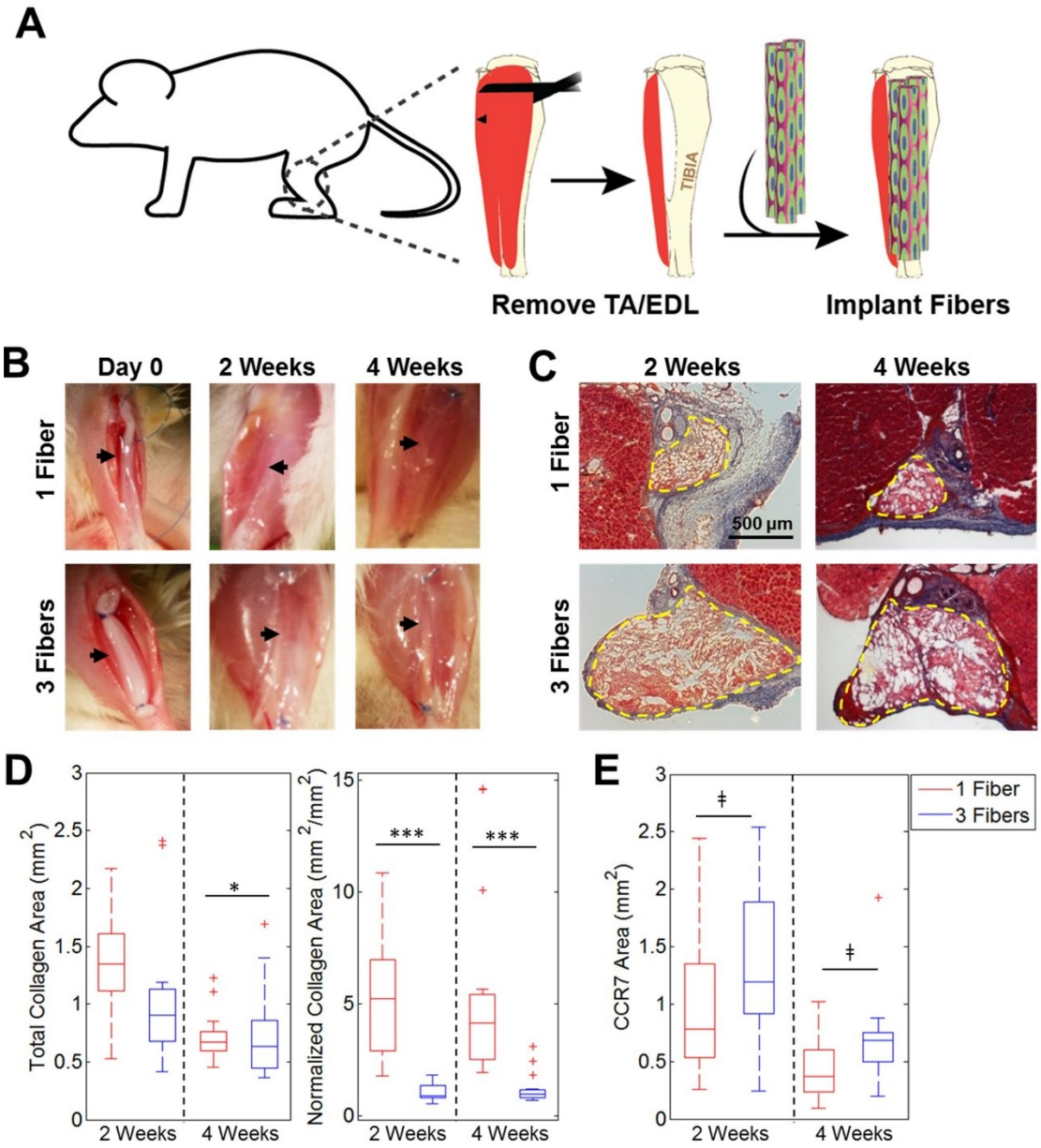

Figure 3.2. Fibrosis resulting from implantation of acellular fibers into VML defect. A) Schematic illustrating fiber implantation into a murine VML defect model. **B)** Gross images of defects with 1 or 3 fibers/defect at Day 0 and 2 or 4 weeks post-transplantation. Black arrows illustrate fiber location within defect site. **C)** Masson's Trichrome staining demonstrates varying levels of fibrosis among groups. Dashed yellow lines denote fiber boundaries. **D)** Quantification of total collagen area and normalized collagen area over time for both groups (n=14-15). (E) Quantification of total CCR7 staining area (n=15).

Cell-Seeded Scaffolds Retain Fiber Cross-Sectional Area

Bilateral murine VML defects were implanted with three fibers/defect that were acellular, uninduced, or induced and harvested after 1 or 3 months. The schematic in **Fig. 3.3A** demonstrates how fibers were distributed in the 14 mice used for this study. Upon removal at 1 month, there were distinct visible differences in the appearances of cell-seeded versus acellular fibers, where both cell-seeded groups had robust, opaque fibers visible between the sutures while the acellular fibers were translucent (**Fig. 3.3B**, top). These differences correlated with histology data and Masson's Trichrome staining, where cell-seeded fibers had larger cross-sectional areas than those of acellular fibers (**Fig. 3.3B**, bottom). Masson's Trichrome staining also demonstrated that all three groups had minimal fibrosis at both time points and there was no significant difference in normalized fibrosis between all three groups (**Fig. 3.3C**). When compared to the cross-sectional area of an early-stage implant, cell-seeded fibers had significantly higher retention of fiber cross-sectional area than acellular fibers at both time points (**Fig. 3.3D**). The percentage of ASCs in the cell-seeded fibers was measured comparing the number of human-specific LaminAC+ nuclei to the number of other nuclei in the fiber cross-sections. Over 50% of cells in the fibers were ASCs for both groups at both time points and there were no statistically significant differences in the numbers of ASCs between groups (**Fig. 3.3E)**.

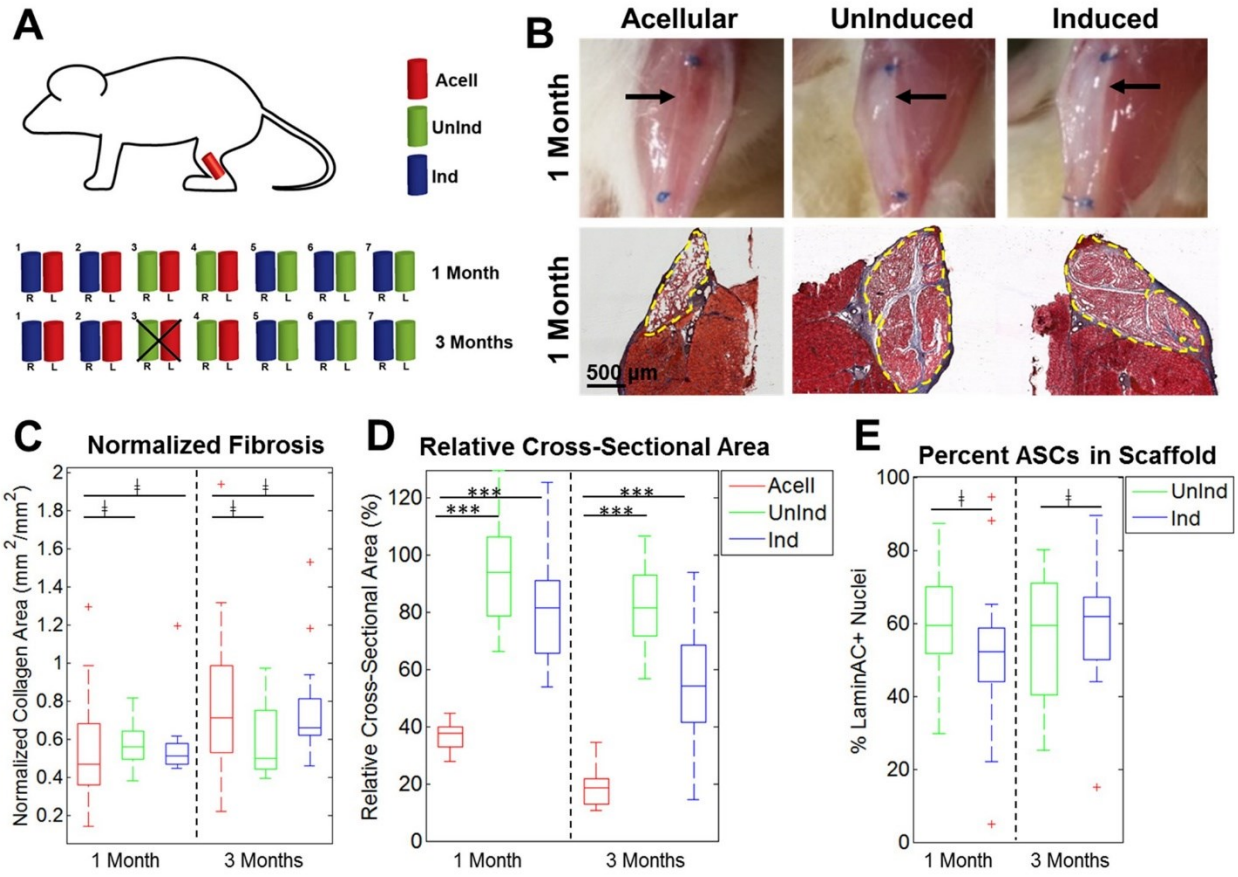

Figure 3.3. Analysis of cell-seeded fibers implanted in VML defects. A) Schematic illustrating the experimental plan. Two fibers were implanted per mouse and harvested at 1 or 3 months. Mouse #3 in the 3-month cohort died before the study ended. **B)** Differences in appearance were visible between acellular and cell-seeded groups immediately before harvest, with acellular groups appearing more translucent and cell-seeded groups more opaque (top). Black arrows illustrate fiber location within defect site. Masson's Trichrome stain demonstrates minimal fibrosis in all three groups and the larger cross-sectional area present in cell-seeded groups (bottom). Dashed yellow lines denote fiber boundaries. **C)** Quantification of normalized fibrosis among all three groups at both time points showed that there were no significant differences between both cell-seeded groups and acellular fibers (n=9-15). **D)** Quantification of relative cross-sectional area for all three groups at both time points showed that cell-seeded samples had significantly higher retention of cross-sectional area than acellular samples (n=9-15). **E)** Quantification of the percent of LaminAC+ nuclei in both cell-seeded groups showed high percentages of ASCs in the harvested scaffolds with no significant difference between groups (n=12-15).

Limited Expression of Myogenic Markers In Vivo

Immunostaining with embryonic myosin (eMHC) was used to assess the presence of regenerating muscle within the defect site. A small number of eMHC+ cells were visible within the fiber interior in both ASC groups as well as LaminAC+ nuclei distributed throughout the fibers (**Fig. 3.4A**). In a few cases there were eMHC+ cells whose nuclei were LaminAC+, indicating that those ASCs had differentiated to myogenic cells or had fused with a native regenerating muscle fiber (**Fig. 3.4A,** *right*). Myosin heavy chain (MHC), a mature muscle marker, was found at low levels within the fiber interiors as well (**Fig. 3.4B**). Both induced and uninduced samples contained laminin+ cells with human nuclei, further suggesting that some implanted ASCs had fused with or differentiated into regenerating myofibers within the defect (**Fig. 3.4C**). At 1 month, there were significantly more eMHC+ cells in fibers with uninduced ASCs than there were in acellular fibers, although there was no significant difference for fibers with induced ASCs. At 3 months, all three groups had similar numbers of eMHC+ cells (**Fig. 3.4D**). At 1 month, 67.7 ± 27.0 percent of eMHC+ cells in fibers with uninduced ASCs and 42.4 ± 34.2 percent of eMHC+ cells in fibers with induced ASCs had a LaminAC+ nucleus immediately adjacent. At 3 months, 43.0 ± 23.0 percent of eMHC+ cells in fibers with uninduced ASCs and 49.2 ± 28.8 percent of eMHC+ cells in fibers with induced ASCs had a LaminAC+ nucleus immediately adjacent. At both 1-month and 3-month time points, there were significantly more MHC+ cells in fibers with uninduced ASCs than there were in acellular fibers. Fibers with induced ASCs, however, had similar numbers of MHC+ cells to those in acellular fibers at both time points. At 1 month, 41.8 ± 32.6 percent of MHC+ cells in fibers with uninduced ASCs and 27.5 ± 28.2 percent of MHC+ cells in fibers with induced ASCs had a LaminAC+ nucleus immediately adjacent. At 3 months, 61.6 ± 33.0 percent of MHC+ cells in fibers with uninduced ASCs and 43.8 ± 35.6 percent of MHC+ cells in fibers with induced ASCs had a LaminAC+ nucleus immediately adjacent. When cross-sections of the

excised defect site at 12 weeks were stained for mouse CD31, host vascular infiltration was apparent within the fibers among all three groups (**Fig. 3.4E**).

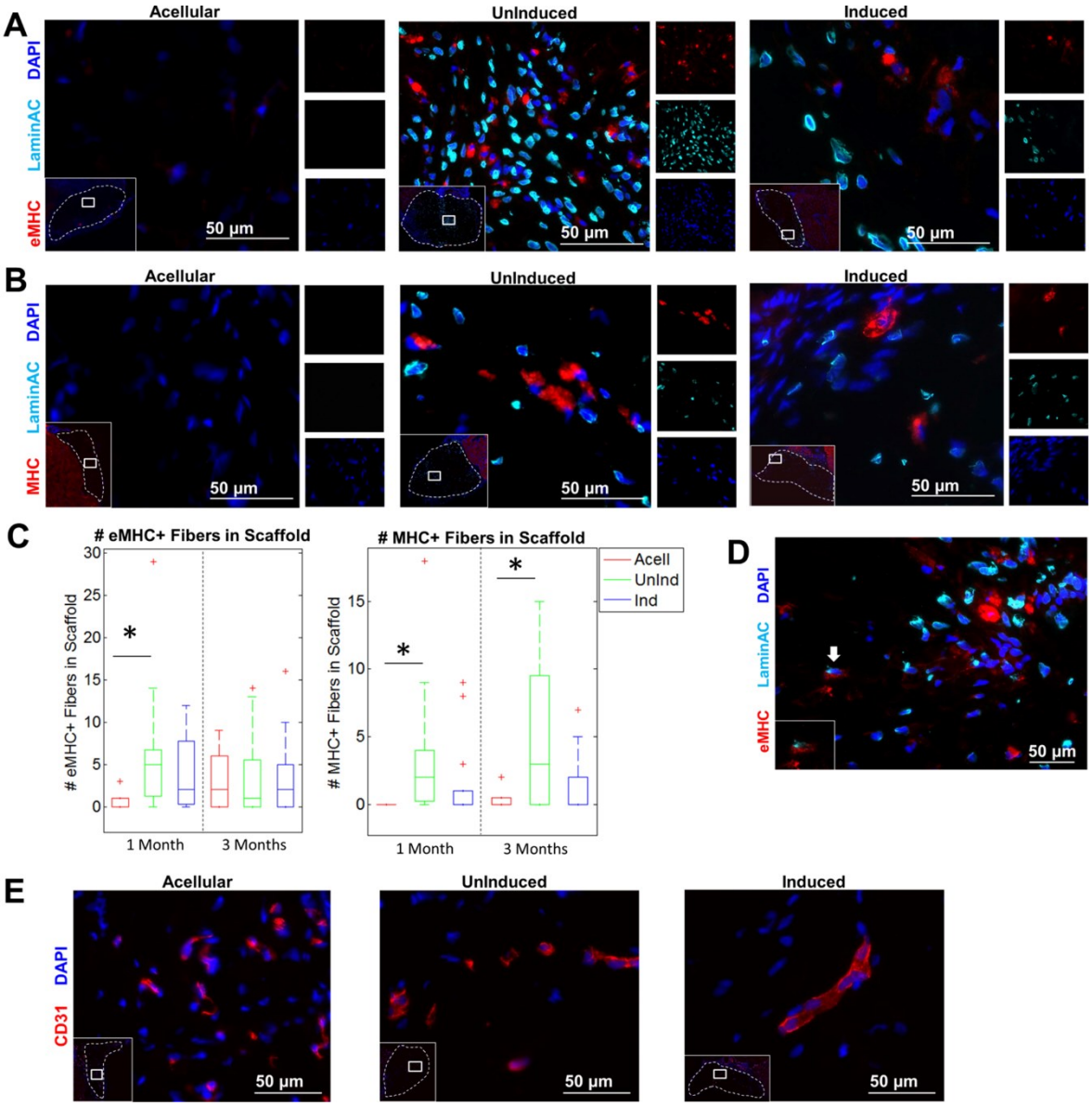

Figure 3.4. Immunostaining of embryonic myosin, myosin heavy chain, and LaminAC+ nuclei in the fiber interior. A) Sections of the excised defect site were stained with embryonic myosin (eMHC; red), human-specific LaminAC (cyan), and DAPI (blue). Inset (left): concentrations of eMHC were found in the center of the implanted fibers. Dotted line denotes fiber boundary. Inset (right): Example of colocalizing eMHC+ and human LaminAC+ cell in fibers with induced ASCs. Images depict fibers at 4 weeks. **B)** Sections of the excised defect site were stained with myosin heavy chain (MHC; red), human-specific LaminAC (cyan), and DAPI (blue). Inset: concentrations of MHC were found in the center of the implanted fibers. Dotted line denotes fiber boundary. Images depict fibers at 12 weeks. **C)** Sections of the excised defect site were stained with laminin (red), human-specific LaminAC (cyan), and DAPI (blue). Inset: concentrations of laminin+ cells with human nuclei were found in the center of the implanted fibers. Dotted line denotes fiber boundary. Image depicts uninduced fibers at 4 weeks. **D)** Quantification of the number of eMHC+ and MHC+ cells inside fibers among the three groups (n=9-15). There were significantly more eMHC+ cells at 1 month in fibers with uninduced ASCs than in acellular fibers. There was no significant difference in eMHC expression among groups at 3 months. There were significantly more MHC+ cells at both 1 month and 3 months in fibers with uninduced ASCs than in acellular fibers. **E)** Sections of the excised defect site were stained for mouse CD31 (CD31; red) and DAPI (blue). Inset: host vascular infiltration was found in the interior of the implanted fibers in all groups at 3 months. Dotted line denotes fiber boundary.

3.4 Discussion

There are limited therapeutic options available for the treatment of VML. ASCs are potentially advantageous for tissue engineered muscle because of their ease of isolation, higher stem cell yields and proliferation rates, and reported myogenic potential[158,159,170,173,174,160–164,166–168]. Their biological relevance arises from the fact that adipocytes and myoblasts share a common Myf5+ precursor[178] and brown preadipocytes express high levels of myogenic genes[179]. Even so, the ability of ASCs to directly differentiate into myoblasts is limited[150]. In addition to their differentiation capabilities, ASCs have the potential to promote muscle regeneration by providing a pro-regenerative environment and modulating the immune system[171,172]. ASCs have also been shown to be pro-angiogenic and the ASC secretome includes the angiogenic factors VEGF, HGF, and IGF-1[180]. The current study assessed the *in vitro* and *in vivo* myogenic potential of both uninduced and induced ASCs on a myomimetic electrospun fibrin scaffold.

The scaffold utilized in this study is highly suited for muscle regeneration and has successfully treated VML when combined with C2C12 myoblasts[25]. Fibrin is a naturally occurring biocompatible and biodegradable material generated during the blood clotting process. As a scaffold material, it can be degraded gradually *in vivo* in the presence of plasmin. It is a vital component of the native coagulation cascade and thus is present in the native wound healing environment. As a surgical adhesive, *in-situ* gelled fibrin hydrogel has been widely used in the clinic with an excellent safety profile[181]. Electrospinning fibrinogen onto a rotating collection dish where it rapidly crosslinks with thrombin under tension enables internal alignment capture of the hydrogel fiber[147] that mimics the alignment of fibers in native muscle. Cellular alignment is a prerequisite for the uniaxial contraction of functional muscle and construct alignment has been shown to enhance myoblast fusion and stem cell myogenesis[148,149]. The electrospun fibers also mimic the macroscopic structure of muscle, where groups of muscle fibers are bundled to form fascicles, which in turn are bundled to form the muscle tissue. Each fibrin fiber is a collection of bundled microfibers, mimicking the native fascicle, and assembling multiple fibrin fibers is scalable to replace an entire muscle. Substrates that mirror the stiffness of native muscle have been shown to enhance stem cell differentiation and myogenesis[150,151,182], with an ideal range of 8–17 kPa[182]. The stiffness of the fibrin fibers has been optimized to mimic the mechanics of native muscle with an average Young's Modulus of 11 kPa. In addition to providing an environment that mimics the alignment, structure, and mechanics of native muscle, the electrospun fibrin fibers are suturable and mechanically robust. The fibrin fibers also have the potential to be used as an off-the-shelf material that can be stored long term and rehydrated prior to cell seeding and implantation. These capabilities as well as their ability to closely mimic the native muscle

environment make electrospun fibrin fibers a highly suitable candidate material for tissue engineered skeletal muscle.

When ASCs were seeded onto the electrospun fibrin fibers, they proliferated to cover the fiber surface and grow into the interior with good cell viability at a range of time points. The fiber surface topography encouraged ASC alignment with the fiber's major axis. Alignment alone has been shown to stimulate increased ASC myogenic differentiation[148]. To further promote ASC myogenesis, 5'-azacytidine was added to the culture medium as a biochemical induction factor. Azacytidine, a DNA methyl transferase inhibitor, has been used previously to encourage both ASC as well as MSC myogenic differentiation by reversing gene silencing and potentially activating a subset of myogenic genes[183]. However, the yield of ASC myogenesis *in vitro* is reported to be as low as 0.1% with potential increases in ASC differentiation when they are co-cultured with myoblasts[184]. This is in keeping with the *in vitro* components of this study, where ASCs on electrospun fibers attained very low levels of myogenic characteristics after 2 months of culture with no visible differences between uninduced and induced ASCs. It is possible that the fiber alignment [148,149] and stiffness [150,151,182] alone may be sufficient to promote the low levels of ASC myogenesis seen, which was not further improved by biochemical induction with 5-azacytidine. ASCs from two donors were used to demonstrate that results are not dependent on age or demographic.

ASCs have much higher reported levels of muscle differentiation when implanted into a regenerating muscle environment *in vivo* than *in vitro* and have demonstrated incorporation into the regenerating muscle tissue[184]. Bacou *et al* found that cells from the stromal vascular fraction contributed up to 10% of regenerating muscle fibers in damaged TA muscles[185], and Di Rocco *et al* found that ASCs injected into ischemia-injured adductor muscles contributed up to 10-20% of

regenerating fibers[162]. A number of studies have assessed the muscle regenerative potential of ASCs injected *in vivo*[162], but implanting ASCs on a 3D scaffold to assess resulting skeletal muscle formation is still relatively unexplored. ASCs attached to PLGA microsphere carriers transplanted subcutaneously in nude mice formed new muscle tissue after 60 days[164], and NG2+ ASCs seeded onto hyaluronic acid scaffolds transplanted subcutaneously in nude mice expressed muscle markers after 30 days[175]. Animal models of VML vary greatly in the extent and mechanism of injury, muscle group, and location. VML models previously utilized for tissue engineered skeletal muscle include removal of 30% of the tibialis anterior[146], 50% of the lattissimus dorsi[186], and 75% of the quadriceps muscles[54]. Regeneration in partial excision models likely relies in part on muscle stem/progenitor cell and vascular ingrowth from the remaining muscle tissue, as it has been shown that muscle progenitor cells can migrate to regenerate distal injuries[187]. Here, we provide a significantly more challenging VML model by excising the entire TA and EDL muscles and utilize this model to assess the muscle regenerative potential of ASCs. The robust VML model used in this study mimics some of the most severe patient cases with little hope for positive regenerative outcomes[36].

In the current study, ASC-seeded fibers implanted in a VML defect had increased volume retention relative to acellular fibers with uninduced ASCs at 3 months exhibiting up to 4X higher volume retention than acellular fibers. Volume retention for fibers with induced ASCs was slightly lower, but the values for the two cell-seeded groups were not statistically different. This indicates that the addition of ASCs to the fibers preserves them from degradation. Both uninduced and induced ASCs showed low levels of fibrosis, similar ratios of human to mouse cells within the fibers at three months post-transplantation, and similar numbers of cells at 3 months that were eMHC+. However, fibers seeded with uninduced ASCs had significantly more regenerating

muscle cells positive for MHC when compared to acellular fibers, while fibers seeded with induced ASCs did not. Paired with the *in vitro* data, this suggests that 5-azacytidine may not be sufficiently potent to induce ASCs down a myogenic lineage and future studies should evaluate additional biological and biochemical factors that could work synergistically with the biophysical cues provided by the electrospun fibrin fibers.

Despite low levels of muscle regeneration in all treatment groups and limited evidence of ASC myogenesis both *in vitro* and *in vivo*, there is some evidence that ASCs may improve regenerative outcomes for VML. In this study, acellular fibers had eMHC+ regenerating muscle cells at 3 months but no mature MHC+ muscle cells at either time point. Interestingly, ASC-seeded fibers had eMHC expression at 1 month and significantly earlier than that seen in acellular fibers, suggesting that the addition of ASCs hastened the muscle's regenerative response. Additionally, unlike the acellular fibers, muscle cells within ASC-seeded fibers were MHC+ at both time points demonstrating the presence of mature muscle cells within the fiber interior. The source of regenerating muscle cells within the fibers is unclear. There were some cases where individual regenerating eMHC+ muscle cells contained Lamin AC+ nuclei but the majority of eMHC+ and MHC+ cells within the fibers did not have an ASC-derived nucleus. In addition, there laminin+ cells with Lamin AC+ nuclei were present in both induced and uninduced ASC samples. It is possible that implanted ASCs directly differentiated into muscle *in vivo* and/or fused with infiltrating host muscle cells. It is important to note that the eMHC, MHC, and laminin antibodies used stain both mouse and human proteins. It is also possible that implanted ASCs provided paracrine signaling to promote muscle progenitor cell infiltration from the host and subsequent regeneration. ASCs are known to provide a pro-regenerative environment and modulate the immune system[171,172] as well as secrete pro-angiogenic factors[180]. A large number of

regenerating muscle cells within the fibers were immediately adjacent to ASCs suggesting a correlation between ASC location and the presence of regenerating muscle. Our findings suggest that human ASCs promote moderate muscle reconstruction in VML models. Nonetheless, complete removal of the TA and EDL muscles is an aggressive VML injury model for testing the efficacy of this approach due to the lack of endogenous cell infiltration and potential paracrine signaling benefit. It is likely that ASCs implanted in a VML defect involving partial removal of a single muscle would yield further improved regenerative outcomes. Further studies into ASC-mediated muscle regeneration in VML models will be required to understand the mechanism by which ASCs promote regeneration within the harsh VML injury environment.

3.5 Conclusions

In this study, the muscle regenerative potential of ASCs combined with an electrospun fibrin fiber mimicking the structure, alignment, and mechanical properties of native skeletal muscle was assessed. The fibers promoted limited *in vitro* myogenic properties in both induced and uninduced ASCs but both groups failed to fully replicate myotube characteristics *in vitro*. When implanted in a severe VML defect model, the fibers integrated well with the native tissue, eliciting little scarring, promoting long-term survival of transplanted ASCs, and stimulating cellular and vascular ingrowth. Although the number of eMHC+ and MHC+ cells in this model is modest up to 3 months, it should be noted that any amount of muscle regeneration is significant due to the severe VML model that was utilized. Interestingly, *ex vivo* differentiation of ASCs down the myogenic lineage via 5-azacytidine induction did not significantly improve *in vivo* muscle regeneration as was hypothesized. Implanted fibers with uninduced ASCs contained more muscle cells than acellular fibers at both 1 and 3 months, indicating that the addition of

uninduced ASCs on electrospun fibrin fibers may enhance muscle regeneration post-VML. In addition, several regenerating muscle cells had LaminAC+ nuclei indicating the possibility of direct contribution of ASCs to those regenerating cells. Taken together, this data illustrates that despite low *in vitro* myogenic potential, electrospun fibrin fibers combined with ASCs promote moderate muscle reconstruction in a severe VML injury.

Chapter 4 Human Pluripotent Stem Cells: Assessment of Myogenic Potential *In Vitro* and *In Vivo*

4.1 Introduction

Volumetric muscle loss (VML) occurs when large-scale damage to skeletal muscle overwhelms the natural repair mechanisms and leads to chronic functional deficits[146]. Current clinical treatment options for VML are limited by low success rates in restoring muscle function and at best provide aesthetic benefits and prevent further necrosis[36,146]. Tissue engineered grafts offer a potentially more effective regenerative medicine treatment option for VML that may alleviate the varied limitations of current treatments and lead to improved functional outcomes. A broad range of cell sources has been utilized to develop tissue engineered muscle grafts, including satellite cells or other muscle-derived precursor cells[21,33,56,69–73], mesenchymal stem cells[74,75], adipose-derived stem cells[76–78], and human pluripotent stem cells[79–81]. While satellite cells and myoblasts enable robust myogenic differentiation, they have limited proliferative capabilities and necessitate invasive, large biopsies from the patient[47,188]. Mesenchymal and adipose-derived stem cells are more easily isolated and have a higher proliferative capacity but often are quite limited in myogenic potential[77,188]. Human pluripotent stem cells (hPSCs) offer a translatable cell source that is sourced noninvasively from the patient, has unlimited self-renewal in culture, and can be differentiated into skeletal muscle[47,189].

The myogenic differentiation capability of hPSCs has been widely established in monolayer cultures[80,190–192] and primarily utilizes either forced overexpression of a muscle gene or induction via small molecule signaling[189]. Despite extensive use in monolayer cultures, only two published studies thus far have described the development of an implantable hPSC-derived 3D muscle construct and have evaluated its engraftment potential in non-VML animal

models[79,81]. In both studies, the implanted hPSC-derived constructs were induced towards myogenesis utilizing transduction and overexpression of Pax7 or MyoD. While genetic modification of iPSCs often results in higher levels of myogenesis it has been known to induce cancer-causing genetic abnormalities and has limited translational potential[47,189]. Our collaborators in the lab of Dr. Gabsang Lee have successfully developed a small-molecule based method to induce hPSC myogenesis that results in a robustly expandable population of myogenic precursor cells with the ability to engraft into injured skeletal muscle[80]. Our group has previously utilized electrospun fibrin microfiber bundles that mimic the native properties of skeletal muscle combined with C2C12 myoblasts to promote functional and histological regeneration post-VML [25]. In the current study we assess the *in vitro* and *in vivo* myogenic potential of small molecule-induced hPSC-derived myoblasts (hPDMs) in a 3D electrospun fibrin construct. We test the hypothesis that the combination of hPDMs on electrospun fibrin fibers promotes *in vitro* myogenesis and *in vivo* engraftment utilizing several murine skeletal muscle defect models. We further test the hypothesis that the *in vitro* maturation time point of hPDM muscle constructs impacts its engraftment and regenerative potential following implantation.

4.2 Methods

Electrospinning Fibrin Scaffolds

Fibrin scaffolds were electrospun in a sterile environment with sterile solutions as previously described [25,77,193]. Parallel syringes containing solutions of fibrinogen (Sigma) or sodium alginate (Sigma) were connected via a y-syringe and extruded by syringe pumps with an applied voltage of 3-5 kV applied to a 27G needle tip utilizing 1% fibrinogen with an extrusion rate of 4 ml/hr and 0.75% alginate with an extrusion rate of 1 ml/hr. Polyethylene oxide (average

Mv ~ 4 000 kDa, Sigma) was added to each solution at 0.2 wt% to increase viscosity during electrospinning. The electrospun hydrogel solutions were collected for 5.75 minutes on a rotating dish (~35rpm) containing 50 mM $CaCl_2$ and 20 U/ml thrombin (Sigma) as crosslinking agents. Samples were allowed to crosslink and additional 3-5 min after electrospinning and were then wrapped around a 3.0 × 1.5 cm acrylonitrile-butadiene-styrene frame 4 times to yield a hydrogel microfiber bundle ~700 μm in diameter. Scaffolds were incubated overnight in 250 mM sodium citrate (Sigma) to dissolve the alginate and then transferred to DI water for storage up to 2 weeks.

hPSC Myogenic Commitment and Expansion

Human embryonic stem cells (H9 hESCs; WiCell) were cultured in Dr. Gabsang Lee's lab as previously described [80]. Briefly, hESCs were cultured using a mouse embryonic fibroblast (MEFs; GlobalStem or AppliedStemCell) feeder layer at 12,000-15,000 cells/cm^2. Expansion media contained DMEM/F12, 20% knockout serum replacement, 1 mM L-glutamine, 100 mM MEM non-essential amino acids, 0.1 mM b-mercaptoethanol, and 10 ng/ml FGF2. Subsequent steps utilized N2 media containing DMEM/F12 powder, glucose, sodium bicarbonate, insulin, putrescine, progesterone, sodium selenite, and transferrin. For myogenic commitment, sterile filtered N2 media conditioned by MEFs for 24 hours was utilized. hESCs were seeded at a density of 1.5 x 10^5 cells/well of a 24 well plate coated with 1% Geltrex and fed with MEF-conditioned N2 media supplemented with 10 ng/ml FGF2 and 10 μM Y-27632 (Cayman Chemical) for the first 24 hours of culture. For culture days 1-4, N2 media was supplemented with 3 μM CHIR99021 (Cayman Chemical) and media was changed every other day. For culture days 4-12, media was switched to N2 media containing 10 μM DAPT (Cayman Chemical). Following myogenic commitment, the cells were expanded for 5-6 passages in N2 media containing 5% FBS prior to seeding in monolayers or on electrospun scaffolds. For

experiments utilizing Pax7-sorted hPDMs, hESCs were genetically manipulated prior to myogenic commitment using the CRISPR/Cas9 system to express a Pax7::GFP reporter as previously described[80]. Cells were then cultured following the myogenic commitment protocol described above in N2 media containing 5% FBS, 1% P/S, and 10 ng/ml FGF2. After 30 days of expansion, cells were sorted using fluorescence activated cell sorting (FACS) for the Pax7::GFP+ subpopulation. Pax7-sorted cells were then expanded for 5-6 passages prior to use in experiments.

Cell Seeding on Scaffolds

hPDMs were expanded as described above. For Geltrex-coated scaffolds, scaffolds were incubated in Geltrex dissolved in cold DMEM/F12 (1:100; Life Technologies) for 1 hour at 37 °C then 1 hour at RT. For fibronectin-coated scaffolds, scaffolds were incubated in 10 μg/ml fibronectin in 50 mM HEPES Buffer. In preparation for cell seeding, scaffolds were incubated in DMEM/F12 media for 20 min at RT. The scaffolds were then transferred to 6-well cell culture plates coated with 2% agarose type VII (Sigma) to minimize cell adhesion to the plate surface, which increases the seeding efficiency. A total seeding volume of 40 μl at 15,000 cells/μl was pipetted onto the scaffold surface in a series of 5 μl droplets (for a total seeding density of 600,000 cells/scaffold).

Various modifications to the regular seeding protocol were evaluated as follows. For the Geltrex Gel protocol, hPDMs were resuspended in liquid Geltrex at 15,000 cells/μl (for a total of 600,000 cells/fiber) and quickly pipetted onto the scaffold surface prior to gelling. For the Injected Cells protocol, hPDMs were suspended in N2 media at 15,000 cells/μl (for a total of 600,000 cells/fiber), loaded into a 1 ml syringe, and injected into the scaffold interior. For the 3D Printed Mold protocol, molds were designed to hold the electrospun scaffolds in a small volume of liquid

and 3D printed using acrylonitrile-butadiene-styrene. hPDMs were suspended in N2 media at 15,000 cells/µl and scaffolds were incubated with 40 µl of cell solution per mold. For the Gel on Frame protocol, hPDMs were suspended in 32 µl of 1% fibrinogen at 15,000 cells/µl then mixed with 8 µl of 10 U/ml thrombin and immediately pipetted along a 3.0 x 1.5 cm acrylonitrile-butadiene-styrene frame. For the bulk gel protocol, PDMS molds were created to hold a 40 µl volume and sterilized. hPDMs were suspended in 32 µl of 1% fibrinogen at 15,000 cells/µl then mixed with 8 µl of 10 U/ml thrombin and immediately pipetted into the PDMS molds to gel. For hybrid seeding, hPDMs were suspended in 20 µl of thrombin at 1.25 U/ml in N2 media containing 40 mmol/L $CaCl_2$. Fibrinogen was diluted in N2 media to 40 mg/ml and 20 µl of fibrinogen was mixed with 20 µl of thrombin and immediately pipetted onto the scaffold surface in 5 µl increments. All seeded scaffolds were incubated for 1 hour at 37°C with hydration levels maintained by addition of 15 µl of N2 media containing 5% FBS and 1% P/S halfway through. After the 1 hour incubation, 3 ml of N2 media containing 5% FBS, 1% P/S, and 30 µg/ml aprotinin (Affymetrix) was added to each well and care was taken to ensure the scaffolds had been submerged in the media. For induced samples, on day 3 or day 7 of culture myoblasts were transferred to low-serum Induction Medium: N2 media with 1% P/S and 30 µg/ml aprotinin and remained in Induction Medium for the extent of *in vitro* culture and media was changed every other day. For Pax7-sorted hPDMs, expansion and culture in monolayers and on fibers was in Pax7 Media: N2 media supplemented with 5% FBS, 1% P/S, 10 ng/ml FGF2 (PeproTech), and 5 ng/ml FGF8 (PeproTech).

Whole Mount Immunostaining

Scaffolds were fixed in 4% formaldehyde at 4°C on a rocker at 80 rpm for 3 hours. Following 3 washes with PBS, scaffolds were blocked and permeabilized (Block/Perm Solution)

for 3 hours with 0.2% Triton X-100, 10% normal goat or donkey serum (Sigma). Scaffolds were then incubated with primary antibodies diluted in Block/Perm Solution overnight at 4°C on a rocker at 135 rpm, followed by three 1-hour washes with PBS. Primary antibodies included myogenin (5 μg/ml; DSHB), myosin heavy chain (5 μg/ml; DSHB), desmin (1:400; Abcam), α-actinin (1:200; Abcam), titin (5 μg/ml; DSHB), and Pax7 (5 μg/ml; DSHB). Scaffolds were then incubated with secondary antibodies diluted in 10% normal goat or donkey serum and 0.1% Tween in PBS overnight at 4 °C on a rocker at 135 rpm, followed by three 1 hour washes with PBS. DAPI was incorporated in the second wash at a dilution of 1:2000. Secondary antibodies included DyLight 488-conjugated donkey anti-mouse (1:400; Jackson ImmunoResearch), Alexa Fluor 647-conjugated donkey anti-rabbit (1:400; Jackson ImmunoResearch), or Cy3-conjugated donkey anti-mouse (1:400; Jackson ImmunoResearch). Samples were then imaged with a Zeiss LSM 510 confocal microscope.

Animal Models

Animal and surgical procedures were approved by the Institutional Animal Care and Use Committee at Johns Hopkins University School of Medicine. Female 2-4 month old NOD-scid IL2Rg^{null} (NSG) immunodeficient mice (Jackson Lab) were utilized to enable implantation of human cells. Mice were randomly assigned across all groups. In vitro constructs were prepared and cultured with hPDMs as described above. Muscle defects were created as previously described[25]. Mice were anesthetized with isofluorane, the TA muscle was exposed, and approximately 30-50% (VML defects) or 7-12% (sub-critical defects) of the muscle was removed. After bleeding ceased, scaffolds were placed in the defect site and ligated on both ends to the remaining TA muscle with non-absorbable sutures (6-0 Nylon, Express Medical Supplies). Surgical glue (Histoacryl, B. Braun) and sutures were used to close the skin. Rimadyl was injected

subcutaneously post-surgery for pain management (5 mg/kg). Mice were sacrificed at 1 or 2 weeks post-implantation by isoflurane overdose and cervical dislocation. Upon harvest, implanted scaffolds and surrounding TA muscle tissue were removed and cryopreserved.

Histology

Samples were sectioned on a cryostat (Leica) at a thickness of 10 μm for cross-sections and 70 μm for longitudinal sections. Masson's Trichrome stains were imaged on a Zeiss Axio Imager upright microscope. For immunohistochemistry, slides were fixed in cold 4% formaldehyde for 10 min and rinsed with PBS three times for 15 min each, then blocked in 10% normal donkey or goat serum (Sigma) in PBS for 1 hour at RT. Slides were incubated with antigen-specific primary antibodies in blocking solution overnight at 4°C. Primary antibodies included mouse anti-myosin heavy chain (5 μg/ml; DSHB), goat anti-mouse CD31 (1:100; R&D Systems), rabbi anti-LaminAC (1:500; Abcam), mouse anti-Pax7 (5 μg/ml; DSHB), and mouse anti-embryonic myosin (5 μg/ml; DSHB). After three 5 min washes with PBS, slides were incubated with secondary antibodies and DAPI (1:2000) diluted in blocking solution for 1 hour at RT. Secondary antibodies included Cy3-conjugated donkey anti-mouse, Alexa Fluor 488-conjugated donkey anti-goat, DyLight 488-conjugated goat anti-mouse, or Alexa Fluor 647-conjugated donkey anti-rabbit (1:400; Jackson ImmunoResearch). Slides staining for phalloidin-TRITC (1:40; Sigma) or phalloidin-AF488 (1:40; Thermo Fisher) incorporated the stain into the secondary antibody stain. Slides were washed three times for 5 min then mounted with 50% glycerol and imaged on a Zeiss Axio Observer inverted fluorescence microscope or Zeiss Axio Observer 7. To quantify staining within the defect regions, tiled images covering the entire defect region were taken on a Zeiss Axio Observer 7 with a 20x objective.

Statistics

Statistical analysis was performed using GraphPad Prism 5 software. Statistical significance was determined by t test or one-way ANOVA with Dunnett or Bonferroni post-test. Error bars represent standard error of the mean (SE). *: $p < 0.05$; **: $p < 0.01$; ***: $p < 0.001$; ǂ: not significant

4.3 Results

Unsorted hPSC-Derived Myoblasts Form Myotubes on Electrospun Fibers with Some Variability

Unsorted hPSC-derived myoblasts (hPDMs) committed to undergo myogenesis and expanded showed no difference in myogenic potential in monolayer culture between uninduced cells and those induced at day 3 of culture (**Fig. 4.1A-C**). When seeded on electrospun fibrin microfiber bundles and cultured for 10 days, hPDMs expressed the muscle markers myogenin and myosin heavy chain (MHC), forming MHC+ aligned and multinucleated myotubes in both uninduced and induced culture conditions. To further optimize hPDM seeding efficiency and myogenesis, fibers were coated with geltrex, fibronectin, a geltrex gel, or left uncoated. In all fiber coating groups, hPDMs were either uninduced or induced at day 3 or day 7 of culture (**Fig. 4.1E**). Differences in MHC coverage were present between early and late induction time points for fibers in all coating groups, however fibers seeded with uninduced hPDMs had statistically similar amounts of MHC coverage to those induced at day 7 in most groups. MHC coverage for uncoated fibers was similar to other coating groups, leading to the selection of uncoated fibers induced on day 7 or uninduced for use in subsequent experiments (**Fig. 4.1F**).

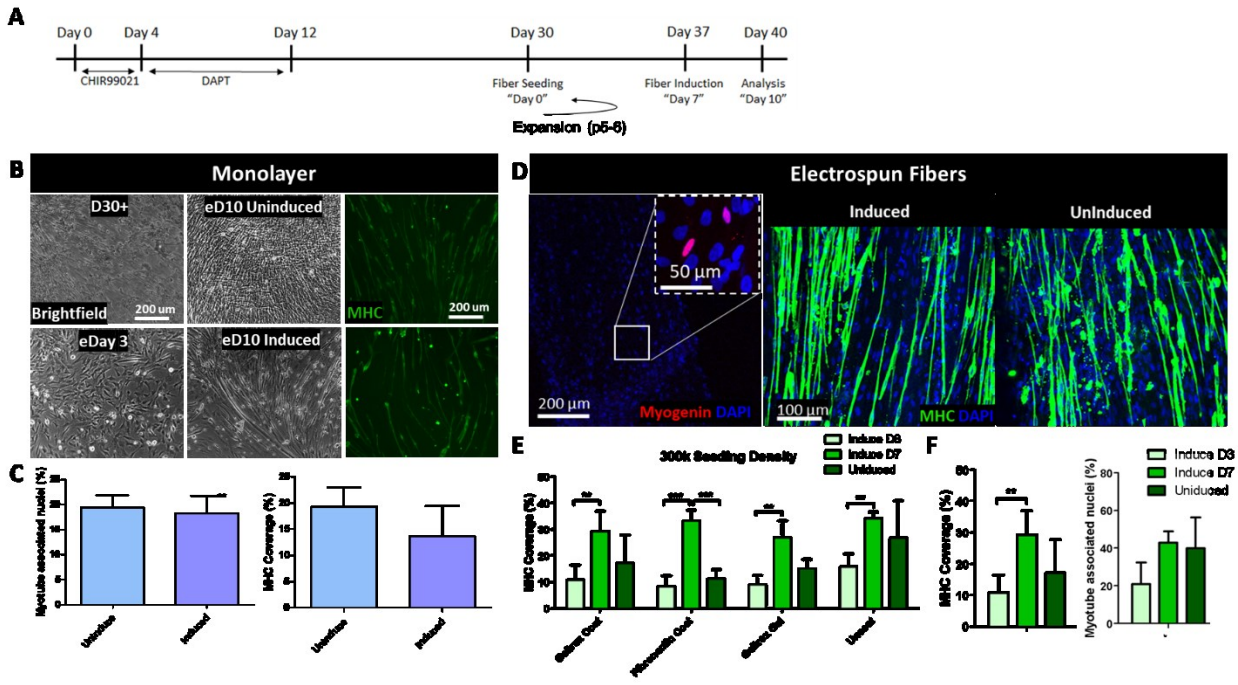

Figure 4.1. Uninduced and induced unsorted hPDMs form myotubes on electrospun fibrin scaffolds. A) Timeline of hPSC myogenic induction, expansion, and seeding on electrospun fibers. **B)** *Left:* Brightfield imaging demonstrating cell morphology following monolayer expansion for 30 days and uninduced or induced replated monolayers. *Right:* Uninduced and induced monolayers immunostained for myosin heavy chain (MHC; green). **C)** Quantification of multinucleation and MHC coverage for uninduced and induced monolayers demonstrating no difference in myogenesis. **D)** Whole mount immunostaining for myogenin (red) and MHC (green) demonstrating myogenesis and myotube morphology for induced and uninduced hPSC-derived myoblasts cultured on electrospun fibers for 10 days. **E)** Quantification of the MHC coverage on day 10 of culture comparing various fiber coatings and induction timelines. **F)** Quantification of MHC coverage and multinucleation of uncoated fibers seeded with hPSC-derived myoblasts at day 10 of culture. **: $p < 0.01$; ***: $p < 0.001$

Unsorted hPDM-Derived Muscle Constructs Demonstrate Survival but Little Regeneration Following Implantation in VML Defects

To evaluate the regenerative potential of unsorted hPDM constructs, uninduced and induced constructs were implanted in murine VML defects of the TA muscle for two weeks in immunodeficient mice. Although both induced and uninduced constructs had significant cell coverage *in vitro,* little MHC expression was seen at the time point of implantation further

demonstrating variability in myogenic potential between batches of unsorted hPDMs (**Fig. 4.2A**). Following implantation for 2 weeks, induced and uninduced constructs resulted in mild fibrosis within the defect region and maintained the defect volume (**Fig. 4.2Bi**). Human nuclei were visible within the defect region with no difference in the percent of human nuclei between groups (**Fig. 4.2Bii,C**). Although blood vessels infiltrated into implanted constructs, there was little evidence of MHC expression and muscle regeneration within the defect with no difference in MHC coverage between groups.

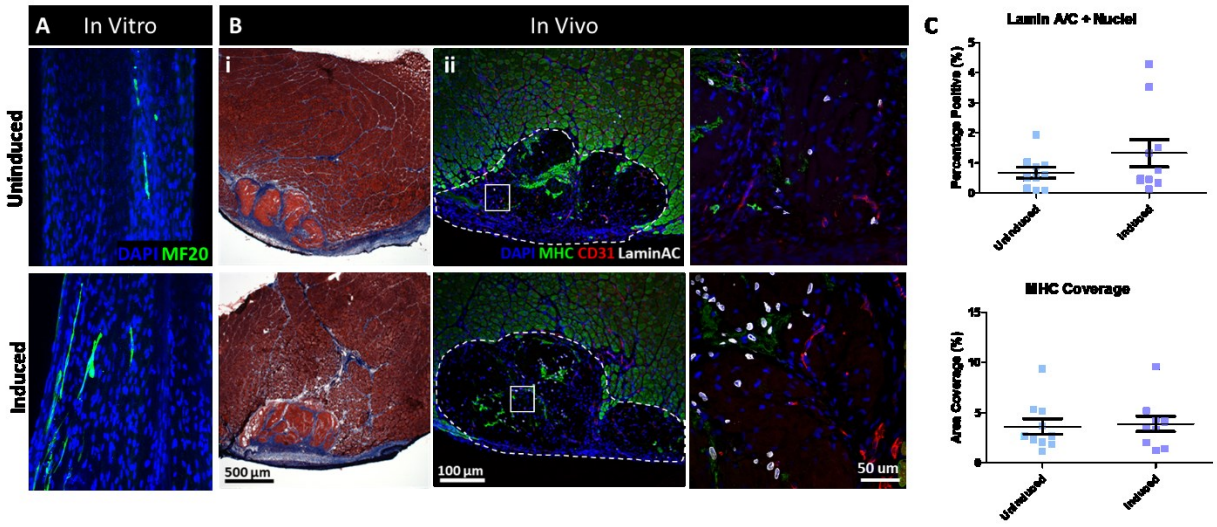

Figure 4.2. Unsorted hPDM constructs demonstrate survival at 2 weeks post-VML with little regeneration. A) *In vitro* uninduced and induced constructs demonstrated little myosin heavy chain (MF20; green) expression at day 12 of culture. **B)** Masson's trichrome staining (i) and immunostaining (ii) for myosin heavy chain (MHC; green), vasculature (CD31; right), and human nuclear protein (LaminAC; white). **C)** No difference was seen in the percent of human nuclei or MHC coverage between uninduced and induced constructs within the defect.

Pax7-Sorted hPDMs Enable Improved *In Vitro* 3D Myogenesis

A purified population of Pax7-sorted hPDMs was investigated for its myogenic potential on electrospun fibrin fibers. hPSCs were initially tagged with a Pax7-driven green fluorescent protein (GFP) reporter gene, underwent the same myogenic commitment protocol, and were subsequently sorted using Fluorescence Activated Cell Sorting (FACS) for the GFP+ population.

Pax7-sorted hPDMs were then expanded for several passages and utilized for experiments (**Fig. 4.3A**). Pax7-sorted hPDMs exhibited significantly more MHC expression and multinucleation compared to unsorted hPDMs when cultured in monolayer for 10 days (**Fig. 4.3B,C**). Pax7-sorted hPDMs seeded onto electrospun fibrin fibers demonstrate a characteristic time-dependent expression profile of common muscle proteins (**Fig. 4.4**). Early proliferating hPDMs are positive for Pax7 at day 3 of culture which decreases in expression up to day 10. As the hPDMs mature and fuse into myotubes by day 10, they express increasing levels of desmin and MHC. Day 10 hPDM-derived myotubes also express the mature muscle markers α-actinin and titin with characteristic striations. The level of multinucleation is low at day 3 and increases up to day 10 as well.

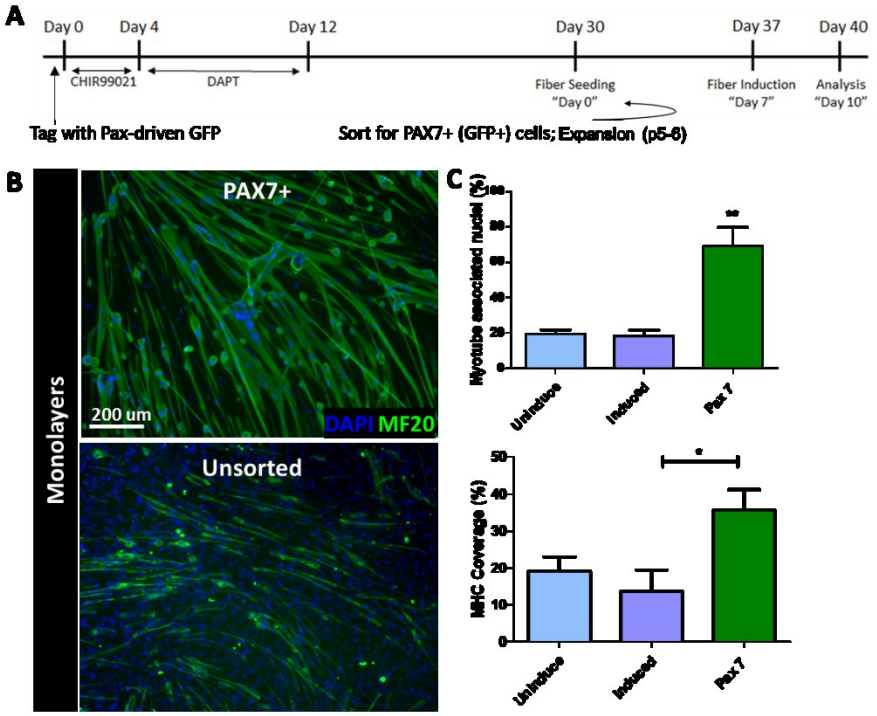

Figure 4.3. Pax7-Sorted hPDMs form more myotubes in monolayers than unsorted cells. A) Timeline of hPSC Pax::GFP reporter tagging, myogenic induction, expansion, sorting, and seeding on electrospun fibers. **B)** Pax7::GFP+ or unsorted hPSC-derived myoblast monolayers stained for myosin heavy chain (MF20; green) demonstrate increased presence of MHC+ myotubes for sorted cells. **C)** Quantification demonstrating increased multinucleation and MHC coverage for Pax7::GFP+ monolayers. *: $p < 0.05$; **: $p < 0.01$

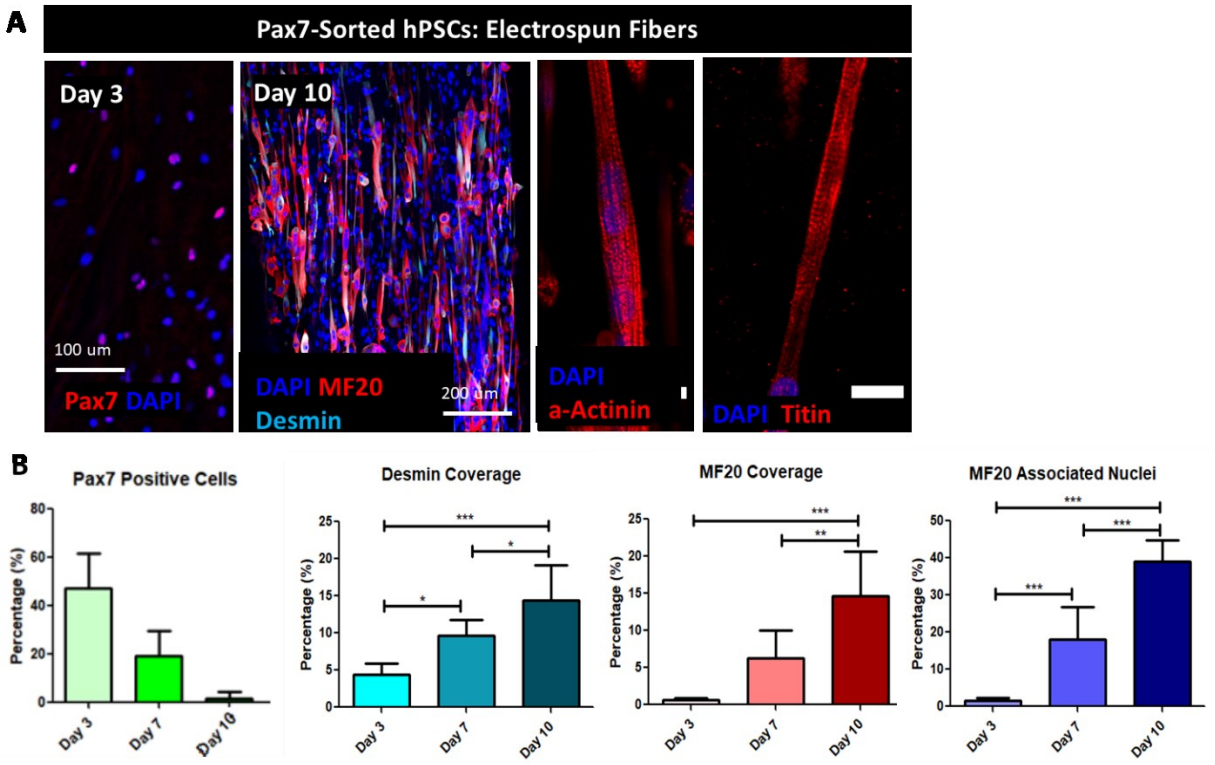

Figure 4.4. Pax7-Sorted hPDMs follow muscle protein expression timeline and form mature myotubes on 3D constructs. A) Pax7::GFP+ hPDMs seeded on electrospun fibers demonstrate expression of Pax7 (red) at day 3 of culture and myosin heavy chain (MF20; red), desmin (cyan), α-actinin (red), and titin (red) at da 10 of culture. Myotubes had visible striations at day 10 of culture. **B)** Expression of Pax7 decreased over time as cells matured while expression of desmin and MHC as well as the level of multinucleation increased over time. *: $p < 0.05$; **: $p < 0.01$; ***: $p < 0.001$

To improve seeding efficiency of hPDMs onto the fibers, a variety of seeding techniques were evaluated (**Fig. 4.5A**). Despite proliferation and myogenesis on the fibers, the regular seeding technique used previously resulted in significantly less cells one day post-seeding than seeding cells within a bulk fibrin gel. Despite increased cell retention, bulk gel seeding resulted in MHC and desmin positive myotubes at day 10 with a stunted and disorganized morphology (**Fig. 4.5B**). To utilize the benefits of bulk gel seeding while maintaining the pro-myogenic stiffness and alignment cues of electrospun fibrin fibers, a new hybrid seeding method was developed where hPDMs were suspended in a fibrin gel and seeded onto electrospun fibers in the gel prior to gel crosslinking. This resulted in significantly more cell retention at the electrospun

fiber surface at day 4 post-seeding compared to the regular seeding protocol used previously (**Fig. 4.5C**).

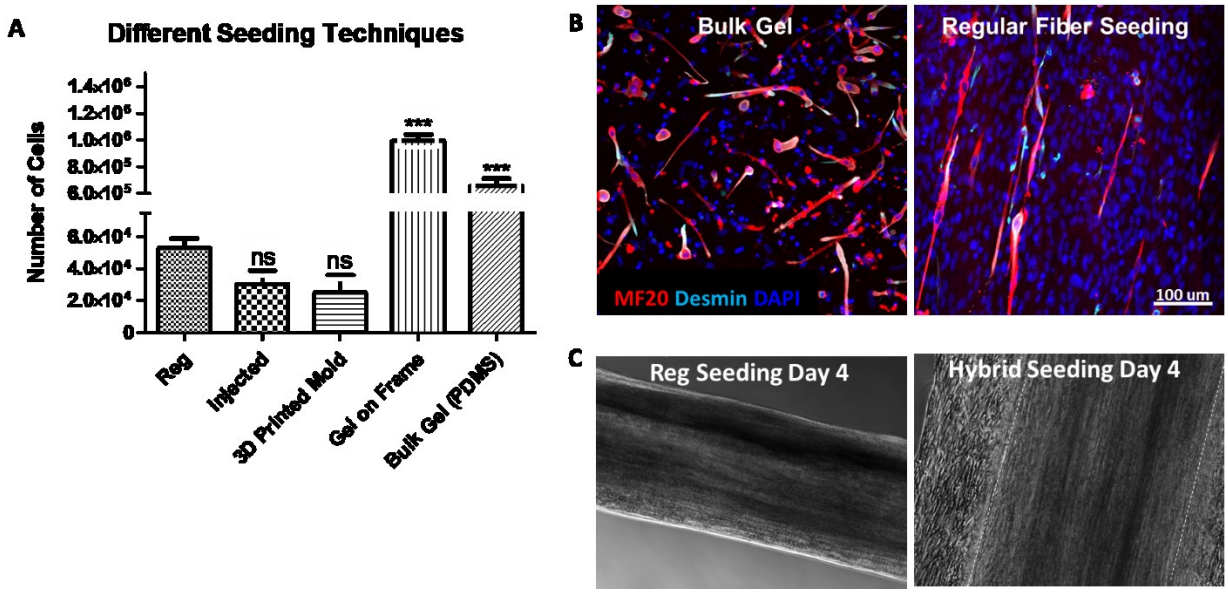

Figure 4.5. Variability in seeding efficiency led to the development of a modified "hybrid" seeding method. A) Cell content day 1 post-seeded on electrospun fibers seeded with various protocol differed significantly. **B)** Immunostaining at day 10 of culture for myosin heavy chain (MF20; red) and desmin (cyan) demonstrated that despite increased seeding efficiency for bulk gel constructs, myotubes had increased alignment using the regular seeding protocol. **C)** Brightfield imaging demonstrating a difference in cell retention on the fiber exterior at day 4 of culture between the regular seeding protocol and a new hybrid protocol. ***: $p < 0.001$

Pax7-Sorted hPDM-Derived Muscle Constructs Have Limited Survival and Regenerative Potential Following Implantation in Sub-Critical Defects

The engraftment and regenerative potential of day 10 Pax7-sorted hPDM-derived muscle constructs was evaluated in a sub-critical sized defect in immunodeficient mice at 1 and 2 weeks post-implantation. A sub-critical sized defect was utilized to decrease the inflammatory response to injury and promote cell survival. Pax7-sorted constructs maintained the defect volume but resulted in moderate fibrosis at both 1 and 2 weeks post-implantation (**Fig. 4.6Ai**). Immunostaining demonstrated the presence of blood vessel infiltration at both 1 and 2 weeks (**Fig. 4.6Aii**) but the presence of implanted human cells decreased significantly between 1 and 2

weeks post-implantation (**Fig. 4.6B**). Little MHC expression was present within the defect regions at both time points demonstrating the limited regenerative potential of hPDM-derived muscle constructs within this defect model. Despite the lack of muscle regeneration, longitudinal sectioning demonstrated the positive engraftment potential of hPDMs implanted for 1 week with dense human nuclei visible within the defect region (**Fig. 4.6C**).

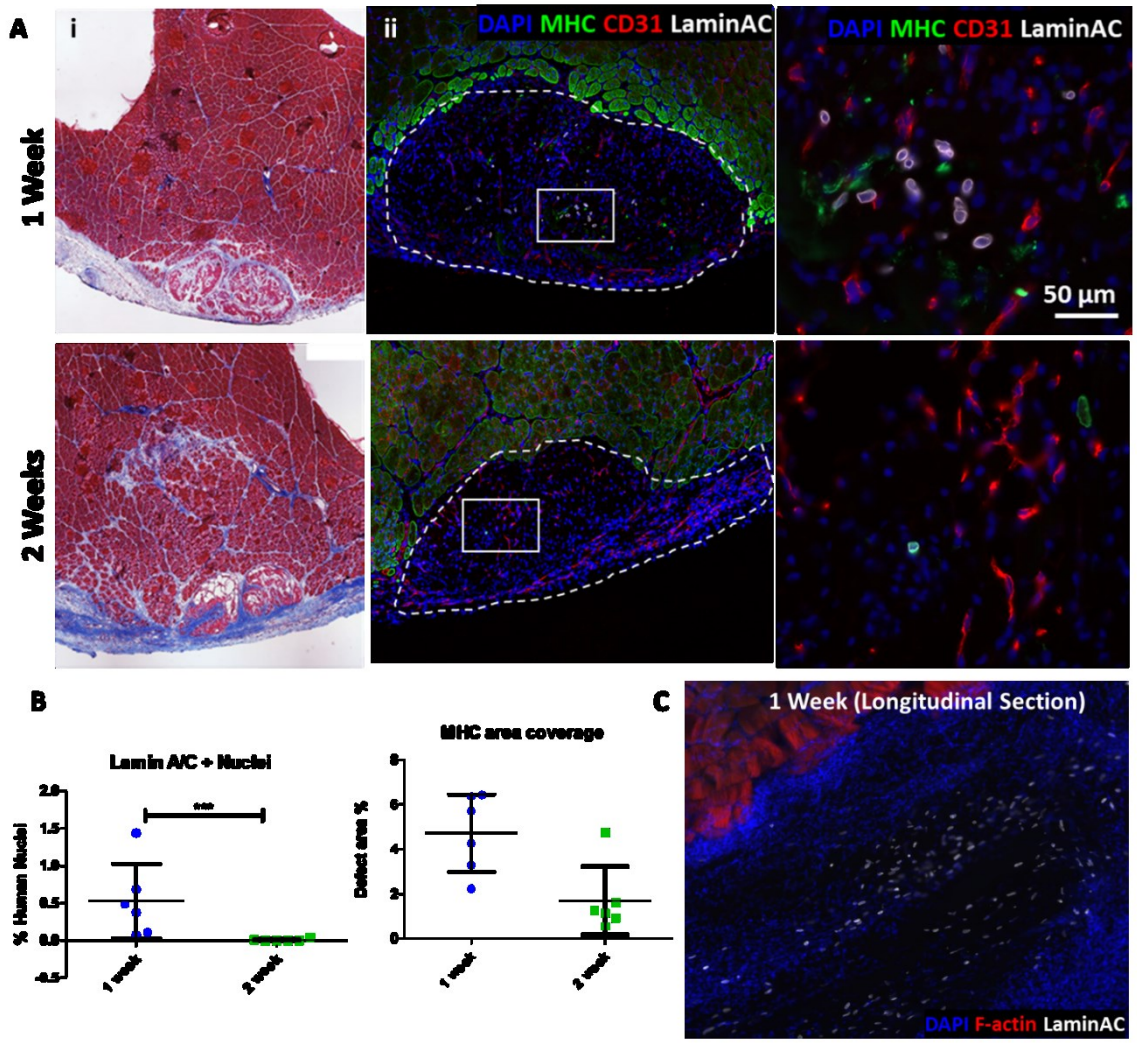

Figure 4.6. Pax7-sorted hPSC-derived muscle constructs demonstrate survival at 1 week but not 2 weeks in sub-critical defect. A) Masson's trichrome staining *(left)* and immunostaining *(right)* for myosin heavy chain (MHC; green), vasculature (CD31; right), and human nuclear protein (LaminAC; white). **B)** Pax7-sorted hPSC-derived muscle constructs implanted for 1 week contained significantly more human nuclei than those implanted for 2 weeks with no difference in myogenesis. **C)** Longitudinal sectioning and immunostaining for phalloidin (F-actin; red) and human nuclear protein (LaminAC; white) at 1 week post-implantation demonstrates dense human nuclei visible within the defect region. ***: $p < 0.001$

In Vitro Maturation Time Point of Pax7-Sorted hPDM-Derived Muscle Constructs May Impact *In Vivo* Engraftment and Regenerative Potential

Pax7-sorted hPDM-derived muscle constructs at either day 3 or day 10 of *in vitro* culture were implanted in sub-critical defects for 1 week to evaluate differences in engraftment and regenerative potential based on the *in vitro* maturation time point. Bulk fibrin gels seeded on the day of implantation were utilized as a near 100% seeding efficiency control. The *in vitro* day 3 and day 10 constructs exhibited characteristic early (Pax7) and late (MHC) protein expression, respectively (**Fig. 4.7A**). Following implantation in a sub-critical defect for 1 week, bulk gels demonstrated significant construct resorption and a failure to maintain the defect volume. Implanted day 3 and day 10 fibers both maintained the defect volume with day 10 fibers resulting in a higher level of fibrosis (**Fig. 4.7Bi**). Immunostaining for Pax7 demonstrated the presence of human nuclei within the defect and satellite cells surrounding the defect regions for all groups (**Fig. 4.7Bii**). Myotube-like structures containing multiple human nuclei were visible in the defect regions of all groups with bulk gels and day 3 fibers resulting in more than day 10 fibers (**Fig. 4.7Biii**). To further assess differences in the regenerative potential of Pax7-sorted hPDM-derived muscle constructs at different maturation time points, embryonic myosin (eMHC), a transient marker of muscle regeneration, was evaluated for co-expression with human nuclear LaminAC (**Fig. 4.8**). All three groups contained eMHC+ myofibers with human nuclei within and surrounding the defect region as well as blood vessel infiltration into the defect, demonstrating the ability of early- and late-stage hPDMs to form regenerating myofibers following implantation in injured skeletal muscle tissue.

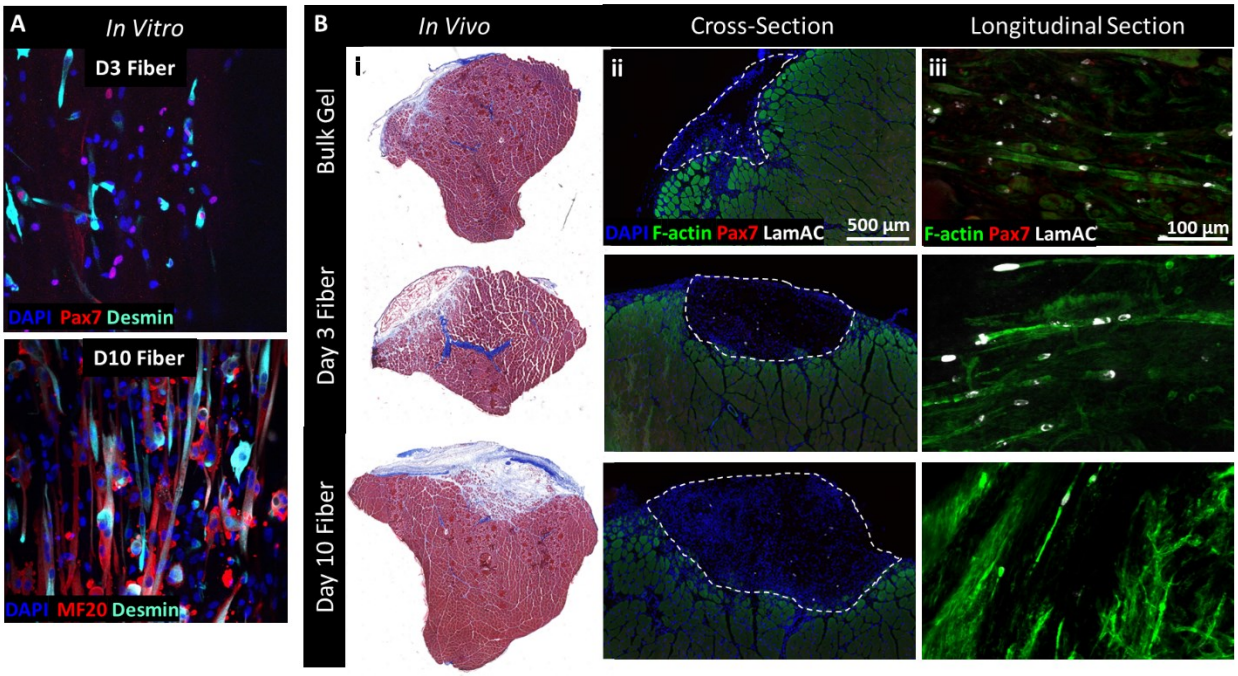

Figure 4.7. The *in vitro* maturation time point of Pax7-sorted hPSC-derived muscle constructs may impact survival and regenerative potential. A) *In vitro* constructs show expression of Pax7 (red) and some desmin (cyan) at day 3 of culture and significant expression of myosin heavy chain (MF20; red) and desmin at day 10 of culture. **B)** Differences in defect volume retention, fibrosis, and cell survival were visible via **i)** Masson's trichrome staining, **ii)** immunostaining for phalloidin (F-actin; green), Pax7 (red), and human nuclear protein (LaminAC; white) in cross-sections, and **iii)** immunostaining for phalloidin, Pax7, and human nuclear protein in longitudinal sections within the defect region.

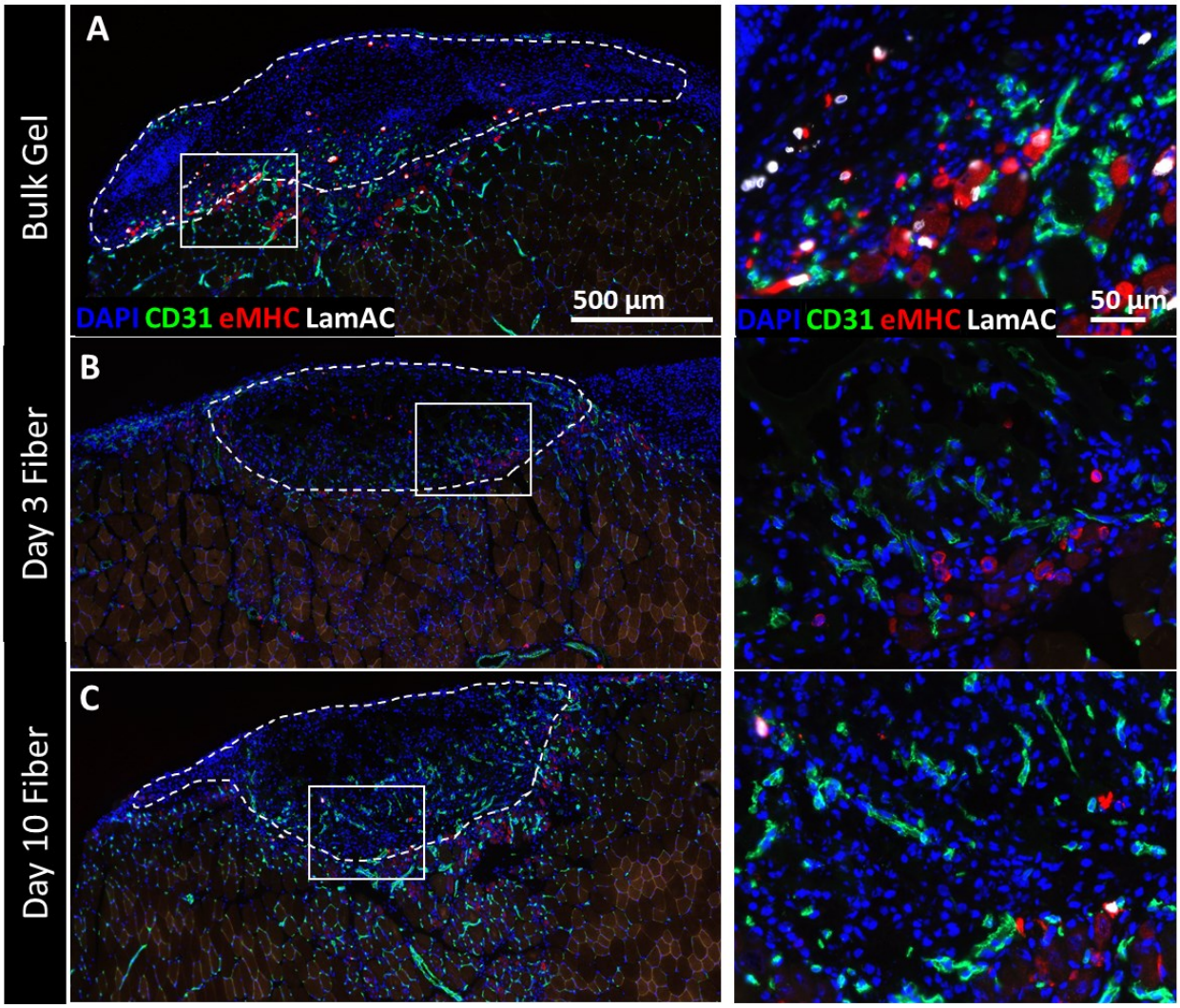

Figure 4.8. Regenerating myofibers with human nuclei are present inside and surrounding the defect with blood vessel infiltration to defect. Immunostained cross-sections demonstrate expression of vasculature (CD31; green), regenerating myofibers (eMHC; red), and human nuclear protein (LaminAC; white) in **A)** bulk gels, **B)** day 3 fibers, and **C)** day 10 fibers implanted for one week.

4.4 Discussion

The translational potential of tissue engineered muscle grafts relies on the use of a practical, expandable, and highly myogenic cell source. While hPSCs have been myogenically differentiated with significant success in monolayer cultures[80,190–192], the use of hPSCs to form an implantable 3D muscle construct has been described just twice before[79,81]. This discrepancy is likely due to difficulty in successfully translating monolayer culture protocols to a 3D tissue

engineered construct as well as the inherent variability posed by hPSC culture[194]. In both previously published hPSC-derived 3D muscle constructs, the implanted constructs utilized genetic modification to force overexpression of an early muscle gene and thereby induce hPSC myogenesis. One study assessed both genetic modification and small molecule induction protocols and selected the transgene-based protocol for subsequent experiments due to better myogenesis, scalability, and cost-effectiveness[79]. Although frequently resulting in higher levels of myogenesis, genetic modification has limited translational potential[47,189]. To effectively develop a translational tissue engineered muscle graft, both the cell source and the myogenic induction protocol should be clinically feasible and safe. To that end, in the current study we have developed an implantable 3D hPSC-derived muscle construct utilizing small-molecule induction. Both prior studies evaluated the engraftment and myogenic potential of hPSC-derived 3D muscle constructs in various non-VML models, which fail to assess the survival capability of hPSCs when implanted in the harsh post-injury environment. We have evaluated the survival, engraftment, and myogenesis of our hPSC-derived muscle constructs in both critical and sub-critical muscle defects to advance understanding of hPSC survival in the unforgiving post-VML environment into which they would ultimately be implanted within patients.

Although unsorted hPDMs successfully formed MHC+ myotubes on electrospun fibers, there was significant variability between batches of expanded cells. Since hPSCs are an inherently heterogeneous cell population[194] it is likely that various non-myoblast cell populations remain present following the small-molecule myogenic induction. The process of seeding of hPDMs on electrospun fibers in addition to their expansion over the 10 day culture period may exacerbate differences in the heterogeneous population in several ways. First, a fibroblast-like subpopulation would have faster adhesion capabilities than myogenic precursors

and may adhere to the scaffold during seeding at a higher rate. The proportion of fibroblast-like cells to myogenic precursors in the starting population as well as inherent variability in the seeding process would thus lead to significant batch to batch variability in ultimate myogenic potential. It is also possible that hPDMs contain non-myoblasts subpopulations with an increased expansion rate and affinity for expansion on a soft hydrogel substrate compared to myogenic precursors. The observed variability myogenic potential between batches of unsorted hPDMs motivated the use of Pax7-sorted cells in subsequent experiments.

Sorting hPDMs for the Pax7::GFP+ subpopulation prior to expansion resulted in a higher myogenic potential in monolayer cultures and significant myogenesis on electrospun fibers. Some batch to batch variability was still observed following seeding onto 3D constructs which may be due to de-differentiation of some Pax7+ cells during expansion and subsequent variability in myogenic potential. Significantly, over 40% of cells remained Pax7+ at day 3 of culture on electrospun fibers. Pax7-sorted hPDM constructs matured over time demonstrating a decrease in Pax7 expression and subsequent increase in expression of mature muscle markers, multinucleation, and contractile proteins with visible sarcomeric striations. This is similar to the level of maturation seen in *in vitro* hPSC-derived 3D muscle constructs published previously.

Unsorted hPDM constructs were implanted in a murine VML defect to the TA muscle to evaluate cell survival in the harsh non-regenerative injury environment typical of VML. Similar levels of cell survival were seen 2 weeks post-implantation between induced and uninduced hPDM constructs. This result is not surprising given the similarity in DAPI coverage between the implanted *in vitro* induced and uninduced hPDM constructs. Although no muscle regeneration was seen, the implanted constructs of this batch had very little MHC coverage at the time point of implantation demonstrating the likely significant presence of a non-myogenic cells within the

hPDM population. To evaluate engraftment potential of Pax7-sorted hPDM constructs, a less damaging sub-critical muscle defect was utilized with approximately 75% less muscle removed than the previous VML defects. Interestingly, despite survival of unsorted hPDMs in the harsh VML environment up to 2 weeks post-implantation, the implanted Pax7-sorted hPDM constructs only survived up to 1 week post-implantation in a less severe defect model. This indicates a potential protective effect of the unsorted hPDMs. Previous reports have demonstrated that implantation of satellite cells along with non-muscle supporting cell types into a muscle defect results in improved regenerative potential compared to implantation of satellite cells alone[21]. It is possible that sorting hPDMs for the Pax7+ subpopulation negatively impacts their engraftment potential despite improving *in vitro* myogenic outcomes.

Despite the presence of dense Pax7-sorted hPDMs and blood vessels within the defect region 1 week post-implantation, there remained little evidence of muscle regeneration due to the implanted muscle constructs. Previous experiments implanting hPDMs into cardiotoxin-injured muscle resulted in successful engraftment and fusion with host myofibers[80]. Due to measured differences in the expression of early and late muscle proteins during *in vitro* culture of hPDMs on electrospun fibers, we hypothesized that implantation of hPDM constructs with a higher proportion of satellite cells at day 3 of culture would more closely approximate the engraftment potential of recently expanded hPDMs seen previously. To account for differences in hPDM myogenic potential due to low seeding efficiency on electrospun fibers, hPDMs seeded within a bulk fibrin hydrogel on the day of implantation were included as a control. Following 1 week of implantation in sub-critical defects, hPDMs seeded on electrospun fibers at both time points demonstrated significantly improved defect volume retention compared to the implanted bulk gels. Promising preliminary data indicates the presence of myotube-like structures with human

nuclei within the defect regions of all implantation groups. It appears that day 3 hPDM constructs contained a higher proportion of myotube-like structures and further quantification is necessary to identify differences between treatment groups. In addition, eMHC+ regenerating myofibers containing human nuclear LaminAC were present within and surrounding the defect regions of all treatment groups. Quantification of eMHC+LaminAC+ co-expression will determine if there was a treatment group that promoted improved engraftment and *in vivo* myogenesis of implanted hPDMS.

Future work on this study will include immunostaining for macrophage and neutrophil markers to determine if there is a correlation between hPDM survival and any immune response by the host. Despite the use of immunodeficient mice, preliminary data has shown a broad macrophage presence within and surrounding the defect region. It is likely that persistent inflammation in the injury environment negatively effects hPDM survival. In addition, flow cytometry will be used to determine the various non-muscle subpopulations present within unsorted and Pax7-sorted hPDMs that may contribute to differences in *in vitro* myogenic potential and survival following implantation. Further immunostaining and quantification of protein expression of the *in vivo* data will also be utilized to identify the various cell types present within the defect region of different treatment groups as there is a significant amount of DAPI staining not correlated with an immunostain utilized thus far. In conclusion, Pax7-sorted hPDM constructs have significant *in vitro* myogenic potential and survive one week post-implantation in muscle defects with little regeneration. Further characterization and optimization of the Pax7-sorted hPDM constructs may improve its regenerative outcomes and enable the development of a fully translational engineered muscle construct.

Chapter 5 Pre-Treatment of *In Vitro* Muscle Constructs to Promote Neuromuscular Regeneration Post-VML

5.1 Introduction

Volumetric muscle loss (VML) is a defect that overwhelms skeletal muscle's natural repair mechanisms and leads to chronic functional deficits [146,195]. Current treatments are often unsuccessful in restoring muscle function and are limited by donor site morbidity, lack of donor tissue, and the need for highly skilled surgical teams [36]. It was recently demonstrated that VML causes significant motoneuron axotomy and lost interaction between neurons and the injured skeletal muscle, a probable cause for the heightened levels of lost muscle function seen post-VML [17]. Tissue engineered grafts have great potential to create clinical treatment options for regeneration of VML but previous approaches to regenerate the injured muscle remain limited in their ability to encourage neuromuscular regeneration within the healing tissue. Engineered muscle constructs that incorporate methods to encourage neural infiltration and the formation of functional NMJs post-VML provide promising avenues to restore interaction between the muscle and nerve.

Prior strategies to promote neuromuscular regeneration post-VML have included neurotization [50,86], the use of rehabilitative exercise [21,46,84,121], and implantation of a pre-innervated construct [196], and have resulted in some increased neural infiltration, force recovery, and neuromuscular junction (NMJ) formation within and around the defect site. Despite incremental neuromuscular regeneration, the nerve and NMJ densities within the defects remain low and the newly formed NMJs exhibit immature morphologies. In addition, there has been little effort to quantify neuromuscular regeneration across the entire defect area, instead relying on

subsets of the defect region at high magnifications that do not accurately represent variability in expression across the defect region. In native tissues, the mature NMJ contains densely clustered postsynaptic acetylcholine receptors (AChR) optimized for efficient signal transfer across the neuromuscular synapse and effective muscle contraction [117]. Agrin, a large heparan sulfate proteoglycan secreted by the nerve terminal, is vital for acetylcholine receptor (AChR) cluster stabilization during embryonic development [114] and has been utilized extensively to induce AChR clustering in cultured myotubes [130–138]. Muscle constructs containing agrin physically mixed into a fibrin hydrogel and seeded with C2C12 myoblasts were implanted subcutaneously in a non-VML defect near the peroneal nerve for 8 weeks and resulted in increased nerve infiltration, NMJ formation, and vascular infiltration [130], demonstrating the potential neuromuscular therapeutic benefits of scaffold-mediated agrin delivery *in vivo*. In this study, we resolved to test whether the delivery of soluble or chemically-tethered agrin could promote improved NMJ regeneration in the treatment of VML defects.

Although release of bioactive molecules from engineered constructs has been utilized in VML treatment to promote vascular infiltration [24,33,88,106] and myogenesis [24,88,89], there have been no previously published constructs that have incorporated pharmacologic factors specific to neuromuscular regeneration for VML treatment. In addition, prior VML treatments with scaffold-mediated delivery of bioactive molecules have utilized physical entrapment or passive adsorption to the scaffold prior to implantation, which rely on diffusion of the bioactive agent to the surrounding tissues [52]. In contrast, scaffolds incorporating immobilized bioactive agents offer the ability to control spatiotemporal presentation and local signaling to the regenerating tissue, avoid poor targeting efficiency, and extend factor bioactivity over time following implantation [197–199]. Our group has previously utilized electrospun fibrin microfiber bundles that mimic the native

properties of skeletal muscle combined with C2C12 myoblasts to promote functional and histological regeneration post-VML [25]. In the current study we have enhanced our *in vitro* muscle constructs to promote neuromuscular regeneration in VML defects through the delivery of agrin. Therefore, in this current study, we tested the hypothesis that immobilized agrin tethered to the surface of C2C12-seeded microfiber bundles would maintain its *in vitro* bioactivity and induce AChR clustering in myotubes cultured on the 3D constructs. In addition, we tested the ability of tethered agrin constructs implanted in a murine VML defect model to improve neuromuscular regeneration at 4 weeks compared to constructs pre-treated with soluble or zero agrin.

5.2 Materials and Methods

Electrospinning Fibrin Scaffolds

Fibrin scaffolds were electrospun in a sterile environment with sterile solutions as previously described [25,77]. Parallel syringes containing solutions of fibrinogen (Sigma) or sodium alginate (Sigma) were connected via a y-syringe and extruded by syringe pumps with an applied voltage of 3-5 kV applied to a 27G needle tip utilizing 1% fibrinogen with an extrusion rate of 4 ml/hr and 0.75% alginate with an extrusion rate of 1 ml/hr. Polyethylene oxide (average Mv ~ 4 000 kDa, Sigma) was added to each solution at 0.2 wt% to increase viscosity during electrospinning. The electrospun hydrogel solutions were collected for 5.75 minutes on a rotating dish (~35rpm) containing 50 mM $CaCl_2$ and 20 U/ml thrombin (Sigma) as crosslinking agents. Samples were allowed to crosslink and additional 3-5 min after electrospinning and were then wrapped around a 1.5 × 1.5 cm acrylonitrile-butadiene-styrene frame 4 times to yield a hydrogel microfiber bundle ~700 μm in diameter. Scaffolds were incubated overnight in 250 mM sodium citrate (Sigma) to dissolve the alginate and then transferred to DI water for storage up to 2 weeks.

Protein Tethering to Scaffolds

Scaffolds with tethered proteins underwent the following tethering protocol one day prior to cell seeding. All incubation steps were performed at room temperature. Activation Buffer was prepared using 0.1M 4-Morpholineethanesulfonic acid (MES; Sigma) and 0.5M sodium chloride (Sigma) and adjusted to have pH 5-6. N-Ethyl-N′-(3-dimethylaminopropyl)carbodiimide hydrochloride (EDC; Sigma) and N-hydroxysuccinimide (SNHS; ThermoFisher Scientific) were dissolved at 10 mg/ml in Activation Buffer immediately prior to use. Agrin (R&D Systems) or Cy3 was diluted to 2, 10, 50, or 100 µg/ml (0.08, 0.4, 2, 4 µg/fiber) in sterile PBS with pH 7.2-7.5. Scaffolds were incubated with Activation Buffer on a rocker at 100 rpm for two 30 min washes then transferred to EDC/SNHS Buffer on a rocker at 120 rpm for 15 min. Scaffolds were then transferred to custom small-volume molds designed to suspend the scaffolds within 40 µl of agrin or Cy3 on a rocker at 80 rpm for 3 hours. Scaffolds were then washed with DI water for two 20 min washes and stored in fresh DI water overnight.

Cell Culture and Seeding on Scaffolds

C2C12 myoblasts were expanded in C2C12 Growth Medium: high-glucose DMEM (Invitrogen), 10% fetal bovine serum (FBS; Atlanta Biologicals), and 1% penicillin/streptomycin (P/S; Invitrogen) and used for experiments at passage 8. In preparation for cell seeding, scaffolds were incubated in high glucose DMEM for 20 min at 37 °C. The scaffolds were then transferred to 6-well cell culture plates coated with 2% agarose type VII (Sigma) to minimize cell adhesion to the plate surface, which increases the seeding efficiency. For all experiments, a total seeding volume of 40 µl at 7,500 cells/µl was pipetted onto the scaffold surface in a series of 5 µl droplets (for a total seeding density of 300,000 cells/scaffold). Scaffolds were incubated for 1 hour at 37°C with hydration levels maintained by addition of 15 µl of C2C12 Growth Medium at 30 minutes. After the 1-hour incubation, 3 ml of C2C12 Growth Medium containing 30 µg/ml aprotinin

(Affymetrix) was added to each well and care was taken to ensure the scaffolds had been submerged in the media. On day 3 of culture myoblasts were transferred to C2C12 Induction Medium: high-glucose DMEM, 2% horse serum (ThermoFisher Scientific), 1% P/S, 1% insulin-tranferrin-selenium (ITS; Corning Cellgro), and 30 μg/ml aprotinin and media was changed every other day. Constructs with zero agrin or tethered agrin remained in C2C12 Induction Medium for the extent of in vitro culture. For soluble agrin constructs, recombinant rat agrin protein (agrin; R&D Systems) was added to C212 Induction Medium at 5 or 50 ng/ml at day 6 of culture and replenished at day 7 of culture. Zero agrin and tethered agrin constructs were used for experiments on day 7 of culture while soluble agrin constructs were used for experiments at day 8 of culture.

Agrin Release Kinetics

Scaffolds were electrospun and underwent agrin tethering with 50 μg/ml agrin as described above. Control scaffolds with untethered agrin were fabricated by incubating scaffolds in small-volume molds containing 50 μg/ml agrin for 3 hours without the prior Activation Buffer and EDC/SNHS incubation steps. Immediately following the agrin incubation, all scaffolds were rinsed once in 1 ml of 1% BSA in PBS (Reagent Diluent Buffer; R&D Systems) which was collected and stored at -20°C. Scaffolds were then incubated in fresh buffer at 37°C. Excess residual agrin remaining within the small-volume molds following scaffold removal from the molds was also collected in buffer and stored at -20°C. At 1, 4, and 7 days post-tethering the buffer was removed, replaced with fresh buffer, and stored at -20°C. Control wells that served as a 100% release control contained 50 μg/ml agrin in 1 ml of buffer and were incubated at 37°C with 100 μl samples collected at days 1, 4, and 7. Agrin concentration for all samples was analyzed via ELISA (DuoSet ELISA for Rat Agrin, DY550; R&D Systems) with optical density determined using a microplate reader set to 450 nm.

In Vitro Mechanical Testing

Scaffolds that were either untreated or pre-treated with EDC/SNHS buffer as described above were loaded into a custom bioreactor and stiffness analyzed as described previously [152,200]. Briefly, scaffolds were adjusted to zero strain, then stretched beyond 15% strain at ~1% strain/s as force sensors generated a stress-strain curve. Elastic modulus was calculated from a linear fit of the first 15% strain and corresponding stress. Diameter of the fibers was used to estimate the cross-sectional area for stress calculation and was measured as an average of the diameter of two different regions of each fiber due to variability along the fiber length.

Whole Mount Immunostaining

Scaffolds were fixed in 4% formaldehyde at 4°C on a rocker at 80 rpm for 3 hours. Following 3 washes with PBS, scaffolds were blocked and permeabilized (Block/Perm Solution) for 3 hours with 0.2% Triton X-100, 10% normal goat serum (Sigma), and 2% bovine serum albumin (BSA; Sigma) in PBS. Scaffolds were then incubated with mouse anti-myosin heavy chain, fast (1:400; Sigma) diluted in Block/Perm Solution overnight at 4°C on a rocker at 135 rpm, followed by three 1-hour washes with PBS. Scaffolds were then incubated with DyLight 488-conjugated goat anti-mouse (1:400; Jackson ImmunoResearch) and tetramethylrhodamine α-bungarotoxin (1:50; Thermo Fisher) diluted in 10% normal goat serum, 2% BSA, and 0.1% Tween in PBS overnight at 4 °C on a rocker at 135 rpm, followed by three 1 hour washes with PBS. DAPI was incorporated in the second wash at a dilution of 1:2000. Samples were then imaged with a Zeiss LSM 510 confocal microscope. All *in vitro* staining was performed with n=3 samples per group and imaged with at least two 20x z-stack images per sample. To quantify AChR clusters, bungarotoxin stains were analyzed using Fiji software [201] with a size threshold of 3-225 μm^2. Cluster density was determined as the total area of positive bungarotoxin staining divided by the

total area of MHC. Cluster spatial location was determined by quantifying the percent area coverage of each slice within a z-stack image using a size threshold of 3-225 μm^2 and determining the distance above the scaffold with the Fiji Plot Z-axis Profile plugin.

VML Defect Model

Animal and surgical procedures were approved by the Institutional Animal Care and Use Committee at Johns Hopkins University School of Medicine. Unilateral VML defects in 17 two-month-old female NOD-scid IL2Rg^{null} (NSG) immunodeficient mice (Jackson Lab) were utilized for in vivo testing of zero agrin (n=3 mice), soluble agrin (n=7 mice), and tethered agrin (n=7 mice) constructs. Mice were randomly assigned across all groups. In vitro constructs were prepared and cultured with C2C12s as described above. VML defects were created as previously described[25]. Mice were anesthetized with isofluorane, the TA muscle was exposed, and approximately 30-50% of the muscle removed. After bleeding ceased, scaffolds were placed in the defect site and ligated on both ends to the remaining TA muscle with non-absorbable sutures (6-0 Nylon, Express Medical Supplies). Surgical glue (Histoacryl, B. Braun) and sutures were used to close the skin. Rimadyl was injected subcutaneously post-surgery for pain management (5 mg/kg). Mice were sacrificed at 4 weeks post-implantation by isoflurane overdose and cervical dislocation. Upon harvest, implanted scaffolds and surrounding TA muscle tissue were removed and cryopreserved.

In Vivo Functional Testing

In vivo assessment of mouse TA muscle contractility was performed at 4 weeks as previously described [25,154]. Briefly, mice were anesthetized with isoflurane and the leg was stabilized in a custom-made apparatus. The foot was taped to a foot plate connected to a torque sensor and stepper motor and the ankle was positioned at 20° of plantarflexion, which has been

shown to be the optimum length to achieve maximum ankle dorsiflexor torque (in which the TA muscle accounts for the majority of ankle dorsiflexion). Electrodes were placed subcutaneously at the fibular head to stimulate the fibular nerve and induce dorsiflexion. Voltage and frequency were optimized for each leg during tetanic contractions (300 ms duration) and the maximal isometric torque was quantified per leg at each time point (n=7). Functional data for zero agrin (n=7) and untreated (n=6) groups is from previously published results [25].

Histology

Samples were sectioned on a cryostat (Leica) at a thickness of 10 μm for cross-sections and 70 μm for longitudinal sections. Masson's Trichrome stains were imaged on a Zeiss Axio Imager upright microscope. For immunohistochemistry, slides were fixed in cold 4% formaldehyde for 10 min and rinsed with PBS three times for 15 min each, then blocked in 10% normal donkey or goat serum (Sigma) in PBS for 1 hour at RT. For β tubulin III staining, slides were blocked in 10% normal donkey serum, 2% BSA, and 0.2% Triton X-100 in PBS for 3 hours at RT. For agrin staining, slides were fixed in a 1:1 mixture of ice-cold acetone and methanol for 10 min, rinsed with PBS, then blocked in 5% normal donkey serum and 5% BSA in PBS for 1 hour at RT. For YAP staining, slides were quenched in 50 mM ammonium chloride for 5 min at RT prior to blocking in 10% donkey serum and 1% BSA in PBS for 2 hours at RT. Slides were incubated with antigen-specific primary antibodies in blocking solution overnight at 4°C. Primary antibodies included mouse anti-embryonic myosin (5 μg/ml; DSHB), mouse anti-myosin heavy chain (fast-twitch) (1:400; Sigma Aldrich), goat anti-mouse CD31 (1:100; R&D Systems), rabbit anti-β tubulin III (1:200; Sigma), mouse anti-Pax7 (5 μg/ml; DSHB), rabbit anti-Ki67 (1:1000; Abcam), and rabbit anti-YAP (1:100; Cell Signaling Technology). After three 5 min washes with PBS, slides were incubated with Cy3-conjugated donkey anti-mouse, Alexa Fluor 488-conjugated

donkey anti-goat, DyLight 488-conjugated goat anti-mouse, or Alexa Fluor 647-conjugated donkey anti-rabbit (1:400; Jackson ImmunoResearch) and DAPI (1:2000) diluted in blocking solution for 1 hour at RT. Slides staining for α-bungarotoxin (1:50; Thermo Fisher) or phalloidin-TRITC (1:40; Sigma) incorporated the stains into the secondary antibody stain. Slides were washed three times for 5 min then mounted with 50% glycerol and imaged on a Zeiss Axio Observer inverted fluorescence microscope or Zeiss Axio Observer 7. To quantify staining within the defect regions, tiled images covering the entire defect region were taken on a Zeiss Axio Observer 7 with a 20x objective. An AChR cluster was determined to be within an NMJ when the area of positive bungarotoxin staining was within 2 μm of an area with positive β-tubulin III staining.

Statistics

Statistical analysis was performed using GraphPad Prism 5 software. Statistical significance was determined by t test or one-way ANOVA with Dunnett or Bonferroni post-test. Error bars represent standard error of the mean (SE). *: $p < 0.05$; **: $p < 0.01$; ***: $p < 0.001$; ǂ: not significant

5.3 Results

AChR Cluster 3D Spatial Distribution is Determined by Agrin Delivery Method

Electrospun fibrin hydrogels designed to mimic the hierarchical structure and alignment of skeletal muscle were fabricated as previously described [25,77]. A protocol to chemically tether proteins to the electrospun fibrin scaffolds using the EDC zero-length crosslinker was initially developed and validated using a fluorescent Cy3 antibody which has a similar size to agrin (**Fig.**

5.1A). Agrin was chemically tethered to acellular scaffolds at 0.08-2 μg/scaffold prior to seeding with C2C12 myoblasts, after which C2C12-seeded constructs were cultured for 7 days (**Fig. 5.2A**). Tethered agrin constructs exhibited significantly higher mechanical stiffness than controls lacking the EDC crosslinker (**Fig. 5.1B**), likely due to increased crosslinking of the fibrin scaffold by EDC which is visible in scaffold cross-sections (**Fig. 5.2B**). Soluble agrin was tested in parallel and was delivered to muscle constructs at 10 or 100 ng/scaffold for 24 or 48 hours at days 6-8 of culture. Both soluble and tethered agrin induced some amount of AChR clustering in myotubes on 3D constructs at all concentrations, with differences in cluster density dependent on duration and concentration (**Fig. 5.3A-C**). To control for nonspecific adsorption of agrin to the scaffold, untethered control scaffolds were fabricated by incubation with agrin at 2 μg/scaffold without the addition of the EDC crosslinker. Despite evidence of some agrin binding, the bioactivity of scaffolds with untethered agrin was significantly lower than those with agrin tethered at the same concentration (**Fig. 5.3C-E**). Tethered agrin at 2 μg/scaffold and soluble agrin at 10 ng/scaffold for 48 hours had the highest cluster densities while still retaining normal myotube morphology and were selected for subsequent experiments. Few AChR clusters were visible in day 7 muscle constructs with no agrin, and both soluble and tethered agrin resulted in myotubes with significantly higher AChR cluster density, area, and length than zero agrin controls (**Fig. 5.2C-F**). Interestingly, tethered and soluble agrin resulted in significant differences in the spatial location of AChR clusters when analyzed in 3D using confocal imaging. Clusters induced by tethered agrin were primarily located about 10 μm from the scaffold surface while clusters induced by soluble agrin were visible throughout the myotube layer with two similar peaks in cluster density at about 10 and 30 μm from the scaffold surface (**Fig. 5.2G**). Localization of clusters to the scaffold side

of myotubes in the tethered agrin group was visible in immunostained cross-sections as well (**Fig. 5.2H**).

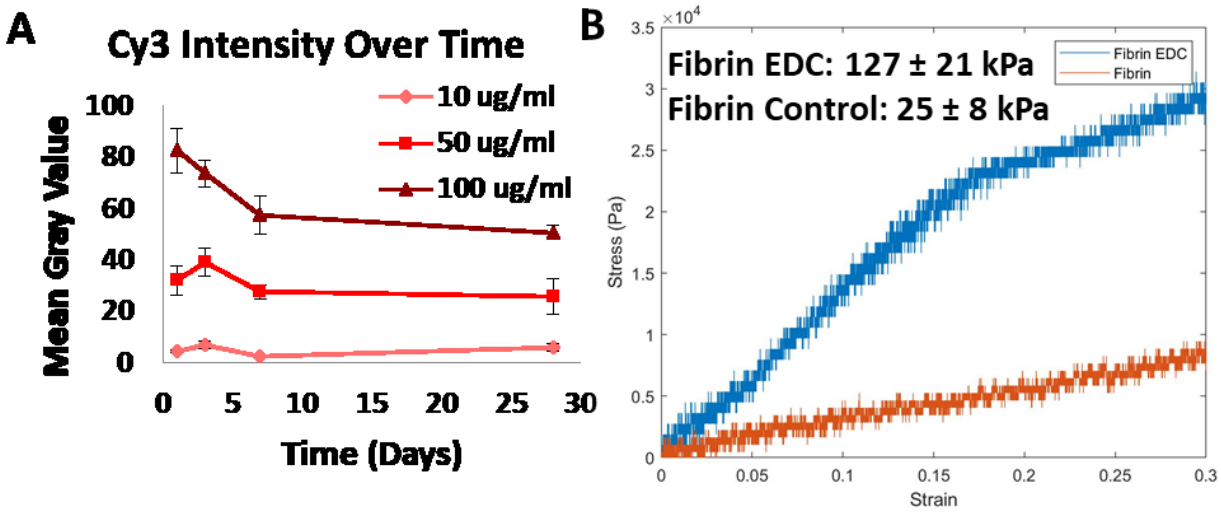

Figure 5.1. Protein tethering to scaffolds and mechanical testing. A) Fluorescence intensity over time for Cy3 tethered scaffolds at various concentrations. **B)** Mechanical testing demonstrating a five-fold increase in scaffold stiffness due to the tethering protocol.

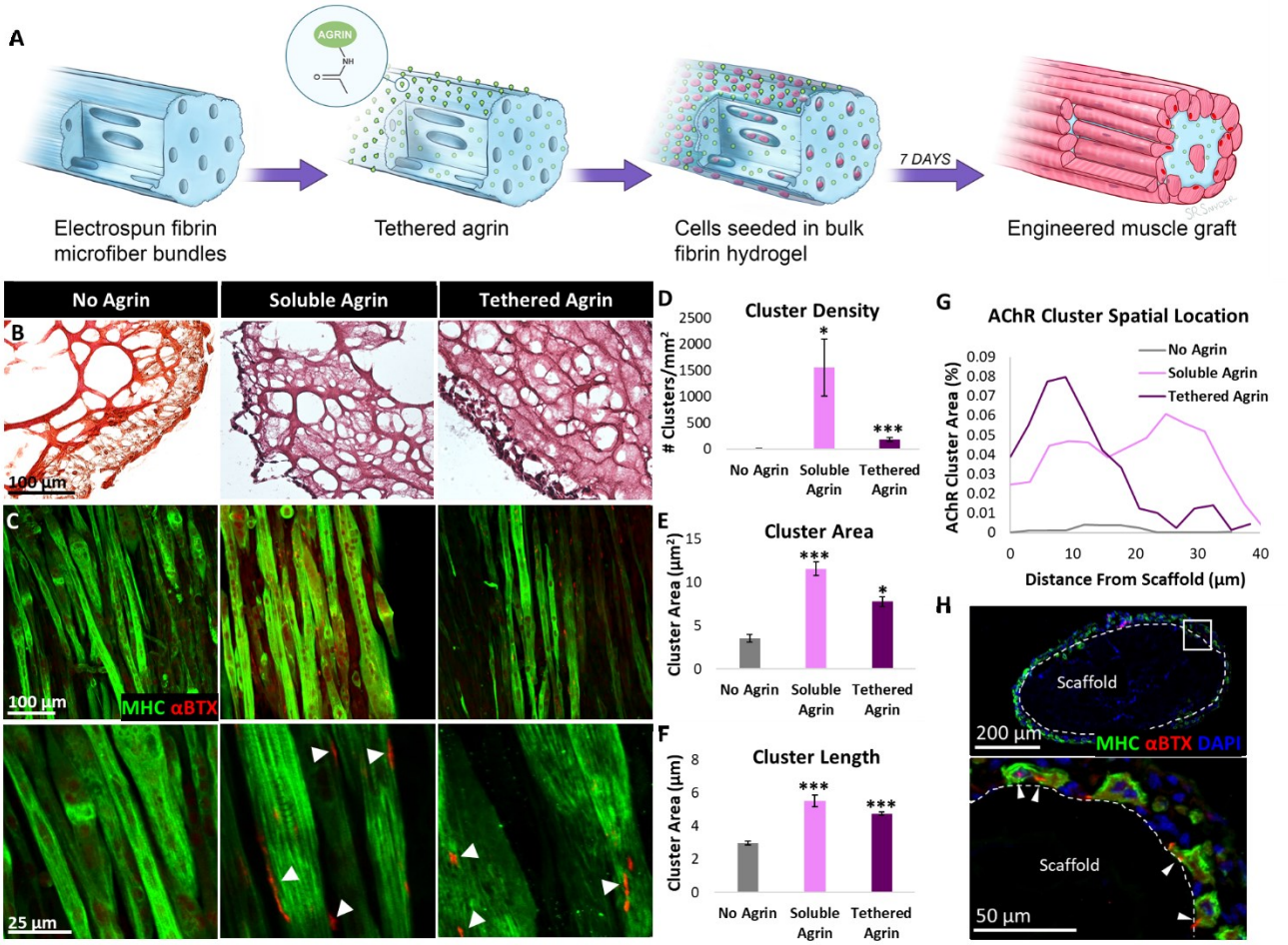

Figure 5.2. Soluble and tethered agrin induce increased acetylcholine receptor clustering with spatial effects in 3D muscle constructs. A) Schematic illustrating agrin tethering and cell seeding on electrospun fibrin microfiber bundles. **B)** Masson's Trichrome stain of cell-seeded scaffold cross-sections demonstrating differences in crosslinking density in tethered agrin scaffolds. **C)** Aligned myotubes positive for myosin heavy chain (MHC; green) in all groups exhibit AChR clusters positive for α-bungarotoxin (αBTX; red) in agrin treatment groups. **D)** Density of AChR clusters is significantly increased in agrin treatment groups. **E,F)** The area and length of individual AChR clusters in agrin treatments groups was significantly higher than clusters in constructs with no agrin. **G)** The spatial location of AChR clusters differed significantly between groups: tethered agrin induced clusters close to the scaffold surface while soluble agrin induced AChR clusters independent of distance from the scaffold surface. **H)** Cross-section of cell-seeded tethered agrin scaffold immunostained for MHC and αBTX demonstrating the spatial location of AChR clusters at the scaffold surface. *: $p < 0.05$; ***: $p < 0.001$

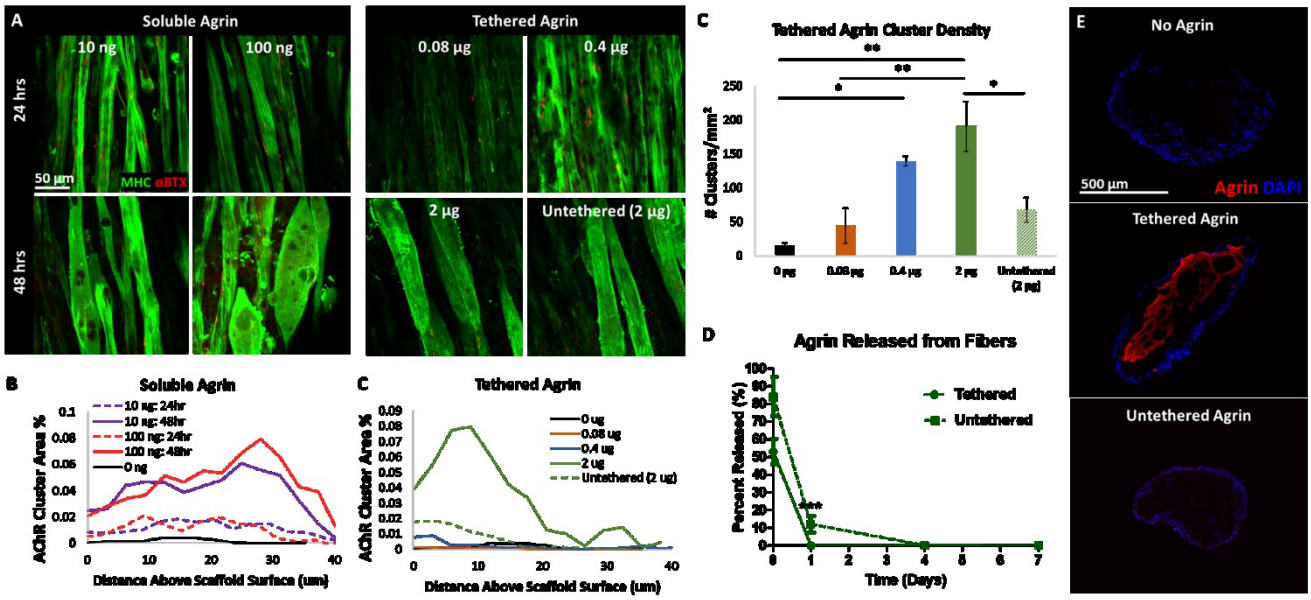

Figure 5.3. Tethering preserves in vitro bioactivity of agrin. A) Aligned myotubes positive for myosin heavy chain (MHC; green) exhibit AChR clusters positive for α-bungarotoxin (αBTX; red) in agrin treatment groups at differing concentrations and time points of application. **B,C)** The spatial location of AChR clusters differed significantly between groups for both soluble and tethered agrin. **D)** AChR cluster density varied between tethered agrin concentrations. At the highest 2 µg concentration, tethered agrin resulted in significantly higher cluster density than untethered agrin. **E)** Cross-sections of cell-seeded scaffolds immunostained for agrin demonstrate the presence of agrin (red) through the scaffold interior in tethered agrin groups while zero agrin and untethered agrin have little to no positive agrin staining. *: $p < 0.05$; **: $p < 0.01$

Agrin Pre-Treatment did not Improve Muscle Function in VML Defects

At 4 weeks post-implantation in VML defects all treatment groups exhibited a healthy morphology with no signs of infection or graft rejection. Gross images revealed that defects treated with tethered agrin contained scaffolds that were significantly more visible within the tissue than other groups (**Fig. 5.4A**). Masson's Trichrome staining of histologic sections demonstrated low levels of fibrosis and defect volume retention in all groups. Defects treated with soluble agrin contained dense muscle tissue similar to zero agrin controls (and previous observations [25]) while defects treated with tethered agrin resulted in dense muscle tissue containing distinct regions with persistent scaffold material and little visible regenerating muscle (**Fig. 5.4B**). Immunostaining for

agrin demonstrated visibly higher levels of agrin on all four implanted scaffolds in the tethered agrin treatment group when compared to soluble or zero agrin, demonstrating that tethering agrin to the scaffold surface causes persistent agrin presentation to surrounding tissues up to four weeks post-implantation (**Fig. 5.5**). Explanted muscles treated with tethered agrin had a higher wet weight and significantly higher defect cross-sectional area compared to soluble and zero agrin (**Fig. 5.4C,D**). Despite these differences in histology and size for the tethered agrin group, there was no difference in either maximum torque or the force-frequency relationship between groups (**Fig. 5.4E,F**).

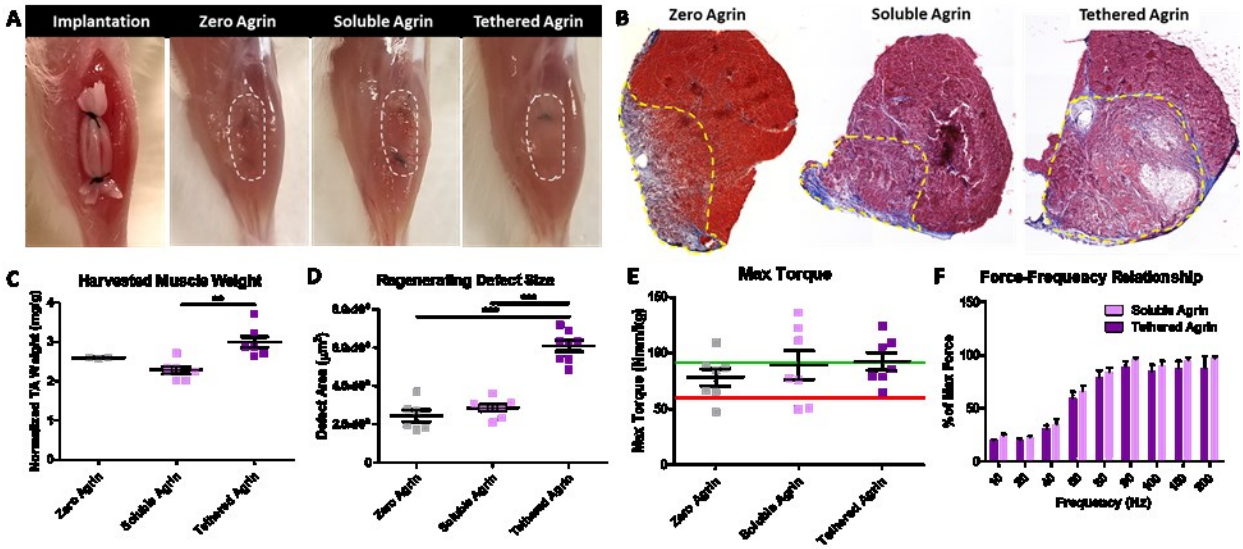

Figure 5.4. Muscle function following VML defects improved equally in no agrin and agrin-treated groups. A) Gross morphology at scaffold implantation and 4 weeks post-implantation for zero, soluble, and tethered agrin constructs. **B)** Cross-sections of the explanted tibialis anterior muscle stained for Masson's Trichrome demonstrate differences in defect area (yellow dashed line) and morphology between groups. **C,D)** Differences were present between groups in the harvested TA weight and defect size in cross-section. **E,F)** No difference in muscle function was seen between treatment groups. Green line: average max torque of age-matched uninjured TA muscle; Red line: average max torque of untreated VML defects at 4 weeks post-injury. All treatment groups were statistically similar to uninjured values. **: $p < 0.01$; ***: $p < 0.001$

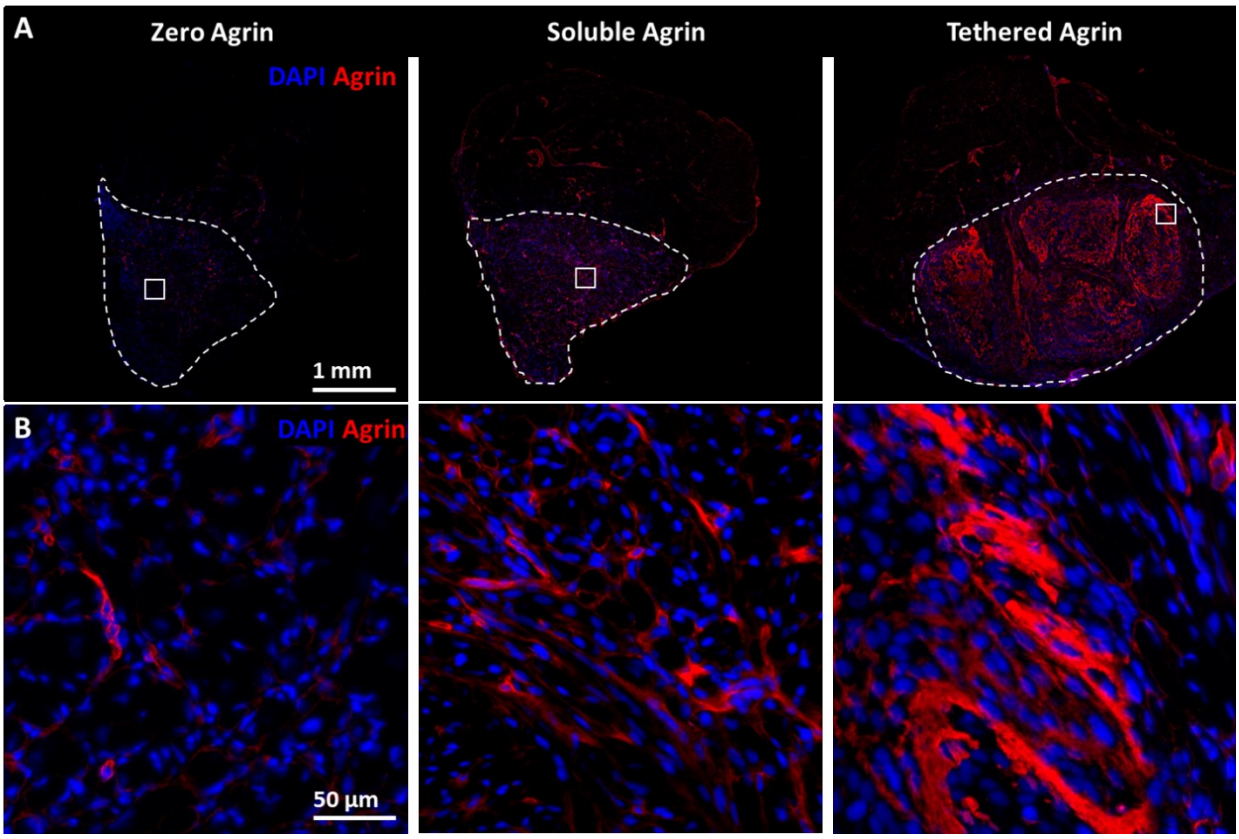

Figure 5.5. Agrin remains in VML defect up to 4 weeks post-implantation. A) Agrin was present within the defect region (white dashed line) at low levels in the zero and soluble agrin treatment groups. Defects treated with tethered agrin constructs contained persistent high levels of agrin visible as the four implanted scaffolds. **B)** High magnification images demonstrating differences in agrin distribution.

Agrin Pre-Treatment Increased NMJ Formation with Differences in NMJ Morphology

Immunostaining for myosin heavy chain (MHC) demonstrated densely packed myofibers in the defect regions for zero and soluble agrin while tethered agrin had dense MHC+ regions in addition to distinct areas lacking mature muscle (**Fig. 5.6A**). Tethered agrin treatment groups did contain higher total MHC area compared to zero agrin (**Fig. 5.6B**), although this is likely due to the increased defect size for tethered agrin as the myofiber density did not differ between tethered and zero agrin and was higher for soluble agrin compared to tethered agrin (**Fig. 5.7**).

Neurofilament and acetylcholine receptor clusters were visible within the defects of all groups with tethered agrin treatment groups containing more total nerves than zero agrin (**Fig. 5.6C**). Neuromuscular junctions defined as positive αBTX staining within 2 μm of a nerve were quantified and soluble agrin treatment groups had statistically more AChR clusters within a NMJ than zero agrin (**Fig. 5.6D**). Tethered agrin samples also had a higher average percent of AChR clusters within a NMJ compared to zero agrin but with increased variability between samples.

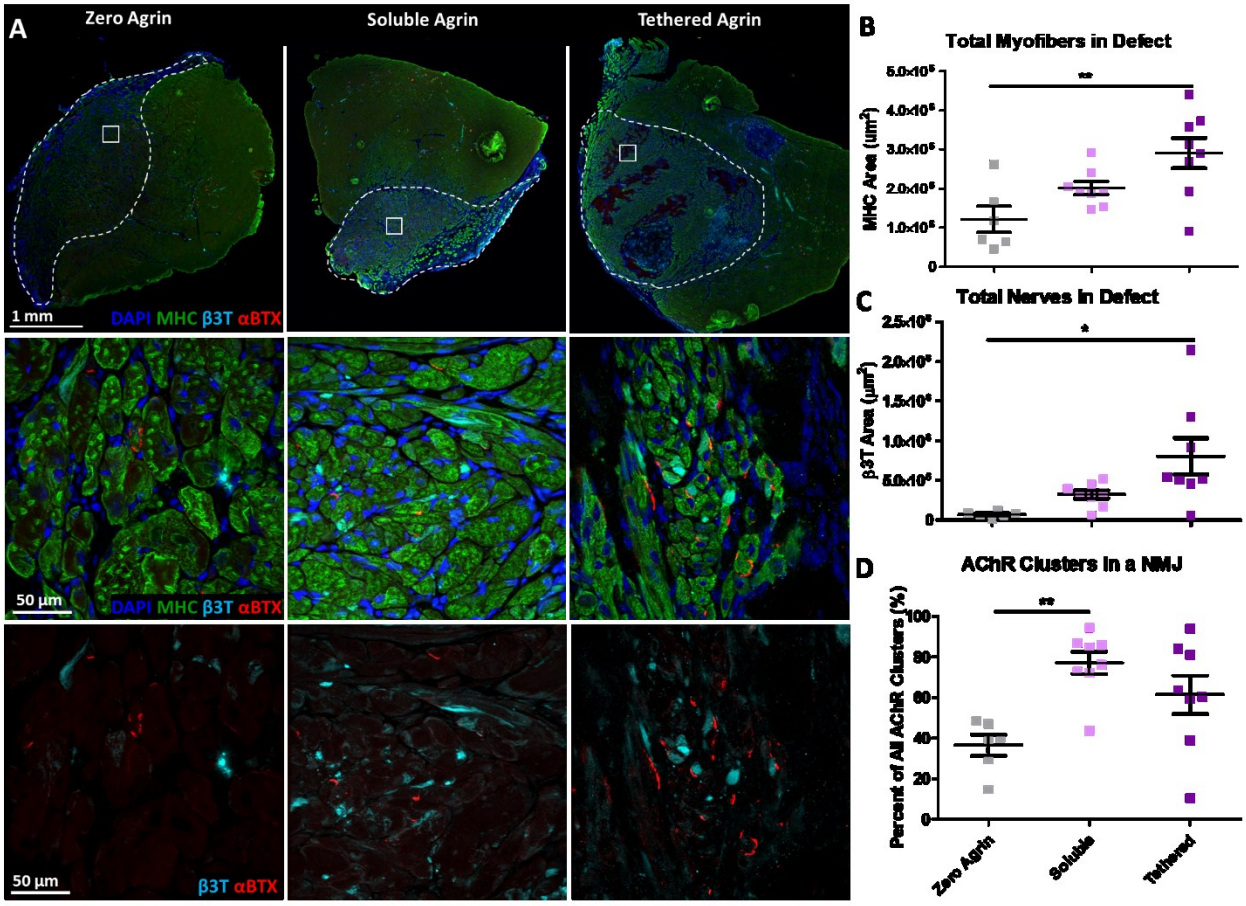

Figure 5.6. VML treatment with soluble and tethered agrin constructs increases NMJ formation in vivo. A) Cross-sections of explanted muscle stained for myosin heavy chain (MHC; green), neurofilament (β3T; cyan), and acetylcholine receptors (αBTX; red) with dense myotubes and NMJs within the defect area (white dashed line). **B)** Tethered agrin constructs resulted in more total myofibers within the defect region than other treatment groups. **C)** Tethered agrin constructs resulted in more total nerves in the defect region than other treatment groups. **D)** Both soluble and tethered agrin constructs resulted in higher percentages of AChR clusters within a NMJ than zero agrin. *: $p < 0.05$; **: $p < 0.01$

Due to the presence of some NMJs within the defect regions of all treatment groups, longitudinal sections were utilized to assess for differences in NMJ morphology within the defect that would otherwise not be visible in cross-section (**Fig. 5.7A**). NMJs for all VML treatment groups were smaller than those in native skeletal muscle and had a less mature morphology (**Fig. 5.7B**). Despite differences in size and shape, visible overlap between the AChR clusters and neurofilament was visible in the soluble and tethered agrin groups but not zero agrin (**Fig. 5.7C**). NMJs visible within defects treated with tethered agrin constructs had an immature plaque morphology while the soluble agrin group contained some NMJs with a more complex rounded architecture.

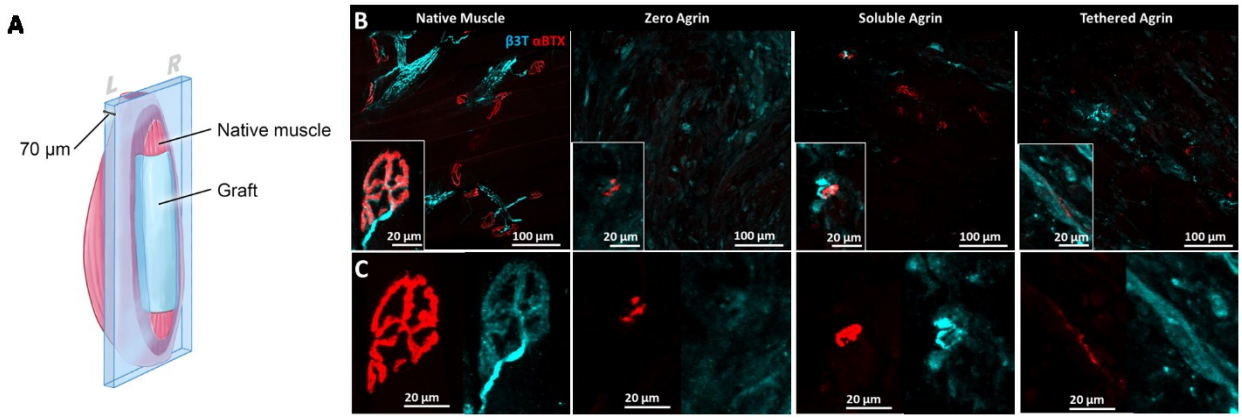

Figure 5.7. Soluble agrin constructs result in NMJs with a more mature morphology than zero and tethered agrin constructs. A) Thick longitudinal sections of explanted muscles enable visualization of NMJ morphology. **B)** Immunostaining of NMJs within native muscle and the defect regions of all treatment groups demonstrate positive staining for pre-synaptic neurofilament (β3T; cyan), and post-synaptic acetylcholine receptors (αBTX; red) with differences in morphology between groups. Inset: high magnification images of NMJs. **C)** High magnification images of NMJs showing degree of overlap between pre- and post-synaptic components.

Persistent Agrin within Implanted Tethered Agrin Constructs Causes Localized Neurofilament Clustering

Interesting patterns of protein expression were visible within the defect regions of the tethered agrin samples (**Fig. 5.8**). Overall, defect regions were highly positive for Pax7, CD31, and β3-tubulin compared to host muscle (**Fig. 5.8A,B**). Four regions of persistent undegraded scaffold were visible within the defect region that were primarily negative for mature muscle, as demonstrated above with Masson's Trichrome and MY32 staining. Topographical differences in protein expression were visible within undegraded scaffold regions compared to between the scaffolds. Expression of Pax7 was fairly consistent across the defect region both within the four implanted scaffolds and between scaffolds (**Fig. 5.8C,D**) while blood vessel infiltration into the defect region was primarily between the implanted scaffolds (**Fig. 5.8Aii,D)**. Overall, defect regions in tethered agrin groups contained higher total neurofilament as well as higher neurofilament density compared to other treatment groups.. Interestingly, undegraded scaffolds within the tethered agrin defect region were highly positive for the neurofilament stain β3-tubulin but not the areas between the scaffolds (**Fig. 5.8Aiii,C,D)**. It is likely that persistent presentation of agrin within these undegraded scaffold regions contributed to the differences in protein expression across the defect.

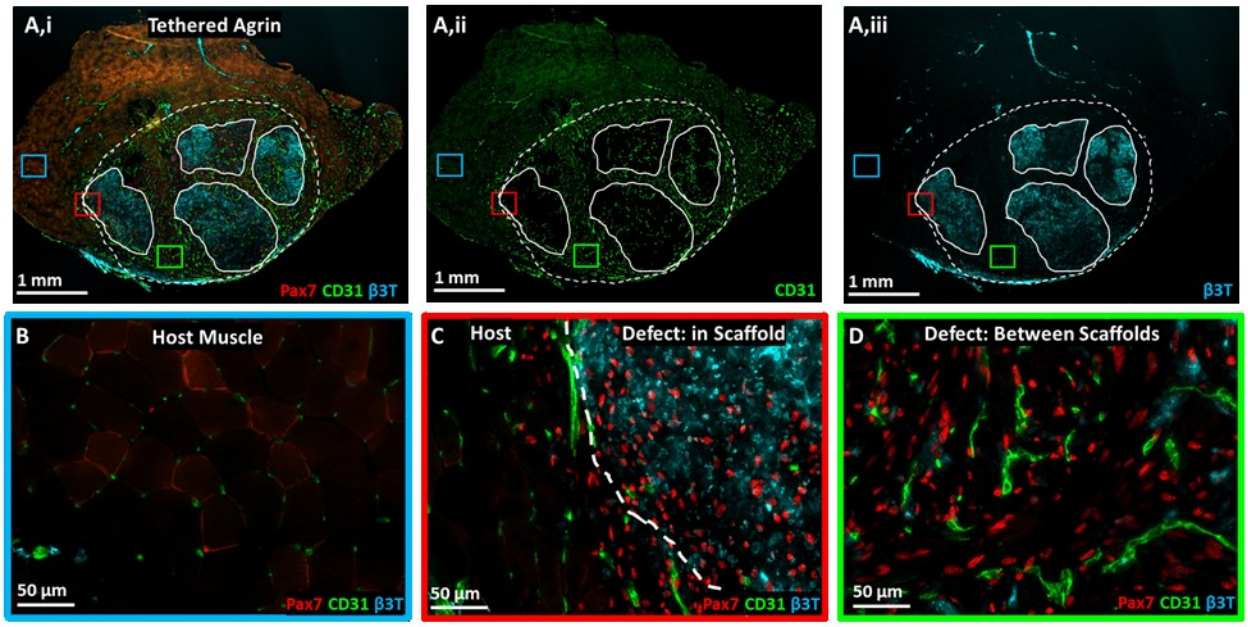

Figure 5.8. Satellite cell, vascular, and neural proteins were upregulated within and surrounding implanted tethered agrin constructs compared to host muscle. A) Low magnification image of TA cross-section treated with tethered agrin constructs and immunostained for (i) Pax7 (red), CD31 (green), and β3-tubulin (cyan), (ii) CD31 alone, or (iii) β3-tubulin alone. Dashed line: defect region; Solid lines: undegraded scaffold regions. Insets: three regions with corresponding high magnification images demonstrating variations in protein expression in host muscle (blue inset), at the host-defect border (red inset), and within the defect region but between implanted scaffolds (green inset). **B)** High magnification image of host muscle with low levels of Pax7, CD31, and β3T staining. **C)** High magnification image of the border between host muscle and an implanted tethered-agrin scaffold within the defect region. Increases in Pax7, CD31, and β3T expression are visible going into the defect region. **D)** High magnification image within the defect region but between implanted scaffolds. Pax7 and CD31 remain upregulated between scaffolds but β3T expression is decreased.

Tethered Agrin Resulted in Increased Blood Vessels and Regenerating Myofibers

VML treatment with soluble and tethered agrin resulted in significant differences in a range of regenerative metrics. Total expression of embryonic myosin (eMHC), a marker of regenerating myofibers, was significantly higher in defects treated with tethered agrin compared to zero or soluble agrin (**Fig. 5.9A,D**) and the density of eMHC expression differed significantly between

both agrin treatment groups and the zero agrin control as well as between soluble and tethered agrin, with tethered agrin resulting in the highest overall eMHC density (**Fig. 5.10**). Soluble and tethered agrin constructs also resulted in increases in total blood vessels within the defect region compared to zero agrin (**Fig. 5.9A,E**). Tethered agrin resulted in higher total blood vessel content compared to soluble agrin but when normalized to the defect area, soluble agrin groups contained a higher blood vessel density than tethered agrin groups (**Fig. 5.10**). Total expression of the satellite cell marker Pax7 also increased due to tethered agrin constructs (**Fig. 5.9B,F**) and dense satellite cells were visible even within undegraded scaffold regions of tethered agrin groups that did not contain MHC+ myofibers (**Fig. 5.9B**). Total cell content within the defect region was also significantly higher due to tethered agrin compared to both other treatment groups (**Fig 5.9C**). These results indicate that persistent agrin presentation in tethered agrin treatment groups within regenerating VML defects causes significantly higher levels of eMHC+ regenerating myofibers compared to soluble and zero agrin treatment groups. Tethered agrin also increased total cell content, blood vessel infiltration, and satellite cell presence within VML defects.

Due to the striking increase in both total eMHC+ myofibers and eMHC+ myofiber density within defects treated with tethered agrin compared to other treatment groups, we next evaluated co-expression of eMHC and nuclear YAP, a transcriptional coactivator with nuclear expression in its active form (**Fig. 5.11**). Defects treated with tethered agrin constructs resulted in significantly higher total nuclear YAP expression compared to those treated with zero and soluble agrin (**Fig. 5.11A,B**) while the density of nuclear YAP within defects was equal between groups (**Fig. 5.12A**). Both soluble and tethered agrin groups also had significantly higher total levels of cells co-expressing eMHC and nuclear YAP compared to zero agrin (**Fig. 5.11C**). Due to the high levels of Pax7+ cells within defect regions of all groups, we also evaluated co-expression of Pax7 and

the proliferation marker Ki67 (**Fig. 5.12B**). Although tethered agrin constructs resulted in significantly more Ki67 compared to soluble agrin, there was no difference in the level of Pax7 and Ki67 co-expression between groups. These data demonstrate that persistent agrin presentation within regenerating VML defects results in both higher total nuclear YAP expression and co-expression of eMHC+ regenerating myofibers with nuclear YAP, as well as increased overall cell proliferation.

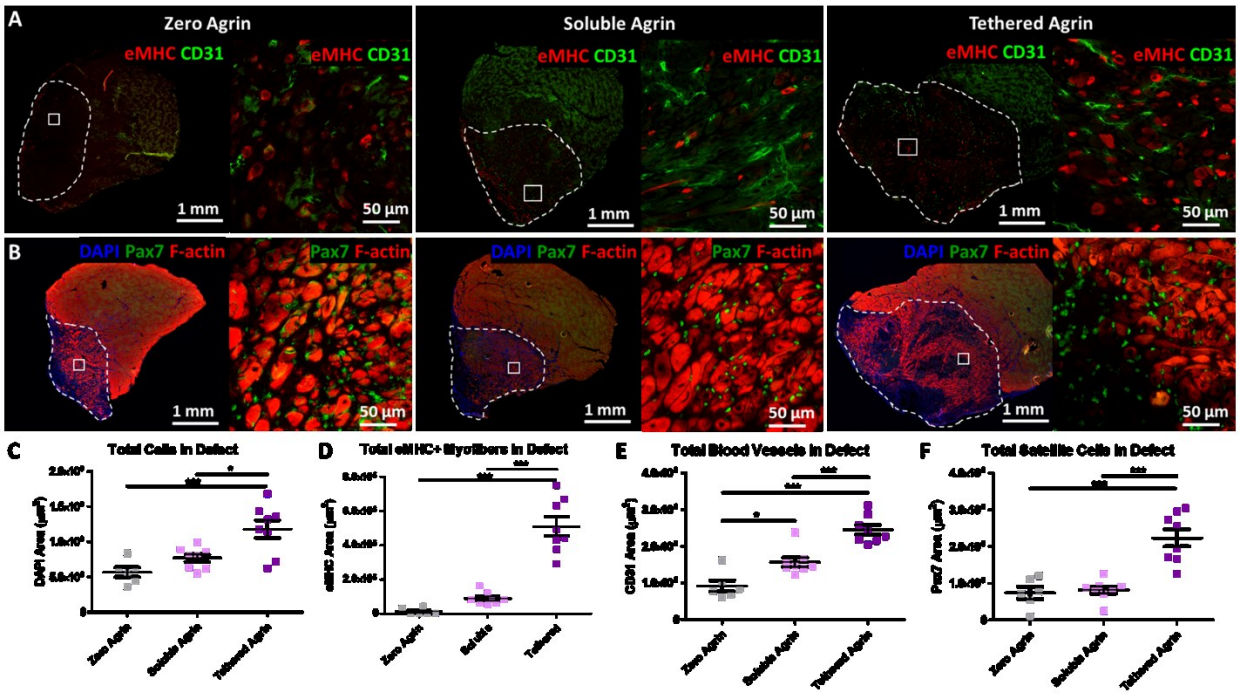

Figure 5.9. Tethered agrin increases the presence of regenerating myofibers, blood vessels, and satellite cells within VML defects. A) Differences in expression within the defect site (white dashed line) between groups are visible via immunostaining for embryonic myosin (eMHC; red) and blood vessels (CD31; green). Inset: high magnification image. **B)** Immunostaining for satellite cells (Pax7; green) and filamentous actin (F-actin; red) demonstrated differences in satellite cell recruitment between treatment groups. **C)** Defects treated with tethered agrin contained more cells than zero or soluble agrin groups. **D)** Tethered agrin resulted in significantly more embryonic myosin positive cells within the defect region than zero or soluble agrin. **E)** Significant differences in total blood vessel coverage were seen between all treatment groups with tethered agrin inducing the highest amount of blood vessels within the defect region. **F)** Tethered agrin constructs resulted in higher satellite cell numbers within the defect region than zero or soluble agrin. *: $p < 0.05$; ***: $p < 0.001$

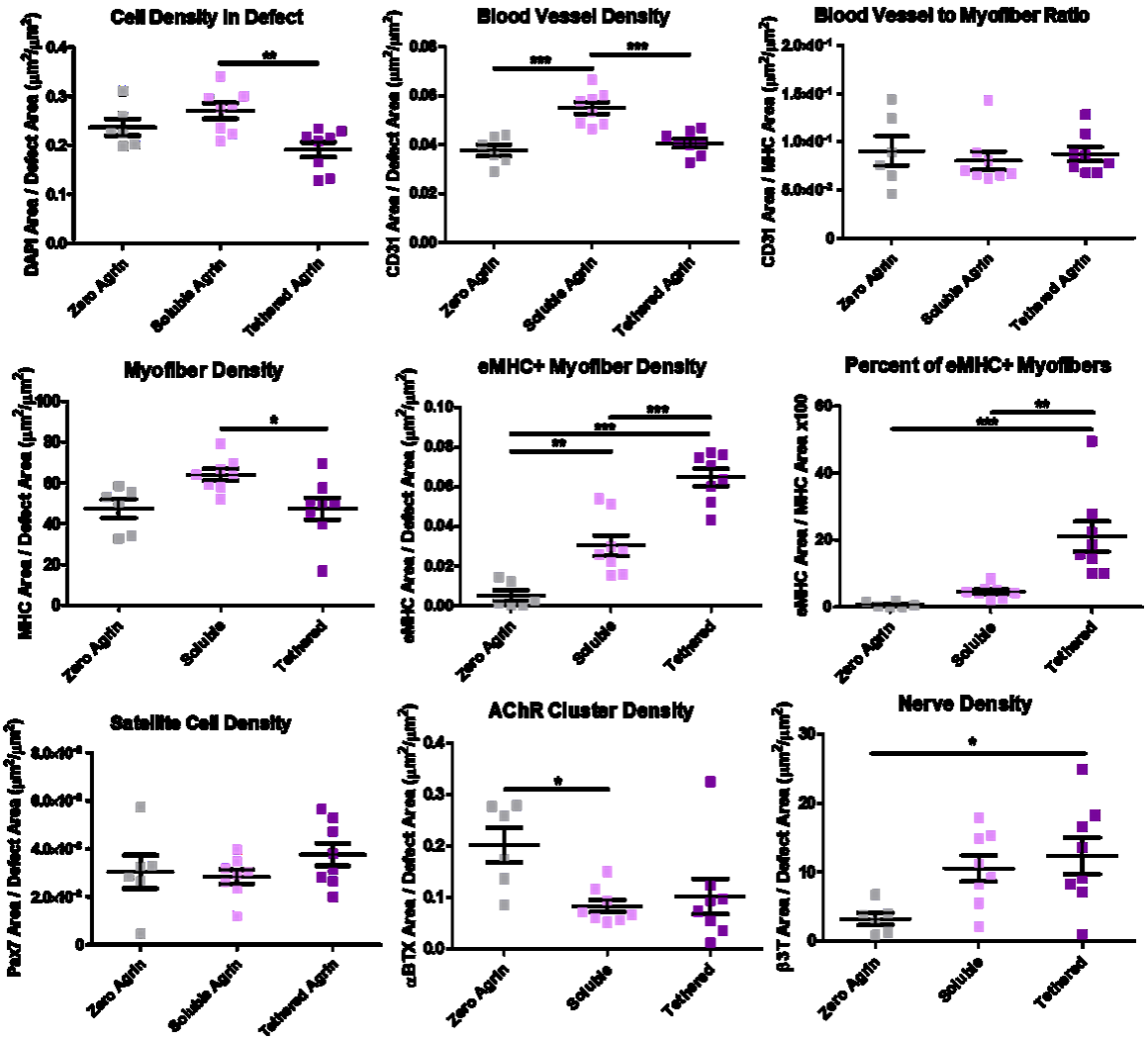

Figure 5.10. Further quantification of regenerative markers within VML defects treated with zero, soluble, or tethered agrin constructs. Significant differences were seen in the defect region between treatment groups in the density of total cells, blood vessels, regenerating myofibers, acetylcholine receptor clusters, and neurofilament. *: $p < 0.05$; **: $p<0.01$; ***: $p < 0.001$

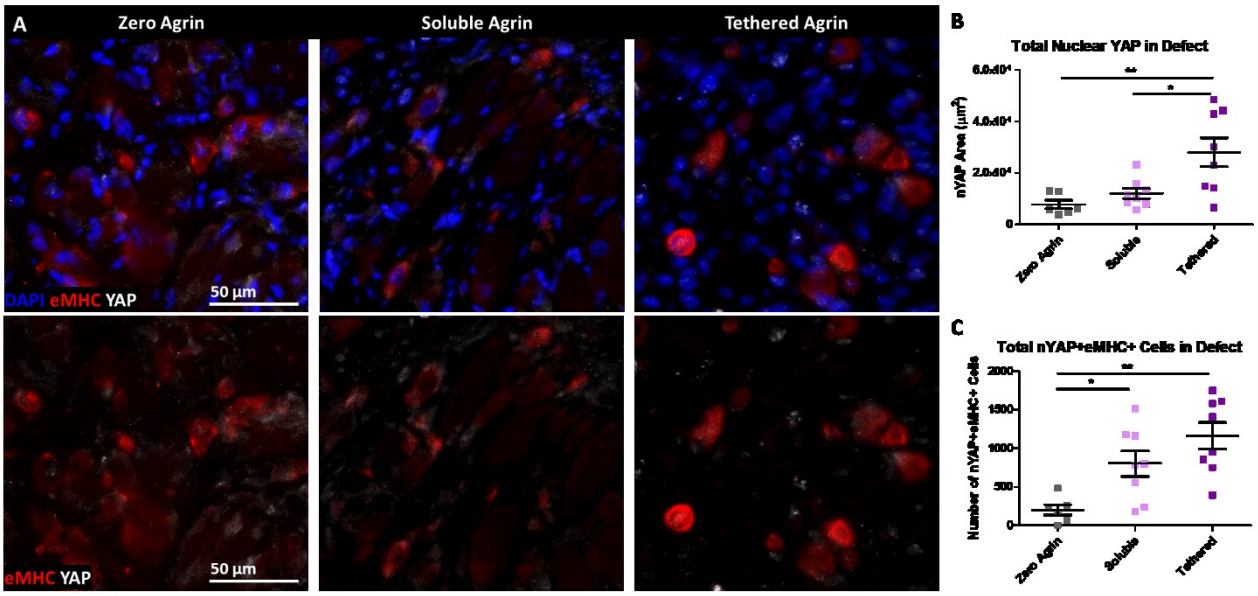

Figure 5.11. Co-expression of nuclear YAP and embryonic myosin within regenerating defects. A) In all treatment groups, some regenerating myofibers positive for embryonic myosin (eMHC; red) within the defect region also had nuclei positive for YAP (white). **B)** Total nuclear YAP (nYAP) was significantly higher in defects treated with tethered agrin constructs compared to other groups. **C)** Both soluble and tethered agrin constructs resulted in higher levels of eMHC+ myofibers with nuclear YAP co-expression compared to zero agrin. *: $p < 0.05$; **: $p<0.01$

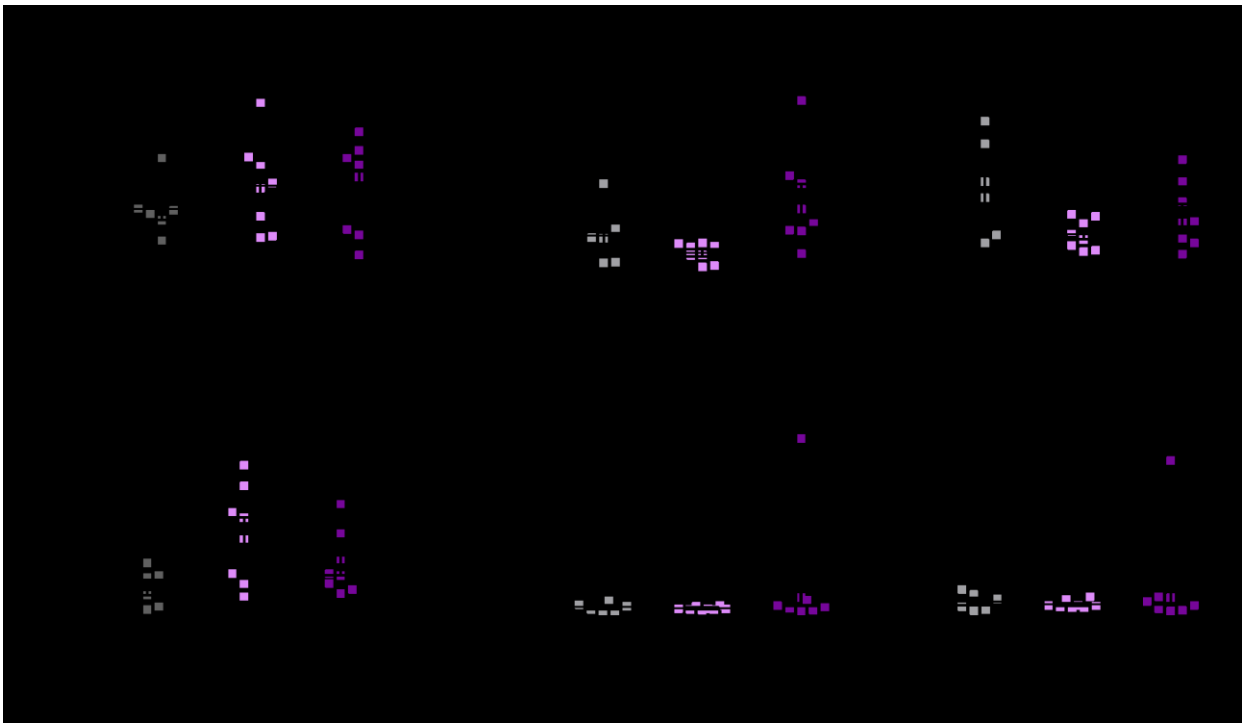

Figure 5.12. Further quantification of YAP staining and analysis of Ki67 and Pax7 co-expression. A) The density of nuclear YAP within defect regions did not differ between groups while the percent of eMHC+ myofibers containing YAP+ nuclei was significantly higher for soluble agrin compared to zero agrin. **B)** Defects treated with tethered agrin constructs contained significantly more Ki67+ nuclei compared to those treated with soluble agrin but the density of Ki67+ nuclei was higher for zero agrin compared to soluble agrin. All groups had very low co-expression of Ki67 and Pax7 with no difference between groups in the total level of co-expression or the percent of co-expressing nuclei within the defect. *: $p < 0.05$

5.4 Discussion

Successful regeneration of VML defects includes the formation of mature NMJs that allow for efficient neural signal propagation and subsequent muscle contraction. Significant advances in the field of skeletal muscle tissue engineering have demonstrated varied levels of muscle tissue regeneration and functional recovery post-VML [16,21,71–73,22,33,56,66–70] but remain limited in their ability to promote neuromuscular regeneration and few studies have been designed with this goal in mind. To date, there have been no previously published constructs that have incorporated pharmacologic factors specific to neuromuscular regeneration for VML treatment. Agrin has been

previously utilized to induce AChR clustering in cultured myotubes [130–138] and agrin-loaded muscle constructs have resulted in increased nerve infiltration and NMJ formation upon subcutaneous implantation in a non-VML model [130]. We thus identified agrin as a putative pharmacologic factor to induce neuromuscular regeneration post-VML and modified our previously developed electrospun muscle constructs [25,77] to incorporate agrin delivery within *in vitro* cultured muscle constructs as well as to the regenerating environment post-implantation.

Two methods of agrin delivery to 3D cultured myoblasts were examined for their neuromuscular potential *in vitro* and *in vivo.* Agrin provided in solution within cell culture media most closely mimics previous studies utilizing soluble agrin to induce AChR clustering in myotube monolayers via transient delivery to mature myotubes. Preliminary studies demonstrated that soluble agrin applied to immature C2C12 myoblast monolayers (day 2) did not cause AChR clustering while agrin applied to mature myotubes late in culture (day 8) was successful in inducing AChR clustering (data not shown). We thus applied agrin at a late time point (days 6-8) in the soluble agrin group. Chemically tethering agrin to electrospun fibrin scaffolds changes the cell microenvironment by enabling agrin signaling to cells throughout the duration of culture. In addition to inducing AChR clustering, *in vitro* agrin application to myotubes has been shown to increase contractile properties and dystrophin expression [134], myotube motility [202], and maturation of the excitation-contraction coupling machinery [203] further motivating prolonged agrin signaling via tethering to the scaffold surface. In addition, implanted constructs incorporating tethered agrin enable sustained local agrin signaling over time to the regenerating VML environment post-implantation with potential extended therapeutic benefit.

Scaffold-mediated delivery of immobilized bioactive factors may be limited by the potential for decreased factor bioactivity by denaturing or deactivating the protein during the

tethering process [204]. The EDC crosslinking paradigm used in this study has been used previously to tether agrin to polymeric microparticles for application to *in vitro* cultured myotubes with preserved agrin bioactivity [132]. In the current study, the bioactivity of tethered agrin was maintained as well and resulted in significantly more AChR clustering than passively adsorbed agrin. The difference in the *in vitro* 3D spatial location of AChR clusters seen between soluble and tethered agrin delivery methods is similar to previous reports where spatial control of AChR clusters is controlled by localized agrin signaling [132] and further motivates the potential benefit of tethering agrin to the implanted scaffold to prolong agrin signaling *in vivo* such that AChR clusters are induced to form within the defect site.

The EDC tethering protocol resulted in increased crosslinking of microfiber bundles and a significantly higher mechanical stiffness than other treatment groups with implications for both *in vitro* myogenesis and regeneration upon implantation. In the current study, *in vitro* myotubes formed within tethered agrin constructs had no visible difference in morphology compared to myotubes in other groups. Following implantation in VML defects for four weeks, tethered agrin constructs resulted in regions with distinct undegraded scaffold clearly visible via histological staining and likely due to the increased crosslinking and mechanical stiffness. In addition, despite resulting in a higher regenerating defect cross-sectional area, tethered agrin constructs did not confer functional improvements compared to defects treated with zero or soluble agrin constructs. The lack of a functional difference between treatment groups is similar to a variety of previous studies demonstrating that VML treatment with acellular scaffolds provides functional improvements compared to untreated defects at similar levels to cell-seeded scaffolds, even without corresponding histological muscle regeneration [21,22,25,46,54,56,57]. In addition, a study comparing VML treatment with fibrin microthreads with adsorbed hepatocyte growth factor

(HGF) found no difference in maximum tetanic force with or without the loaded HGF [12,24]. In fact, a recent meta-analysis of various VML treatments found that while treatment resulted in improved muscle function compared to untreated VML, there was little difference in functional improvement between the various treatment options [205]. It is therefore unsurprising that VML treatment with myoblast-seeded constructs containing zero, soluble, or tethered agrin resulted in similar levels of functional improvement. Although the presence of agrin within the defect region four weeks post-implantation was highest for tethered agrin constructs, agrin was visible at low levels in the other two treatment groups as well. Agrin is endogenously expressed at neuromuscular junctions and some neural synapses [206,207] and immunostaining for agrin within the defect region may be identifying endogenous protein expression in addition to the implanted agrin constructs.

Improved neuromuscular regeneration was seen for VML treatment with both soluble and tethered agrin constructs compared to zero agrin constructs. The total nerve area and nerve density within defects treated with tethered agrin was higher than zero agrin, and soluble agrin constructs resulted in a higher percentage of AChR clusters within a NMJ compared to zero agrin. This is in keeping with a previous study where agrin-loaded muscle constructs were implanted subcutaneously and resulted in increased numbers of NMJs at 2, 4, and 8 weeks post-implantation [130]. Quantification of NMJ density and morphology post-VML has been primarily limited to thin histological cross-sections, which do not enable morphological analysis of the complete NMJ [208]. In the current study, when NMJs were viewed via longitudinal sectioning, differences in morphology were apparent between agrin treatment groups with soluble agrin constructs inducing a more mature NMJ morphology than tethered agrin constructs. It has been previously demonstrated in monolayer cultures that agrin preferentially induces AChR clusters with an immature plaque shape [137], possibly explaining the higher incidence of an immature, plaque-

shaped NMJ morphology in VML defects exposed to sustained agrin presentation over time via tethered agrin constructs.

The sustained presentation of agrin combined with increased scaffold stiffness of tethered agrin constructs appears to have caused spatial differences in protein expression within the regenerating defect region. Soluble and tethered agrin constructs resulted in increased overall blood vessel infiltration, but blood vessels in zero and soluble agrin samples were uniform across the defect region while tethered agrin samples resulted in blood vessels primarily infiltrating between implanted scaffolds. This was likely due to increased stiffness of tethered agrin constructs and subsequent decreased ability for blood vessel penetration to the scaffold interior. In future studies we will assess the role of increased scaffold stiffness by utilizing EDC-treated scaffolds lacking agrin. Implanted tethered agrin constructs also contained high densities of neurofilament within the undegraded scaffold regions compared to regions between the implanted scaffolds and within host muscle tissue. Agrin treatment has been previously linked to increased nerve outgrowth [130] and neural proteolytic cleavage of agrin has been shown to induce formation of dendritic filopodia synaptic precursors [209]. The persistent agrin presence at four weeks post-implantation within tethered agrin scaffolds may have induced the high levels of neurofilament seen here.

A high incidence of eMHC+ regenerating myofibers within the defect is perhaps the most striking result of implanted tethered agrin constructs. Embryonic myosin is a transient marker of regenerating skeletal muscle and we have demonstrated previously that C2C12-seeded electrospun fibrin scaffolds implanted in VML defects resulted in significant eMHC expression at 2 weeks but not 4 weeks post-implantation [25]. Here, both agrin groups resulted in a significant increase in eMHC expression within the defect region compared to zero agrin controls, with tethered agrin resulting in the highest amount of eMHC. It appears that agrin treatment induces a prolonged state

of eMHC expression within VML defects, with the sustained signaling of tethered agrin causing the highest level of eMHC. Agrin administration has recently been shown to suppress cardiomyocyte maturation and enable cardiac regeneration in adult mice with a link to increased nuclear YAP expression [210]. It is possible that the skeletal muscle constructs pre-treated with soluble and tethered agrin are causing a similar suppressed maturation state of the myofibers present within VML defect regions, resulting in sustained eMHC expression. Additionally, tethered agrin constructs resulted in increased total nuclear YAP expression and both agrin treatment groups resulted in increased myofibers with co-expression of eMHC and nuclear YAP. Agrin has recently been correlated with YAP activation and increased nuclear YAP expression in various tissues [207,211], and nuclear YAP expression has been linked to increased cell proliferation and decreased myoblast maturity [212,213]. The sustained agrin delivery provided by implanted tethered agrin constructs may thus promote the increased nuclear YAP, increased cell proliferation, and increased expression of eMHC found within regenerating VML defect regions here. While prolonged agrin signaling within the post-VML regenerating environment provides therapeutic benefit, optimization of the construct degradation timeline to match the rate of muscle regeneration would likely further improve the construct regenerative potential by enabling increased blood vessel and myofiber infiltration to the scaffold interior. Due to the increased fibrin crosslinking caused by EDC, utilization of a lower EDC concentration or alternative tethering chemistry could increase the construct degradation rate. As soluble agrin constructs provided improved blood vessel and myofiber density as well as increased NMJ maturity, pretreating muscle constructs with both soluble and tethered agrin could combine the benefits of both delivery approaches. In addition, defect regions in tethered agrin treatment groups were significantly larger than the other

groups, indicating possible overgrowth within the regenerating muscle in response to sustained agrin signaling and a potential need for regulating the temporal release of agrin in future studies.

In conclusion, engineered muscle constructs pre-treated with agrin form dense AChR clusters *in vitro* and promote neuromuscular regeneration upon implantation in VML defects for four weeks. While all treatment groups resulted in improved muscle function, constructs pre-treated with both soluble and tethered agrin caused increased neurofilament and blood vessel infiltration, NMJ formation, and the presence of eMHC+ regenerating myofibers compared to zero agrin controls. In addition, sustained *in vivo* agrin signaling in tethered agrin treatment groups caused heightened neurofilament and eMHC density compared to soluble agrin. Future studies should further investigate the role of agrin in the regenerating muscle environment post-VML over longer time periods, as well as incorporate the delivery of other factors to promote neuromuscular regeneration post-VML.

Chapter 6 Conclusions and Future Perspectives

The data presented in this thesis demonstrate the regenerative potential of engineered muscle constructs following volumetric muscle loss. Electrospun fibrin scaffolds seeded with myoblasts enabled robust muscle regeneration post-VML, *in vitro* myogenesis of translatable cell sources, and neuromuscular regeneration post-VML when chemically modified for sustained agrin delivery to the regenerating tissue. This final chapter summarizes the most important conclusions, contributions, and future directions that have resulted from this work.

6.1 Conclusions and Contributions

Aim 1 Conclusions

Chapter 2 describes the initial development of an engineered muscle construct utilizing an electrospun fibrin hydrogel scaffold and a mouse myoblast cell line. The electrospun scaffolds were designed to mimic the native stiffness and hierarchical structure of skeletal muscle. Engineered muscle constructs demonstrated spontaneous and electrically stimulated contraction *in vitro* and myotubes expressed mature muscle markers with characteristic striations. Following implantation for two or four weeks in murine VML defects, the engineered muscle constructs enabled functional recovery and robust regeneration of vascularized skeletal muscle tissue with little to no fibrosis at the graft-host interface.

The extent of muscle and vascular regeneration following VML injury when treated with C2C12-seeded electrospun scaffolds seen here is a significant improvement over previous treatment modalities, resulting in a high density of myofibers and perfusable vasculature within the defect. Despite the inability of acellular constructs to support muscle regeneration, both

myoblast-seeded and acellular scaffolds recovered the contractile function of injured muscle. This initially surprising result has since been demonstrated repeatedly by other labs and is thought to be due to scaffold mediated functional fibrosis, where the implanted scaffold provides a mechanical bridge to prevent prolonged overload injury to the remaining muscle after injury. In conclusion, the experiments comprising Aim 1 demonstrate the development of a novel construct system that enabled previously unprecedented levels of functional muscle and vascular regeneration. The body of work described in this aim resulted in one journal publication and three conference abstracts.

Aim 2 Conclusions

The work described in Chapters 3 and 4 evaluated the ability of electrospun fibrin scaffolds to promote *in vitro* myogenesis and *in vivo* regeneration and engraftment of two translatable cell sources. Human adipose-derived stem cells expanded on electrospun scaffolds and formed elongated tube-like structures but had limited expression of muscle proteins *in vitro* even when induced with a DNA methyltransferase inhibitor shown previously to promote ASC myogenesis. Following implantation in an extensive VML model involving the complete removal of two entire muscles, implanted ASCs survived up to three months but myogenesis was low. After one month of implantation, there were slightly higher levels of regenerating and mature myofibers in defects treated with uninduced ASCs indicating a potential paracrine benefit of ASC implantation despite a lack of direct myogenesis. In rare instances, several myofibers containing a human nucleus were visible in the defect region demonstrating the feasibility of ASC contribution to muscle regeneration *in vivo* albeit at an extremely low level. Due to the

limited *in vitro* and *in vivo* myogenesis of ASCs, human pluripotent stem cells were next investigated as an alternative translatable cell source.

Both unsorted and Pax7-sorted hPSCs that underwent a small molecule myogenic commitment protocol successfully formed myotubes on electrospun scaffolds *in vitro*. Sorting the hPSCs for Pax7 resulted in improved myogenesis and constructs that exhibited a characteristic muscle protein expression timeline, sarcomeric striations, and multinucleation. Following implantation in critical or sub-critical defects, unsorted hPSC-derived muscle constructs enabled cell survival two weeks post-implantation while Pax7-sorted constructs only survived up to one week *in vivo.* Although there was little to no muscle regeneration present following implantation of unsorted hPSC-derived muscle constructs, Pax7-sorted constructs resulted in a significant amount of regenerating myofibers, many of which contained human nuclear protein. In addition, longitudinal views of the defect region contained myotube-like structures that were multinucleated with human nuclei. Preliminary data suggests that implantation of day 3 Pax7-sorted constructs improves regenerative outcomes compared to implantation of day 10 constructs. Further analysis and quantification will provide a broader understanding of the *in vivo* regenerative potential of Pax7-sorted constructs. In conclusion, the experiments comprising Aim 2 demonstrate the ability of electrospun fibrin scaffolds to promote *in vitro* myogenesis of translatable cell sources. ASCs were determined to have insufficient myogenic potential while hPSC-derived myoblasts sorted for the Pax7+ subpopulation demonstrated promising myogenic potential. The body of work described in this aim resulted in one journal publication and five conference abstracts.

Aim 3 Conclusions

Chapter 5 describes the pre-treatment of engineered muscle constructs with the proteoglycan agrin in order to promote neuromuscular regeneration. Incorporating both soluble and chemically tethered agrin into the *in vitro* muscle constructs promoted clustering of acetylcholine receptors, a necessary precursor to the formation of functional neuromuscular junctions. Tethering agrin to the scaffold surface changed the spatial location of AChR clusters compared to soluble agrin delivery, inducing clusters to form near the scaffold surface. Following four weeks of implantation in a VML defect, muscle constructs pre-treated with soluble or tethered agrin caused increased neuromuscular junctions, regenerating myofibers, vascular infiltration, neural infiltration, and nuclear yes-associated protein compared to constructs with no agrin. Sustained local agrin delivery to the regenerating environment post-VML also increased the density of regenerating myofibers and neurofilament compared to constructs pre-treated with soluble agrin.

The improvements to neuromuscular regeneration caused by agrin pre-treatment are a significant improvement over previous attempts to promote neuromuscular regeneration post-VML. Previous attempts to encourage neuromuscular regeneration are limited to the use of rehabilitative exercise or neurotization, and there have been no previous engineered muscle constructs designed to delivery bioactive factors for neuromuscular regeneration post-VML. The differences in regenerative potential between soluble and tethered agrin seen here also broaden understanding of the potential benefits of sustained release drug delivery platforms for regeneration post-VML. In conclusion, the experiments comprising Aim 3 demonstrate the remarkable neuromuscular regenerative capabilities of agrin when combined with our electrospun engineered muscle constructs. The body of work described in this aim resulted in one submitted journal publication and one conference abstract.

6.2 Future Perspectives

This dissertation established the myogenic potential of electrospun fibrin scaffolds and the *in vivo* regenerative potential of engineered muscle constructs. While Chapter 2 demonstrates robust functional and histological regeneration of muscle post-VML, the engineered muscle constructs used were limited by a non-translational mouse myoblast cell line. In addition, despite extensive regeneration of the muscle and vasculature there was little neuromuscular regeneration within the defect region. Chapters 3 and 4 address the first of these limitations by evaluating the myogenic potential of two translational human stem cell sources on electrospun fibers both *in vitro* and *in vivo.* Chapter 5 addresses the promotion of neuromuscular regeneration through modifications to the engineered muscle construct to enable sustained local delivery of agrin. Although this body of work has resulted in significant progress toward the goal of a translational tissue engineered muscle graft, there remains a need for additional optimization and future experiments.

Further research is required on the utility of hPSC-derived myoblasts to regenerate VML defects. Although Pax7-sorted hPDMs resulted in significant *in vitro* myogenesis on 3D constructs, the cells only survived up to one week post-implantation. This poses a significant challenge towards the implementation of these cells for therapeutic use in animals and humans. It is possible that the host immune response to implanted hPDMs creates an environment in which the cells cannot survive past one week. Although the mice are immunodeficient and lack mature T and B cells, they retain some macrophage function as well as the primary immune response. It is unlikely that the mice are responding negatively purely based on implantation of human cells, however, due to the survival of implanted human ASCs up to 3 months in a significantly harsher

VML defect model. Differences in implanted hPDM survival were also observed between unsorted and Pax7-sorted populations, indicating that multiple factors contributed to the lack of survival seen here. Future experiments investigating the use of anti-fibrotic agents in combination with hPDM constructs may promote cell survival and muscle regeneration. In addition, preliminary differences in regenerative potential were seen between implantation of early versus late-stage hPDM constructs. Further investigation into the potential therapeutic benefits of early-stage hPDM constructs would broaden understanding of the therapeutic benefit of these cells.

Although remarkable neuromuscular regeneration was achieved in the experiments described in Chapter 5, the regenerative potential of tethered agrin constructs is limited by diminished scaffold degradation following implantation. The EDC crosslinker used to tether agrin to the electrospun fibers resulted in increased crosslinking of the fibrin hydrogel and subsequent increased scaffold stiffness and decreased degradation *in vivo.* This resulted in pockets of undegraded scaffold lacking mature muscle within the defect region four weeks post-implantation. Future experiments investigating lower crosslinker concentrations or alternative tethering mechanisms that enable a higher scaffold degradation rate would benefit the construct's regenerative potential. Additionally, AChR clusters induced by agrin had a morphology that was primarily immature and plaque shaped. Utilization of additional proteins or AChR cluster-inducing agents would benefit the maturation of NMJs forming within the treated VML defects. Rehabilitative exercise and neurotization have been shown to enhance neuromuscular regeneration post-VML. Future work should investigate the combinatorial effects of engineered muscle constructs pre-treated to promote AChR clustering in combination with rehabilitative exercise and neurotization.

Ultimately, the patients requiring VML treatment have often sustained their injury months if not years before receiving treatment. Currently, the vast majority of preclinical studies utilize VML models in which the animal undergoes VML injury and is immediately treated with an engineered muscle construct. This differs from the clinical environment, where extensive scarring and fibrosis of a VML injury sustained years prior must first be debrided prior to treatment. In addition, the engineered muscle grafts implanted into a fresh VML injury with its associated satellite cell recruitment and regenerative milieu can be expected to have a different regenerative potential than when implanted into a chronic VML injury. To enable clinical translation, future studies should evaluate the muscle, vascular, and neuromuscular regenerative potential of engineered muscle constructs implanted into chronic VML defects.

Finally, immunodeficient animal models as well as small animal models have been utilized extensively in preclinical research of VML treatment. While immunodeficient animals enable implantation of muscle grafts composed of human cells, it is likely that the engineered muscle grafts would perform differently if implanted in animals with an intact immune system. The immune response to muscle injury plays a vital role in muscle regeneration and is often ignored when researching treatments for VML. For this reason, future studies should utilize engineered muscle grafts composed of autologous or allogeneic cells to enable the use of immune-competent animals. In addition, future work should focus on scale-up to larger size defects and larger animal models to test the limits of engineered muscle construct survival and regenerative potential. Numerous studies have investigated muscle regeneration in small defect models that don't require an external vascular source and rely on oxygen diffusion and vascular infiltration from the host. In large VML defects, implanted muscle constructs would not survive in the harsh ischemic injury environment by relying on oxygen diffusion and the slow timeline of

host blood vessel infiltration alone. Future studies should address this limitation by incorporating an external vascular source or other angiogenic component to encourage blood vessel infiltration, anastomosis, and ultimately successful muscle regeneration of large VML defects.

Bibliography

[1] I. Janssen, S. B. Heymsfield, Z. Wang, R. Ross, *J Appl Physiol* **2000**, *89*, 81.

[2] K. Garg, C. L. Ward, B. J. Hurtgen, J. M. Wilken, D. J. Stinner, J. C. Wenke, J. G. Owens, B. T. Corona, *J. Orthop. Res.* **2015**, 40.

[3] B. T. Corona, J. C. Rivera, J. G. Owens, J. C. Wenke, C. R. Rathbone, *J. Rehabil. Res. Dev.* **2015**, *52*, 785.

[4] N. J. Turner, S. F. Badylak, *Cell Tissue Res.* **2012**, *347*, 759.

[5] J. M. Grasman, M. J. Zayas, R. L. Page, G. D. Pins, *Acta Biomater.* **2015**, *25*, 2.

[6] B. M. Sicari, V. Agrawal, B. F. Siu, C. J. Medberry, C. L. Dearth, N. J. Turner, S. F. Badylak, *Tissue Eng. Part A* **2012**, *18*, 1941.

[7] B. T. Corona, J. C. Wenke, C. L. Ward, *Cells Tissues Organs* **2016**, *202*, 180.

[8] B. D. Owens, J. F. Kragh, J. Macaitis, S. J. Svoboda, J. C. Wenke, *J. Orthop. Trauma* **2007**, *21*, 254.

[9] B. D. Owens, J. F. Kragh, J. C. Wenke, J. Macaitis, C. E. Wade, J. B. Holcomb, *J. Trauma - Inj. Infect. Crit. Care* **2008**, *64*, 295.

[10] S. B. P. Charge, M. A. Rudnicki, *Physiol. Rev.* **2004**, *84*, 209.

[11] J. Huard, Y. Li, F. H. Fu, *J. Bone Joint Surg. Am.* **2002**, *84-A*, 822.

[12] J. A. Passipieri, G. J. Christ, *Cells Tissues Organs* **2016**, *202*, 202.

[13] S. M. Greising, J. C. Rivera, S. M. Goldman, A. Watts, C. A. Aguilar, B. T. Corona, *Sci. Rep.* **2017**, *7*, 1.

[14] N. Bursac, M. Juhas, T. A. Rando, *Annu. Rev. Biomed. Eng.* **2015**, *17*, 217.

[15] S. M. Greising, C. L. Dearth, B. T. Corona, *Cells Tissues Organs* **2016**, *202*, 237.

[16] C. A. Aguilar, S. M. Greising, A. Watts, S. M. Goldman, C. Peragallo, C. Zook, J. Larouche, B. T. Corona, *Cell Death Discov.* **2018**, *4*, DOI 10.1038/s41420-018-0027-8.

[17] B. T. Corona, K. E. Flanagan, C. M. Brininger, S. M. Goldman, J. A. Call, S. M. Greising, *Muscle and Nerve* **2018**, *57*, 799.

[18] T. L. Sarrafian, S. C. Bodine, B. Murphy, J. K. Grayson, S. M. Stover, *Vet. Surg.* **2018**, *47*, 524.

[19] C. R. Slater, *Int. J. Mol. Sci.* **2017**, *18*, DOI 10.3390/ijms18102183.

[20] S. E. Anderson, W. M. Han, V. Srinivasa, M. Mohiuddin, M. A. Ruehle, J. Y. Moon, E. Shin, C. L. San Emeterio, M. E. Ogle, E. A. Botchwey, et al., *Tissue Eng. Part C Methods* **2019**, *25*, 59.

[21] M. Quarta, M. Cromie, R. Chacon, J. Blonigan, V. Garcia, I. Akimenko, M. Hamer, P. Paine, M. Stok, J. B. Shrager, et al., *Nat. Commun.* **2017**, *8*, 15613.

[22] B. Kasukonis, J. Kim, L. Brown, J. Jones, S. Ahmadi, T. Washington, J. Wolchok, *Tissue Eng. Part A* **2016**, *22*, 1151.

[23] J. T. Kim, B. M. Kasukonis, L. A. Brown, T. A. Washington, J. C. Wolchok, *Exp. Gerontol.* **2016**, *83*, 37.

[24] J. M. Grasman, D. M. Do, R. L. Page, G. D. Pins, *Biomaterials* **2015**, *72*, 49.

[25] J. Gilbert-Honick, S. R. Iyer, S. M. Somers, R. M. Lovering, K. Wagner, H. Mao, W. Grayson, *Biomaterials* **2018**, *164*, 70.

[26] K. M. Haizlip, B. C. Harrison, L. A. Leinwand, *Physiology* **2015**, *30*, 30.

[27] H. Yin, F. Price, M. a Rudnicki, *Physiol. Rev.* **2013**, *93*, 23.

[28] S. Welle, R. Tawil, C. A. Thornton, *PLoS One* **2008**, *3*, DOI 10.1371/journal.pone.0001385.

[29] S. Levenberg, J. Rouwkema, M. Macdonald, E. S. Garfein, D. S. Kohane, D. C. Darland, R. Marini, C. A. van Blitterswijk, R. C. Mulligan, P. A. D'Amore, et al., *Nat. Biotechnol.* **2005**, *23*, 879.

[30] A. Lesman, J. Koffler, R. Atlas, Y. J. Blinder, Z. Kam, S. Levenberg, *Biomaterials* **2011**, *32*, 7856.

[31] J. Koffler, K. Kaufman-Francis, S. Yulia, E. Dana, A. P. Daria, A. Landesberg, S. Levenberg, *Proc. Natl. Acad. Sci. U. S. A.* **2011**, *108*, 14789.

[32] Y. Shandalov, D. Egozi, J. Koffler, D. Dado-Rosenfeld, D. Ben-Shimol, A. Freiman, E. Shor, A. Kabala, S. Levenberg, *Proc. Natl. Acad. Sci.* **2014**, *111*, 6010.

[33] L. Perry, S. Landau, M. Y. Flugelman, S. Levenberg, *Commun. Biol.* **2018**, *1*, DOI 10.1038/s42003-018-0161-0.

[34] D. Rosenfeld, S. Landau, Y. Shandalov, N. Raindel, A. Freiman, E. Shor, Y. Blinder, *Proc. Natl. Acad. Sci.* **2016**, *113*, 3215.

[35] L. Perry, M. Y. Flugelman, S. Levenberg, *Mol. Ther.* **2017**, *25*, 935.

[36] B. F. Grogan, J. R. Hsu, *J. Am. Acad. Orthop. Surg.* **2011**, *19*, 35.

[37] J. P. Mertens, K. B. Sugg, J. D. Lee, L. M. Larkin, *Regen. Med.* **2014**, *9*, 89.

[38] T. H. Qazi, D. J. Mooney, M. Pumberger, S. Geißler, G. N. Duda, *Biomaterials* **2015**, *53*, 502.

[39] M. T. Wolf, C. L. Dearth, S. B. Sonnenberg, E. G. Loboa, S. F. Badylak, *Adv. Drug Deliv. Rev.* **2015**, *84*, 208.

[40] G. Cittadella Vigodarzere, S. Mantero, *Front Physiol* **2014**, *5*, 362.

[41] C. G. Y. Ngan, A. Quigley, R. M. I. Kapsa, P. F. M. Choong, *J. Tissue Eng. Regen. Med.* **2018**, *12*, e1.

[42] M. Juhas, N. Bursac, *Curr. Opin. Biotechnol.* **2013**, *24*, 880.

[43] M. Juhas, J. Ye, N. Bursac, *Methods* **2015**, *99*, 81.

[44] C. Fuoco, L. L. Petrilli, S. Cannata, C. Gargioli, *J. Orthop. Surg. Res.* **2016**, *11*, 86.

[45] B. M. Sicari, C. L. Dearth, S. F. Badylak, *Anat. Rec.* **2014**, *297*, 51.

[46] A. Aurora, J. L. Roe, B. T. Corona, T. J. Walters, *Biomaterials* **2015**, *67*, 393.

[47] M. N. Pantellic, L. M. Larkin, *Tissue Eng. Part B Rev.* **2018**, *24*, ten. TEB.2017.0451.

[48] K. J. A. McCullagh, R. C. R. Perlingeiro, *Adv. Drug Deliv. Rev.* **2015**, *84*, 198.

[49] J. H. Kim, I. K. Ko, A. Atala, J. J. Yoo, *Sci. Rep.* **2016**, *6*, 38754.

[50] K. W. VanDusen, B. C. Syverud, M. L. Williams, J. D. Lee, L. M. Larkin, *Tissue Eng. Part A* **2014**, *20*, 2920.

[51] S. Carosio, L. Barberi, E. Rizzuto, C. Nicoletti, Z. Del Prete, A. Musarò, *Sci. Rep.* **2013**, *3*, 1420.

[52] K. H. Nakayama, M. Shayan, N. F. Huang, *Adv. Healthc. Mater.* **2019**, *8*, e1801168.

[53] K. Sadtler, K. Estrellas, B. W. Allen, M. T. Wolf, H. Fan, A. J. Tam, C. H. Patel, B. S. Luber, H. Wang, K. R. Wagner, et al., *Science (80-.).* **2016**, *352*, 366.

[54] B. M. Sicari, J. P. Rubin, C. L. Dearth, M. T. Wolf, F. Ambrosio, M. Boninger, N. J. Turner, D. J. Weber, T. W. Simpson, A. Wyse, et al., *Sci. Transl. Med.* **2014**, *6*, 1.

[55] M. T. Conconi, P. De Coppi, S. Bellini, G. Zara, M. Sabatti, M. Marzaro, G. Franco Zanon, P. G. Gamba, P. P. Parnigotto, G. G. Nussdorfer, *Biomaterials* **2005**, *26*, 2567.

[56] B. T. Corona, C. L. Ward, H. B. Baker, T. J. Walters, G. J. Christ, *Tissue Eng. Part A* **2014**, *20*, 705.

[57] B. T. Corona, X. Wu, C. L. Ward, J. S. McDaniel, C. R. Rathbone, T. J. Walters, *Biomaterials* **2013**, *34*, 3324.

[58] V. J. Mase, J. R. Hsu, S. E. Wolf, J. C. Wenke, D. G. Baer, J. Owens, S. F. Badylak, T. J. Walters, *Orthopedics* **2010**, *33*, 511.

[59] N. J. Turner, A. J. Yates, D. J. Weber, I. R. Qureshi, D. B. Stolz, T. W. Gilbert, S. F. Badylak, *Tissue Eng. Part A* **2010**, *16*, 3309.

[60] J. Dziki, S. Badylak, M. Yabroudi, B. Sicari, F. Ambrosio, K. Stearns, N. Turner, A. Wyse, M. L. Boninger, E. H. P. Brown, et al., *Nat. Regen. Med.* **2016**, *1*, 1.

[61] B. M. Sicari, J. P. Rubin, C. L. Dearth, M. T. Wolf, F. Ambrosio, M. Boninger, N. J. Turner, D. J. Weber, T. W. Simpson, A. Wyse, et al., *Sci. Transl. Med.* **2014**, *6*, 234ra58.

[62] N. E. Gentile, K. M. Stearns, E. H. P. Brown, J. P. Rubin, M. L. Boninger, C. L. Dearth, F. Ambrosio, S. F. Badylak, *Am. J. Phys. Med. Rehabil.* **2014**, *93*, 1.

[63] X. K. Chen, T. J. Walters, *J. Plast. Reconstr. Aesthetic Surg.* **2013**, *66*, 1750.

[64] K. Garg, C. L. Ward, C. R. Rathbone, B. T. Corona, *Cell Tissue Res.* **2014**, *358*, 857.

[65] J. A. Passipieri, X. Hu, E. Mintz, J. Dienes, H. B. Baker, C. H. Wallace, S. S. Blemker, G. J. Christ, *Tissue Eng. Part A* **2019**, *00*, ten. tea.2018.0280.

[66] C. L. Ward, L. Ji, B. T. Corona, *Biores. Open Access* **2015**, *4*, 198.

[67] S. M. Goldman, B. E. P. Henderson, T. J. Walters, B. T. Corona, *PLoS One* **2018**, 1.

[68] M. T. A. Li, N. J. Willett, B. A. Uhrig, R. E. Guldberg, G. L. Warren, *J. Biomech.* **2014**, *47*, 2013.

[69] L. Madden, M. Juhas, W. E. Kraus, G. A. Truskey, N. Bursac, *Elife* **2015**, *4*, e04885.

[70] R. L. Page, C. Malcuit, L. Vilner, I. Vojtic, S. Shaw, E. Hedblom, J. Hu, G. D. Pins, M. W. Rolle, T. Dominko, *Tissue Eng Part A* **2011**, *17*, 2629.

[71] J. A. Passipieri, H. B. Baker, M. Siriwardane, M. Ellenburg, M. Vadhavkar, J. M. Saul, S. Tomblyn, L. Burnett, G. J. Christ, *Tissue Eng. Part A* **2017**, *23*, 556.

[72] H. B. Baker, J. A. Passipieri, M. Siriwardane, M. Ellenburg, M. Vadhavkar, C. R. Bergman, J. M. Saul, S. Tomblyn, L. Burnett, G. J. Christ, *Tissue Eng. Part A* **2017**, *23*, 572.

[73] M. Juhas, G. C. Engelmayr, A. N. Fontanella, G. M. Palmer, N. Bursac, *Proc. Natl. Acad. Sci.* **2014**, *111*, 5508.

[74] X. Qiu, S. Liu, H. Zhang, B. Zhu, Y. Su, C. Zheng, R. Tian, M. Wang, H. Kuang, X. Zhao, et al., *Stem Cell Res. Ther.* **2018**, *9*, DOI 10.1186/s13287-018-0821-5.

[75] E. K. Merritt, M. V Cannon, D. W. Hammers, L. N. Le, R. Gokhale, A. Sarathy, T. J. Song, M. T. Tierney, L. J. Suggs, T. J. Walters, et al., *Tissue Eng Part A* **2010**, *16*, 2871.

[76] V. Kesireddy, *Int. J. Nanomedicine* **2016**, *11*, 1461.

[77] J. Gilbert-Honick, B. Ginn, Y. Zhang, S. Salehi, K. R. Wagner, H.-Q. Mao, W. L. Grayson, *Cell Transplant.* **2018**, *27*, 1644.

[78] M. Pilia, J. S. McDaniel, T. Guda, X. K. Chen, R. P. Rhoads, R. E. Allen, B. T. Corona, C. R. Rathbone, *Eur. Cells Mater.* **2014**, *28*, 11.

[79] S. M. Maffioletti, S. Sarcar, A. B. H. Henderson, I. Mannhardt, L. Pinton, L. A. Moyle, H. Steele-Stallard, O. Cappellari, K. E. Wells, G. Ferrari, et al., *Cell Rep.* **2018**, *23*, 899.

[80] I. Y. Choi, H. T. Lim, K. Estrellas, J. Mula, T. V. Cohen, Y. Zhang, C. J. Donnelly, J. P. Richard, Y. J. Kim, H. Kim, et al., *Cell Rep.* **2016**, *15*, 2301.

[81] L. Rao, Y. Qian, A. Khodabukus, T. Ribar, N. Bursac, *Nat. Commun.* **2018**, *9*, 1.

[82] B. T. Corona, M. A. Machingal, T. Criswell, M. Vadhavkar, A. C. Dannahower, C. Bergman, W. Zhao, G. J. Christ, *Tissue Eng Part A* **2012**, *18*, 1213.

[83] J. Ma, K. Holden, J. Zhu, H. Pan, Y. Li, *J. Biomed. Biotechnol.* **2011**, *2011*, 1.

[84] K. H. Nakayama, C. Alcazar, G. Yang, M. Quarta, P. Paine, L. Doan, A. Davies, T. A. Rando, N. F. Huang, *npj Regen. Med.* **2018**, *3*, 16.

[85] C. A. Rossi, M. Flaibani, B. Blaauw, M. Pozzobon, E. Figallo, C. Reggiani, L. Vitiello, N. Elvassore, P. De Coppi, *FASEB J.* **2011**, *25*, 2296.

[86] T. Kaufman, B. Kaplan, L. Perry, Y. Shandalov, S. Landau, I. Srugo, D. Ad-El, S. Levenberg, *Am. J. Transplant.* **2019**, *19*, 37.

[87] V. Chaturvedi, D. Naskar, B. F. Kinnear, E. Grenik, D. E. Dye, M. D. Grounds, S. C. Kundu, D. R. Coombe, *J. Tissue Eng. Regen. Med.* **2016**, DOI 10.1002/term.

[88] K. Hagiwara, G. Chen, N. Kawazoe, Y. Tabata, H. Komuro, *J. Tissue Eng. Regen. Med.* **2016**, *10*, 325.

[89] Y. M. Ju, A. Atala, J. J. Yoo, S. J. Lee, *Acta Biomater.* **2014**, *10*, 4332.

[90] V. Hosseini, S. Ahadian, S. Ostrovidov, G. Camci-Unal, S. Chen, H. Kaji, M. Ramalingam, A. Khademhosseini, *Tissue Eng. Part A* **2012**, *18*, 2453.

[91] N. Han, M. A. Yabroudi, K. Stearns-Reider, W. Helkowski, B. M. Sicari, J. P. Rubin, S. F. Badylak, M. L. Boninger, F. Ambrosio, *Phys. Ther.* **2015**, *96*, 540.

[92] C. K. Colton, *Cell Transplant.* **1995**, *4*, 415.

[93] M. W. Laschke, Y. Harder, M. Amon, I. Martin, J. Farhadi, A. Ring, N. Torio-Padron, R. Schramm, M. Rücker, D. Junker, et al., *Tissue Eng.* **2006**, *12*, 2093.

[94] J. Folkman, M. Hochberg, *J. Exp. Med.* **1973**, *138*, 745.

[95] M. T. Webster, U. Manor, J. Lippincott-Schwartz, C. M. Fan, *Cell Stem Cell* **2015**, 1.

[96] Y. H. A. M. Kusters, E. J. Barrett, *Am J Physiol Endocrinol Metab.* **2015**, *310*, E379.

[97] D. N. Granger, E. Senchenkova, *Inflammation and the Microcirculation: Colloquium Series on Integrated Systems Physiology: From Molecule to Function*, Morgan & Claypool Life Sciences, **2010**.

[98] G. G. Emerson, S. S. Segal, *J Appl Physiol* **1997**, *82*, 42.

[99] R. T. Hepple, *Med. Sci. Sport. Exerc.* **2000**, *31*, 117.

[100] I. M. Olfert, O. Baum, Y. Hellsten, S. Egginton, *Am. J. Physiol. Heart Circ. Physiol.* **2016**, *310*, H326.

[101] V. W. M. Van Hinsbergh, A. Collen, *Ann. N. Y. Acad. Sci.* **2001**, *936*, 426.

[102] G. H. Borschel, D. E. Dow, R. G. Dennis, D. L. Brown, *Plast. Reconstr. Surg.* **2006**, *117*, 2235.

[103] A. Messina, S. K. Bortolotto, O. C. S. Cassell, J. Kelly, K. M. Abberton, W. a Morrison, *FASEB J.* **2005**, *19*, 1570.

[104] A. D. Bach, A. Arkudas, J. Tjiawi, E. Polykandriotis, U. Kneser, R. E. Horch, J. P. Beier, *J. Cell. Mol. Med.* **2006**, *10*, 716.

[105] M. L. Williams, T. Y. Kostrominova, E. M. Arruda, L. M. Larkin, *J. Tissue Eng. Regen. Med.* **2013**, *7*, 434.

[106] W. Zhou, D.-Q. He, J.-Y. Liu, Y. Feng, X.-Y. Zhang, C.-G. Hua, X.-F. Tang, *J. Tissue Eng. Regen. Med.* **2015**, *9*, 1404.

[107] J. Zhang, Z. Q. Hu, N. J. Turner, S. F. Teng, W. Y. Cheng, H. Y. Zhou, L. Zhang, H. W. Hu, Q. Wang, S. F. Badylak, *Biomaterials* **2016**, *89*, 114.

[108] B. J. Jank, L. Xiong, P. T. Moser, J. P. Guyette, X. Ren, C. L. Cetrulo, D. A. Leonard, L. Fernandez, S. P. Fagan, H. C. Ott, *Biomaterials* **2015**, *61*, 246.

[109] M. T. Li, M. Ruehle, H. Stevens, N. Servies, N. Willett, S. Karthikeyakannan, G. L. Warren, R. Guldberg, L. N. Krishnan, *Tissue Eng. Part A* **2017**, *23*, 989.

[110] Y.-J. Choi, Y.-J. Jun, D. Y. Kim, H.-G. Yi, S.-H. Chae, J. Kang, J. Lee, G. Gao, J.-S. Kong, J. Jang, et al., *Biomaterials* **2019**, *206*, 160.

[111] A. Aurora, N. Wrice, T. J. Walters, R. J. Christy, S. Natesan, *Acta Biomater.* **2018**, *65*, 150.

[112] J. Gilbert-Honick, S. M. Somers, W. L. Grayson, in *Biomater. Stem Cells From Basics to Appl.* (Eds: B. Garipcan, A. Denizli), Palme Yayınevi, Istanbul, Turkey, **2018**, pp. 143–153.

[113] I. Y. Kuo, B. E. Ehrlich, *Cold Spring Harb. Perspect. Biol.* **2015**, *7*, 1.

[114] V. Witzemann, *Cell Tissue Res.* **2006**, *326*, 263.

[115] W. Liu, J. V. Chakkalakal, in *Curr. Top. Dev. Biol.*, Elsevier Inc., **2017**, pp. 99–124.

[116] M. Gautam, P. G. Noakes, L. Moscoso, F. Rupp, R. H. Scheller, J. P. Merlie, J. R. Sanes, *Cell* **1996**, *85*, 525.

[117] N. Singhal, P. T. Martin, *Dev. Neurobiol.* **2011**, *71*, 982.

[118] E. Frank, K. Gautvik, H. Sommerschild, *Cold Spring Harb. Symp. Quant. Biol.* **1976**, *40*, 275.

[119] P. Konofaos, R. D. Wallace, *J. Reconstr. Microsurg.* **2015**, *31*, 481.

[120] S. Schiaffino, T. Partridge, *Skeletal Muscle Repair and Regeneration*, **2008**.

[121] B. T. Corona, K. Garg, C. L. Ward, J. S. McDaniel, T. J. Walters, C. R. Rathbone, *Am. J. Physiol. Physiol.* **2013**, *305*, C761.

[122] A. S. T. Smith, S. L. Passey, N. R. W. Martin, D. J. Player, V. Mudera, L. Greensmith, M. P. Lewis, *Cells Tissues Organs* **2016**, *202*, 143.

[123] J. A. Umbach, K. L. Adams, C. B. Gundersen, B. G. Novitch, *PLoS One* **2012**, *7*, 3.

[124] P. H. Chipman, Y. Zhang, V. F. Rafuse, *PLoS One* **2014**, *9*, DOI 10.1371/journal.pone.0091643.

[125] Y. Morimoto, M. Kato-Negishi, H. Onoe, S. Takeuchi, *Biomaterials* **2013**, *34*, 9413.

[126] X. Guo, M. Gonzalez, M. Stancescu, H. H. Vandenburgh, J. J. Hickman, *Biomaterials* **2011**, *32*, 9602.

[127] T. A. Dixon, E. Cohen, D. M. Cairns, M. Rodriguez, J. Mathews, R. R. Jose, D. L. Kaplan, *Tissue Eng. Part C Methods* **2018**, *24*, 346.

[128] O. F. Vila, S. G. M. Uzel, S. P. Ma, D. Williams, J. Pak, R. D. Kamm, G. Vunjak-Novakovic, *Theranostics* **2019**, *9*, 1232.

[129] R. Lozano, K. J. Gilmore, B. C. Thompson, E. M. Stewart, A. M. Waters, M. Romero-Ortega, G. G. Wallace, *Acta Biomater.* **2016**, *45*, 328.

[130] I. K. Ko, B. K. Lee, S. J. Lee, K. E. Andersson, A. Atala, J. J. Yoo, *Biomaterials* **2013**, *34*, 3246.

[131] B. G. X. Zhang, A. F. Quigley, J. L. Bourke, C. J. Nowell, D. E. Myers, P. F. M. Choong, R. M. I. Kapsa, *Dev. Neurobiol.* **2016**, *76*, 551.

[132] J. B. Scott, C. L. Ward, B. T. Corona, M. R. Deschenes, B. S. Harrison, J. M. Saul, G. J. Christ, *Front. Pharmacol.* **2017**, *7*, 1.

[133] M. J. Ferns, J. T. Campanelli, W. Hoch, R. H. Scheller, Z. Hall, *Neuron* **1993**, *11*, 491.

[134] W. Bian, N. Bursac, *FASEB J.* **2012**, *26*, 955.

[135] A. Tourovskaia, N. Li, A. Folch, *Biophys. J.* **2008**, *95*, 3009.

[136] L. K. Lee, D. D. Kunkel, J. Stollberg, *BMC Neurosci.* **2002**, *3*, 1.

[137] E. G. Bruneau, P. C. Macpherson, D. Goldman, R. I. Hume, M. Akaaboune, *Dev. Biol.* **2005**, *288*, 248.

[138] D. J. Burkin, J. E. Kim, M. Gu, S. J. Kaufman, *J. Cell Sci.* **2000**, *113*, 2877.

[139] S.-B. Kang, J. L. Olson, A. Atala, J. J. Yoo, *Tissue Eng. Part A* **2012**, *18*, 1912.

[140] T. L. Criswell, B. T. Corona, Z. Wang, Y. Zhou, G. Niu, Y. Xu, G. J. Christ, S. Soker, *Biomaterials* **2013**, *34*, 140.

[141] V. Dhawan, I. F. Lytle, D. E. Dow, Y.-C. Huang, D. L. Brown, *Tissue Eng.* **2007**, *13*, 2813.

[142] A. Aurora, K. Garg, B. T. Corona, T. J. Walters, *BMC Sport. Sci. Med. Rehabil.* **2014**, *6*, 1.

[143] F. Ambrosio, R. J. Ferrari, G. Distefano, J. M. Plassmeyer, G. E. Carvell, B. M. Deasy, M. L. Boninger, G. K. Fitzgerald, J. Huard, *Tissue Eng. Part A* **2009**, *16*, 839.

[144] T. D. Brutsaert, T. P. Gavin, Z. Fu, E. C. Breen, K. Tang, O. Mathieu-Costello, P. D. Wagner, *BMC Physiol.* **2002**, *2*, 1.

[145] T. A. Rando, F. Ambrosio, *Cell Stem Cell* **2018**, *22*, 306.

[146] K. Garg, C. L. Ward, B. J. Hurtgen, J. M. Wilken, D. J. Stinner, J. C. Wenke, J. G. Owens, B. T. Corona, *J. Orthop. Res.* **2015**, *33*, 40.

[147] S. Zhang, X. Liu, S. F. Barreto-Ortiz, Y. Yu, B. P. Ginn, N. A. DeSantis, D. L. Hutton, W. L. Grayson, F.-Z. Cui, B. A. Korgel, et al., *Biomaterials* **2014**, *35*, 3243.

[148] Y. S. Choi, L. G. Vincent, A. R. Lee, K. C. Kretchmer, S. Chirasatitsin, M. K. Dobke, A. J. Engler, *Biomaterials* **2012**, *33*, 6943.

[149] M. Chen, Y. Sun, Y. Chen, *Acta Biomater.* **2013**, *9*, 5562.

[150] Y. S. Choi, L. G. Vincent, A. R. Lee, M. K. Dobke, A. J. Engler, *Biomaterials* **2012**, *33*, 2482.

[151] A. J. Engler, M. A. Griffin, S. Sen, C. G. Bönnemann, H. L. Sweeney, D. E. Discher, *J. Cell Biol.* **2004**, *166*, 877.

[152] C. A. Cook, P. Y. Huri, B. P. Ginn, J. Gilbert-Honick, S. M. Somers, J. P. Temple, H. Mao, W. L. Grayson, *Biotechnol. Bioeng.* **2016**, *113*, 1825.

[153] S. G. Dubois, E. Z. Floyd, S. Zvonic, G. Kilroy, X. Wu, S. Carling, Y. D. C. Halvorsen, E. Ravussin, J. M. Gimble, in *Methods Mol. Biol. Mesenchymal Stem Cells Methods Protoc.*, **2008**, pp. 69–79.

[154] S. R. Iyer, A. P. Valencia, E. O. Hernandez-Ochoa, R. M. Lovering, *Methods Mol. Biol.* **2016**, *1460*, 293.

[155] C. H. J. da Pinheiro, J. C. F. de Queiroz, L. Guimarães-Ferreira, K. F. Vitzel, R. T. Nachbar, L. G. O. de Sousa, A. L. de Souza-Jr, M. T. Nunes, R. Curi, *Stem Cell Rev. Reports* **2012**, *8*, 363.

[156] M. Gautam, D. Fujita, K. Kimura, H. Ichikawa, A. Izawa, M. Hirose, T. Kashihara, M. Yamada, M. Takahashi, U. Ikeda, et al., *J. Mol. Cell. Cardiol.* **2015**, *81*, 139.

[157] S. Gehmert, C. Wenzel, M. Loibl, G. Brockhoff, M. Huber, W. Krutsch, M. Nerlich, M. Gosau, S. Klein, S. Schreml, et al., *Biomed Res. Int.* **2014**, *2014*, 1.

[158] H. Mizuno, P. A. Zuk, D. Ph, M. Zhu, H. P. Lorenz, P. Benhaim, M. H. Hedrick, *Plast. Reconstr. Surg.* **2002**, *109*, 199.

[159] Y. Lin, L. Liu, Z. Li, J. Qiao, L. Wu, W. Tang, X. Zheng, X. Chen, Z. Yan, W. Tian, *Mol. Cell. Biochem.* **2006**, *291*, 1.

[160] V. Bayati, Y. Sadeghi, M. A. Shokrgozar, N. Haghighipour, K. Azadmanesh, A. Amanzadeh, S. Azari, *Tissue Cell* **2011**, *43*, 359.

[161] F. Y. Meligy, K. Shigemura, H. M. Behnsawy, M. Fujisawa, M. Kawabata, T. Shirakawa, *Vitr. Cell. Dev. Biol. - Anim.* **2012**, *48*, 203.

[162] G. Di Rocco, M. G. Iachininoto, A. Tritarelli, S. Straino, A. Zacheo, A. Germani, F. Crea, M. C. Capogrossi, *J. Cell Sci.* **2006**, *119*, 2945.

[163] Y. Liu, X. Yan, Z. Sun, B. Chen, Q. Han, J. Li, R. C. Zhao, *Stem Cells Dev.* **2007**, *16*, 695.

[164] M. Kim, Y. S. Choi, S. H. Yang, H.-N. Hong, S.-W. Cho, S. M. Cha, J. H. Pak, C. W. Kim, S. W. Kwon, C. J. Park, *Biochem. Biophys. Res. Commun.* **2006**, *348*, 386.

[165] R. L. Page, C. Malcuit, L. Vilner, I. Vojtic, S. Shaw, E. Hedblom, J. Hu, G. D. Pins, M. W. Rolle, T. Dominko, *Tissue Eng. Part A* **2011**, *17*, 2629.

[166] A. S. de la Garza-Rodea, I. van der Velde-van Dijke, H. Boersma, M. A. F. V Goncalves, D. W. van Bekkum, A. A. F. de Vries, S. Knaan-Shanzer, *Cell Transplant.* **2012**, *21*, 153.

[167] L. Labusca, F. Zugun-Eloae, V. Nacu, K. Mashayekhi, *Rec. Pat. Regen. Med.* **2013**, *3*, 132.

[168] Y. Zhang, Y. Zhu, Y. Li, J. Cao, H. Zhang, M. Chen, L. Wang, C. Zhang, *Hum. Mol. Genet.* **2015**, *24*, 6029.

[169] C. Fuoco, M. Salvatori, A. Biondo, K. Shapira-Schweitzer, S. Santoleri, S. Antonini, S. Bernardini, F. S. Tedesco, S. Cannata, D. Seliktar, et al., *Skelet. Muscle* **2012**, *2*, 24.

[170] P. A. Zuk, D. Ph, M. I. N. Zhu, H. Mizuno, P. Benhaim, H. P. Lorenz, *Tissue Eng.* **2001**, *7*, 211.

[171] P. Zuk, *ISRN Stem Cells* **2013**, *2013*, 1.

[172] O. DelaRosa, B. Sánchez-Correa, S. Morgado, C. Ramírez, B. del Río, R. Menta, E. Lombardo, R. Tarazona, J. G. Casado, *Stem Cells Dev.* **2012**, *21*, 1333.

[173] J.-H. Lee, D. M. Kemp, *Biochem. Biophys. Res. Commun.* **2006**, *341*, 882.

[174] J. M. Gimble, W. Grayson, F. Guilak, M. Lopez, G. Vunjak-Novakovic, *Front Biosci (Schol Ed)* **2013**, 69.

[175] V. Desiderio, F. De Francesco, C. Schiraldi, A. De Rosa, A. La Gatta, F. Paino, R. d'Aquino, G. A. Ferraro, V. Tirino, G. Papaccio, *J. Cell. Physiol.* **2013**, *228*, 1762.

[176] P. Yilgor Huri, C. A. Cook, D. L. Hutton, B. C. Goh, J. M. Gimble, D. J. DiGirolamo, W. L. Grayson, *Biochem. Biophys. Res. Commun.* **2013**, *438*, 180.

[177] Y. Zhang, O. D. King, F. Rahimov, T. I. Jones, C. W. Ward, J. P. Kerr, N. Liu, C. P. E. Jr, L. M. Kunkel, T. A. Partridge, et al., **2014**, *23*, 3180.

[178] M. Rosenwald, C. Wolfrum, *Adipocyte* **2014**, *3*, 4.

[179] J. A. Timmons, K. Wennmalm, O. Larsson, T. B. Walden, T. Lassmann, N. Petrovic, D. L. Hamilton, R. E. Gimeno, C. Wahlestedt, K. Baar, et al., *Proc. Natl. Acad. Sci.* **2007**, *104*, 4401.

[180] A. J Salgado, R. L Reis, N. Sousa, J. M Gimble, *Curr. Stem Cell Res. Ther.* **2010**, *5*, 103.

[181] S. P. Mandell, N. S. Gibran, *Expert Opin. Biol. Ther.* **2014**, *14*, 821.

[182] A. J. Engler, S. Sen, H. L. Sweeney, D. E. Discher, *Cell* **2006**, *126*, 677.

[183] A.-M. Rosca, A. Burlacu, *Stem Cells Dev.* **2011**, *20*, 1213.

[184] C. A. Dechesne, D. F. Pisani, S. Goudenege, C. Dani, *Stem Cells Regen. Med.* **2011**, 77.

[185] J. Micallef, F. Bacou, R. Boubaker, J. M. Levin, M. Chammas, L. Casteilla, Y. Reyne, J. Nougue, *Cell Transplant.* **2004**, *13*, 103.

[186] M. A. Machingal, B. T. Corona, T. J. Walters, V. Kesireddy, C. N. Koval, A. Dannahower, W. Zhao, J. J. Yoo, G. J. Christ, *Tissue Eng. Part A* **2011**, *17*, 2291.

[187] D. J. Watt, J. E. Morgan, M. A. Clifford, T. A. Partridge, *Anat. Embryol. (Berl).* **1987**, *175*, 527.

[188] J. M. Fishman, A. Tyraskis, P. Maghsoudlou, L. Urbani, G. Totonelli, M. A. Birchall, P. De Coppi, *Tissue Eng.* **2013**, *19*, 503.

[189] M. del Carmen Ortuño-Costela, M. García-López, V. Cerrada, M. E. Gallardo, *J. Cell. Mol. Med.* **2019**, *23*, 3784.

[190] E. Shoji, K. Woltjen, H. Sakurai, in *Methods Mol. Biol. 1353* (Eds: A. Nagy, K. Turksen), Springer, **2015**, pp. 89–99.

[191] J. Chal, Z. Al Tanoury, M. Hestin, B. Gobert, S. Aivio, A. Hick, T. Cherrier, A. P. Nesmith, K. K. Parker, O. Pourquié, **2016**, *11*, DOI 10.1038/nprot.2016-110.

[192] S. M. Maffioletti, M. F. M. Gerli, M. Ragazzi, S. Dastidar, S. Benedetti, M. Loperfido, T. Vandendriessche, M. K. Chuah, F. S. Tedesco, *Nat. Protoc.* **2015**, *10*, 941.

[193] S. M. Somers, N. Y. Zhang, J. B. F. Morrissette-McAlmon, K. Tran, H. Q. Mao, W. L. Grayson, *Acta Biomater.* **2019**, DOI 10.1016/j.actbio.2019.06.024.

[194] K. H. Narsinh, N. Sun, V. Sanchez-freire, A. S. Lee, P. Almeida, S. Hu, T. Jan, K. D. Wilson, D. Leong, J. Rosenberg, et al., *J. Clin.* **2011**, *121*, 1217.

[195] J. Gilbert-Honick, W. Grayson, *Adv. Healthc. Mater.* **2019**, *1900626*, 1.

[196] S. Das, K. D. Browne, F. A. Laimo, J. C. Maggiore, H. Kaisaier, C. A. Aguilar, Z. S. Ali, F. Mourkioti, D. K. Cullen, *bioRxiv* **2019**, 840124.

[197] C. J. Kearney, D. J. Mooney, *Nat. Mater.* **2013**, *12*, 1004.

[198] P. Tayalia, D. J. Mooney, *Adv. Mater.* **2009**, *21*, 3269.

[199] P. R. Kuhl, L. G. Griffith-Cima, *Nat. Med.* **1996**, *2*, 1022.

[200] S. M. Somers, N. Y. Zhang, J. B. F. Morrissette-McAlmon, K. Tran, H. Q. Mao, W. L. Grayson, *Acta Biomater.* **2019**, *94*, 232.

[201] J. Schindelin, I. Arganda-Carreras, E. Frise, V. Kaynig, M. Longair, T. Pietzsch, S. Preibisch, C. Rueden, S. Saalfeld, B. Schmid, et al., *Nat. Methods* **2012**, *9*, 676.

[202] C. S. Uhm, B. Neuhuber, B. Lowe, V. Crocker, M. P. Daniels, *J. Neurosci.* **2001**, *21*, 9678.

[203] E. Bandi, M. Jevšek, T. Mars, M. Jurdana, E. Formaggio, M. Sciancalepore, G. Fumagalli, Z. Grubič, F. Ruzzier, P. Lorenzon, *Am. J. Physiol. - Cell Physiol.* **2008**, *294*, 66.

[204] R. R. Chen, D. J. Mooney, *Pharm. Res.* **2003**, *20*, 1103.

[205] S. M. Greising, B. T. Corona, C. McGann, J. K. Frankum, G. L. Warren, *Tissue Eng. Part B Rev.* **2019**, *25*, DOI 10.1089/ten.teb.2019.0207.

[206] P. Koulen, L. S. Honig, E. L. Fletcher, S. Kröger, *Eur. J. Neurosci.* **1999**, *11*, 4188.

[207] S. Chakraborty, W. Hong, *Cancers (Basel).* **2018**, *10*, 15.

[208] S. J. P. Pratt, S. R. Iyer, S. B. Shah, R. M. Lovering, in *Methods Mol. Biol.*, **2018**, pp. 57–72.

[209] K. Matsumoto-Miyai, E. Sokolowska, A. Zurlinden, C. E. Gee, D. Lüscher, S. Hettwer, J. Wölfel, A. P. Ladner, J. Ster, U. Gerber, et al., *Cell* **2009**, *136*, 1161.

[210] E. Bassat, Y. E. Mutlak, A. Genzelinakh, I. Y. Shadrin, K. Baruch Umansky, O. Yifa, D. Kain, D. Rajchman, J. Leach, D. Riabov Bassat, et al., *Nature* **2017**, *547*, 179.

[211] S. Chakraborty, K. Njah, A. V. Pobbati, Y. B. Lim, A. Raju, M. Lakshmanan, V. Tergaonkar, C. T. Lim, W. Hong, *Cell Rep.* **2017**, DOI 10.1016/j.celrep.2017.02.041.

[212] K. I. Watt, R. Judson, P. Medlow, K. Reid, T. B. Kurth, J. G. Burniston, A. Ratkevicius, C. De Bari, H. Wackerhage, *Biochem. Biophys. Res. Commun.* **2010**, *393*, 619.

[213] A. M. Tremblay, E. Missiaglia, G. G. Galli, S. Hettmer, R. Urcia, M. Carrara, R. N. Judson, K. Thway, G. Nadal, J. L. Selfe, et al., *Cancer Cell* **2014**, DOI 10.1016/j.ccr.2014.05.029.

Vita

Jordana earned her B.S. in biomedical engineering from Rutgers University in 2013. She conducted her main undergraduate research in the lab of Dr. Li Cai (Department of Biomedical Engineering), where she studied enhancer and transcription factor control of CD44 upregulation in breast cancer stem cells. This work resulted in 1 journal publication and an undergraduate research award. Jordana also conducted research in the lab of Dr. Laura Fabris (Department of Materials Science and Engineering) studying gold nanoparticle drug delivery for cancer diagnosis and treatment as well as in the lab of Dr. Rachela Popovtzer (Bar Ilan University, Department of Biomedical Engineering) studying gold nanoparticle inter-plasmon resonance.

Jordana entered the Biomedical Engineering Ph.D. program at Johns Hopkins University in 2013 and joined the lab of Dr. Warren Grayson to focus on craniofacial and orthopedic tissue engineering. Her project, presented in this dissertation, was to develop a 3D skeletal muscle construct using a biomimetic electrospun fibrin scaffold and evaluate its regenerative potential in volumetric muscle loss defects in mice. During her time as a Ph.D. student, Jordana authored 6 journal publications (4 first author), 1 textbook chapter, and 10 conference abstracts (4 oral presentations). She was also awarded the NIH National Research Service Award fellowship.